UNIVERSITY OF SOUTHAMPTON

QUANTITATIVE MODELLING OF SPATIAL VARIABILITY IN THE NORTH ATLANTIC SPRING PHYTOPLANKTON BLOOM

John Christopher Paul Hemmings

A thesis submitted in candidature for the degree of
Doctor of Philosophy
School of Ocean and Earth Science

March 1999

UNIVERSITY OF SOUTHAMPTON

ABSTRACT

FACULTY OF SCIENCE
OCEAN AND EARTH SCIENCE

Doctor of Philosophy

QUANTITATIVE MODELLING OF SPATIAL VARIABILITY IN THE NORTH ATLANTIC SPRING PHYTOPLANKTON BLOOM

by John Christopher Paul Hemmings

The effects of variability in the physical environment on the development of the spring phytoplankton bloom are investigated using a physically forced model of the annual plankton cycle in the ocean mixed layer. The model is optimised to fit survey data from the eastern North Atlantic, collected over a 1500 × 1500 km area between 39°N and 54°N, from April-June 1991, establishing the feasibility of using spatially distributed point-in-time data in model calibration.

Measurements made below the seasonal pycnocline show the existence of an empirical relationship between preformed nitrate and salinity in this area, allowing salinity-based estimates of pre-bloom mixed layer nitrate concentration to be made. These estimates provide important additional constraints for the model. The observed spatio-temporal patterns, at scales between 36 km and 1500 km, in nutrients, chlorophyll and measures of bloom progression derived from these data with reference to pre-bloom nitrate are discussed, together with the corresponding patterns in seasonal stratification.

During the spring bloom, when biogeochemical concentrations vary rapidly in response to the developing stratification, absence of data defining its history limits the value of comparison between point-in-time observations and model results. Predictions of variation in stratification at the seasonal time-scale from general circulation models (GCMs) can be used in place of observational data to force ecosystem models. However, the degree to which observations are used to constrain the model solutions should allow for both model error in stratification and misrepresentation of the seasonal development of stratification by the observations. The latter occurs due to sampling error associated with short-term fluctuations. It can be corrected for if a suitable contemporary sea surface temperature data set is available to define the variation of mixed layer temperature at the seasonal time-scale.

It is shown that the accuracy of the GCM predictions can be improved by the application of meteorology specific to the year of observation. It is also shown that the sensitivity of the ecosystem model predictions to error in the physical forcing can be reduced by matching model and observations by a stratification measure, rather than by time, when comparing fields. The survey data show an important contribution to the stratification arising from the 'tilting' action of vertical shear on pre-existing horizontal buoyancy gradients in the winter-time mixed layer. This effect was severely underestimated by the GCM. The discrepancy can be accounted for by the absence of density fronts and mesoscale dynamics in the model.

Ecosystem model results suggest that spatial variance in zooplankton grazing, due to the effect of differences in the depth and duration of winter-time mixing on the over-wintering success of plankton populations, is one of the major factors controlling the spatial and temporal characteristics of the phytoplankton bloom.

CONTENTS

LIST OF FIGURES

LIST OF TABLES

ACKNOWLEDGEMENTS

This work was carried out part-time under the supervision of Kelvin Richards and Mike Fasham. I'd like to thank both Kelvin and Mike for many helpful and stimulating discussions and generally keeping me on the right track. In particular, I'd like to thank Mike for his guidance and understanding in the combined role of line manager and research advisor while I worked in the Institute of Oceanographic Sciences (later part of Southampton Oceanography Centre) and his continued support and encouragement thereafter.

Thanks are also due to everyone aboard the Charles Darwin on cruises CD58 and CD59 who worked extremely hard to make the Vivaldi '91 survey a great success. My thanks go out especially to Stuart Cunningham and everyone else involved in the mammoth task of working up over 700 hours of SeaSoar data, to Susan Holley for her work on the nutrient data, to Morag Stirling for keeping me sane while processing chlorophyll samples at sea on CD59 and to Tom Anderson for holding the chlorophyll processing together so well on CD58.

I am exceptionally grateful to Yanli Jia for her help with running the MICOM general circulation model and Simon Josey for his help with extracting and processing COADS data. Also my thanks extend to a number of other people who have given very constructive comments and advice on this work: Ian Totterdell, Tom Anderson, Peter Challenor, George Nurser, Mike McCulloch, Raymond Pollard and my examiners Ric Williams and Jonathan Sharples.

I'd finally like to thank all my friends and family for their patience (Trog deserves a special mention here) and most of all Sue for showing me the way, making it possible for me to take it and never letting me even think of giving up!

Chapter 1
INTRODUCTION

1.1 The Role of Plankton in the Global Climate System

In the last decade or so oceanographers have taken on a new challenge: to develop a realistic model of the ocean for the purposes of understanding its role in Earth's climate system (Mooney 1992). It is recognised that anthropogenic activities, principally fossil fuel burning and land-use changes, have led to a dramatic increase in atmospheric concentrations of radiatively active gases, with the potential to cause significant changes in climate through a warming of the planet's surface at the global scale (Intergovernmental Panel on Climate Change, 1990 & 1996). These gases are often referred to as *greenhouse gases* because they act by reducing the amount of heat escaping through the atmosphere. While anthropogenically induced changes in climate are currently difficult to measure in the presence of natural variability, the 1996 IPCC report concludes that "the balance of evidence suggests that there is a discernible human influence on global climate".

The most important of these anthropogenic greenhouse gases is carbon dioxide, the atmospheric concentration of which has increased from a pre-industrial level of about 280 ppmv to 358 ppmv in 1994 (IPCC, 1996). Only about half the anthropogenic input remains in the atmosphere. The remainder must be accounted for by increases in uptake by the ocean and by terrestrial ecosystems. An enormous amount of research effort is currently directed at improving our understanding of the roles of these sub-systems in the global carbon cycle.

Moore (1992) discusses the ocean's role in the overall system. Carbon uptake by the oceans is essentially driven by two processes, which together draw down carbon away from the surface waters and maintain a vertical gradient of dissolved inorganic carbon (DIC) in the ocean. One of these processes, known as the *solubility pump*, is the physical transport of

DIC to the ocean depths as a result of deep water formation at high latitudes. The other process is the vertical carbon flux due to biological activity, or *biological pump*, by which a proportion of the carbon fixed by primary production in the euphotic zone is eventually remineralised in deep water or in the sediments (Longhurst and Harrison, 1989). Estimates from modelling studies (Bacastow and Maier-Raimer, 1990; Shaffer, 1993) suggest that about three quarters of the difference in DIC between the surface and deep waters is attributable to the biological pump.

It is important to understand the different processes involved in the carbon cycle, in order to predict how sensitive they might be to increases in carbon dioxide and what feedbacks might result. These could be positive, increasing atmospheric concentrations and speeding up climate change, or negative, decreasing atmospheric concentrations and slowing it down. At present we do not know whether there has been any significant change in the biological pump as a result of human activities. In contrast to terrestrial ecosystems, a direct carbon fertilisation effect is considered unlikely because of the abundance of DIC throughout the ocean, although it has been shown that primary production may be carbon limited in certain phytoplankton species which are only able to take up carbon in the form of dissolved carbon dioxide gas (Riebesell *et al.*, 1993). Indirect effects resulting from climate changes induced by the increase in carbon dioxide and other greenhouse gases could be of much greater importance (Williamson, 1992). Such feedback mechanisms are not yet well understood and climate modellers are only just beginning to tentatively include them in their models (Klepper *et al.*, 1994, Sarmiento and LeQuere, 1996; Woods and Barkmann, 1993).

Finally, although most of the research into the role of plankton in the planet's climate system, is focused on the carbon cycle, this is not the only source of feedback by which changes in plankton ecology could affect climate. Another potentially important feedback mechanism which has been identified concerns the role of the biogenic gas dimethyl sulphide (DMS) in cloud formation. Charlson *et al.*, (1987) hypothesised that DMS, which is produced by most marine phytoplankton species, is the main source of cloud condensation nuclei in the marine environment. Cloud cover can have a net warming or cooling effect at the

planet's surface depending on cloud height, thickness and radiative properties (IPCC, 1996). Phytoplankton also affect the vertical distribution of solar heating of the water column by virtue of their influence on the inherent optical properties of the water (Kirk, 1988). Absorption and scattering of light by phytoplankton pigments increases the efficiency of heating near the surface. This increases water column stability, with implications for the exchange of heat, nutrients and biogenic particles between the surface layer and the ocean interior (Sathyendranath *et al.*, 1991).

At high and temperate latitudes, plankton ecology and the associated action of the biological pump and other climate system processes are dominated by seasonal variability. If the action of these processes is to be properly represented in climate models it is therefore necessary for the models to resolve, or at least parameterise, variability at the seasonal time-scale. Further understanding of this variability and the consequent changes in property fluxes is required before they can be simulated with a useful degree of confidence. One of the most obvious expressions of seasonal variability in the oceanic pelagic ecosystem is the annual increase in primary production occurring in the spring. Nowhere is this expression more dramatic than in the North Atlantic, where it is invariably associated with a large accumulation of phytoplankton standing stock (Yoder *et al.*, 1993). This phenomenon is referred to as the spring phytoplankton bloom and its simulation with reference to observational data is the subject of the present study.

1.2 The North Atlantic Spring Bloom

In, 1889 Victor Hensen set out on the German Plankton Expedition to test his hypothesis that plankton, which he was to describe as "dies blut des meeres" ("this blood of the sea"), was evenly distributed throughout the ocean in space and time and that oceanic production could therefore be estimated by a suitable sampling programme (Mills, 1989). It was after this expedition, from which he was forced to conclude that his objective was unfeasible, that the concept of the spring phytoplankton bloom was first introduced by the Kiel School of Oceanography. Now, a century later, we are able to directly observe the annual phenomenon of the spring bloom from satellites as a dramatic change in ocean colour across the whole of the temperate North Atlantic (Esaias *et al.*, 1986; U.S. JGOFS, 1989; McClain *et al.*, 1998).

The basic dynamics of the spring bloom are described in Section 1.2.1 and the various factors causing spatial variability in the bloom at scales from tens to thousands of km are discussed in Section 1.2.2. Observations and recent modelling studies of the spring bloom in the North Atlantic are outlined briefly in Section 1.2.3 and Section 1.2.4 respectively.

1.2.1 Bloom Dynamics

The major factors affecting phytoplankton growth rates in the ocean are light, nutrients and temperature. The effect of temperature on phytoplankton growth has been reviewed by Eppley (1972), who shows that we should expect temperature to set an upper limit on the growth rate of phytoplankton. However, under most conditions in the ocean, growth is either light or nutrient limited and it is difficult to obtain evidence for a temperature effect from environmental observations. Accumulation of phytoplankton biomass under favourable conditions for growth is controlled mainly by consumption or "grazing" by zooplankton. However, export from the euphotic zone as a result of physical

transport or passive sinking can also cause major losses, as indicated by the appearance of large amounts of phytodetritus on the ocean floor some weeks after the occurrence of phytoplankton blooms at the surface (Billet *et al.*, 1983). Sinking rates for phytoplankton vary greatly between species and this may be an important factor in succession. Many large diatom species for example are adapted to turbulent conditions and rely on turbulent mixing to keep them in the surface layer (Harris, 1986). In order for a phytoplankton bloom to occur primary production must exceed these losses.

In the temperate and polar zones of the North Atlantic where spring blooms occur, nutrients are abundant in the euphotic zone in winter and light is the limiting factor for phytoplankton growth. Most of the primary production in the ocean takes place in the turbulent surface boundary layer, often referred to as the surface mixed layer, or simply the mixed layer. The average amount of light available to phytoplankton cells in the mixed layer is reduced in winter due to a combination of deeper vertical mixing and reduced day length and solar elevation. It is widely accepted that the dominant factor contributing to the initiation of the bloom is the shoaling of the mixed layer due to stabilisation of the water column in spring, caused by a seasonal increase in heat input to the ocean, combined with a reduction in the input of turbulent kinetic energy from the wind stress. This theory has been formalised in terms of a *critical depth* for the mixed layer at which blooms can occur, a concept first introduced by Gran and Braarud (1935) and developed as a quantitative model of bloom initiation by Sverdrup (1953).

Sverdrup's critical-depth model is based around the idea of a *compensation depth* at which biomass gain due to photosynthesis is balanced, over a 24 hour period, by loss due to respiration. Phytoplankton cells in an actively mixing surface layer experience rapidly fluctuating light conditions and, when the mixed layer is deeper than the compensation depth, a bloom can occur only if the average primary production in the mixed layer exceeds respiration. The critical depth is defined as the mixed layer depth for which the average light intensity, over 24 hours, equals the light intensity at the compensation depth. It is assumed that photosynthesis is proportional to irradiance. In the original model, as we are reminded

by Smetacek and Passow (1990), the term respiration refers to total community respiration, whereas it has often been interpreted as phytoplankton respiration only. Smetacek and Passow argue that the term respiration is, in fact, inappropriate because community respiration does not fully account for phytoplankton losses: not all phytoplankton consumed is subsequently respired on a 24 hour time-scale and sedimentation plays a major role in removing biomass from the mixed layer. They also point out that there is no evidence to suggest that either phytoplankton respiration or grazing pressure is constant with depth, making practical use of the model difficult. The idea of a well-mixed layer is also an idealisation, as acknowledged by Sverdrup (1953). In reality, the time-scales of turbulence may not be sufficiently short, compared with time-scales of phytoplankton growth, to redistribute biomass evenly throughout the surface layer.

Despite the problems associated with the critical depth model, it is conceptually useful and has recently been extended by Platt *et al.* (1991a). These authors introduced a more realistic non-linear photosynthesis-irradiance curve and a daily irradiance cycle. They also extended the approach to determine a characteristic time scale for development of a bloom, which must be short compared with the time interval between storm events causing mixed layer deepening in order for a bloom to occur.

Global satellite imagery shows that, while spring phytoplankton blooms do occur in other temperate regions, the bloom in the North Atlantic is a much more dramatic event (Yoder *et al.*, 1993). It has been shown to deplete surface nitrate over much of the region, causing a seasonal transition between eutrophic and oligotrophic regimes (Strass and Woods, 1988; Weeks *et al.*, 1993b). Once nitrate is depleted in the mixed layer a deep chlorophyll maximum tends to become established as significant new primary production is confined to the seasonal pycnocline. New production is defined as that in which assimilated nitrogen is obtained from nitrate, as opposed to regenerated production in which ammonium is used (Dugdale and Goering, 1967). The depth of the chlorophyll maximum appears to increase during the summer as the nutrients at the top of the pycnocline are used up (Strass and Woods, 1991).

In contrast with the situation in the North Atlantic, seasonal increases in primary production at mid- and high- latitudes in the North Pacific and the Southern Ocean are not matched by a large accumulation of phytoplankton stock and nitrate is not depleted. This has led to the classification of these as high-nutrient low-chlorophyll (HNLC) regions, in contrast to the North Atlantic which is described as a low-nutrient high-chlorophyll (LNHC) region. While light limitation has been put forward as a possible explanation for the absence of a spring bloom in the Southern Ocean (Mitchell *et al.*, 1991; Nelson and Smith, 1991), it cannot explain the differences between the North Atlantic and the North Pacific where summer-time mixed layer depths and cloud cover are very similar (Fasham, 1995). This indicates that the spring shoaling of the mixed layer is not always a sufficient condition for bloom initiation.

One of the main hypotheses put forward to explain the absence of a bloom and maintenance of high nitrate concentrations in the HNLC areas, is the potential limitation of phytoplankton growth rates due to low concentrations of iron (Martin and Fitzwater, 1988). This micronutrient is important in nitrate uptake, because of its role in nitrate reduction, and in photosynthesis, because of its role in chlorophyll synthesis and electron transport. In apparent contradiction to this hypothesis, biomass specific growth rates in the HNLC subarctic region of the Pacific do not appear to be low. In fact, measurements by Welshmeyer *et al.* (1993) suggest that they are among the highest for any open-ocean environment. However, experiments in the same region (Boyd *et al.*, 1996) have shown a rapid accumulation of phytoplankton biomass following the addition of iron. These results can be reconciled in the light of evidence presented by Boyd *et al.* (1996) which indicates a size dependence in iron limitation of phytoplankton growth. Initially, small (<5 μm) celled autotrophs were dominant. Growth rates were high but rates of biomass accumulation were low, suggesting strong grazer control. The blooms observed after adding iron were dominated by large diatoms, formerly low in abundance, with growth rates increased to near their theoretical maximum. No corresponding increase was observed in the growth rates of the

smaller phytoplankton. The blooms occurred despite a high abundance of micro- and meso-zooplankton grazers, probably due to the development of cells which were too large for grazing at a significant rate by the microzooplankton. Similar results have been obtained from experiments in the HNLC region of the equatorial Pacific (Chavez *et al.*, 1991; Price *et al.*, 1994). It is possible that under natural conditions, low iron concentrations may prevent a spring bloom in the North Pacific by favouring smaller-celled algae which are grazed more efficiently by fast growing microzooplankton, thus allowing a balance between production and consumption to be maintained as the mixed layer shoals.

Other hypotheses put forward to explain the differences between the northern basins concern aspects of the zooplankton ecology which might cause a mismatch between production and consumption in the Atlantic, but not in the Pacific. Differences in grazing rates (Frost 1987,1991,1993; Miller *et al.*, 1991) and differences in the size of over-wintering zooplankton populations (Evans and Parslow, 1985; Fasham 1995) have both been invoked, the latter potentially arising as a consequence of much deeper winter-time mixing in the North Atlantic than elsewhere.

1.2.2 Spatial Variability

The mechanisms which generate spatial pattern in plankton abundance can be classified as vectorial, co-active, reproductive, social and stochastic (Hutchinson, 1953; Haury *et al.*, 1978). Haury *et al.* considered the stochastic mechanism as a factor inherent within the other four mechanisms rather than as a separate process in its own right. The vectorial class covers all passive transport of organisms as a result of the physical dynamics of the ocean. Co-active processes include grazing, predator-prey interactions, parasitism and competition. Each of these mechanisms has the potential to generate pattern acting in isolation, but the actual patterns of variability in the marine environment are the consequence of a complex interaction between all four. Because plankton and the nutrients on which they depend tend to move passively with the water, physical variability is normally seen as the driving force. Different species have evolved different physiological

and behavioural responses to cope with variability in the physical environment at a range of frequencies, from annual cycles to the rapid fluctuation in light conditions experienced by phytoplankton in the mixed layer. Aspects of this variability can be seen as resources which are exploited more or less effectively by different species, potentially determining the outcome of competition (Harris, 1980). With regard to the spatial scales of variability, Denman and Powell (1984) suggested as a generalisation that the important physical processes with respect to a particular biological process are a subset of those having similar time scales. The spatial scales of these physical processes then determine the spatial scales of the biological response.

Basin-scale variability in the characteristics of the North Atlantic spring is best summarised with reference to the biogeochemical domains defined by Longhurst (1995). The area in which spring blooms occur is divided between the *westerlies* domain to the south of the Polar Front, which separates the sub-polar and sub-tropical gyres, and the *polar* domain to the north. Within the polar domain, seasonal ice melt causes the development of a brackish layer which has a stabilising effect on the water column. The influence of melt water extends southwards from the ice edge as lenses of low salinity water are transported around the sub-arctic gyre. The enhanced stability can lead to blooms as early as those much further south, despite lower levels of solar irradiance at the sea surface. In this domain, nutrient concentrations are high, due to a combination of deep winter mixing (Glover and Brewer, 1988) and Ekman upwelling (McClain and Firestone, 1993). Primary production is mainly light limited and shows a summer maximum. In the westerlies domain, the important physical characteristics are seasonality in heat flux and wind stress, which cause a deepening of the mixed layer in winter, entraining nutrients and setting up the conditions for a bloom when the layer shoals again in spring. In this domain there are typically spring and autumn blooms with a nutrient limited period of low production during the summer.

Winter-time mixed layer nutrient concentration estimates (Glover and Brewer, 1988) show the existence of strong latitudinal gradients in major nutrients (nitrate, phosphate and silicate) over much of the westerly domain. These patterns, together with variability in

mixed layer depth caused by weather patterns and the gyre-scale circulation, in particular the Gulf Stream and its downstream expression to the north-east as the North Atlantic Drift, are the most obvious factors contributing to variability of the spring bloom at sub-basin scales.

Biological and chemical concentrations in the ocean are highly variable at much smaller scales too. Watson *et al.* (1991) have shown that spatial variability at scales less than 100 km could be a significant source of error in estimating global carbon fluxes from existing data. Satellite images of ocean colour show that patchiness in phytoplankton abundance on scales of tens to hundreds of km is ubiquitous and clearly related to features in the turbulent flow (Gower *et al*, 1980). This range of scales spans the peak in the kinetic energy spectrum of the ocean associated with *geostrophic turbulence*, which exceeds that associated with the ocean gyres by a factor of nearly 100 (Woods, 1980). The physical dynamics at this scale, often referred to as the ocean mesoscale, is dominated by eddy features which, to a first approximation, exist in *geostrophic balance*: a state in which the water motion is such that the Coriolis force due to the Earth's rotation balances pressure gradients in the fluid and flow is along iso-lines of geopotential. Mesoscale eddies have widely varying properties (Allen *et al.*, 1991). Diameters from less than 10 km to around 200 km have been recorded. Maximum flow rates can sometimes be more than 1 m s^{-1}, although speeds in the order of 10 cm s^{-1} are more typical. They occur in all areas of the ocean although there is great regional variability in the intensity of eddy activity, with a maximum in regions of permanent fronts and western boundary currents (Robinson, 1983).

The main mechanisms for eddy generation are *baroclinic instability*, where the eddy kinetic energy is derived from available potential energy associated with inclined density surfaces, and *barotropic instability* resulting from shear in the mean flow field, where eddy kinetic energy is derived from mean flow kinetic energy. Strass *et al.* (1992) presented evidence for a seasonal increase in mesoscale variability in the North Atlantic Drift region, which they attributed to enhanced conditions for baroclinic instability as a consequence of seasonal pycnocline formation in a baroclinic environment. Variations in the wind stress at

the sea surface can be another important source of eddy activity, particularly in mid-ocean regions away from major fronts. Eddies can also spin up as a consequence of subduction of water bodies as they are advected downwards along sloping isopycnals (Woods, 1985). This occurs when the stratification of the subducted water parcel is different from the surrounding water. The water parcel will tend to stretch or compress in the vertical, under gravity, such that the stratification anomaly is decreased. During this process, known as *geostrophic adjustment*, the change in spacing between isopycnals is accompanied by a change in *relative vorticity* (i.e. the vertical component of the vorticity relative to the rotating earth) such that the *potential vorticity* of the water parcel is conserved (Rossby, 1940; Ertel, 1942). Cyclonic eddies can be formed by subduction of strongly stratified water from the upper pycnocline, as the enhanced stratification gives the water a high potential vorticity. However, eddies generated by subduction are more commonly anticyclonic, having a core of low potential vorticity water formed by mixing in the surface boundary layer (Allen *et al.*, 1991).

It is chaotic interaction between eddies which leads to the existence of a geostrophic turbulence field in the ocean. Some aspects of this field can be understood with reference to two-dimensional turbulence theory (Kraichnan, 1967, 1971; Kraichnan and Montgomery, 1980) which predicts an *enstrophy cascade* by which turbulence transfers *enstrophy* (vorticity variance) from a source region in wave number space to higher wave numbers over an *inertial range*. The application of two-dimensional turbulence theory to geostrophic turbulence, in which stratification effects and the Coriolis force must be considered, is discussed by Rhines (1979), who argued that an inertial range would exist for *potential enstrophy* (potential vorticity variance) in mid-ocean areas away from major fronts. This inertial range extends from the source region in wave-number space around 100 km, to length scales of around 1 m at which potential enstrophy is destroyed by processes which cause overturning of density surfaces (Woods, 1980).

The characteristics of spatial patchiness which might be expected from the interaction between two-dimensional turbulence and phytoplankton growth have been

investigated by Bennett and Denman (1985). Their work suggests that non-conservative biological processes cannot introduce patterns which persist against a background of mesoscale turbulence and that phytoplankton behaves largely as a passive tracer over the inertial range. Analysis of the relationship between ocean colour images and corresponding images of sea-surface temperature provides supporting evidence for this theory (Denman and Abbot, 1988; 1994). However, at scales above the inertial range, Bennett and Denman (1989) showed using mixing length theory, in which turbulence is parameterised by an eddy diffusion coefficient, that interaction between annual plankton cycles and mesoscale turbulence might cause the development of patchiness on scales of several hundred km.

As well as affecting the spatial distribution of phytoplankton by means of horizontal transport, mesoscale variability also affects phytoplankton growth rates. It does this by introducing vertical velocities in the flow field and influencing the depth of boundary layer mixing. Both of these effects have implications for light availability in the mixed layer and the exchange of nutrients and phytoplankton biomass between this surface layer and the ocean interior. Patchiness in mixed layer depth can be caused by patterns of shear instability at the base of the mixed layer resulting from interaction between geostrophic turbulence and the wind-driven flow (Klein and Hua, 1988). Such interaction also causes Ekman upwelling and downwelling, as a consequence of horizontal divergence in the boundary layer flow (Walstad and Robinson, 1993). These vertical velocities, of the order of tens of cm per day, are of ecological importance in their own right as well as generating significant spatial patchiness in mixed layer depth on time scales of weeks to months, by modifying the entrainment velocity at the base of the mixed layer. The ecological effects of this patchiness have been investigated in a modelling study by Smith *et al.* (1996). Vertical Ekman velocities are also caused by variations in the wind-stress patterns themselves and upwelling generated in this way can be an important source of nutrients in mid-ocean oligotrophic regions (Falkowski *et al.*, 1991), as well as producing eddies by distorting the subsurface stratification. Away from the mid-ocean regions, vertical advection of a similar magnitude is associated with the frictional decay of eddies formed as meanders are cut off from unstable

density fronts. The upwelling in the interior of anti-cyclonic eddies of this type can likewise provide an important supply of nutrients to the euphotic zone (Nelson *et al.*, 1989).

The vertical velocities associated with the processes described above are relatively weak compared with those which occur as eddies interact. Straining of potential vorticity patterns in the horizontal deformation field associated with geostrophic turbulence causes fronts to develop and intensify. Vigorous mesoscale frontogenesis occurs throughout the ocean, producing transient mesoscale jets of up to 100 km in length on time scales of a few days (Woods, 1988). These features typically persist for several weeks and often develop instabilities with wavelengths of 10-100 km. Vertical velocities associated with the smaller scale ageostrophic dynamics of the fronts between eddies are greater than those in the eddy interiors by typically two orders of magnitude. Modelling studies (e.g. Onken, 1992; Wang, 1993; Zhang and Nurser, 1995) imply vertical velocities of 10-100 m d^{-1} and these are supported by calculations based on survey data from frontal regions which indicate similar values (Pollard and Regier, 1990; 1992). Vertical intrusions of chlorophyll, often extending to depths of more than 200 m, have been attributed to downwelling at fronts (Fasham *et al.*, 1985; Pollard and Regier, 1992; Zhang and Nurser, 1995). Injection of nutrients as a result of upwelling at mesoscale fronts has been put forward by Strass (1992) as the probable cause of observed patchiness in the deep chlorophyll maximum at scales of around 20 km. Modelling studies support this interpretation, suggesting that vertical nutrient fluxes associated with frontal dynamics are likely to be of much greater significance than the fluxes associated with the upwelling in eddy interiors (Kishi, 1994; McGillicuddy *et al.*, 1995b; McGillicuddy and Robinson, 1997).

While the vertical velocities associated with frontal dynamics contribute to exchange between the mixed layer and the interior, ageostrophic vertical shear in the horizontal flow tends to enhance stability, leading to a reduction in the spatially averaged mixed layer depth in the region of the front (Nurser and Zhang, in revision). This has implications for light availability and can potentially lead to a major increase in primary production in a eutrophic environment as demonstrated in a modelling study by Lévy *et al.* (1998).

Finally, in discussing the ecological significance of eddies, Angel and Fasham (1983) make an important distinction between advective eddies with closed circulations (often referred to as rings), which are formed as loops split off from meandering currents, and features such as wind-generated eddies which are propagated across ocean basins in the form of Rossby waves (Gill, 1982). The latter cause transient changes to the water through which they pass on a time scale of weeks to months. In contrast, closed eddies typically persist for much longer (months to years) and can transport the enclosed water body into areas where the physical and/or biological environment is rather different from the source region, causing changes in its ecology. Tranter *et al.* (1980), for example, observed high productivity in a warm-core ring shed from the Australian current, which they attributed to the transport of the core water into a region where the atmosphere was colder, causing deeper mixing and the import of previously unavailable nutrients. Angel and Fasham (1983) suggest diffusive colonisation of the eddy by populations from the surrounding water as another potentially important ecological process.

1.2.3 Observations

Satellite imagery of the spring bloom has been obtained by the Coastal Zone Colour Scanner (CZCS) from 1979-1986 (Esaias *et al.*, 1986) and more recently by SeaWiFs, launched in Autumn 1997 (McClain *et al.*, 1998). These images provide the only basin scale coverage of the event and are vital for extrapolating carbon flux estimates to the scales required for global analysis. However, they give insufficient information for modelling the processes involved in the bloom's development in order to derive these estimates. Little progress could be made without additional data from *in situ* surveys. The available observational data relating to the North Atlantic spring bloom is reviewed briefly in this section.

Seasonal and interannual variability in plankton populations in the North Atlantic are well characterised by a long time series of Continuous Plankton Recorder samples from

voluntary observing ships established in the 1940s (Colebrook, 1982). Some early observations aimed specifically at investigating the relationships between biogeochemical and physical variability over the annual cycle were made during the 1970s at Ocean Weather Station India, located in the Iceland Basin at approximately 60°N 20°W (Williams and Robinson, 1973; Williams 1988). The first study of the impact of mesoscale eddies on biogeochemical properties during the North Atlantic spring bloom was an investigation of a cyclonic cold-core eddy in May 1985 (Mittelstaedt, 1987; Lochte and Pfannkuche, 1987; Beckmann *et al.*, 1987). The eddy was a feature 'cut off' from a meander of the Polar Front and, in common with previous investigations of Gulf Stream rings, the nutrient chemistry and biological populations observed during this survey showed marked differences between the eddy interior and the surrounding water.

With the aim of investigating the relationships between the development of the phytoplankton bloom and seasonal stratification on a larger scale, a series of latitudinal transects were carried out between the Azores and Greenland in the mid 1980s, at different times during spring and summer (Strass and Woods, 1988, 1991). The Kiel "Sea Rover" system was used to obtain high resolution vertical hydrographic sections, including chlorophyll *a* fluorescence as a measure of phytoplankton biomass. These surveys included two repeat transects in late April 1985. The first of these, heading north, showed an early bloom between about 47°N and the end of the data record at 50.5°N. The second transect, heading south, showed that the bloom, though patchy, was evident almost everywhere south of about 51°N. The chlorophyll distribution showed some correlation with spatial patchiness in seasonal stratification, supporting the hypothesis of bloom initiation as a response to the shoaling of the mixed layer. A transect carried out in June/July 1986 appeared to show three different phases of the bloom. North of the Polar Front at 52°N there was little sign of a bloom and nitrate was still fairly high (about 60% of winter-time nitrate estimates). A bloom was observed to the south of the Polar Front as far south as 46°N, but to the south of this nitrate was depleted at the surface and a deep chlorophyll maximum was established. A late summer transect in 1984 showed a deep chlorophyll

maximum, typical of an oligotrophic regime, extending all the way from the Azores to the Polar Front.

A much more comprehensive survey of the spring bloom, on the 20°W meridian, was undertaken by the international community in 1989 as part of the Joint Global Ocean Flux Study (JGOFS) project. A smaller survey of the bloom in the western North Atlantic was also carried out in the same year for comparison (Harrison *et al.*, 1993) and together these surveys comprised the JGOFS North Atlantic Bloom Experiment (NABE, Ducklow and Harris, 1993). The eastern survey included meridional transects between about 42°N and 60°N at approximately monthly intervals from April to August (Weeks *et al.*, 1993b) and intensive studies at 47°N (Lochte *et al.*, 1993) and 59°N (Weeks *et al.*, 1993a) spanning the entire bloom period. Some additional observations were made at 18°N, 33°N, 40°N and 72°N.

NABE observations provided further support for the link between bloom initiation and the development of seasonal stratification. Evidence of a spring phytoplankton bloom was found as far south as 33°N, although oligotrophic conditions were established here by late April (Passow and Peinert, 1993). By late July, surface nitrate was depleted up to 53°N (Weeks *et al.*, 1993b). Observations at 47°N and along the meridional transects up to 60°N showed the initial phase of the bloom to be dominated by diatoms. At 47°N the diatom bloom was succeeded by blooms of smaller phytoplankton, following depletion of silicate in advance of nitrate (Sieracki *et al.*, 1993). Diatoms have an absolute requirement for silicate in their metabolism and it is used in the formation of silica shells or valves (Lewin, 1962). Evidence was presented for a similar pattern of succession further north (Weeks *et al.*, 1993b). The late oligotrophic phase of the bloom when stratification was well developed was dominated by flagellates and dinoflagellates. Maximum primary production at 47°N was associated with the earlier diatom-dominated community (Lochte *et al.*, 1993) and the maximum productivity observed at stations along the transect line between 47°N and 60°N

was similarly associated with large phytoplankton species (>5 μm) (Joint *et al.*, 1993). Intense heterotrophic activity was observed throughout the phytoplankton bloom. The dominant grazers were microzooplankton (Lochte *et al.*, 1993; Burkill *et al.*, 1993; Weeks *et al.*, 1993a), mesozooplankton grazing accounting for just a few percent of primary production (Morales *et al.*, 1991; Dam *et al.*, 1993).

The 1989 NABE investigation made some important contributions to our understanding of the biological pump, confirming that the variability in carbon dioxide concentrations in the surface ocean is closely linked to the dynamics of the spring bloom (Watson *et al.*, 1991; Robertson *et al.*, 1993) and providing useful data relating to vertical carbon fluxes (Buesseler *et al.*, 1992; Martin *et al.*, 1993, Passow and Peinert, 1993). Evidence was obtained for important contributions from sinking particulate material in the form of mesozooplankton faecal pellets (Lenz *et al.*, 1993; Weeks *et al.*, 1993a) and viable diatoms (Passow and Peinert, 1993). The efficiency of CO_2 depletion in the mixed layer observed at 47°N, 75% of production, was surprisingly high considering the high microbial biomass and regeneration rates and carbon budgets could not be closed using vertical flux estimates obtained from sediment trap data. This problem may be attributed to the effects of mesoscale variability. However, analysis of a more comprehensive data set from Bermuda, for which the same problem occurs, favours one or both of two alternative explanations (Ducklow *et al.*, 1995): firstly, that there is a systematic bias in the sediment trap estimates and, secondly, that the export of dissolved organic carbon plays a major role.

One of the problems encountered during the 1989 NABE study was the distorting effect of mesoscale eddies on the time series data collected at the main study sites. Satellite altimeter data revealed 3 interacting cyclonic eddies in the region of the 47°N study site (Robinson *et al.*, 1993) and, despite the Lagrangian nature of the main sampling programmes, which followed float trajectories, interpretation was complicated by the influence of different water masses. With these problems in mind, a Lagrangian survey of the spring bloom, involving co-ordinated spatial and temporal sampling, was carried out in 1990 as part

of the UK Biogeochemical Ocean Flux Study (BOFS) project. A set of drogues were deployed within the interior of a warm-core anticyclonic feature, with the aim of following the progress of the bloom within a discrete body of water over the two month survey period (Savidge *et al.*, 1992). Most of the drogues stayed grouped within the core for the first week of the experiment, after which they were observed to diverge in three main groups, each apparently following different streams in a complex flow pattern. The bloom developed slowly at first within the warm-core eddy but appeared to accelerate rapidly, about 3 weeks into the survey, as the marker drogue moved into a boundary region where water column stability was greater. The drogue appeared to remain within the influence of this boundary region, where the warm-core eddy interacted with a cyclonic cold-core eddy, for the remainder of the survey. A sharp decline of the bloom, observed after less than a week, was attributed more to the advective influence of another water body water in the region of the marker drogue than to biological change. In general, the study served to underline the difficulties of separating temporal and spatial variability and the need for better understanding of the ways in which mesoscale dynamics influence the development of the bloom.

A further contribution of the BOFS programme to our understanding of the role of phytoplankton in the carbon cycle was made by a survey of a large bloom of the coccolithophore *Emiliania huxleyi*, occurring south of Iceland in June 1991 (Holligan *et al.*, 1993). In contrast to production in other phytoplankton groups, coccolithophore production is associated with calcification as the organisms produce "shells" composed of calcite plates called coccoliths. The BOFS study demonstrated that this process is a strong source of carbon dioxide, increasing the partial pressure of the gas at the ocean surface as a result of changes in alkalinity, thereby reducing the air-sea flux. Enhanced surface heating due to the light scattering effect of free coccoliths, present at the surface for about 3 weeks after the 1991 bloom, would have caused an additional reduction. The increase in carbon dioxide concentration as a result of the coccolithophore bloom, following an initial reduction during a diatom bloom, was estimated to have caused a 15% reduction in the draw down of atmospheric carbon dioxide over the summer, when compared with a scenario without

coccolithophores (Robertson *et al.*, 1994). The production of coccoliths allowed the extent of the bloom to be mapped from AVHRR visible range satellite images, showing that it covered an area in the order of 1000 km from east to west and several hundred km from north to south. This emphasises the importance of the phenomenon at basin scales.

Also in 1991, but further south, the World Ocean Circulation Experiment (WOCE) survey, Vivaldi, provided observations of spatio-temporal patterns in the spring bloom in the form of an unprecedented 9900 km of high resolution transect data, including vertical sections to a depth of about 500 m, covering an area 1500 km by 1500 km (Pollard *et al.*, 1991). Carbonate system measurements were made during the first half of this survey and are analysed by Ríos *et al.* (1995). Chlorophyll and nutrient observation from both parts of the Vivaldi 1991 survey, together with the hydrographic data, comprise the data set on which the present study is based and a detailed analysis is presented in Chapter 2.

1.2.4 Modelling

Wroblewski (1989) showed that it was possible to reproduce the major features of the basin-scale spring bloom patterns, as represented by climatological CZCS data, using a simple 3 compartment NPZ model (Wroblewski *et al.*, 1988). This type of model represents nitrogen flows in the mixed layer between nitrate, phytoplankton and zooplankton pools. The model is configured as a set of zero-dimensional models, each representing the dynamics of the plankton ecosystem at a single location. (The individual models are described as one-dimensional by the author. However, they do not resolve vertical structure and so they are referred to here as zero-dimensional models in order to distinguish them from other models which do.) The model was forced by spatially varying time series of mixed layer depth, determined from observed hydrographic profiles (Levitus 1982), and latitudinally varying time series of solar irradiance at the sea surface. Initial conditions were given by a steady state solution corresponding to February conditions, in which the total nitrogen in the system was determined from observed profiles according to the winter-nutrient estimation method of Glover and Brewer (1988).

While Wroblewski's model was restricted to the spring bloom period from February to June, a more sophisticated 3-D modelling approach by Sarmiento *et al.* (1993) provides a basin scale simulation of the complete annual cycle. A solution for a repeating annual cycle, approximating a steady state, was obtained for a seven compartment nitrogen model (Fasham *et al.*, 1990) embedded within an ocean general circulation model. The seven compartment model differs from the simple NPZ model by the inclusion of ammonium, detritus, bacteria and dissolved organic nitrogen (DON) pools. This study was presented as a first step towards the development of a generic ecosystem model capable of simulating annual plankton cycles at ocean basin scales. Such a model would have a single spatially uniform biological parameter set, spatial variability being determined by its physical forcing. In this study, parameters for the nitrogen model were obtained by tuning the zero-dimensional model to fit time series data from Bermuda station 'S' (Fasham *et al.*, 1990). Although a number of problems were noted, the model was able to give a reasonable representation of spatial and seasonal variability in the CZCS data and of annual cycles at both Bermuda station 'S' and Ocean Weather Station India (Fasham *et al.*, 1993). Some of the discrepancies between model and observations could be attributed to deficiencies in the physical simulation. Overall, the results were encouraging with regard to the feasibility of developing generic models.

A number of other modelling studies have been carried out in an attempt to quantitatively reproduce the observations obtained during the 1989 North Atlantic Bloom Experiment. Contributions have been made by Maara and Ho (1993), Taylor *et al.* (1991,1992,1993), Taylor and Stephens (1993), Stramska and Dickey (1994), McGillicuddy *et al.* (1995a,b) and Fasham and Evans (1995a), The major contributions of relevance to the present study are described below.

Taylor *et al.* (1991), coupled a simple phytoplankton model with a model of the carbonate system in seawater in order to investigate the influence of annual cycles of phytoplankton growth on carbon dioxide concentration in the surface ocean. The plankton

model has phytoplankton and nutrient compartments only, the effect of zooplankton grazing and other phytoplankton mortality being introduced by a seasonally varying forcing function. In contrast with the models described above therefore, zooplankton grazing pressure is not directly coupled to prey concentration. The model is one-dimensional, in the sense that it includes a separate "thermocline" layer below the mixed layer for the purposes of modelling the development of the deep chlorophyll maximum following nutrient depletion in the mixed layer. The physical forcing functions required for the model are annual cycles of mixed layer depth, solar irradiance and temperature.

Latitudinal variation in the annual biogeochemical cycles simulated by the model was investigated by introducing latitudinal variation in the amplitudes of the various forcing functions, other physical model parameters and sub-thermocline nutrient concentrations. Parameters representative of latitudes 0°N, 35°N, 47°N and 60°N (including minima and maxima for the forcing functions) were taken from the literature and values for intermediate latitudes were interpolated linearly. With the exception of the mortality function limits, biological parameters were spatially uniform. However, the approach is somewhat different from the "generic ecosystem model" approach of Sarmiento *et al.* (1993). The authors were able to obtain annual primary production figures in general agreement with observational estimates at Ocean Weather Station India (60°N) and Bermuda (32°N), although the model results are rather sensitive to the mortality parameterisation. Comparisons between model results and NABE chlorophyll and carbon dioxide data from 47°N and 60°N show that the model represents the relationship between the two variables well although it was unable to correctly predict the timing of the 1989 bloom without making adjustments to the mixed layer depth forcing function.

Some further experiments were carried out by applying a simpler model which was solved analytically (Taylor *et al.*, 1992). These results were compared with NABE observations of phytoplankton abundance, carbon dioxide concentration and oxygen saturation during May 1989 along a transect between 47°N and 60°N and in the area around

60°N. They showed that many of the essential features of the NABE observations could be reproduced with no temporal variation in physical forcing, the timing of the bloom being determined by prescribed initial conditions in April and latitudinal variation in model parameters.

The other modelling studies described here concentrated more on the plankton dynamics rather than the effect of the bloom on the carbonate system. Taylor *et al.* (1993) carried out a modelling investigation of seasonal succession for the purposes of interpreting the observed appearance and disappearance of various plankton groups and the utilisation of nutrients along the 20°W meridian during the NABE surveys. The model used was a size structured model of plankton interactions in the mixed layer with 12 compartments representing various planktonic groups, silicate, nitrate, ammonium, DOC and detritus. Mesozooplankton grazing was imposed as an external forcing function with prescribed seasonal variations in total grazing pressure and the proportions of different plankton grazed. In the simulation small, fast growing phytoplankton (phytoflagellates and picophytoplankton) dominate the early phase of the bloom but are soon brought under control by micrograzers (microzooplankton and heteroflagellates) which responded rapidly. The small phytoplankton groups are then succeeded by diatoms, the next fastest growers. The diatom bloom phase ends with the depletion of silicate. The diatoms are then succeeded briefly by the small phytoplankton groups, presumably recovering after a predator-prey cycle, before the larger, slow growing dinoflagellates become dominant. This pattern was reproduced at all latitudes (47°N-60°N). The results are generally consistent with the NABE observations and indicate that the fact that nitrate was not used up at 60°N in 1989 can be explained without the need to invoke hypotheses involving limitation by a trace nutrient such as iron.

The modelling work of McGillicuddy *et al.* (1995a,b) directly addressed the issue of discriminating between temporal and spatial variability in the presence of the mesoscale eddy field. These authors carried out simulations of data collected in late April and May

1989 at the 47°N NABE study site. The observations were obtained from sampling two different water masses, in which the pre-bloom nitrate concentration of the mixed layer was estimated to differ by as much as 2.6 mmol m^{-3}, and could be conveniently divided into two separate time series. While the later time series was confined to a homogenous water mass in the interior of a cold-core cyclonic eddy, the earlier time series was collected from water outside this closed feature and showed more variable hydrography. The time series were first simulated by two separate integrations of a one-dimensional model with appropriate initial conditions for each water mass (McGillicuddy *et al.*, 1995a). This simulation showed discrepancies associated with the influence of mesoscale variability in the first time series, but a more sophisticated 3-D simulation (McGillicuddy *et al.*, 1995b), in which the 1-D model was coupled to a quasi-geostrophic model, was able to reconcile the model results with the observations. The simulation also illustrates how the 3-D effects of mesoscale variability become much more important as mixed layer nitrate is used up, because of the introduction of new nitrate by vertical water movements, especially those associated with interaction between eddies.

While McGillicuddy *et al.* (1995a) calibrated their model to the NABE data by carrying out a large number of experiments with different parameter values, Fasham and Evans (1995a) introduced numerical optimisation techniques to the calibration problem. They fitted the seven compartment mixed layer model of Fasham *et al.* (1990) to mixed layer observations at 47°N. In this exercise, all of the available data from the study site was used and mesoscale variability was treated as a noise signal superimposed on the seasonal dynamics. In contrast with other modelling studies of the 1989 bloom which imposed arbitrary initial conditions for plankton concentrations, within reasonable bounds, initial conditions in this study were determined by simulating a steady state annual cycle. Levitus 1982 data was used to define the annual cycle of mixed layer depth required for forcing the model and these data were augmented with observational estimates of mixed layer depth from the NABE survey to improve the phase match between the forcing and observations.

Correctly simulating the timing of the bloom in response to physical forcing is complicated by the effect of the diel cycle in mixed layer depth as illustrated by the modelling experiments of Taylor and Stephens (1993). They showed that the introduction of a diel cycle could change the timing of the simulated bloom by about a week. This, together with other effects of physical variability not represented in the ecosystem model forcing functions must be considered with regard to their potential for biasing parameter estimates during model calibration.

1.3 Project Overview

One of the ways in which the goal of understanding the role of the marine biosphere in the global climate system is being addressed, within the research community, is by attempts to construct physically forced models of a hypothetical generic ecosystem, which capture the important dynamics of the real pelagic ecosystems throughout the world ocean. Such models can be embedded in general circulation models, as demonstrated by Sarmiento *et al.* (1993), and allow us to build on our relatively good understanding of physical variability. The feasibility of developing ecosystem models which are geographically robust, in the sense that they can produce reasonable simulations for any location with a single fixed parameter set, is at present unclear (Fasham, 1993).

Given a candidate model, determination of suitable parameter values is not a trivial problem. While it is possible to determine certain ecosystem model parameters by direct measurement, other parameters are either impossible to measure directly or too inherently variable for mean values to be estimated with any useful degree of confidence from the available observations. These parameters are normally treated as free parameters and optimised to fit particular data sets, either by tuning parameters individually (e.g. McGillicuddy *et al.*, 1995a) or by making use of automated optimisation techniques (Fasham and Evans, 1995a,b; Hurtt and Armstrong, 1996). In these studies, parameters have been optimised to fit time series data at single locations. There is an inevitable risk that parameters obtained in this way will be biased to these locations and may not be applicable to wider areas such as ocean basins or the global ocean. In order to estimate parameters which are more generally applicable it is necessary to increase the spatial coverage of the observational data used. Good time series data are however very sparse and one of the ways in which the observational data sets might be extended is to make use of data from wide-area surveys. A major aim of this study is to investigate the practical problems involved in fitting ecosystem models to point-in-time data from this type of survey.

The Vivaldi 1991 survey data is ideal for this purpose because of its good spatial coverage, corresponding roughly to the North Atlantic Drift biogeochemical province defined by Longhurst (1995). The survey covers the period of the spring bloom which is, as demonstrated by the North Atlantic Bloom Experiment, an important event with respect to the function of the biological pump. This provides an additional motivation for studying the data set in that it should contribute to our understanding of the bloom and the role it plays in the global climate system. To this end, the spatio-temporal variability shown by the data set is examined and the data is used to calibrate a simple candidate ecosystem model. A modelling investigation is then carried out for the purposes of gaining greater insight into how the patterns might have developed. The aims of the study may be broken down into four main components as follows.

1) To develop a method for fitting a simple ecosystem model to spatially distributed survey data, which covers a large area of ocean but provides only point-in-time observations at each location, and to investigate problems associated with the use of such data.

2) To investigate the spatio-temporal patterns in biogeochemical concentrations and seasonal stratification exhibited by the Vivaldi 1991 survey data and examine the relationships between them.

3) To determine the extent to which the observations of the spring bloom may be reproduced using a simple candidate ecosystem model with a single parameter set.

4) To identify processes which are potentially important in controlling patterns of bloom development in the eastern North Atlantic.

The Vivaldi data set is analysed in Chapter 2, both to address the second aim of the study and to provide data products for use in calibrating the ecosystem model. The modelling investigation is presented in Chapter 3 and the final conclusions of the study are outlined in Chapter 4.

Chapter 2
THE VIVALDI 1991 SURVEY

2.1 The Vivaldi '91 Data Set

In 1991, a total of 9900 km of high resolution transect data from a 1500 km by 1500 km area of the eastern North Atlantic was collected during the Vivaldi trial survey (Pollard *et al.*, 1991), during the period of the spring bloom. The data set consists of a series of quasi-meridional transect legs between 39°N and 54°N observed between 25th April and 10th June (Figure 2.1), starting at station B48 and finishing at station A54. Transect legs were spaced 300 km apart relative to the 20°W meridian and labelled W, X, Y, Z, A, B from west to east. The southern part of legs X to B, below 48°N, were sampled in reverse order in late April and early May during cruise CD58. Leg W and the northern parts of legs X to A were sampled in late May and early June on cruise CD59. Zonal sections linking these legs were also sampled including two repeated sections at 48°N which were sampled first on CD58 and again some weeks later on CD59. Each continuous transect was 300 km long and this distance was covered in a little less than one day (typically about 20 hours). Approximate times and locations of each 300 km transect are shown in Table 2.1.

For each of the transects there are vertical sections of temperature, salinity, chlorophyll fluorescence and photosynthetically available radiation (PAR) from a towed undulator (SeaSoar) to a depth of 500 m and current velocities and acoustic back-scatter from an Acoustic Doppler Current Profiler (ADCP) to a depth of about 300 m. Continuous measurements of surface temperature, salinity and chlorophyll fluorescence are available from the ship's pumped sea-water supply. Surface nutrients were measured by taking water samples from the pumped supply at intervals of 15 minutes on CD58 and 30 minutes on CD59 giving spatial resolutions of about 4 and 8 km respectively. The high resolution

underway survey was complemented by deep CTD stations every 3 degrees of latitude, giving full depth hydrographic data (including nutrients, oxygen and chlorophyll) covering the survey area at a grid spacing of approximately 300 km.

Chlorophyll *a* concentration was derived from the *in-situ* measurements of chlorophyll *a* fluorescence. The fluorescence yield (fluorescence per unit pigment concentration) of phytoplankton chlorophyll is highly variable when measured *in vivo*, being dependent on factors affecting photosynthetic activity such as species composition, photo-adaptive state and physiological state of the phytoplankton (Strass 1990). Frequent water samples are therefore required for calibration purposes. Surface water samples were drawn for pigment analysis at approximately hourly intervals during the transects and used in conjunction with in situ PAR data to calibrate the fluorescence measured on the SeaSoar. This calibration, based on surface samples, allows for the variation of fluorescence with depth due to daylight quenching but does not allow for changes with depth due to factors such as species composition or the ratio of chlorophyll *a* to other fluorescent pigments. It must therefore be expected to be less accurate below the mixed layer. Further details of the fluorescence calibration are given in Appendix A. Information regarding the calibration and quality control of the other data from the Vivaldi '91 data set used in this study can be found in Griffiths *et al.* (1992) and Cunningham *et al.* (1992).

In principle, because it covers such a large area to such a high resolution, this data set provides a good sample for use in examining relationships between the development of the spring bloom and various aspects of the physical environment at different spatial scales, with the aim of increasing our understanding of the extent to which the bloom is physically controlled. There are however a number of limitations that must be considered.

One of the main problems in the interpretation of the data is the lack of temporal resolution. Most of the observations made at each location are at a single point in time. Even if physical factors are dominant in determining the patterns of bloom development, we should not necessarily expect to find any correlation between observed biogeochemical and

physical variables, because of the historical influence of physical variability prior to the time of sampling. The amount of information regarding this variability which can be inferred from the data is extremely limited.

The second limitation imposed by the logistics of covering such a large area during the spring bloom is one of spatial resolution. Although the along-track resolution is good (about 4 km for SeaSoar data) each leg of the cruise is 300 km apart and so mesoscale features are difficult to interpret. Also, because the survey was carried out over a period of about 7 weeks which is of a similar order of magnitude to the time taken by a typical spring bloom cycle, it is not possible to consider the large scale patterns emerging from the data as synoptic. Temporal and spatial variations must be considered together and for this reason the data will mostly be presented in the form of time series following the cruise track, rather than mapped spatially.

The final limitation is one of trophic resolution. There is very little data available relating to secondary production which might allow as to measure the response of zooplankton to the phytoplankton bloom and directly assess the effect of variability in grazing pressure on the observed patterns of standing stock. Although ADCP backscatter data were available, these data only reflect the distribution of highly motile zooplankton of 1 cm or more in size, while a major part of the grazing pressure on the spring bloom is thought to be due to micro-zooplankton (Lochte *et al.*, 1993), which were not sampled.

Despite these limitations, which are common to many previous studies and survey data in general, this study provides a useful contribution because of its wide areal coverage. In this chapter the survey data is analysed to determine as far as possible the seasonal components of the variance in both water column stratification and the available biogeochemical data. The patterns shown by the latter are then compared with the observed patterns of seasonal stratification.

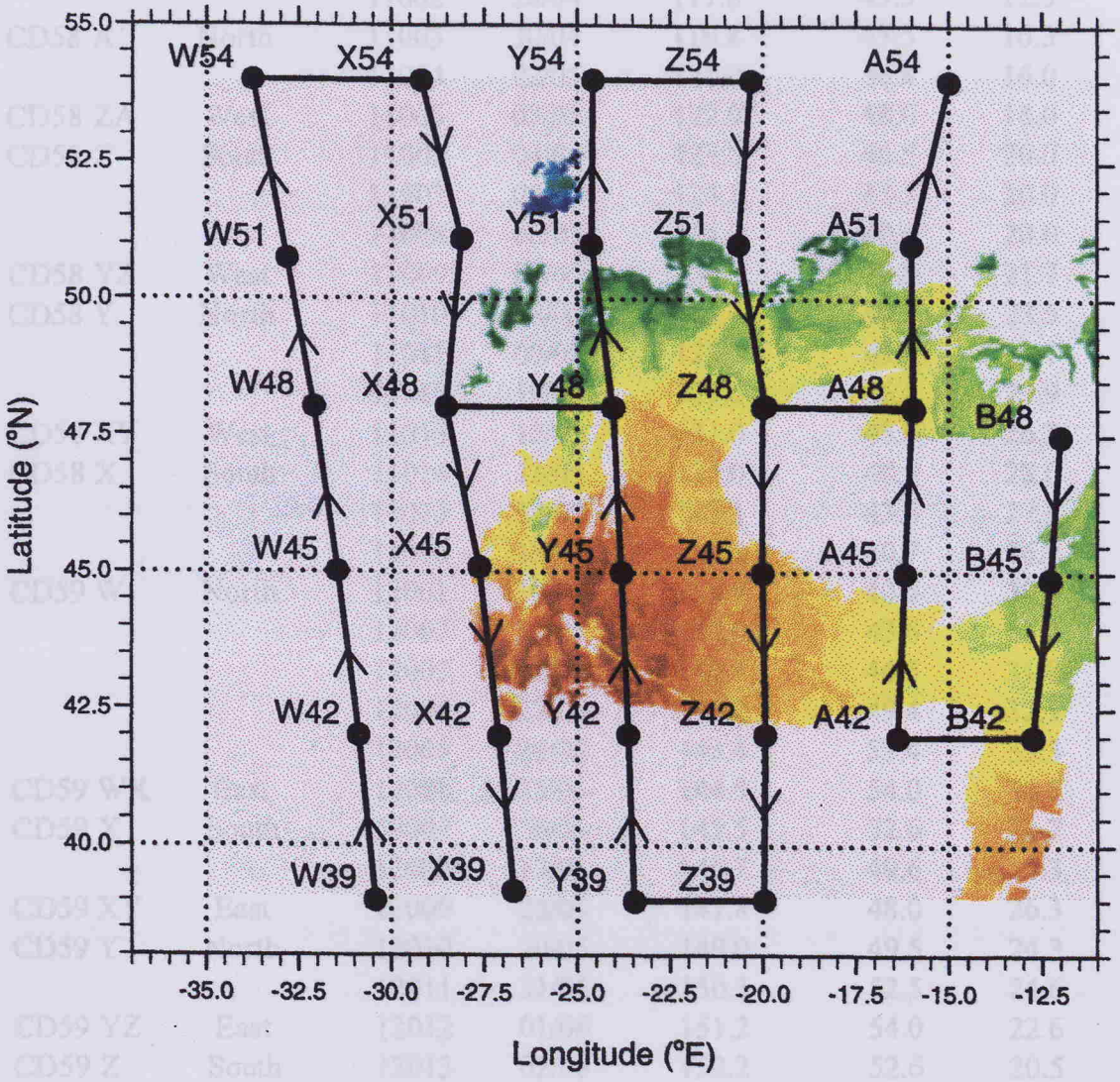

Figure 2.1. The Vivaldi '91 survey area: RRS Charles Darwin CD58 and CD59 cruise tracks and CTD station positions, overlaid on thermal satellite image showing sea-surface temperature features at 0848 GMT on 26/05/91. Cloud is masked out. The lowest temperatures are shown in blue and the highest in red. Data provided by S. Groom, RAGU, University of Plymouth.

Table 2.1 Navigation data for 300 km transect (SeaSoar run) mid-points.

Section	Heading	SeaSoar run	Date	Time (days)*	Lat. (°N)	Lon. (°W)
CD58 B	South	11001	27/04	116.7	46.2	12.2
		11002	28/04	117.8	43.5	12.5
CD58 A	North	11003	30/04	119.8	43.5	16.3
		11004	02/05	121.0	46.8	16.0
CD58 ZA	West	11005	03/05	122.0	48.0	18.0
CD58 Z	South	11006	04/05	123.0	46.5	20.0
		11007	05/05	124.2	43.5	20.0
		11008	06/05	125.3	40.6	20.0
CD58 YZ	West	11009	07/05	126.4	39.0	21.7
CD58 Y	North	11010	08/05	127.4	40.6	23.5
		11011	09/05	128.5	43.5	23.7
		11012	10/05	129.6	46.5	23.9
CD58 XY	West	11013	12/05	131.0	48.0	26.2
CD58 X	South	11014	13/05	132.0	46.5	28.0
		11015	14/05	133.1	43.6	27.4
		11016	15/05	134.1	40.7	26.9
CD59 W	North	12001	19/05	138.9	40.5	30.6
		12002	21/05	140.0	43.6	31.2
		12003	22/05	141.1	46.5	31.8
		12004	23/05	142.2	49.4	32.5
		12005	24/05	143.4	52.4	33.3
CD59 WX	East	12006	25/05	144.5	54.0	31.5
CD59 X	South	12007	26/05	145.5	52.6	28.7
		12008	27/05	146.7	49.6	28.3
CD59 XY	East	12009	28/05	147.8	48.0	26.3
CD59 Y	North	12010	30/05	149.0	49.5	24.3
		12011	31/05	150.3	52.5	24.6
CD59 YZ	East	12012	01/06	151.2	54.0	22.6
CD59 Z	South	12013	02/06	152.2	52.6	20.5
		12014	03/06	153.6	49.6	20.3
CD59 ZA	East	12015	04/06	154.8	48.0	18.0
CD59 A	North	12016	06/06	156.1	49.5	16.0
		12017	07/06	157.7	52.5	15.5

* Time origin is start of calendar year.

2.2 Overview of Data Analysis

The data collected during the survey contains spatial variance generated by processes operating on a number of different time scales. The focus of this study is seasonal change, in particular how variance in the characteristics of the phytoplankton bloom is related to spatial and temporal variation in the development of seasonal stratification. However, the observed variance in density, temperature, salinity and nitrate concentration is dominated by that generated at basin scales over much longer time periods and transferred to the ocean mesoscale by the stirring effect of the eddy field. This structure is largely a consequence of the meridional gradient in incident solar radiation and its interaction with the planet's internal systems on the time scales of climatic change (decades to millennia). Variability at the seasonal time-scale is superimposed on these patterns and is also contaminated by fluctuations due to shorter time-scale processes such as weather events, frontal dynamics, predator-prey cycles, species succession and diel cycles of solar radiation and biological production.

Much of the analysis in this chapter is concerned with removing, where possible, the components of variance at time-scales other than the seasonal scale. This has been achieved to a large extent for the physical variables defining the stratification and to some extent for the mixed layer nitrate concentration. However, there is insufficient data to determine the effect of short time-scale variance in phytoplankton or nitrate concentration which might be introduced by the internal dynamics of the biological system. Biological variance on sub-seasonal time scales must therefore be treated as noise in the analysis.

2.2.1 Seasonal Stratification

The depth of the mixed layer or surface boundary layer is typically used as a measure of seasonal stratification in modelling and observational studies of the pelagic ecosystem. While the apparent depth of the mixed layer derived from hydrographic data

provides a certain amount of information about the state of seasonal stratification at the time of observation, these data must be used with care as the depth of mixing is also affected by fluctuations in meteorological forcing with much shorter time-scales than those in which we are interested. This is particularly true during the heating season before stratification is well established. For example, a modelling study by Woods and Barkmann (1986) shows a diel cycle of mixed layer depth with amplitudes of about 100 m in March at 41°N 27°W.

Another measure of seasonal stratification is the seasonal density anomaly at the sea-surface. This reflects a time integral of surface buoyancy flux from the beginning of the heating season to the time of sampling and is therefore less sensitive to the diel cycle and weather fluctuations or storm events than the mixed layer depth. Also, while the shoaling of the mixed layer tails off as the season progresses, the magnitude of the seasonal density anomaly continues to increase throughout the heating season, giving some indication of the length of time for which stratification has been established. This is particularly important if any information is to be gained from point-in-time biogeochemical data about rates of bloom development.

A method for the determination of seasonal anomalies from hydrographic data is presented in Section 2.3 and the observed patterns of stratification as shown by the mixed layer depth and the seasonal density anomaly are discussed. In the modelling study presented in Chapter 3, the ecosystem model is forced by mixed layer depth from the output of a general circulation model (GCM) and the modelled and observed seasonal density anomalies are compared in order to evaluate the accuracy with which the GCM simulates the development of seasonal stratification.

Although seasonal stratification is caused primarily by increases in air-sea buoyancy flux and relaxation of the wind stress, it is modified by advection. This process has been examined theoretically in primitive equation modelling studies (Franks and Walstad, 1997; Haine and Marshall, 1998; Nurser and Zhang, in revision), but its contribution to the

development of seasonal stratification in the real ocean has not previously been determined, to the author's knowledge. In Section 2.4, that part of the observed seasonal density anomaly which arises from the action of vertical shear on the winter-time mixed layer buoyancy structure is estimated by treating salinity as a tracer. The relative importance of this buoyancy transport component is assessed and its simulation by the GCM is evaluated by comparing modelled and observed seasonal salinity anomalies in Chapter 3.

In Section 2.5, evidence for a significant contribution of short time-scale variations in weather conditions to the observed seasonal density anomaly is demonstrated by comparison of Vivaldi sea-surface temperature (SST) data with an auxiliary SST data set. These data are used to derive a corrected surface seasonal density anomaly which can be considered to reflect more accurately the variance in stratification at the seasonal time scale. This is important because, if the effects of mesoscale variability are largely removed by spatial averaging, the corrected surface seasonal density anomaly can be assumed to show a fairly steady monotonic increase at a particular location. Given a model which predicts the temporal evolution of both the stratification and the spring bloom at that location it is therefore possible to match the model and the survey data by the seasonal density anomaly as an alternative to matching by time. The differences between observed and predicted biogeochemical properties then depend more on how well the model predicts the relationship between the evolution of the stratification and that of the bloom and less on how accurately it predicts the bloom's evolution in time. Errors in the physical model which affect the timing or rate of stratification therefore become less critical. Seasonal density anomaly matching was used in the modelling study described in Chapter 3.

2.2.2 Nitrate Utilisation and Standing Stock

The seasonal component of the spatial pattern in mixed layer nitrate concentration has been determined by comparing the observed surface nitrate with an estimate of the pre-bloom or winter-time nitrate concentration in the mixed layer. The method for deriving the

latter is described in Section 2.6. The difference gives a measure of nitrate utilisation during the bloom. Comparison between nitrate utilisation and phytoplankton standing stock, estimated from observed chlorophyll *a*, then gives an indication of phytoplankton losses since the beginning of the bloom. The observed patterns of nitrate utilisation and phytoplankton standing stock are discussed in Section 2.7 and measures of bloom progression derived from these variables are compared with the observed surface seasonal density anomaly in Section 2.8.

2.3 Seasonal Stratification

This section describes the seasonal stratification as observed during the survey in terms of the depth of the mixed layer and the seasonal density anomaly. Section 2.3.1 gives a practical definition of the seasonal anomalies in density and salinity, the latter being required for the analysis presented in Section 2.4. The method for the determination of these property anomalies is detailed in Section 2.3.2 and the observed spatio-temporal distributions of mixed layer depth and seasonal density anomaly are discussed in Section 2.3.3 and Section 2.3.4 respectively.

2.3.1 Definition of Seasonal Anomalies

For the purposes of this study the seasonal density anomaly $\Delta\rho(z)$ is defined as the difference in potential density ρ between depth z and a carefully chosen depth z_w at which the water properties are considered to reflect those of the winter-time mixed layer. i.e.

$$\Delta\rho(z) = \rho(z) - \rho(z_w).$$

The seasonal salinity anomaly $\Delta S(z)$ is defined by the corresponding salinity difference:

$$\Delta S(z) = S(z) - S(z_w).$$

z_w will be referred to as the *winter-time property depth.* Vertical property gradients at z_w are small and changes at z_w due to the vertical property fluxes may be assumed to be negligible at the time and space-scales under consideration. (This will be justified later in Section 2.3.4.) $\rho(z_w)$ and $S(z_w)$ are therefore assumed to be constant following the horizontal flow at z_w and relative changes in properties above this depth are interpreted as seasonal changes in the water column. The anomalies can then be thought of as a semi-Lagrangian seasonal

anomalies: they are Lagrangian in the sense that the frame of reference moves with the water column at z_w, although the water column itself is subject to vertical shear.

Ignoring the vertical density flux at z_w and treating the equation of state as linear in temperature and salinity (which is reasonable for our purposes given the scale of these property changes), the seasonal density anomaly at a point above z_w may be expressed conceptually in terms of its sources with respect to the water column as

$$\Delta\rho = (\Delta_L \rho)_Q + (\Delta_L \rho)_{E\text{-}P} + (\Delta\rho)_T.$$

Here, $(\Delta_L \rho)_Q$ and $(\Delta_L \rho)_{E\text{-}P}$ are the changes in density of a *material element*, following the fluid motion, due to air-sea fluxes of heat and freshwater respectively and $(\Delta\rho)_T$ is that part of the change in density, relative to the density at z_w, which is due to the action of vertical shear on the horizontal buoyancy structure existing in the winter-time mixed layer. The distribution of these three components of the seasonal density anomaly within the water column is modified by vertical mixing and advection. The term 'material element' refers to a parcel of water which is sufficiently small to retain its identity in the presence of turbulent mixing (Batchelor, 1967). In practice any sample observed will be a mixture of water of varying origin and so the Lagrangian changes represented by Δ_L should be thought of as averages for all material elements making up the sample. For brevity, $(\Delta\rho)_T$ will be referred to as the *buoyancy transport component* on the understanding that it includes the transport of pre-existing buoyancy only. Vertical shear in the ageostrophic velocity field modifies the density anomaly by virtue of its action on both pre-existing and seasonal components of the buoyancy field. However, the latter component is included in the air-sea flux terms.

2.3.2 Determination of Seasonal Anomalies from Hydrographic Data

The problem of correcting the hydrographic data for long time-scale variance, thereby deriving the seasonal anomalies, is essentially one of determining z_w. In choosing z_w,

it is important to ensure as far as possible that the water at this depth was formed during the last winter rather than in winters of previous years. This is because older waters may have travelled much further from the area in which they were subducted than the more recently formed waters and can be expected to show rather different temperatures and salinities. Even if the water was formed locally, as could be the case in areas of very weak circulation, interannual variability in surface fluxes may well have caused significant differences in water mass properties between years.

The procedure for identifying water formed during the last winter involves finding a depth range over which such water is observed. This range is bounded above by the bottom of the seasonal pycnocline and below by the maximum depth of recently ventilated water. Both of these depths vary spatially within the survey area and, in practice, neither is straightforward to determine accurately. Because of this, no attempt was made to estimate the upper and lower depths explicitly. Instead, a depth was chosen which can be shown to lie safely within these bounds over as much of the survey area as possible.

The seasonal input of buoyancy may extend below the maximum depth at which significant solar heating occurs due to downward buoyancy fluxes caused by vertical mixing and advection. The vertical extent of the resulting seasonal pycnocline is shown by the stability of the water ($-\rho^{-1}d\rho/dz$). Unfortunately, the bottom of the seasonal pycnocline can sometimes be obscured by the action of vertical shear on pre-existing buoyancy patterns which means that high values of stability do not necessarily reflect surface heating.

The maximum depth of water ventilated during the last winter may be determined by analysis of the vertical structure of the *apparent oxygen utilisation* or AOU (Redfield, 1942). This property is the difference between the concentration of oxygen gas (O_2) in the water and the water's oxygen saturation value, the latter being a function of temperature and salinity. In surface waters, oxygen concentration tends to equilibrate with atmospheric concentrations or at times may become super-saturated as a result of photosynthesis. AOU

is therefore normally negative or close to zero. This may not be true for recently upwelled water. Once the water is subducted below the euphotic zone respiration dominates and AOU increases. Subject to variation in community respiration rates, the observed AOU therefore reflects the age of the water.

As well as low AOU, newly formed water also tends to have low values of water column stability because of recent mixing and, in regions where vertical shear makes an important contribution to stability, we can expect to see enhanced stability below the depth of the last winter's mixing due to the integral effect of this process over time. Because of this, the vertical extent of the stability minimum below the seasonal pycnocline can sometimes provide independent evidence for the deeper boundary of newly formed water. It is however a less reliable guide than the AOU particularly in regions of weak circulation where low stability may reflect deeper mixing in previous winters. Even in these areas though a sharp increase in stability with depth may be used to put an upper limit on the estimate of the maximum depth of newly formed water.

An analysis of stability and AOU data from the Vivaldi survey (Appendix B) shows strong evidence for the existence, over most of the survey area, of a recently subducted layer of significant thickness within which winter mixed layer properties have been conserved. The evidence is less clear in the west. However, it is assumed that such a layer probably exists throughout the survey area but that the evidence for it is partially obscured here by the effects of vertical shear on the stability field.

A depth of 150 m, which lies within the apparent depth range of the recently subducted layer throughout its horizontal range, was chosen as the winter-time property depth. Support for this choice of depth, as opposed to a deeper one, is given by an analysis of the mixed layer climatology by Lamb (1984) which shows a winter-time mixed layer depth deeper than 150 m over most of the area covered by the Vivaldi survey, with a spatial minimum of approximately 150 m in the far south-western corner. Lamb's data is reproduced in Chapter 3 for comparison with model output (Figure 3.3).

2.3.3 Mixed Layer Depth

Various different criteria have been used in the literature to calculate the mixed layer depth from hydrographic data. In most cases, the mixed layer depth is estimated by finding the depth at which either the density or temperature difference from that observed at the surface exceeds some value. This depth range potentially includes a large part of the water column which, although homogenous with respect to its temperature and salinity, is not actively mixing. The *mixed layer depth* is therefore distinct from the *mixing layer depth* which is more reliably obtained from measurements of turbulent dissipation rates or overturning length scales (Brainerd and Gregg, 1995). Density and temperature criteria used to determine the mixed layer depth vary widely. Temperature differences used range from 1°C (Lamb, 1984) to 0.1°C (Weeks *et al.*, 1993b). Lochte *et al.* (1993) use instead a temperature gradient of 0.02°C m^{-1} to identify the base of the mixed layer. In practice the best criterion to use depends on the information required. For example, using a temperature difference of 1°C or even 0.5°C will probably not show up a diel cycle whereas 0.1°C often will.

The mixed layer depth for the Vivaldi transects according to a range of criteria is represented in Figure 2.2 by contours of density relative to that of the surface water (sampled at a depth of about 4 m by the ship's sea-water supply system). The differences were determined from 4 km gridded data and then averaged in latitude/longitude bins equivalent to 12 km and smoothed using a 3 point running mean to suppress length scales less than 36 km. This should have removed a large part of the variance associated with the most intense short time-scale fluctuations which occur in the region of mesoscale fronts and have typical length scales of order 20 km or less. The same processing is applied to all transect data presented in this chapter.

These data show that seasonal stratification is established to some extent almost everywhere, with the possible exception of a few patches on the earliest legs CD58 B and CD58 A. From CD58 Y onwards, stratification is well established, the depth of the mixed layer based on the 0.1 kg m^{-3} criterion (equivalent to about 0.5°C) being less than 50 m throughout. There are two notable regions though, on CD58 XY and at the far northern end of CD59 W, going into CD59 WX, where it is only just less than 50 m. The variation in mixed layer depth from south to north on leg W shows a definite positive trend, from about 10 m at 39°N to about 40 or 50 m at 54°N, which is consistent with latitudinal variation in solar heating. However this is not true for some of the other latitudinal transects. On legs CD58 Z and CD58 Y for example mixed layer depths are much deeper in the south so other factors are clearly important.

The diel cycle of solar heating is known to be a cause of variability in mixed layer depth. In order to investigate whether this could be the cause of some of the observed variance in the Vivaldi data, reference lines have been marked on Figure 2.2 to indicate the approximate positions corresponding to the times of daily minimum and maximum heat storage. These are based on the time integral of the residual downwelling short-wave radiation measured during the survey, with respect to a 24 hour running mean. Long wave radiative heat flux, sensible heat flux and latent heat flux are not considered here. It is assumed that these fluxes are relatively constant over a 24 hour time-scale compared with the amplitude of the diel cycle in the short-wave flux. It is also assumed that the measured short-wave radiation is a fair approximation to the local time series, on the basis that spatial variation, due mainly to differences in cloud cover, is likely to be small over a length scale of 300 km (the distance travelled in one day) compared with the amplitude of the diel cycle.

Any attempt at identifying the signature of diel cycling of the mixed layer depth in a series which is spatial as well as temporal must be considered speculative. Nevertheless, some evidence is apparent. Starting from the daily maximum at about 44°N on CD58 B, enhanced stratification is observed close to at least three consecutive daily maxima, in each

case followed by sharp deepening of the mixed layer according to the 0.1 kg m^{-3} criterion to over 200 m. (It should be noted that there is a day missing between CD58 B and CD58 A during which a zonal transect was carried out but no SeaSoar data are available.) There is no such deepening associated with the daily minimum at the beginning of CD58 A, however the pattern strongly suggests that the diel cycle is one important factor in this region at the time of sampling. Other notable areas of enhanced stratification corresponding to daily maxima are observed on CD58 Y at about 42N, on CD59 Z at about 49°N and on CD59 A between 52 and 53°N.

2.3.4 Seasonal Density Anomaly

The seasonal density anomaly $\Delta\rho$ is shown in Figure 2.3. The data between 150 m and 200 m are included to indicate the weak vertical density gradient in the region of z_w, generally less than 10^{-3} kg m^{-4} at the time of observation. The assumption that the vertical density flux at z_w is unimportant in this study can be justified by a fairly extreme example: a vertical velocity of 1 m day^{-1} in the presence of a gradient 10^{-3} kg m^{-4} would imply a vertical density flux of 0.03 kg m^{-3} mth^{-1}. The maximum vertical velocities at scales above 36 km are normally those associated with Ekman pumping and geostrophic adjustment in eddy interiors. These are more typically in the order of tens of cm per day as described in Chapter 1. Even if a vertical velocity as large as 1 m day^{-1} had persisted over a period of a month or so since the time at which the water at 150 m was subducted, the change in density at z_w of about 0.03 would be relatively small compared with the seasonal signal shown in Figure 2.4, which is at least an order of magnitude greater than this from the latter part of CD58 Y onwards.

The seasonal density anomaly shows the same general picture as the mixed layer depth, of weak stratification during the early part of CD58 and well established stratification elsewhere. Whereas most of the variance in mixed layer depth was observed early in the survey though, the opposite is true for the seasonal density anomaly, suggesting

an increase in the variance of the seasonal density anomaly as the anomaly intensifies. This may simply be due to the cumulative effect of spatial heterogeneity in air-sea fluxes over time. As with the mixed layer depth there is a clear latitudinal trend on leg W. A similar trend is also evident later over the northern part of the survey area, with the greatest negative values to be found on the more southerly of the zonal transects at 48°N and on the southern end of CD59 Z. The values on the final leg CD59 A however are surprisingly small.

Although the large scale patterns in the seasonal density anomaly tend to dominate, a large amount of mesoscale structure is apparent. Part of this structure may be associated with local effects of mesoscale dynamics, although the short time-scale fluctuations caused by vertical advection and vertical shear are expected to be most intense over the smaller length scales associated with frontal systems and should have been largely removed by the averaging. Some of the mesoscale structure in the 36 km mean series could be caused by relatively slow upwelling of the seasonal pycnocline in the interior of eddies resulting in entrainment of denser water into the mixed layer. This is most likely to be significant where the pycnocline is strong and the mixed layer is shallow, although even under exceptionally favourable conditions the effect is unlikely to be great. For example, a vertical velocity of 1 m day^{-1} acting on a gradient of 0.03 kg m^{-4} (as observed at the southern end of CD59 Z) would cause a density flux of 0.9 kg m^{-3} mth^{-1}, increasing the density in a 20 m mixed layer by just 0.045 kg m^{-3} in one month.

The mesoscale structure in the seasonal density anomaly is much more likely to be a consequence of the effect of sea surface temperature (SST) patterns on air-sea heat fluxes. Evidence for this effect is shown by the existence of positive correlation between the surface seasonal density anomaly $\Delta\rho(0)$ and the temperature at 150 m which reflects the winter-time temperature of the mixed layer (Figure 2.4). This is most evident on leg W, where a clear correlation can be seen over 10 degrees of latitude from 41°N to 51°N. Barnier *et al.* (1995) give an estimate of the variation of air-sea heat flux with SST for the latitude range 25

to 70°N of about 32 W m^{-2} K^{-1} in March, decreasing to a summer minimum of about 29 W m^{-2} K^{-1}. The temperature difference between the local minimum north of 44°N on leg W and the maximum just south of 46°N is about 3°C. We can therefore expect the heat flux into the ocean at the beginning of the heating season to have been around 100 W m^{-2} greater within the interior of the cold feature than the warm feature, equivalent to differences in the rates of change of temperature or buoyancy in a 100 m layer of about 0.65°C or 0.13 kg m^{-3} mth^{-1}. This suggests that the difference in heat flux due to heterogeneity in SST could certainly account for the observed difference in $\Delta\rho(0)$ of about 0.3 kg m^{-3} by the time of sampling in mid May.

One other pattern of interest in the seasonal anomaly fields, which was also noted in the earlier analysis of the stability distribution, is a tendency for the pycnocline to extend to greater depths on the more westerly sections. For example, on leg W the -0.5 kg m^{-3} $\Delta\rho$ isoline is found at a depth of more than 100 m over most of the section, whereas on CD59 Z it is found at a depth of around 70 m, despite the fact that the magnitude of $\Delta\rho(0)$ is greater, suggesting a similar or greater seasonal heat storage. Such differences could be interpreted as evidence for differences in the rate of initial stratification. A less rapid shoaling of the mixed layer allows more time for seasonal heating of the detrained water, causing a stronger seasonal anomaly in temperature, and therefore density, to develop at depth. However, in this case the deeper pycnoclines are believed to be the result of vertical shear in regions of larger horizontal buoyancy gradients and stronger flow. This is supported by the structure of the seasonal salinity anomaly discussed in Section 2.4.

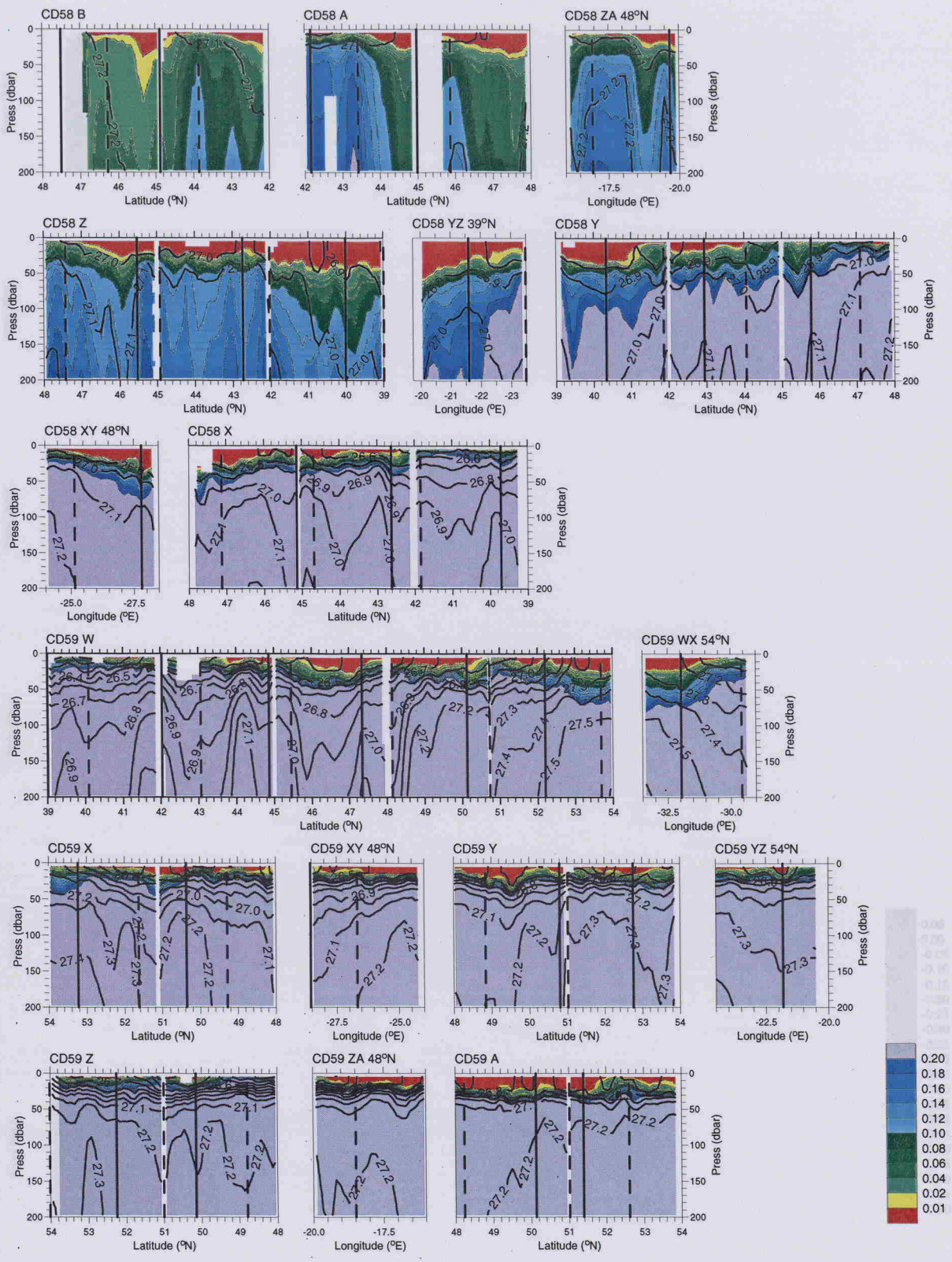

Figure 2.2. Vertical sections of density relative to the sea surface (kg m^{-3}). Isopycnals overlaid showing σ_θ (kg m^{-3}). Reference lines show positions of daily minimum (solid) and maximum (dashed) heat storage.

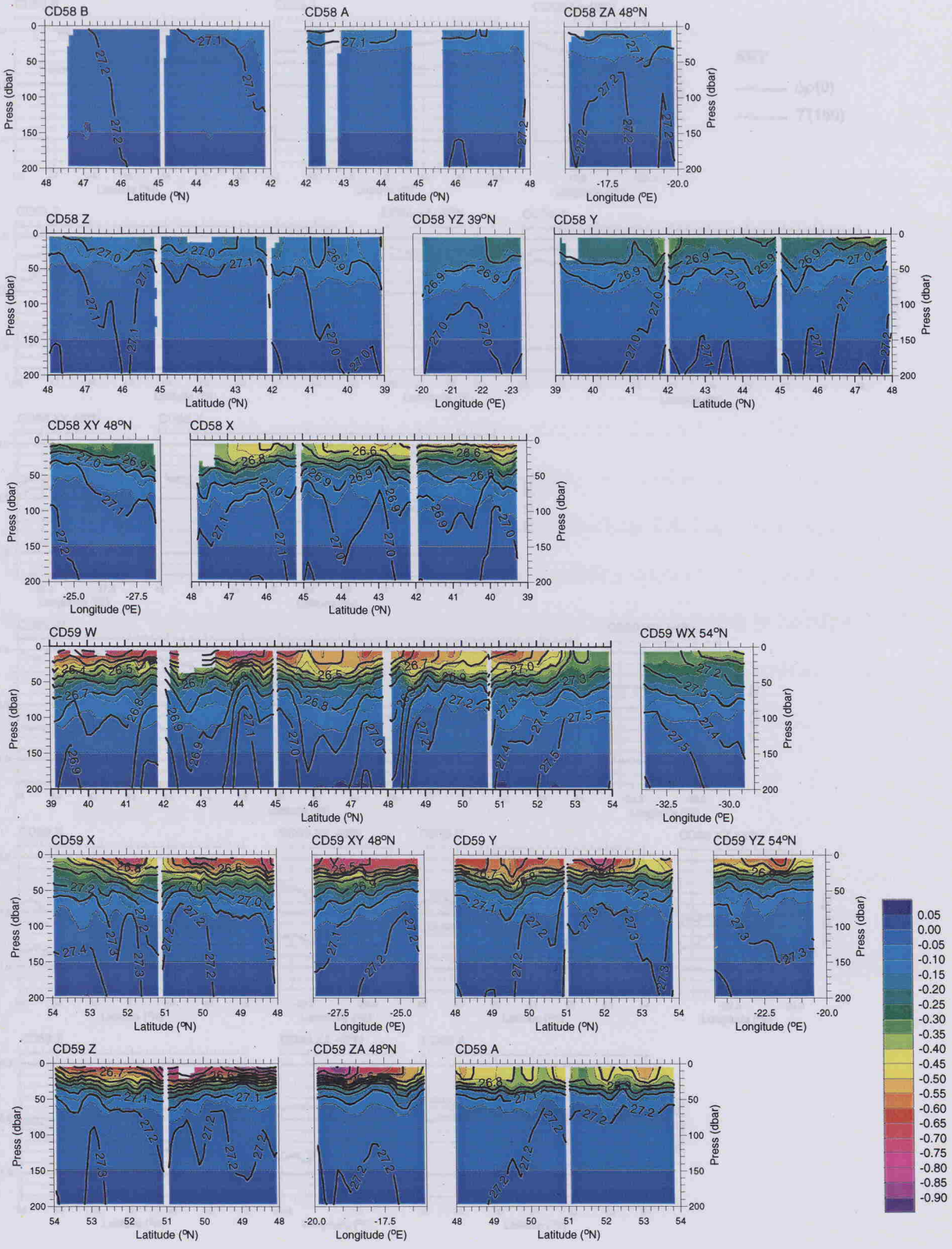

Figure 2.3. Vertical sections of seasonal density anomaly $\Delta\rho$ (kg m^{-3}). Isopycnals overlaid showing σ_θ (kg m^{-3}).

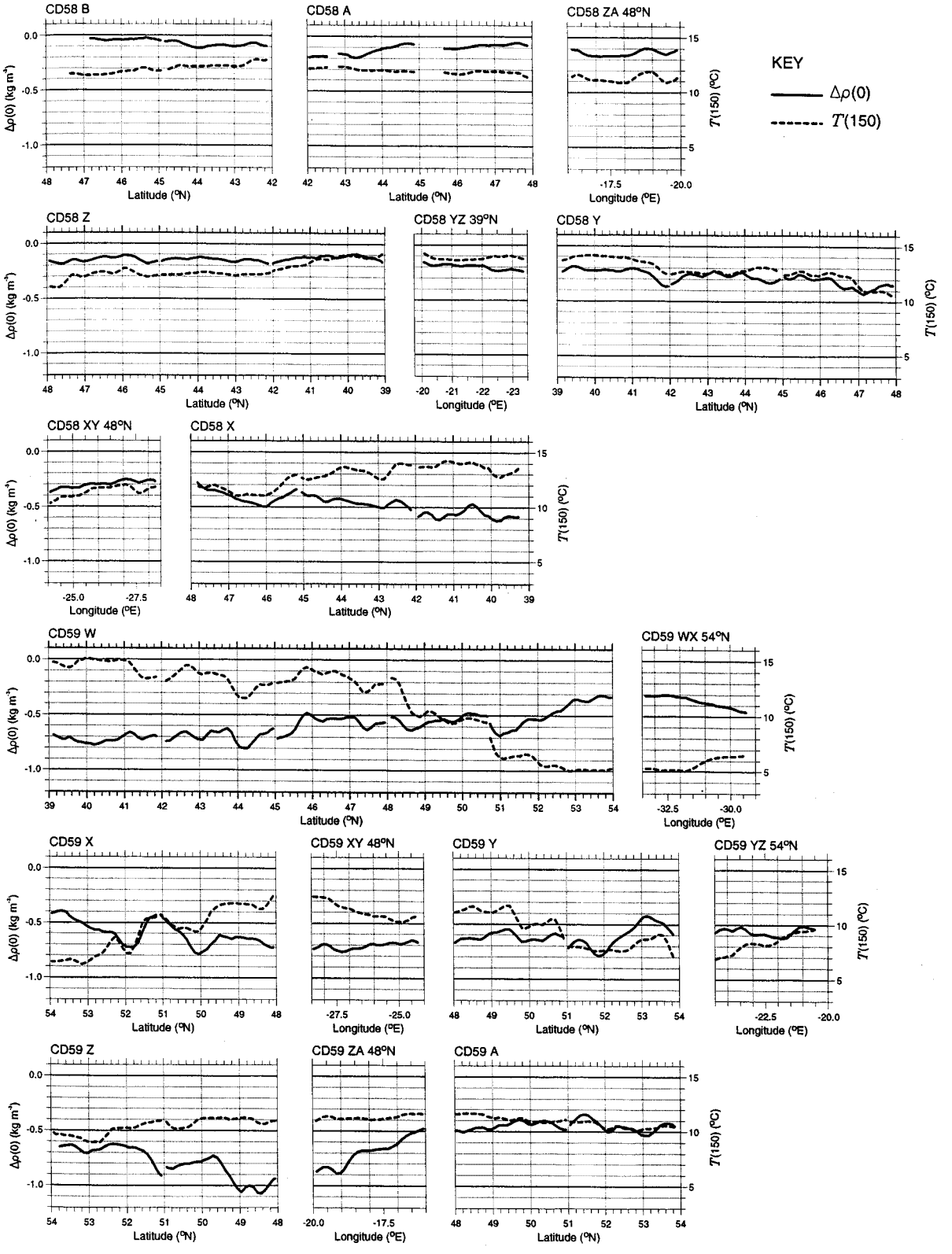

Figure 2.4. Surface seasonal density anomaly $\Delta\rho$ (0) and temperature at150 m $T(150)$.

2.4 Contribution of Buoyancy Transport to the Seasonal Stratification

In this section, the effect of the re-distribution of pre-existing buoyancy structure in the winter-time mixed layer on the seasonal stratification is investigated. The existence of a pseudo-linear θ-S relationship throughout most of the survey area makes it possible to derive an estimate of the buoyancy transport component of the seasonal density anomaly from the seasonal salinity anomaly. This θ-S relationship was used in a similar way by McCulloch (1996) to determine the winter-time temperature of water sampled in the spring and thus infer seasonal changes in heat content from single hydrographic profiles. In both cases salinity is treated as a conservative tracer. The likely effect of air-sea freshwater fluxes on salinity over the time scale of interest is discussed in Section 2.4.1 in order to show that this is justified. The observed patterns of the seasonal salinity anomaly are presented in Section 2.4.2, the method for converting this to a density anomaly is given in Section 2.4.3 and finally its contribution to the total observed seasonal density anomaly is discussed in Section 2.4.4.

2.4.1 Salinity as a Conservative Tracer

The seasonal salinity anomaly may be expressed in terms of its air-sea flux component and its transport component using the same terminology introduced for the density anomaly in Section 2.3. Thus

$$\Delta S = (\Delta_L S)_{E\text{-}P} + (\Delta S)_T.$$

The likely magnitude of the air-sea flux term $(\Delta_L S)_{E\text{-}P}$ can be quantified by considering the climatology. Seasonal maps of net evaporation rate (evaporation minus precipitation) for the North Atlantic produced by Schmitt *et al.* (1989) show spring-time averages varying from -3 cm per month to 4 cm per month over the survey area. The effect of a net evaporation rate

of E - P on the salinity S of a material element within a homogenous mixed layer of depth h over time t since the beginning of the heating season is

$$(\Delta_L S)_{E-P} = \int \frac{(E-P)\,S}{h}\,dt$$

A rather high value for E - P of magnitude 4 cm month^{-1} would therefore cause a salinity change in a mixed layer of constant depth h m of approximately 1.4 / h mth^{-1}, assuming a salinity S of about 35. Any air-sea flux will have a large effect when the mixed layer is shallow. However subsequent deepening of the mixed layer will dilute this effect so temporary shoaling of the turbocline may be ignored. The change in surface salinity can therefore be modelled as the cumulative effect of the air-sea freshwater flux on a mixed layer of monotonically decreasing depth. If we model the change in mixed layer depth as a simple exponential decay and assume a constant air-sea flux we can get an analytical solution from which we can estimate the order of magnitude of $(\Delta_L S)_{E-P}(0)$. If vertical fluxes below the mixed layer are ignored then $(\Delta_L S)_{E-P}(z)$ is simply that for an element in the mixed layer at the most recent time for which $h \geq z$.

A model $h = 150\ e^{-2t}$ where t is time in months gives a mixed layer shoaling from 150 m to about 20 m over the period of 1 month. This is compatible with the two sets of mixed layer depth data for the zonal section ZA which was repeated after an interval of 33 days. Again taking E - P as 4 cm per month this then gives

$$(\Delta_L S)_{E-P}(0) = 4.7 \times 10^{-3} e^{2t},$$

implying a salinity change of 0.035 after 1 month. If vertical fluxes below the mixed layer are ignored then $(\Delta_L S)_{E-P}(z)$ is simply that for an element in the mixed layer at the time of detrainment when $h = z$. Substituting t as a function of h in the expression for $(\Delta_L S)_{E-P}(0)$ and equating h to z we get

$$(\Delta_L S)_{E-P}(z) = \frac{0.7}{z}$$

so at 50 m the change is as small as 0.014. Given that the stratification observed during CD59 ZA is at least as advanced as in any other part of the survey it seems unlikely that stratification had been established for much more than 1 month elsewhere. It would seem safe then to assume that the maximum salinity change due to air-sea fluxes is of the order of 0.035.

2.4.2 Seasonal Salinity Anomaly

The structure shown by the seasonal salinity anomaly (Figure 2.5) is in general at least an order of magnitude greater than the likely effect of air-sea fluxes so it is reasonable to treat salinity as a conservative tracer over this time period. The structure can therefore be interpreted in terms of internal transport fluxes and the absolute salinity distribution is shown in Figure 2.6 for comparison.

It is immediately apparent that the salinity anomalies are much greater on the more westerly legs where the currents are generally stronger and the horizontal salinity gradients greater. This effect is emphasised by temporal variation in the southern part of the survey where the western legs were sampled later in the survey and reduced in the northern part where they were sampled earlier. Changes in the vertical gradient of ΔS with depth are small compared with those in $\Delta\rho$, suggesting that much of the shear acting on the horizontal salinity gradient is not dependent on the development of seasonal stratification.

Further interpretation of the patterns is aided by an examination of the observed θ-S characteristics. Pollard *et al.* (1996) showed that the whole area is occupied by North Atlantic Central Water (NACW) except for a small region in the north-west corner where colder, fresher Atlantic Subarctic Intermediate Water (ASIW) outcrops to the north of the Polar Front associated with the North Atlantic Current. This water, formed in the sub-polar

gyre to the north and sometimes referred to as Atlantic Subarctic Upper Water (ASUW) in this region, is characterised by temperatures in the range 0.0 - 4.0°C and salinities from 34.0 - 35.0 (Emery and Meincke, 1986). Salinities less than 35.0 are observed above 150 m at the northern end of legs W and CD59 X and zonal transect CD59 WX. A small fraction of this water is also found between 100 and 150 m as far east as leg CD59 Y and zonal section CD59 YZ but the surface water here is more representative of NACW. Pollard *et al.* (1996) defined a θ-S reference curve for NACW referred to as V91 (Vivaldi 91), based on the properties of water bounded by the two branches of the North Atlantic Current where they crossed leg W. This is shown in Figure 2.7 together with the θ-S profiles for the Vivaldi CTD stations.

It may be seen from the θ-S relationship that any increase in salinity due to transport within the region occupied by NACW will be accompanied by a corresponding increase in temperature and there will therefore, counter-intuitively, be a net increase in buoyancy, enhancing stratification. Decreases in salinity are likewise associated with decreases in buoyancy and so the development of negative salinity anomalies tends to be inhibited by water column instability until this is overcome by the strength of the seasonal thermocline. This explains the strong positive bias shown by the salinity anomaly field and the fact that, where negative anomalies do occur within the horizontal range of NACW, they are found above about 50 m. Such anomalies are noted to the south of the Polar Front on leg W, at about 50°N on CD59 X, at the far north of CD59 Y and also on CD59 YZ. All of these are within or close to the North Atlantic Current (NAC) region identified by Pollard *et al.* (1996) and are probably due to cross-frontal transport in the region of the main Polar Front, shown by the 27.3 isopycnal, and the weaker front to the south, shown by the 27.2 isopycnal.

2.4.3 Conversion of Salinity Anomaly to Density Anomaly

Ignoring non-linearity in the equation of state, as in Section 2.3, the buoyancy transport component of the seasonal density anomaly is given by

$$(\Delta\rho)_T = \frac{\partial\rho}{\partial\theta}(\Delta\theta)_T + \frac{\partial\rho}{\partial S}(\Delta S)_T,$$

where $\Delta\theta_T$ and ΔS_T are the temperature and salinity changes, relative to z_w, due to the action of vertical shear on pre-existing horizontal property gradients. The salinity change is

$$(\Delta S)_T = \Delta S - (\Delta_L S)_{E\text{-}P}$$

and, for NACW (water with salinity greater than 35.0), an estimate of the temperature change is given by

$$(\Delta\theta)_T \approx \frac{d\theta}{dS}\{(\Delta S)_T - (\Delta\,\delta S)_T\}$$

where $d\theta/dS$ is the gradient of the V91 θ–S curve and the property δS is the salinity anomaly defined by Pollard *et al.* (1996), which is the difference at constant temperature between the local salinity and that of the V91 curve. It has already been shown that the air-sea flux term $(\Delta_L S)_{E\text{-}P}$ is small compared with ΔS and this term will be ignored. $(\Delta\,\delta S)_T$, the change in δS relative to z_w due to vertical shear, is difficult to quantify but the data presented by Pollard *et al.* show that the horizontal gradients in δS are typically around 20% of those in salinity. For the purposes of obtaining a rough approximation of $(\Delta\rho)_T$ this term too will therefore be ignored. Within the range of NACW then, the estimate of the transport component of the seasonal density anomaly is

$$(\Delta\rho)_T \approx \left(\frac{\partial\rho}{\partial S} + \frac{\partial\rho}{\partial\theta}\frac{d\theta}{dS}\right)\Delta S.$$

The curve is almost linear over the whole range above a salinity of 35.0 so $d\theta/dS$ is fixed at a constant 6.5°C.

2.4.4 Distribution of the Buoyancy Transport Component

Neglecting the small effect of the air-sea freshwater flux, the seasonal density anomaly is divided into two components: one due to the air-sea heat flux and the other due to buoyancy transport only. i.e.

$$\Delta\rho \approx (\Delta_L\rho)_Q + (\Delta\rho)_T.$$

Figure 2.8a shows the observed 300 km mean seasonal density anomaly at the surface for each SeaSoar run, with and without the estimated transport component, the latter being an estimate of the seasonal density anomaly due to the air-sea heat flux. This quantity is undefined for the three SeaSoar runs which lie mostly to the north of the Polar front where ASIW outcrops at the surface. These are the CD59 runs at the end of leg W, along the zonal transect WX and at the beginning of leg X. Figure 2.8b shows the 300 km mean buoyancy transport component as a percentage of the total seasonal density anomaly. The effect of transport in enhancing stratification appears to be most important in the south and south-western regions of the survey area, on CD58 legs Z to X and the southern part of leg W. The effect is particularly notable at the far south of leg Z and on zonal transect ZY where the redistribution of horizontal buoyancy structure present in the winter-time mixed layer accounts for about 50% of the observed stratification.

In order to better understand these observations the processes which might be responsible for the buoyancy transport are considered. Because geostrophic flow is aligned along the pressure gradients associated with buoyancy fronts, shear flow which enhances stratification by re-distributing buoyancy must necessarily be ageostrophic. In the open ocean, possible candidates are ageostrophic shear associated with baroclinic instability and Ekman drift. In the case of the former, the time-averaged correlation between cross-frontal velocity and layer thickness in the eddies generated by unstable fronts causes light water to progressively spread out over heavier water near the surface, while heavy water slumps beneath lighter water in lower layers. A scale analysis by Lee *et al.* (1997) shows that, on the time scales of interest in the present study (i.e. weeks to months) this eddy-induced advection has a small effect on transport compared with eddy-diffusion. However, as shown by Nurser and Zhang (in revision), it can potentially have a major effect on stratification. This occurs through 'tilting' of density surface on scales of just a few km. Because unstable fronts are a ubiquitous feature of the mesoscale eddy field in the ocean, a significant contribution at larger scales is to be expected.

While shear flow associated with baroclinic instability is inherently biased towards re-stratification, the same is not true of Ekman drift in a frontal region. As demonstrated in the modelling study of Franks and Walstad (1997), winds aligned with the frontal jet tend to weaken the stratification by driving cold (dense) water across the front, while winds blowing in the opposite direction intensify the stratification by driving warm (light) water across the front. During the heating season, we should expect the magnitude of the negative effect on water column stability to be rather limited initially, due to the already low stability, but the asymmetry should disappear once seasonal stratification is well established. Where the horizontal structure in the buoyancy field is dominated by mesoscale variability, it is reasonable to assume the wind direction to be uncorrelated with the orientation of the fronts. In that case, we should expect the average contribution of Ekman drift to water column stability, over a 300 km length scale, to be positive during the early stages of stratification development and tend towards zero later. In the region of more permanent, larger scale

frontal systems the effect after the establishment of stratification will depend on the wind direction and may be positive or negative.

It is hypothesised that the processes described above account for the observed buoyancy transport component of the seasonal density anomaly $(\Delta\rho)_T$. Some attempt is made here to quantify the effect of these processes in regions away from major fronts, by referring to an order of magnitude estimate for the re-stratifying effect of eddies presented by Nurser and Zhang (in revision). The observations in the NAC region will be discussed separately later. The estimate of Nurser and Zhang (in revision) is one based on the basin-averaged potential energy budget in the absence of air-sea buoyancy forcing. Re-stratification in their analysis includes a vertical 'stretching' effect, as vertical convergence acts to strengthen or weaken existing stratification, as well as the 'tilting' effect. Unfortunately, the former is in part due to the existence of stratification in the top 150 m caused by seasonal heating and that part is not included in the buoyancy transport component. Additionally, the analysis does not include the effect of Ekman drift at mesoscale fronts. Nevertheless, in the context of obtaining a rough order of magnitude for the expected buoyancy transport, application of their result is considered reasonable.

On the supposition that the increase in stratification is distributed uniformly over a thermocline depth of order 500 m, Nurser and Zhang estimated the eddy-induced rate of change in the square of the buoyancy frequency, averaged over a typical ocean basin, to be of the order of 10^{-13} s^{-3} (2.6×10^{-7} s^{-2} mth^{-1}). This is equivalent to the development of a density anomaly over 150 m of 0.15 kg m^{-3} in one month; a value directly comparable with the observationally derived buoyancy transport component, the latter being of the order of 0.1 kg m^{-3} over much of the survey area (Figure 2.8a). The relative importance of the effect of Ekman drift at mesoscale fronts is presently unclear. However, we expect it to strengthen rather than weaken the stratification. It therefore seems reasonable to deduce that the combined impact of baroclinic instability and Ekman drift at mesoscale fronts is generally sufficient to explain the magnitude of the observed $(\Delta\rho)_T$.

Given the hypothesised importance of mesoscale eddies in explaining the advective contribution to the stratification, it is useful to examine the distribution of $(\Delta\rho)_T$ with reference to the observed eddy field. The distribution of eddy activity over the survey area is indicated here by the observed current velocities at 100 m depth (Figure 2.9).

The most vigorous activity appears to occur in a broad band to the south of the main Polar Front, extending to about 48°N on legs Y and Z and much further south in the western part of the survey area, on legs W and X. This general distribution pattern is reflected by the baroclinicity, as shown by the slopes of the isopycnals shown in Figure 2.6. Large horizontal density gradients are particularly common on leg W, where several strong mesoscale density anomalies are seen between the Polar Front and 41°N. The high eddy activity in the west seems a likely explanation for the deeper extent of the seasonal pycnocline noted in section 2.3. It may also explain the location of the highest magnitude $(\Delta\rho)_T$ of about -0.1 kg m^{-3} on leg W. It should be remembered though that the east to west increase over the south of the survey area is likely to be due in part to the later sampling time. Unfortunately, it is not clear from the available data why $(\Delta\rho)_T$ on CD58 Y and the adjoining zonal transect YZ is similar to that observed on CD58 X despite the fact that there seems to be significantly less eddy activity along the former transects. In addition, it is at first sight surprising that there appears to be virtually no transport contribution in the region of the NAC where eddy activity and horizontal buoyancy gradients are particularly strong. The region is sampled on CD59 X, Y, YZ and Z where the contribution is less than 5% and immediately to the south of the Polar Front on leg W where it is actually negative. This observation is relatively easy to explain though, because the sub-surface salinity anomaly distribution (Figure 2.5) suggests that there was an important positive contribution earlier in the season, which has since been negated by southward and westward spreading of colder, fresher water across the region. This is thought to be due to Ekman drift acting on the horizontal structure associated with the major fronts. The hypothesis will be supported

here by an attempt to quantify the likely effect of Ekman drift where leg W crosses the Polar Front.

The contribution of Ekman advection to the heat and freshwater budgets at the location under consideration was investigated by McCulloch and Leach (1997). Climatological forcing used to drive their model indicates a southward Ekman transport across the front in May. The predicted heat content change due to this transport was -40 W m^{-2} and the corresponding freshwater increase was 4 mm d^{-1}. May predictions based on 1991 forcing were much less, as southerly winds drove an Ekman flow eastwards along the Polar Front in that month. However, an examination of data for April 1991, taken from the Comprehensive Ocean Atmosphere Data Set (COADS, Woodruff *et al.*, 1993), shows that the earlier Ekman transport in the region would have been directed southward. The low salinity observed to the south of the Polar Front on leg W will therefore be interpreted in terms of the April transport.

The magnitude of the transport implied by the April COADS data would have been about 1.4 m^2s^{-1}, compared with about 0.9 m^2s^{-1} implied by the May climatology used by McCulloch and Leach (1997). We should therefore expect property transports to have been some 50% larger, i.e. a heat transport of around -60 W m^{-2} and a freshwater transport of around 6 mm d^{-1}. If we assume an Ekman layer depth of 50 m in April, based on the vertical extent of the negative salinity anomaly (Figure 2.5), then the corresponding changes in temperature and salinity over a time scale of 1 month are about -0.8°C and -0.13 respectively, giving a density change of 0.19 kg m^{-3}. This density change is opposite to and greater in magnitude than the large negative values of $(\Delta\rho)_T$ seen further south on leg W (Figure 2.8a). It therefore explains why $(\Delta\rho)_T$ is almost zero at time 142 d, at a location where we might have expected to see even larger negative values due to strong baroclinicity and vigorous eddy activity.

Encouragingly, the freshening effect is of the same order of magnitude as that seen in the ΔS field (~ -0.1, Figure 2.5) extending over about 2 degrees of latitude (about 220 km) to the south of the Polar Front. The Ekman flow over a 50 m layer would be about 3 cm s^{-1}, equivalent to about 80 km mth^{-1}, so we might expect to see a salinity or density anomaly introduced by the Ekman shear having a length scale of order of magnitude 100 km. The apparent length scale based on the transect data is a factor of two or so greater than this, which is not unreasonable if later advection by the geostrophic flow is taken into account.

As a final note, following the argument of McCulloch and Leach (1997), although the denser water would have had the effect of weakening the seasonal stratification in the short-term, the associated reduction in SST may have led to an opposite effect in the longer term. This is because the consequent reduction in heat loss to the atmosphere would have increased the net air-sea heat flux.

In conclusion, the analyses presented here give a reasonable degree of confidence in the hypothesis that Ekman drift and baroclinic instability, together with the positive air-sea heat flux, are the main processes responsible for the observed seasonal stratification. The effect of the two advective processes is generally secondary to that of the heat flux, but should not be ignored. The effects of both these processes are highly dependent on the existence of horizontal buoyancy structure at the mesoscale as well as that associated with major, more permanent frontal systems.

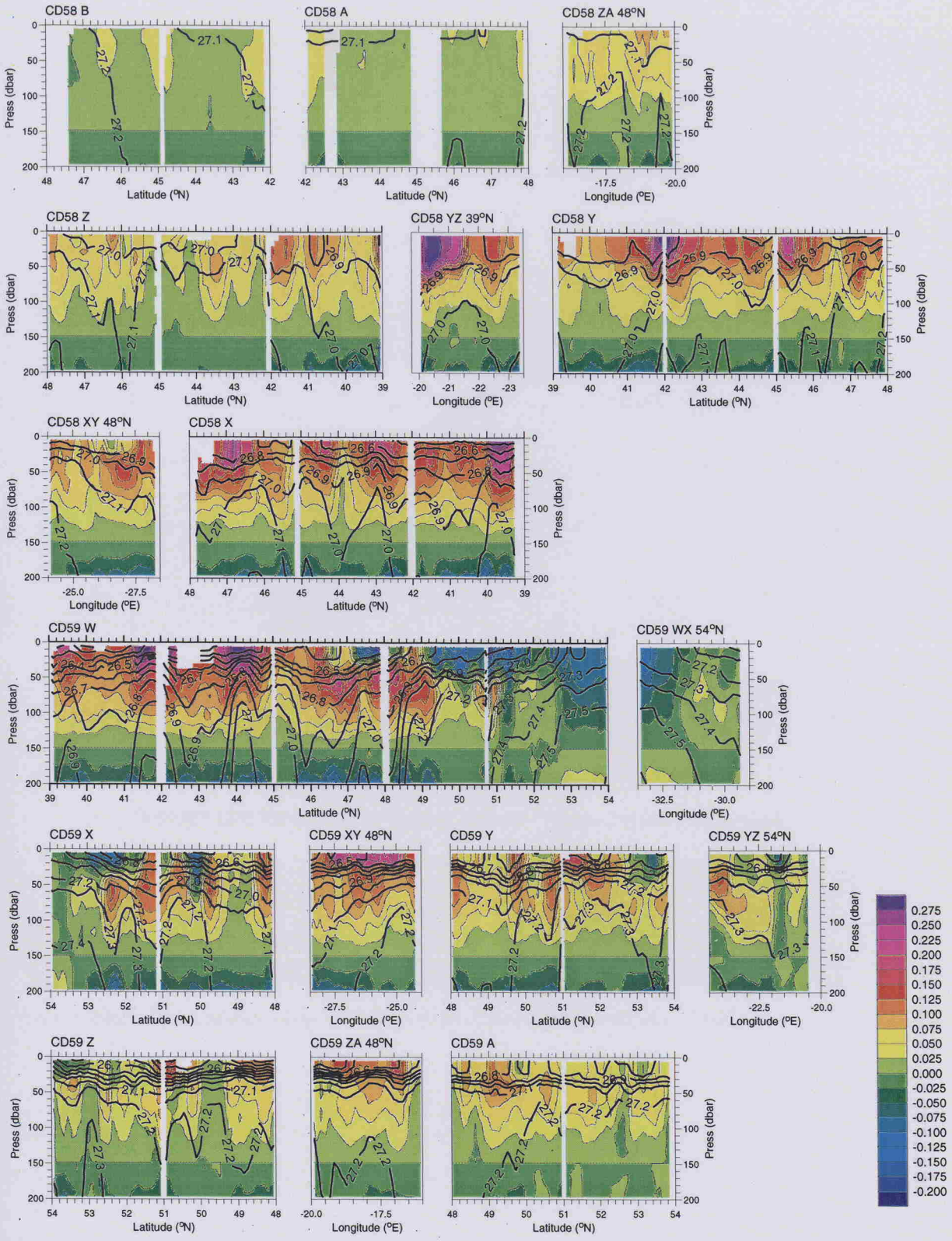

Figure 2.5. Vertical sections of seasonal salinity anomaly ΔS. Isopycnals overlaid showing σ_θ (kg m^{-3}).

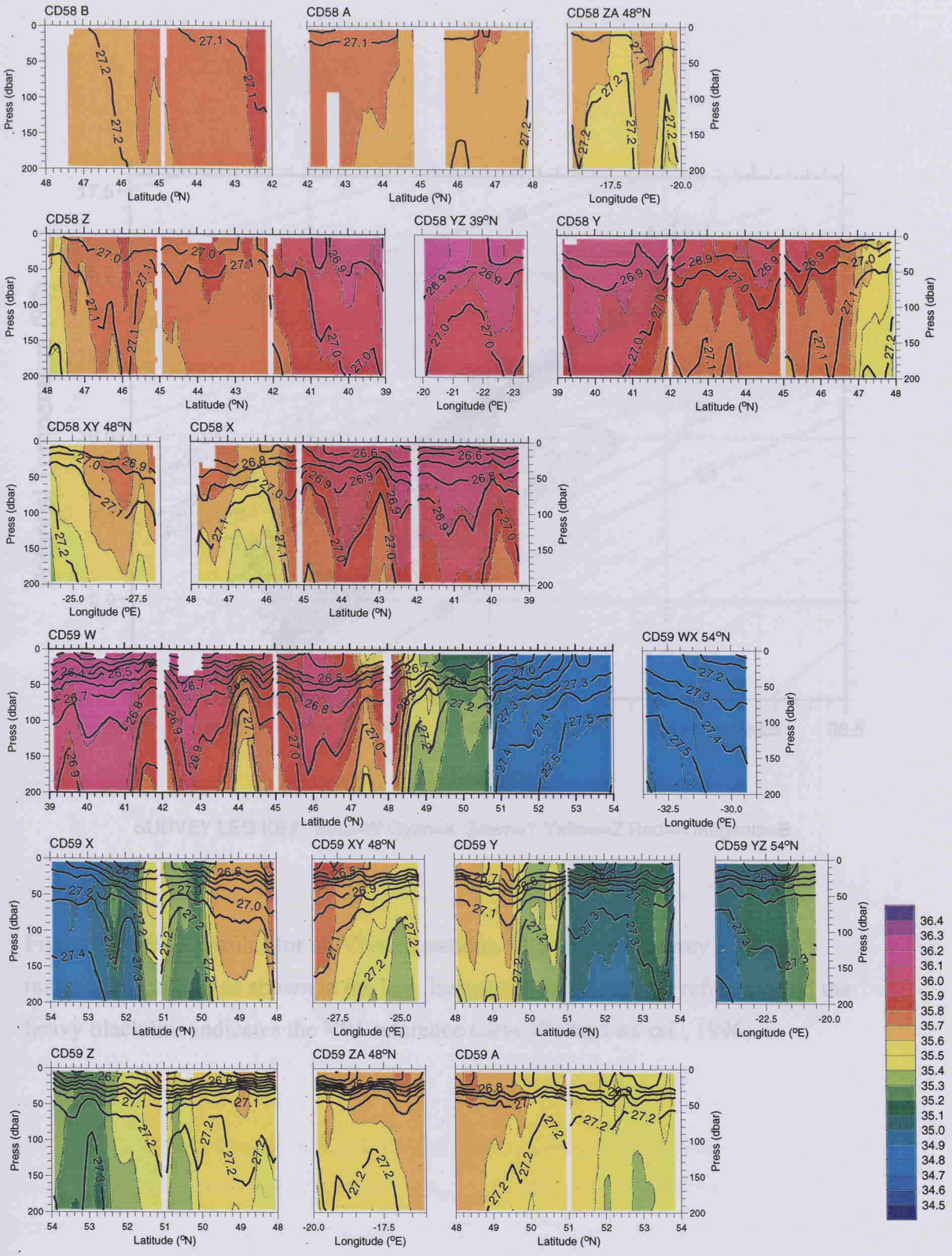

Figure 2.6. Vertical sections of salinity S. Isopycnals overlaid showing σ_θ (kg m^{-3}).

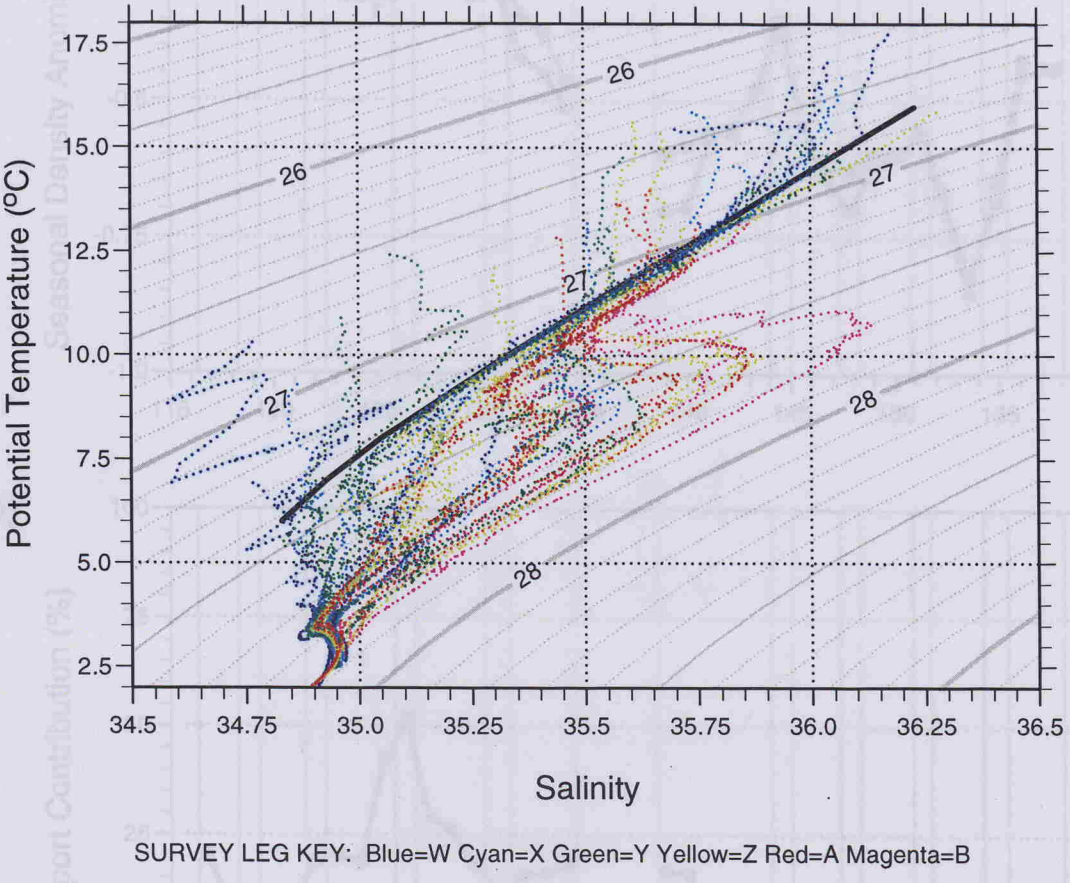

Figure 2.7. θ-S profiles for all Vivaldi stations. The different survey legs are indicated by colour as shown in the key. Isopycnals are shown for reference and the heavy black line indicates the V91 reference curve (Pollard *et al.*, 1996).

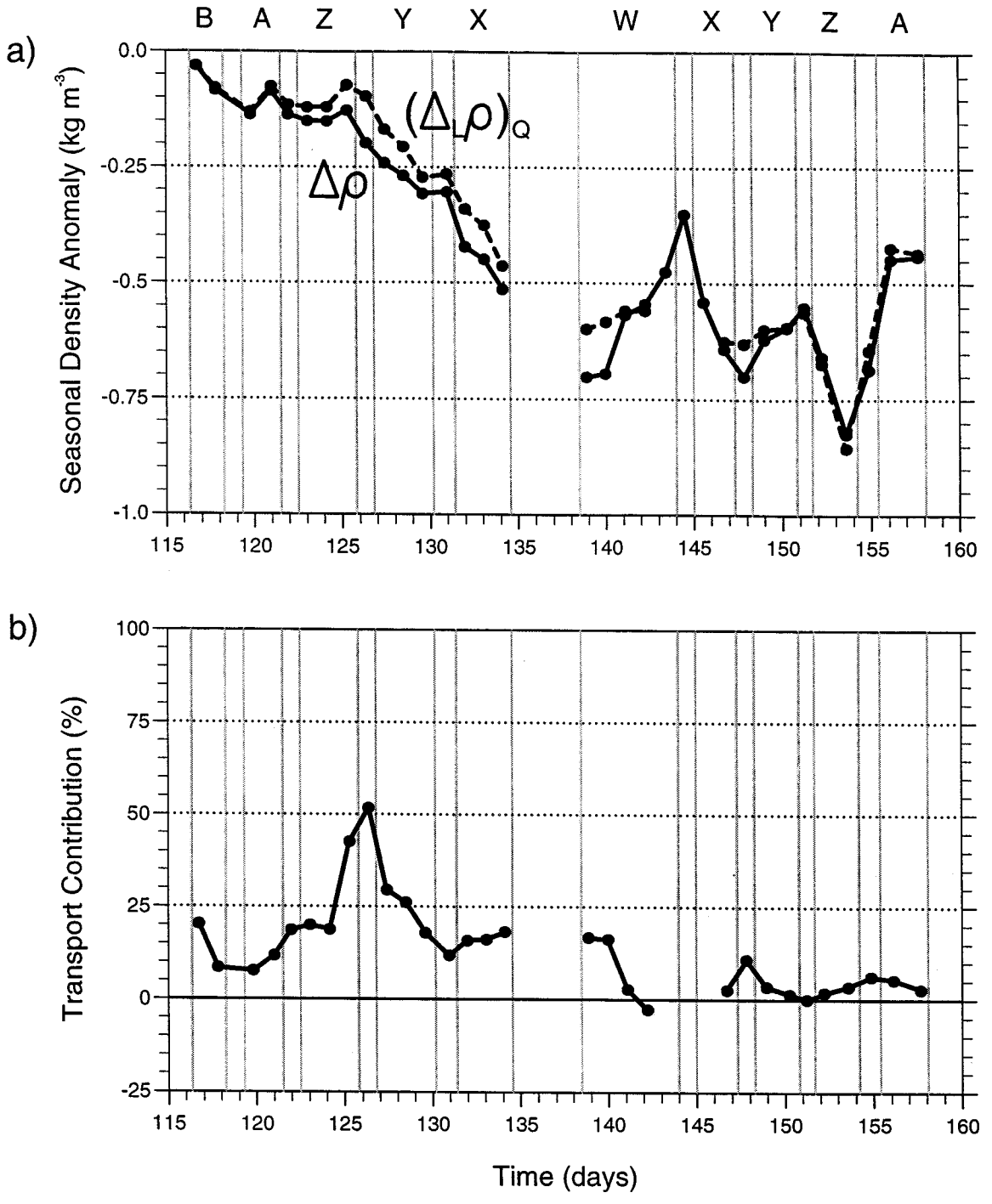

Figure 2.8. (a) 300 km mean surface seasonal density anomaly $\Delta\rho(0)$ and estimated density anomaly due to air-sea fluxes only $(\Delta_L\rho)_Q(0)$. The difference is the estimated buoyancy transport component $(\Delta\rho)_T(0)$. (b) The percentage contribution made by transport of pre-existing buoyancy to the observed seasonal density anomaly. i.e. $(\Delta\rho)_T(0) / \Delta\rho(0)$.

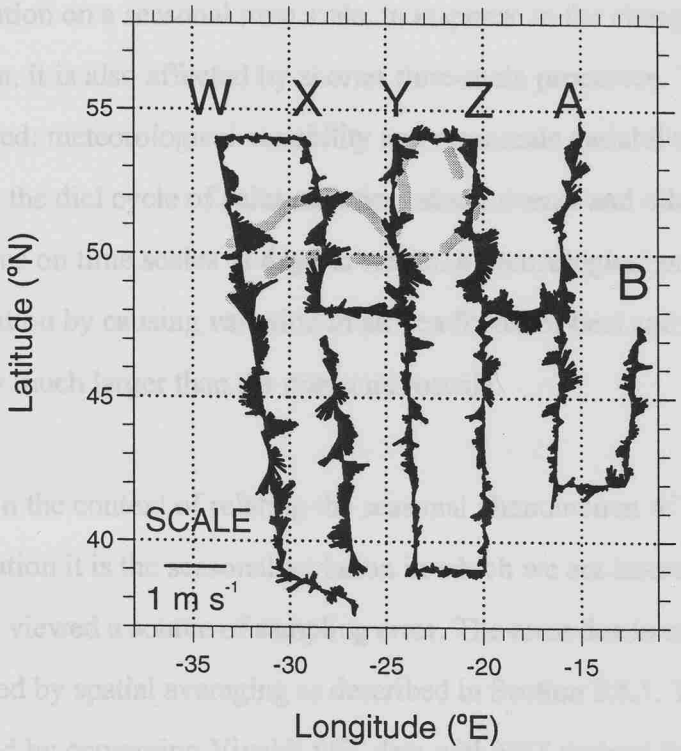

Figure 2.9. ADCP current velocity at 100 m depth. The approximate positions of major fronts, as identified by Pollard *et al.* (1996), are also shown. These are the Polar Front (solid line) and the weaker front associated with the southern branch of the NAC (dashed line).

2.5 Short-term Fluctuations in the Seasonal Stratification

The analysis in the last two sections has been restricted to the seasonal density anomaly as observed. While we expect this quantity to largely reflect the development of stratification on a seasonal time scale, in response to the changing day length and solar elevation, it is also affected by shorter time-scale processes. Two types of process must be considered: meteorological variability and mesoscale variability in the ocean. The former includes the diel cycle of solar radiation, storm events and other fluctuations in weather conditions on time scales of days to weeks. Meteorological processes affect the stratification by causing variation in air-sea fluxes of heat and momentum at spatial scales typically much larger than the ocean mesoscale.

In the context of relating the seasonal phenomenon of bloom development to the stratification it is the seasonal variation in which we are interested and the shorter time-scale signal is viewed a source of sampling error. The error due to mesoscale variability is attenuated by spatial averaging as described in Section 2.5.1. The remaining errors are estimated by comparing Vivaldi SST data with SST derived from an auxiliary data set according to the method given in Section 2.5.2. The processing of the SST data is described in detail in Appendix C. The differences in SST are discussed in Section 2.5.3 and corrected seasonal density anomaly data are presented in Section 2.5.4.

2.5.1 Reduction of Mesoscale Eddy Interference

Assuming the short time-scale variations in stratification caused by the mesoscale eddy field can be considered random and statistically stationary over the time and length scales of interest, the effects of spatial and temporal averaging are equivalent and some of the short-time scale variance may effectively be removed from the survey data by spatial averaging.

Each of the SeaSoar runs during the Vivaldi survey consisted of a 300 km straight line transect sampled over a period of a little less than 1 day and as such provides a natural unit over which to average. This length scale is large compared with the inertial range discussed in Chapter 1 at which rapid fluctuations associated with frontal dynamics and the enstrophy cascade occur. Above the inertial range, an analysis of satellite sea surface height data by Le Traon (1991) for the area between 40 to 50°N and 10 to 30°W shows a spectral peak at length scales between 200 and 600 km. However, this is associated with time scales greater than 100 days, so variability at these scales is unlikely to be a major source of interference at sub-seasonal time scales. The 300 km mean value of the observed surface seasonal density anomaly for each SeaSoar run is therefore considered to be a much better estimate of its seasonal component at the mid point of the transect than the local value. Because each Vivaldi SeaSoar run lasted approximately 1 day, using the SeaSoar runs as the averaging unit has the added advantage that most of the variance in the data set introduced by the diel cycle is removed.

2.5.2 Estimation of Event-Scale Stratification Anomaly

The time scale of days to weeks associated with variability in weather conditions will be referred to as the event-scale and fluctuations in the seasonal density anomaly caused by event-scale processes will be referred to as event scale density anomalies. The contribution of event scale anomalies to the observed seasonal density anomaly has been estimated by comparing the point-in-time sea-surface temperature (SST) data obtained during the Vivaldi survey with 1991 data derived from the Comprehensive Ocean Atmosphere Data Set, release 1a (COADS 1a, Woodruff *et al.* 1993). The data is from a modified version used in the compilation of the Southampton Oceanography Centre global air-sea heat flux climatology (Josey *et al.*, in press), which includes corrections for observational biases made by Kent *et al.* (1993) using procedural information from the World Meteorological Office list of ships (WMO, 1994).

The COADS data were processed to derive SST time series at Vivaldi sampling locations. These time series were averaged over a time scale T_s of 30 days which is long compared with the event scale and short compared with the time scale of seasonal change (1 year). An estimate of the sampling error with respect to the seasonal variation in SST, referred to here as the event-scale SST anomaly, is given by

$$\delta T(0) = T(0) - T_{30}(0)$$

where $T(0)$ is the Vivaldi SST and $T_{30}(0)$ is the value of the smoothed SST time series at the time of sampling. Estimates for the event-scale SST anomaly were calculated and converted to event-scale density anomalies $\delta\rho\ (0)$ on the assumption that the event-scale density anomaly is a function of temperature only, such that

$$\delta\rho\ (0) = \rho[S(0), T(0)] - \rho[S(0), T(0) - \delta T(0)]$$

where $S(0)$ is the local sea surface salinity. These $\delta\rho\ (0)$ estimates were then used to calculate a corrected surface seasonal density anomaly

$$\Delta\rho_{30}(0) = \Delta\rho(0) - \delta\rho\ (0)$$

on the further assumption that the event-scale anomaly is zero at z_w, which is reasonable if event-scale density anomalies are due to meteorological forcing only. The previous assumption, that the density anomaly is a function of temperature only, requires that short time-scale fluctuations in air-sea and internal fluxes of freshwater have a negligible effect on the large scale density field. The most likely source of error is probably fluctuations in the direction of Ekman transport in regions of large horizontal gradients such as the Polar Front.

The SST values used in the method described here are estimates of a large scale mean SST. This is important, not only because single observations suffer from the problem of

interference caused by mesoscale variability as described in Section 2.5.1, but also because we need to compare values of SST at a location over a finite time period T_s, during which water is displaced horizontally by both the eddy field and the mean flow. It is therefore necessary to average over a spatial scale L which is large compared with the length scale of displacement in time T_s. Ideally then, L should be as large as possible without being so large compared with the spatial scales of the fluctuations in meteorological forcing in which we are interested that their effects are averaged out. Data have been processed to give estimates of a 5° mean as described in Appendix C. Maximum velocities associated with the mean geostrophic flow are about 6 cm s^{-1}, occurring in the region of the North Atlantic Current (McCulloch and Leach, 1997). This is equivalent to about 156 km in 30 days which is small compared with the scale of averaging so horizontal advection by the mean flow may be ignored.

2.5.3 Event-scale SST Anomaly

The time series of estimated event-scale SST anomalies along the cruise track is shown in Figure 2.10 with estimated 95% confidence intervals shown at ±2 standard deviations. The origin for the time axis is the beginning of the calendar year and this convention is used throughout the study. Unfortunately, there are large gaps during CD59 where COADS data coverage was insufficient to estimate $T_{30}(0)$.

Significant negative SST anomalies appear to be fairly common in the survey data, being found on all CD58 legs apart from CD58 B, on zonal transect CD58 XY and also on CD59 A. In contrast, there are only two significant positive anomalies. These are found on CD59 W and Z. Interpretation of some of the larger SST anomalies is aided by a comparison with the stratification. The large negative anomalies seen during the time period from 130 to 133 d are associated with an apparent deepening of the mixed layer on transects CD58 XY and CD58 X (Figure 2.2). This is almost certainly a response to high winds. Wind speeds of up to about 16 m s^{-1} were measured on the ship during this period

(unpublished data) and conditions were sufficiently rough that the SeaSoar was not recovered between the two transects and no CTD station was carried out (Pollard *et al.*, 1991). The largest positive SST anomaly is seen at time 153 d during transect CD59 Z. Very strong stratification has developed here (Figure 2.3) and Figure 2.2 shows very little evidence of boundary layer mixing below about 5 m on that day. Because of this, most of the diurnal heat storage is confined to a very shallow surface layer resulting in a higher than average SST for that time of year.

2.5.4 Corrected Seasonal Density Anomaly

Figure 2.11 shows the 300 km mean surface seasonal density anomaly before and after correction and illustrates the importance of the correction term. An examination of the distribution of the estimated event-scale density anomaly $\delta\rho$ (0) against the corrected seasonal density anomaly $\Delta\rho_{30}(0)$ (Figure 2.12) shows an apparent increase in the variance of $\delta\rho$ where the stratification is greater. This probably reflects a general tendency for the shallower mixed layer depths to restrict changes in heat storage associated with weather fluctuations to thinner layers.

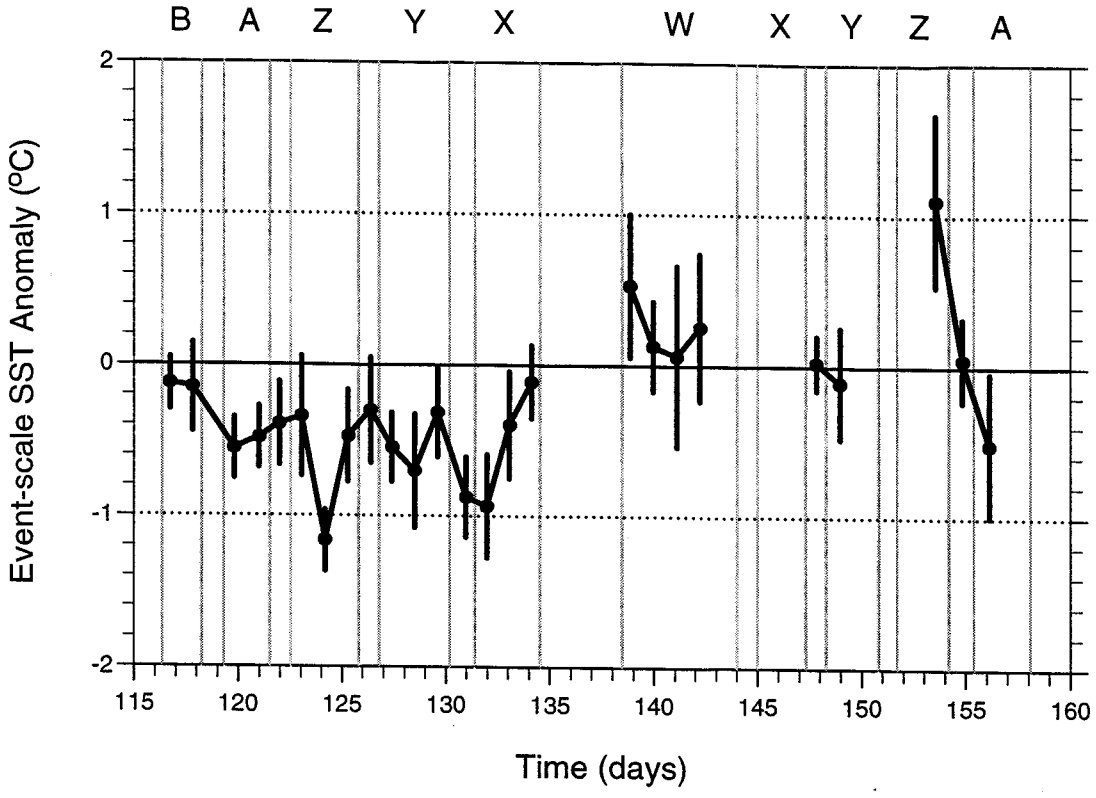

Figure 2.10. Event-scale SST anomaly $\delta T(0)$, showing 95% confidence intervals.

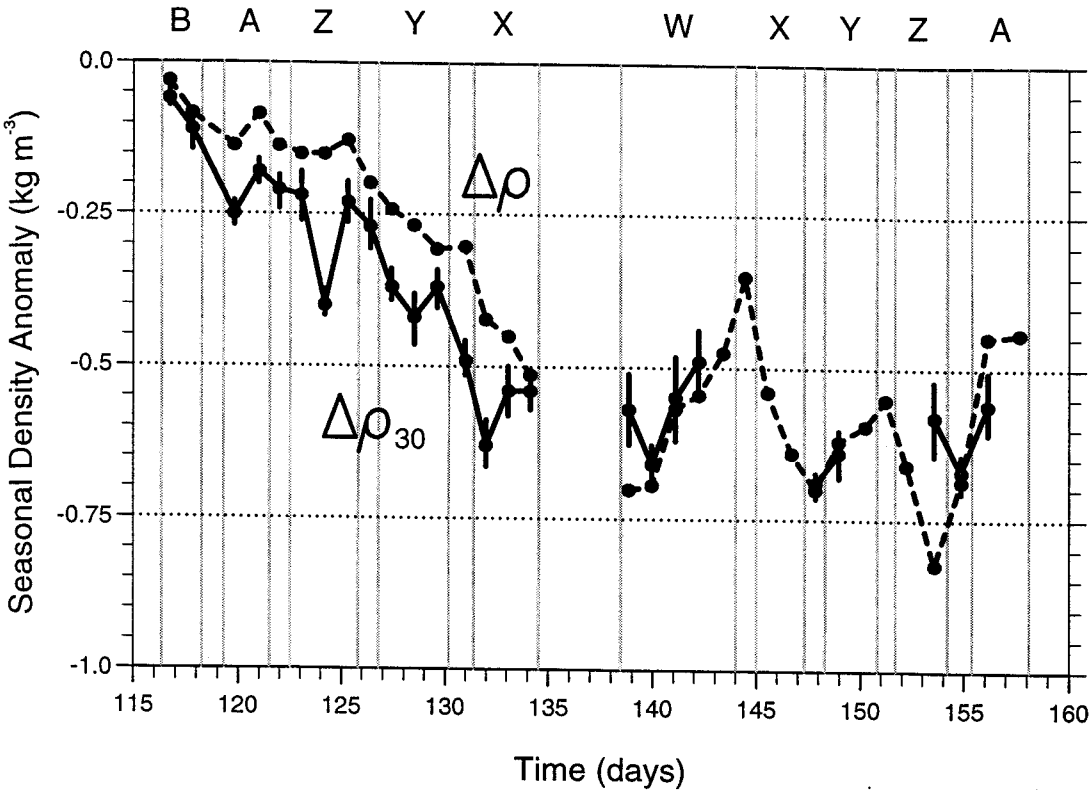

Figure 2.11. 300 km mean surface seasonal density anomaly $\Delta\rho_{30}(0)$, showing 68% confidence intervals. Dotted line shows uncorrected seasonal density anomaly $\Delta\rho(0)$.

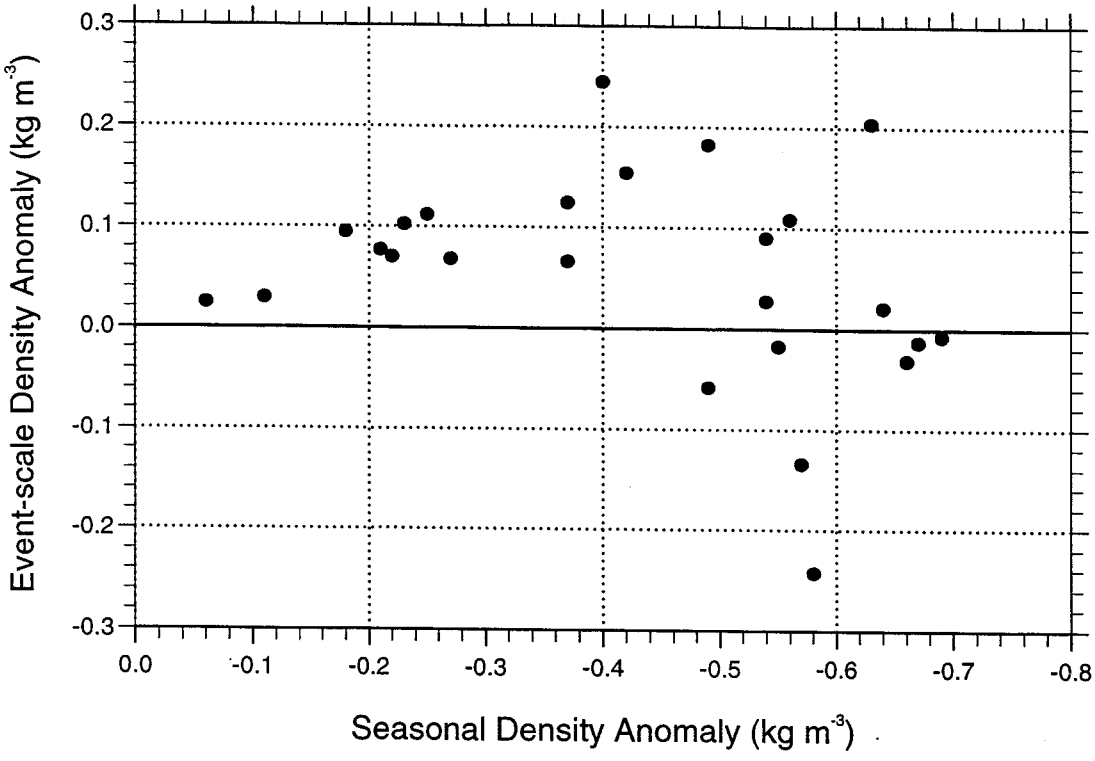

Figure 2.12. Distribution of event-scale density anomaly $\delta\rho(0)$ against seasonal density anomaly $\Delta\rho_{30}(0)$.

2.6 Pre-Bloom Mixed-Layer Nitrate Concentration

Nitrate concentration for a material element following the fluid motion is determined by the balance between uptake by phytoplankton and re-mineralisation. The concentration in the mixed layer reaches a maximum towards the end of winter when new production and uptake are low. This winter-time maximum will be referred to as the pre-bloom nitrate concentration and its estimation allows values for integrated new production between the start of the bloom and the time of sampling to be determined from surface nitrate measurements taken during the survey. These production estimates will be minimum values based on the assumption that mixed layer nitrate concentrations are not significantly increased by vertical mixing and/or upwelling after the initiation of the bloom.

Nutrient concentrations in the winter-time mixed layer are known to vary greatly over the area covered by the survey, the pattern being dominated by a meridional gradient from high winter nutrient levels in the north to low in the south. Maps of winter nutrient concentrations for the North Atlantic are presented by Glover and Brewer (1988). These authors investigated a number of methods for estimating winter-time mixed layer nutrient concentrations. Their preferred method was to interpolate nutrient concentration values from each available CTD profile to a depth corresponding to the climatological winter-time mixed layer depth at the geographical position of the station. These point values are then used as direct estimates of the winter concentrations based on the assumption that water at this depth formed part of the winter mixed layer and has been relatively unaffected by biological uptake of nutrients between the end of winter and the time of sampling.

The method does not take into account advection and this, along with interannual variability in the depth of winter mixing, can lead to errors associated with the choice of depth at which to extract nutrient values. Horizontal advection of the water column between winter and the time of sampling may cause a mismatch between the location of the water column in winter and the station position used to extract the climatological data. Upwelling

or downwelling during the same period can also make the depth chosen invalid. In areas where there is significant vertical shear in the water column above the depth of winter mixing, horizontal advection will also cause errors in the geographical position ascribed to the nutrient values. This will be especially true where there is strong baroclinic eddy activity or Ekman flow.

The meridional winter nitrate gradient in this part of the North Atlantic is accompanied by strong meridional gradients in temperature and salinity. In this study, an end-of-winter or pre-bloom nitrate concentration has been inferred from salinity using a linear nitrate-salinity relationship determined empirically from measurements of water below the seasonal pycnocline. This relationship is used to estimate pre-bloom nitrate for water observed at the surface on the assumption that salinity acts as a conservative tracer during the period between the end of winter and the time of sampling. While there is no obvious reason for a direct link between nitrate and salinity the existence of such a relationship may seem less surprising if it is noted that the NACW θ–S characteristics discussed in Section 2.4 allow us to think of salinity as a proxy for winter-time temperature or density. Section 2.6.1 describes the method for derivation of the nitrate-salinity relationship, the results are presented in Section 2.6.2 and the applicability of the relationship to the surface water sampled during the survey is discussed in Section 2.6.3. In Section 2.6.4, the salinity-based pre-bloom nitrate estimate is compared with the winter nitrate estimate which would have been obtained by applying the Glover and Brewer method to the Vivaldi nitrate profiles.

2.6.1 A Model of the Variation of Pre-Bloom Nitrate with Salinity

In order to derive a nitrate-salinity model for the winter-time mixed layer using the Vivaldi observations, the integral effect of uptake and re-mineralisation processes since the end of winter must be allowed for. During the spring, uptake is very much the dominant process. It may be assumed that uptake occurs mostly above or within the seasonal

pycnocline and so much of its effect can be eliminated if the data used for fitting the model is selected to exclude observations above the bottom of the pycnocline. The approach then is similar to that described in Section 2.3 for the determination of physical winter-time properties. However, unlike temperature and salinity, the nitrate concentration of subducted water is not a conservative tracer but tends to increase over time as a result of re-mineralisation processes.

Fortunately it is possible to predict nitrate changes in the ocean interior from the AOU (Sugiura, 1965; Broecker and Peng, 1982). The AOU of a material element is assumed to be directly proportional to the difference between its present nitrate concentration and its nitrate concentration at the time the water left the surface. The latter is referred to as the *preformed* concentration. This assumption requires firstly that the oxygen content of the newly formed water is close to the saturation value. Secondly, the respiration of nitrogenous material is taken to be a constant fraction of total respiration and is equated with nitrification. Any nitrogen pools associated with intermediate products are ignored.

For water unaffected by the spring bloom (i.e. having nitrate concentration equal to or greater than the winter maximum for the mixed layer) which has been subducted below the euphotic zone since the end of winter, the pre-bloom or end-of-winter mixed layer nitrate concentration we wish to model is by definition equal to the preformed nitrate. The model takes the form

$$N_0 = \beta_0 + \beta_1 S_0 + \varepsilon_1 , \qquad (1)$$

where N_0 is the preformed nitrate concentration, S_0 is the winter-time salinity (equal to the observed salinity S for subducted water), β_0 and β_1 are constants and ε_1 is a random error term. The value of N_0 for surface water of salinity S is given by

$$N_0 = \beta_0 + \beta_1 (S - \Delta_L S_{E\text{-}P}) + \varepsilon_1 , \qquad (2)$$

where the term $\Delta_L S_{E-P}$, defined in Section 2.4, represents the change in salinity of a material element caused by air-sea fluxes of freshwater since the end of winter.

For the purposes of estimating β_0 and β_1, the unknown variable N_o is expressed in terms of the observed nitrate concentration N and AOU $\varnothing$ by

$$N_o = N - \alpha\varnothing + \varepsilon_2, \tag{3}$$

where α is a constant and ε_2 is a random error term. Substituting for N_o in Equation 1 then gives

$$N + \varepsilon_2 = \beta_0 + \beta_1 S + \alpha\varnothing + \varepsilon_1. \tag{4}$$

The coefficients β_0, β_1 and α are estimated using orthogonal distance regression (Boggs and Rogers, 1990) which gives equal weight to the two independent error terms.

The method for selection of data for determination of the nitrate-salinity relationship differs to some extent from that used in Section 2.2 for two reasons. The first is a practical one concerned with the sparse distribution of sub-surface nitrate and AOU data. These data are only available for bottle samples taken at the CTD stations on a 300 km grid and so to ensure a reasonable sample size it is necessary to select data from a range of depths rather than one particular depth z_w. The second is that, while we normally expect most of the nitrate uptake to occur above or within the seasonal pycnocline, it is unreliable to assume that deeper water is unaffected by the bloom. The seasonal pycnocline can be destroyed by strong vertical mixing events some time after the initial stratification and then reform. If the stratification prior to such an event had been sufficient for initiation of a phytoplankton bloom then nitrate concentration would be affected over the range of vertical mixing, leading to reduced nitrate concentration below the observed seasonal pycnocline. The signature of a

major phytoplankton bloom can be stronger and less easily erased by mixing events than that of seasonal heating because of the rapid exponentially increasing nature of the nitrate uptake.

In the same way that nitrate re-mineralisation is associated with oxygen utilisation, nitrate uptake is associated with production of oxygen during photosynthesis. This increase in oxygen often causes super-saturation and negative AOUs and so to a limited extent a model of pre-formed nitrate which takes into account AOU might explain variance introduced below the pycnocline by detrainment of nitrate depleted water. However, much of the oxygen produced during photosynthesis would have been lost to the atmosphere prior to subduction and so it is preferable to omit data which shows any evidence of uptake if possible. This can be achieved by selecting water with AOU above a certain limit, chosen by comparing the AOU data with the pycnocline depth over the whole survey.

As in Section 2.3 it is desirable to avoid observations of water formed in previous years as these waters may have been formed in rather different areas or may have significantly different characteristic because of inter-annual variability. Older water will have higher AOUs and so may be excluded by setting a maximum limit on AOU.

2.6.2 Model Specification for the Survey Area

Data were selected where AOU was between 10 and 35 mmol m^{-3}, these levels being chosen by inspection of the vertical gradients in Figure B.2. Figure 2.13 shows the relationship between nitrate and salinity for the selected data. The θ–S relationship for the same sample is shown in Figure 2.14. The nitrate-salinity data show clearly the existence of a linear relationship for NACW with higher nitrate concentrations in the lower salinity water. This does not however appear to extend to ASIW (identified by salinities less than 35.0). The ASIW data will therefore be treated separately. If ASIW observations are

excluded salinity alone is found to explain 81% of the nitrate variance ($n = 102$). Fitting Equation 4 to these data gives

$$\beta_0 = 325.2,$$

$$\beta_1 = -8.88 \pm 0.38,$$

$$\alpha = 0.073 \pm 0.012.$$

Confidence intervals are specified at 68%. This model explains 86% of the nitrate variance.

Although a relationship between nitrate and salinity for ASIW cannot be ruled out because of the small salinity range in the Vivaldi sample, the data provide no evidence of such a relationship. In fact, 76% of the nitrate variance in the ASIW data is explained by AOU ($n = 10$). β_1 was therefore set to 0 to give a constant pre-formed nitrate concentration determined by β_0. Fitting Equation 4 with $\beta_1 = 0$ gives a value for α of 0.113 ± 0.021. This is not significantly different from that for NACW at the 95% level and so in view of the small sample size the NACW coefficient was used to determine N_o, according to Equation 3 and β_0 was set to the mean N_o for ASIW (14.23 ± 0.13).

Substituting for β_0 and β_1 in Equation 1 gives predicted N_o lines for the two water masses which intersect at $S_o = 35.02$, giving a model estimate of pre-bloom nitrate for the survey area as a whole defined by

$$N_o = 14.23 \pm 0.75 \text{ mmol m}^{-3} \qquad S_o < 35.02,$$

$$N_o = 325.24 - 8.881\, S_o \pm 0.75 \text{ mmol m}^{-3} \qquad S_o \geq 35.02.$$

The estimate of the 68% confidence intervals quoted here is given by the standard deviation of the residuals for both water masses combined, the pre-bloom nitrate being calculated for individual observations using Equation 3. The variance in the residuals actually comes from

error in this 'observed' pre-bloom nitrate (ε_2) as well as error in the model (ε_1) and so the confidence intervals correspond to an upper limit of the model error estimate as ε_2 tends to zero. These confidence intervals are used in the modelling study presented in Chapter 3. However, if ε_2 were assumed instead to be of the same magnitude as ε_1 then a reduction in the standard deviation of ε_1 by a factor of $\sqrt{2}$ would be implied, giving confidence intervals of ± 0.53 mmol m^{-3}. The final model explains 92% of the variance in nitrate ($n = 112$).

Figure 2.15 shows the model prediction for pre-formed nitrate, together with the 'observed' values calculated from the individual observations using Equation 3. The greatest residuals are found at station W51 which was located at the Polar Front and it could be speculated that they are the result of unusual ecosystem dynamics associated with the front, although insufficient data is available to test such a hypothesis. Apart from this there appears to be evidence for a slight positive bias in the region of stations W45, W48, X48 and X51 and some evidence for a negative bias in the middle of the most southerly part of the survey area but no evidence of any larger scale spatial trends.

2.6.3 Applicability of the Model to the Surface Water

The model derived in Section 2.6.2 is applicable to the water observed at the surface under the following assumptions. Firstly, the nitrate-salinity relationship of the water in the range chosen for the reference data set must be representative of the pre-bloom or end-of-winter relationship for the water observed at the surface. Secondly, it must be reasonable to consider salinity as a conservative tracer over the period between the start of the heating season, when stratification begins to develop, and the time of the survey such that $S = S_o$. The propriety of the latter assumption has already been demonstrated in Section 2.3. The analysis presented there suggested a maximum value for $\Delta_L S_{E\text{-}P}$ (0) of around 0.035, which is equivalent to an error of 0.31 mmol m^{-3} in nitrate: only about half the error estimate for the model.

Ignoring vertical shear, the first assumption is satisfied if the winter mixed layer is vertically homogenous such that the nitrate concentration and salinity of water detrained during the heating season match the properties of the surface water. Vertical shear is potentially a problem near the boundary of the survey area as we cannot necessarily assume that the nitrate-salinity relationship used is valid outside the area sampled. In the presence of vertical shear flow, water sampled at the surface may have acquired its winter properties in an area in which the nitrate-salinity relationship is different from that of the sub-surface water sampled in the same location. This is most likely to cause biases on leg W where there is a geostrophic mean flow into the survey area varying from about 2 cm s^{-1} in the south to a maximum of about 5 cm s^{-1} in the North Atlantic Current at about 51°N (McCulloch and Leach, 1997). The maximum surface salinity over the whole survey is about 36.2, found at the southern end of leg W. The minimum, 34.6, is also found on leg W in the region of the North Atlantic Current. Both of these values lie slightly outside the salinity range covered by the reference data set. This, combined with the more erratic distribution of N_0 residuals on leg W than on some of the other legs suggesting a possible change in the relationship to the west of the survey area, implies that errors in the N_0 estimate for surface water may be greater on leg W than elsewhere.

2.6.4 Comparison with the Method of Glover and Brewer

It is useful to compare the winter nitrate estimates obtained here with those obtained by applying the more traditional Glover and Brewer method. For this purpose, Levitus' (1982) mixed layer depth estimates based on a temperature difference criterion of 0.5°C were used. An average winter-time mixed layer depth field (on a 1 degree grid) was determined by averaging the mixed layer depths for February, March and April. This differs slightly from the processing done by Glover and Brewer who calculated the winter-time mixed layer depth from hydrographic profiles averaged over these months. They also used a variable σ_t criterion, although this was chosen to be equivalent to the 0.5°C criterion in the absence of salinity structure. Despite the differences, the resulting mixed-layer depth field

(Figure 2.16a) is very similar to that presented by Glover and Brewer (1988). Winter nitrate estimates were determined for each of the Vivaldi CTD stations by selecting the winter mixed layer depth closest to the station position and interpolating the measured nitrate profile to that depth. The estimated winter nitrate field is shown in Figure 2.16b. Figure 2.16c shows the salinity-based winter nitrate field for comparison. This latter field was determined from the surface salinity, averaged over each 300 km SeaSoar transect.

The two maps show broadly similar patterns dominated by a strong south to north gradient with maximum values in the north-west. In both cases, a comparison of these values with those in the south-west shows a latitudinal range in the western half of the survey area varying from 10-12 mmol m^{-3}. However, the Glover and Brewer type estimates, while being essentially consistent with the winter-time nitrate derived by Glover and Brewer (1988) from rather sparse data, are noticeably higher. The field in Figure 2.16b is also generally less smooth than that in Figure 2.16c and there is a sharp decline in winter nitrate in the south-east which is not seen in the salinity-based estimates.

The positive bias shown by the Glover and Brewer type estimates warrants further investigation. Both methods rely on the existence of a layer of water at some depth which preserves the properties of the winter-time mixed layer, but the choice of depth associated with such a layer differs. In the Glover and Brewer method the depth chosen is the average winter-time mixed layer depth, while in the method presented here a depth range is chosen using the AOU properties of the water. The winter-time mixed layer depth for individual stations along the cruise track is shown in Figure 2.17a. Examination of the AOU at this depth (Figure 2.17b) gives an independent measure of the age of the water. At most stations the AOU lies within the range 10-35 mmol m^{-3} used in the present study. However there are exceptions. Most of these are low AOU values, indicating an influence of water formed very recently which is likely to have been in the mixed layer during the bloom. In particular, the values less than 5 mmol m^{-3} at the southern ends of legs B and A (around time 119 d) should lead us to suspect that the sharp drop in the estimated winter-time nitrate in the south-east (Figure 2.16b) might be an artefact resulting from seasonal uptake. There are two high AOU

values outside the 10-35 mmol m^{-3} range, but there is no evidence to suggest a general influence of older water which might explain the observed positive bias in the Glover and Brewer type estimates.

A much more likely cause of positive bias is the neglect of the nitrate increase due to re-mineralisation after detrainment of the winter-time water. A plausible correction may be made for this effect by using the value of α from the present study to calculate preformed nitrate (Equation 3). Figure 2.17c shows the discrepancy between the Glover and Brewer type winter nitrate estimates and those based on salinity, before and after applying the correction. Here, the salinity-based estimate was determined from the top CTD bottle measurements in the depth range 5-30 m, the salinity in that range being taken as representative of the seasonal mixed layer. The top 5 m are excluded to reduce the potential for error which exists when the effects of extreme air-sea freshwater fluxes are confined to thin surface layers by a shallow diurnal pycnocline. Such errors are likely to be more significant for these individual measurements than for the transect data. The results suggest that typically about half the bias is attributable to re-mineralisation.

Also shown in Figure 2.17c, again referenced to the salinity-based winter nitrate estimate, is the anomaly in the salinity-based preformed nitrate estimate at the average winter-time mixed layer depth. Ignoring stations where the 'error' in the Glover and Brewer type estimate is negative, a very close correspondence can be seen between this anomaly and the error remaining in the corrected estimates. The anomaly in salinity which determines the nitrate anomaly is associated largely with the action of vertical shear on horizontal gradients as discussed in Section 2.4. The remaining positive bias in the Glover and Brewer type estimates can therefore be attributed to the neglect of this process.

A brief mention should be made of the unusual situation at station W51 (time 143 d). Here, the observed nitrate at the winter-time mixed layer depth is anomalously low, despite the AOU being rather high (about 38 mmol m^{-3}). W51 is the station located at the Polar

Front for which large pre-formed nitrate residuals were noted in Section 2.6.3. It is speculated that some aspect of the ecological dynamics associated with the front has lead to a greater imbalance between community respiration and nitrification here than is evident elsewhere.

In conclusion, the method of winter-nitrate estimation described here has a number of advantages over that of Glover and Brewer. It allows for the effects of re-mineralisation and advection which have been shown to be important in this study. It is also a more robust method since multiple data points are involved in determining the winter nitrate concentration $N_o(S)$ at a particular location. The expected error is easily quantified by examination of the N_o residuals for sub-surface water. Furthermore, it allows us to derive winter nitrate concentrations for water sampled during the SeaSoar runs between stations, for which no sub-surface nitrate data is available. The major disadvantage of the method presented here is its lack of generality, in that the model derived is very specific to the survey area and it cannot be assumed that a similar model will give a good fit to data collected elsewhere.

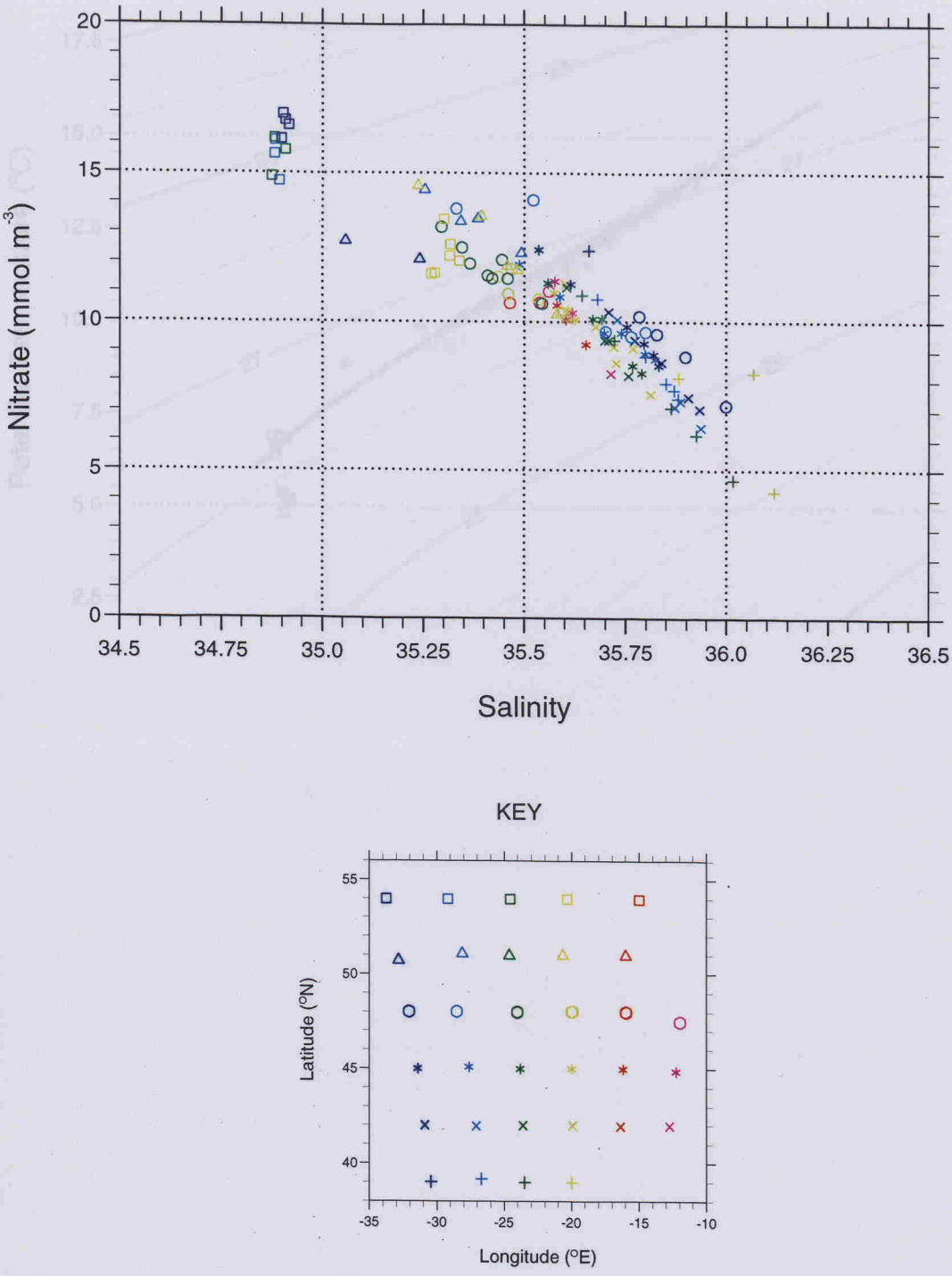

Figure 2.13. *N-S* distribution for winter-time mixed layer water (AOU between 10 and 35 mmol m^{-3}).

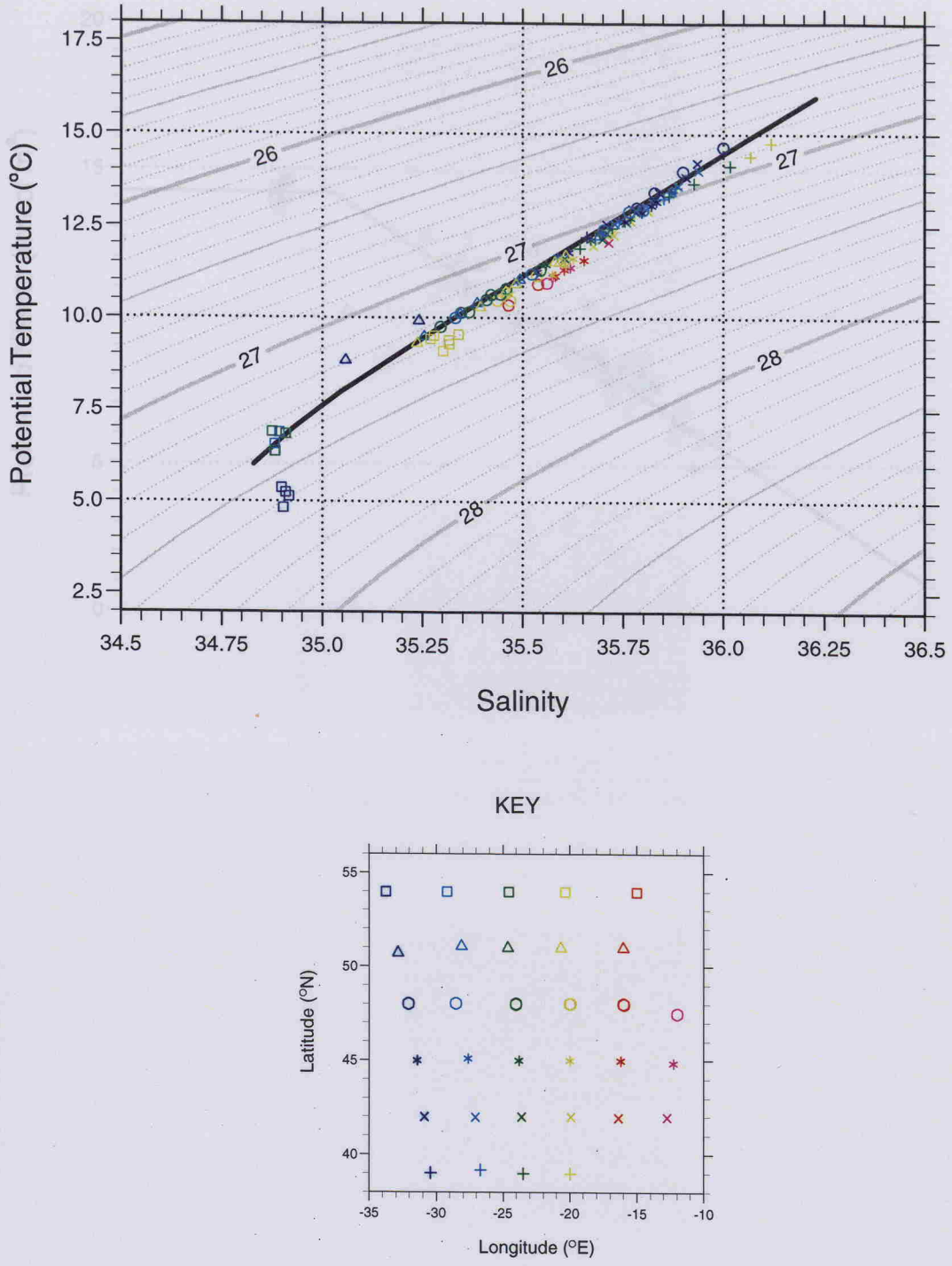

Figure 2.14. θ-S distribution for winter-time mixed layer water (AOU between 10 and 35 mmol m^{-3}). Isopycnals are shown for reference and the heavy black line indicates the V91 reference curve (Pollard *et al.*, 1996).

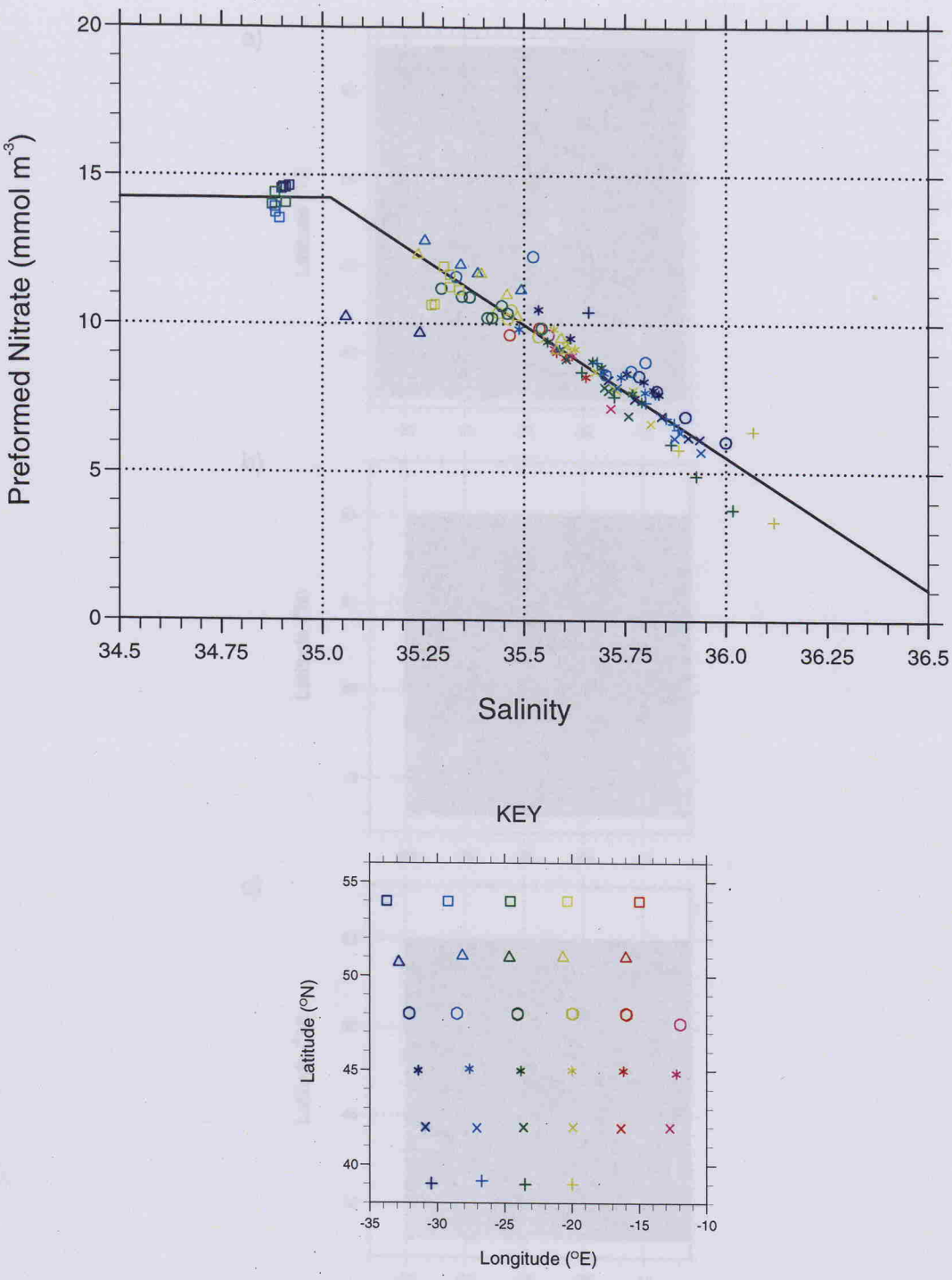

Figure 2.15. N_o-S distribution for winter-time mixed layer water (AOU between 10 and 35 mmol m^{-3}). The model prediction is shown by the solid line.

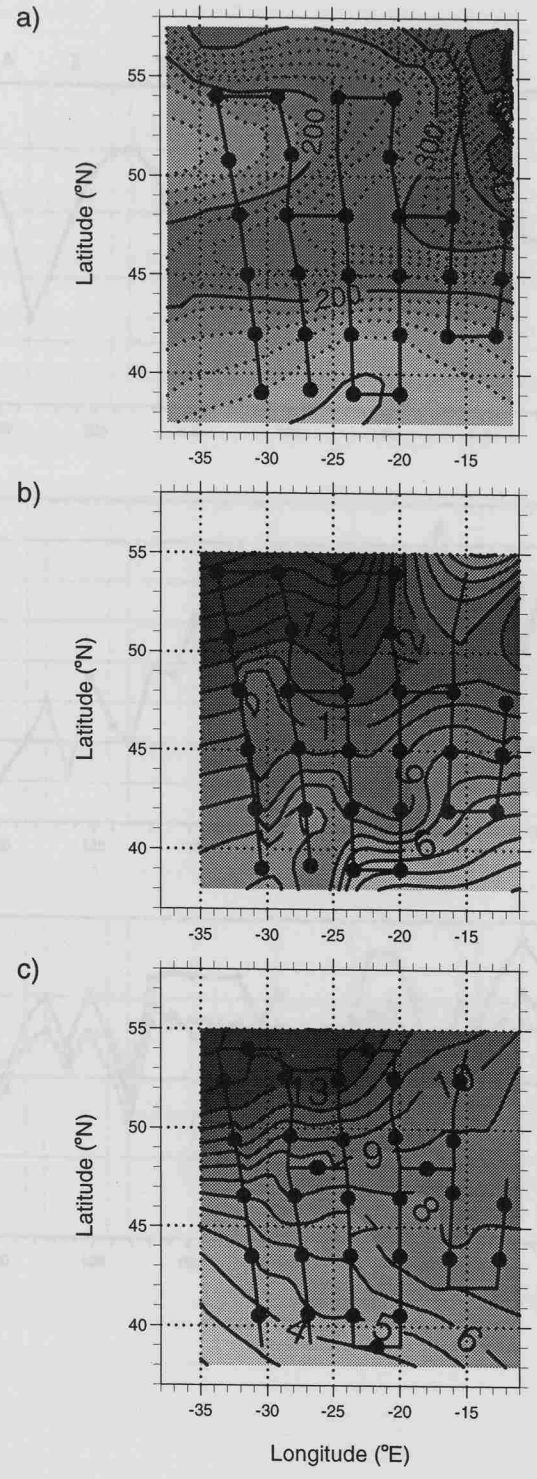

Figure 2.16. (a) Average winter-time mixed layer depth (m) based on Levitus' (1982) climatology. (b) Winter-time mixed layer nitrate concentration (mmol m^{-3}) estimated by the Glover and Brewer method. (c) Winter-time mixed layer nitrate concentration (mmol m^{-3}) estimated by the salinity-based method.

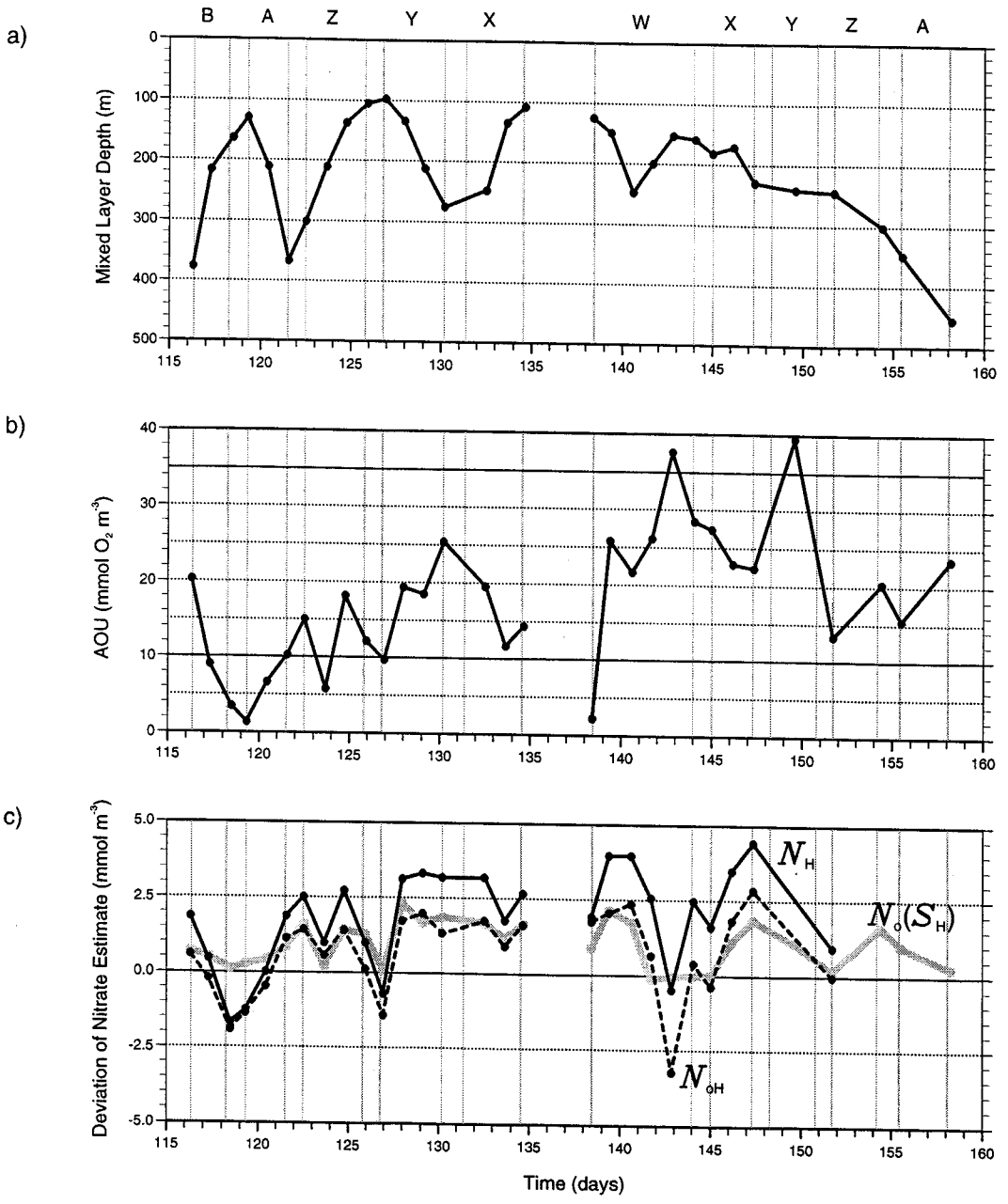

Figure 2.17. (a) Average winter-time mixed layer depth H at Vivaldi station positions. (b) AOU at depth H (c) Deviation of 3 winter-time nitrate estimates from the estimate based on mixed layer salinity $N_o(S_{5\text{-}30})$. The first estimate N_H is the nitrate at depth H (as in Glover and Brewer, 1988), the second is the preformed nitrate at the same depth N_{oH} and the third is the model preformed nitrate based on the salinity at this depth $N_o(S_H)$.

2.7 Nitrate Utilisation and Phytoplankton Standing Stock

In this section, the observed patterns in nutrient and phytoplankton distribution are described and used to assess the state of the spring bloom in different parts of the survey area. The surface nitrate distribution is examined first, in Section 2.7.1. While nitrogen is generally considered to be the main element limiting phytoplankton growth in the ocean, phosphorus and, for diatoms, silicon are also important requirements. Surface phosphate and silicate distributions are also presented in this section in order to identify areas where they might be sufficiently depleted, relative to nitrate, to have a significant effect on phytoplankton growth rates. The main features of the phytoplankton standing stock distribution, as represented by the concentration of chlorophyll *a*, are described in Section 2.7.2. The surface nitrate and chlorophyll concentrations are then combined with pre-bloom nitrate estimates to derive three measures of bloom progression, defined in Section 2.7.3, relating to nitrate utilisation and phytoplankton losses. The observed spatio-temporal patterns in these variables are examined in Section 2.7.4.

2.7.1 Nutrient Distribution

Figure 2.18 shows the surface nitrate data collected during the survey in relation to the estimated pre-bloom nitrate N_0 for the same water. These have been averaged in the same way as the data presented in Section 2.3 to give a 36 km running mean. At the north end of leg W nitrate concentrations are still very high at about 12 mmol m^{-3} and very high concentrations, relative to N_0, are also found at the northern ends of legs CD58 B and A, between about 46 and 47°N on CD58 Z and at about 45°N on CD58 Y. This indicates early bloom conditions in these areas. In contrast, at the southern end of leg W and in patches on CD58 YZ nitrate is almost fully depleted. The chlorophyll distribution (Figure 2.19) also shows the existence of a deep chlorophyll maximum, characteristic of oligotrophic waters, at the southern end of leg W, although it should be remarked on at this point that less intense deep chlorophyll maxima are also found in more eutrophic areas in the region of the North

Atlantic Current (CD59 X, XY, Y and Z). In those areas they are perhaps more likely to be the result of vertical shear acting on horizontal gradients in phytoplankton concentration, causing water low in phytoplankton to be advected over water containing higher concentrations. With the exception of the small areas in the south, nitrate levels are well above 1 mmol m^{-3} almost everywhere throughout the survey area indicating eutrophic conditions. Surprisingly though there are two locations in the northern part of the survey area where observed nitrate concentrations are less than 2 mmol m^{-3}, despite the high estimates for N_o. These are between 51 and 52°N on leg W and between 52 and 53°N on CD59 Y.

Figure 2.20 shows the distribution of the other major nutrients, phosphate and silicate, in relation to that of nitrate. While all phytoplankton require phosphorus, silicon is a requirement only of certain groups, mainly diatoms. The Si:N:P ratio for marine diatoms is *ca* 16:16:1 (Brzezinski, 1985), the N:P ratio matching the more generally applicable Redfield ratio for plankton composition of 16:1 (Redfield, 1934). Phosphate is scaled by a factor of 16 in Figure 2.20 to aid interpretation of the relative concentrations of the nutrients in terms of phytoplankton requirements. Over most of the survey area the scaled phosphate line lies above the nitrate line, although there are a few areas where it does dip below, the most obvious of these being on CD58 Y where the scaled phosphate concentration is only about half the nitrate concentration at 46°N. There is no evidence of phosphate depletion though and, in general, the data suggest that phosphate limitation is unlikely to have been a major factor influencing the development of the bloom prior to the time of sampling. Silicate concentrations, however, are generally much lower than those of nitrate and very low silicates (less than 0.5 mmol m^{-3}) are found on CD58 Z, CD58 YZ, the northernmost part of CD58 Y, CD58 XY and CD59 Z. The extent of the last area is unknown because of missing data. These low concentrations indicate that silicate limitation is likely to have had a major effect on patterns of diatom production prior to sampling and therefore, potentially, patterns of total primary production. It is interesting to note that the silicate concentration on the repeated transect XY is much higher at the later time of sampling indicating some

physical flux of silicate as a result of advection and/or vertical mixing. This is also reflected by the apparent absence of any significant decrease in nitrate concentration in the 17 days between sampling.

2.7.2 Phytoplankton Distribution

Figure 2.19 shows two main regions with particularly high concentrations of standing stock (chlorophyll greater than about 3 mg m^{-3}): one in the south-east of the survey area, sampled on CD58 B, A and around the middle of CD58 Z, and one in the north-west immediately to the north of the Polar Front, sampled from CD59 W to CD59 X about 3 weeks later. The surface chlorophyll concentration north of this front shows a maximum of about 12 mg m^{-3}. Patches were observed in this region where concentrations were in excess of 15 mg m^{-3}. This represents much higher phytoplankton biomass than was expected for the eastern North Atlantic, being a factor of about 3 higher than previous maxima observed in this region during the bloom (Strass and Woods, 1988; Weeks *et al.*, 1993b). The maximum in the south-eastern area is less than this at about 6 mg m^{-3}. The vertical distribution here is very different though. The stratification is much weaker and the mixed layer is very deep in comparison (Figure 2.21a). Chlorophyll concentrations of more than 0.5 mg m^{-3} are found down to depths of 200 - 300 m in parts of the area (Figure 2.21b), compared with just 70 m in the north-west, and the total water column chlorophyll is actually higher than in the north-west, showing a maximum in the middle part of leg B of over 400 mg m^{-2}, compared with about 300 mg m^{-2} immediately north of the Polar Front on leg W.

The presence of significant chlorophyll concentrations at such great depths does not necessarily indicate the occurrence of *in situ* primary production. It could instead be a result of short time-scale fluctuations in mixed layer depth, associated with the diel cycle or weather events. The effects of such short-term fluctuations were studied by Stramska *et al.* (1995) who present time series data, collected during the early phase of the 1989 spring bloom at 60°N, showing a period of strong mixed-layer depth variability. Phytoplankton

biomass was mixed down to deeper layers at night during this period and, although in this case the amplitude of the mixed-layer depth cycle was only about 40 m, the phytoplankton concentration at 40 m was shown to be much greater than would have been expected from productivity estimates.

Stramska *et al.* (1995) also observed a sharp decline in phytoplankton concentrations as the mixed layer deepened in response to stormy weather. In the Vivaldi survey, some of the lowest surface chlorophyll concentrations (around 0.25 mg m^{-3}) were measured on CD58 X, following the storm event which prevented SeaSoar recovery at station X48. These low values could be the result of a similar dilution due to mixed layer deepening, an interpretation supported by the event-scale temperature anomaly (Figure 2.10) which is negative and large (-1°C) at the beginning of the section.

2.7.3 Measures of Bloom Progression

Three measures of bloom progression are defined in this study for interpretation of the survey data and its comparison with model results in Chapter 3. Each of these measures is expected to show a generally monotonic increase within a body of water throughout the bloom period and may therefore be used to compare the phase of the bloom observed at different locations with that predicted by the model.

The first of these measures is the nitrate utilisation defined by

$$\Delta N = N_0 - N,$$

where N_0 is the pre-bloom nitrate concentration for a material element of water and N is its nitrate concentration at the time of sampling. Ignoring the relatively small effect of re-mineralisation over the time scale of the bloom, ΔN may be interpreted as the integrated new production for that element since the bloom began. We should expect the water sampled at

the surface to be a mixture of water which has been continuously in the mixed layer since the beginning of the bloom and water which has been detrained and re-entrained as a result of upwelling or temporary increases in the depth of vertical mixing. Conceptually the phrase "beginning of the bloom" here refers to a different time for each individual element at which its nitrate concentration last matched that of the winter maximum in the mixed layer.

Patterns of nitrate utilisation give most information where observed nitrate concentration is still high. As nitrate is used up the effect of nitrate limitation is increased and the pattern of nitrate utilisation is forced towards that of the pre-bloom nitrate which acts as an upper limit. An alternative measure which gives useful information over a wider area is obtained by normalising for pre-bloom nitrate, giving a ratio of nitrate utilisation to available nitrate

$$R_N = \frac{\Delta N}{N_o}.$$

The third measure is a similar ratio reflecting apparent phytoplankton losses. This is the fraction of nitrate used which is unaccounted for by the observed standing stock P

$$R_P = \frac{\Delta N - P}{\Delta N}.$$

This can be interpreted to some extent as a measure of grazing, although it will tend to under-estimate grazing because a fraction of the nitrogen ingested by zooplankton during the course of the bloom would have been recycled to phytoplankton biomass. Also, in reality, phytoplankton mortality, exudation of dissolved organics and sinking of phytoplankton independently of the water movement also contribute to nitrogen loss. For these reasons, and because in practice it is necessary to estimate P from observations of chlorophyll, R_P should be considered as a qualitative measure of grazing only. P is determined from surface chlorophyll using a N:Chl *a* ratio of 0.6 (mol:g) to convert to

nitrogen units. This is equivalent to a weight ratio of 8.4 or, assuming an atomic C:N ratio of 6.625 in phytoplankton (Redfield, 1934), a C:Chl *a* ratio of 47.7 (by weight). The N:Chl *a* ratio in phytoplankton varies greatly. However, the value chosen is within acceptable bounds for healthy growing plankton and is the highest value which gives a non-negative difference ΔN - P throughout the survey.

2.7.4 Progression of the 1991 Spring Bloom

Figure 2.22 shows the patterns of estimated phytoplankton standing stock P in relation to the nitrate utilisation ΔN and pre-bloom nitrate. If it is assumed that the pre-bloom nitrate accounts for the major part of the nitrogen present in the winter-time mixed layer, then this figure effectively indicates the partitioning of this nitrogen between different ecosystem compartments at the time of observation, giving a clearer picture of the state of the bloom at different locations than the nitrate or chlorophyll data alone. As the bloom progresses at a particular location we expect the rapid increase in nitrate utilisation to be matched initially by a similar increase in phytoplankton concentration. The two then tend to diverge as transfer of nitrogen to different trophic levels becomes important. In this section the latitudinal gradients in ΔN, R_P and R_N are investigated for evidence of northward progression of the bloom.

The most striking feature suggestive of a northward progression of the phytoplankton bloom is seen at the extreme north-west corner of the survey area. The high nitrate water sampled here between CD59 W and CD59 WX has correspondingly low values of ΔN of about 2 mmol m^{-3} and there is a very sharp horizontal gradient to the south of this on leg W in both ΔN and phytoplankton concentration. There is another sharp gradient in both these properties to the west and its similar characteristics suggest that it may be part of a continuous front between areas of high and low plankton biomass which marks the northward extent of the main bloom. Although there are also low values of ΔN to the north of the surface phytoplankton maximum in the south-east, there is as already noted

a large amount of chlorophyll distributed down through the water column, perhaps due to some mixing event after initiation of the bloom. It must therefore be assumed that in this region the northern edge of the bloom lies to the north of the cruise track (i.e. above 48°N) at the time of sampling.

Away from the north-west corner, the picture of bloom progression is less clear. If the spring bloom moved steadily northwards and factors other than light availability had no significant effect on the spatial variance in new production, then we should expect nitrate utilisation to be generally greater towards the south and later in time. The temporal variation introduced by the non-synoptic nature of the sampling would tend to increase a north-south trend on southward legs and decrease it on northward legs. In reality, although there is some evidence of northward progression, the highest values of ΔN are found in the north-west, just to the north of the Polar Front, and there is a very sharp decrease to the south of these peaks on northward heading legs W and Y and also on southward leg X. The picture therefore appears a little more complicated, suggesting either an earlier start to the bloom in the north or highly variable rates of nitrate uptake. The nitrate utilisation actually appears to be much more closely related to the pre-bloom nitrate in the northern part of the survey area than to either latitude or time, suggesting that the pre-bloom nitrate or some other property which tends to co-vary with salinity has a major effect on uptake rates. Apart from the front in the north-west corner, evidence for a steady northward progression is restricted to the southern part of the survey area, where north-south trends are seen in ΔN on CD58 A, B and Z, CD58 Y south of 45.5°N and to some extent on CD59 W south of 45°N. Of these, CD58 A and Z are southward heading legs and so the trends could equally well be explained by temporal change.

The fractional nitrate utilisation R_N (Figure 2.23) emphasises the trends already noted in the southern part of the survey area and also show a clear north-south trend on CD58 X. However in the northern part of the survey area the general trend again tends to be reversed and the patterns are still dominated by the same major features present in ΔN. Even

after normalisation for pre-bloom nitrate then, the nitrate utilisation in this area still seems to be higher in areas of high pre-bloom nitrate or low salinity. This is further illustrated by Figure 2.24, which shows the distribution of R_N against salinity for the whole survey area. A clear inverse relationship can be seen for data points at and above 48°N from salinities between about 35.0 and 35.8. The region in which this relationship is apparent is that dominated by the North Atlantic Current. The salinity and pre-bloom nitrate gradients in this area reflect the influence of the fresher, high nitrate ASIW on the NACW immediately to the south of the Polar Front as a result of horizontal diffusion by the strong eddy field associated with local baroclinic instability. The apparent differences in nitrate utilisation could therefore reflect differences in the ecology of the two water masses.

The fraction of nitrate used unaccounted for by the observed standing stock R_P is also shown in Figure 2.23. It is immediately apparent that R_P is very high in many areas (over about 80%) even when R_N is quite low, suggesting heavy grazing pressure quite early in the bloom period. This is particularly notable on CD58 X. There are sharp changes in R_P at the Polar front on leg W and just to the north of it on leg CD59 X, R_P being lower on the northern side. Examination of the sub-surface salinity distribution (Figure 2.6) shows that the displacement of the latter could be due to the influence of NACW, having salinity higher than about 35.0, to the north of the position at which the 35.0 isohaline outcrops at the surface. There is also some reduction in R_P to the north of the Polar Front on CD59 Y although this is less dramatic, perhaps due again to the greater influence of NACW in this area. Although these patterns may simply reflect differences is timing of the bloom, another possible explanation is that grazing pressure is less in the ASIW sampled than in the higher salinity water. If this were the case, the spatial variance in grazing pressure could be a factor explaining the apparent inverse relationship between nitrate utilisation and salinity. Elsewhere, clear latitudinal trends in R_P are restricted to legs CD58 Z and Y and perhaps more arguably legs CD58 B and A. In all these cases R_P is greater in the south, reflecting the north-south trends in R_N

A final cautionary note must be made regarding the interpretation of the trends in the south. Examination of the sub-surface structure of chlorophyll on legs CD58 A and B (Figure 2.21b) shows that it is distributed over a larger depth range towards the north end of the legs than to the south. This suggests that the fairly steep horizontal gradient in ΔN and R_N on these legs might be explained by deeper vertical mixing in the north between nitrate depleted water from the euphotic zone and the higher nitrate water below, rather than by greater total production in the south. The associated trends in R_P on these legs are less pronounced and those reductions in R_P which are seen could also be the result of mixing if the sub-surface ratio of phytoplankton stock to ΔN is higher than that at the surface. This would occur if grazing pressure were more intense near the surface. There is some evidence that this might be true on leg CD58 B, between 45 and 46.5°N, where the chlorophyll concentration is reduced above about 40 m, from about 3.5 to less than 2.5 mg m^{-3}. The north-south trends in nitrate utilisation noted on the other legs, CD58 Z and Y and CD59 W, are less pronounced than those on CD58 A and B and so evidence suggesting north-south progression over the southern area is not as strong as it first appeared.

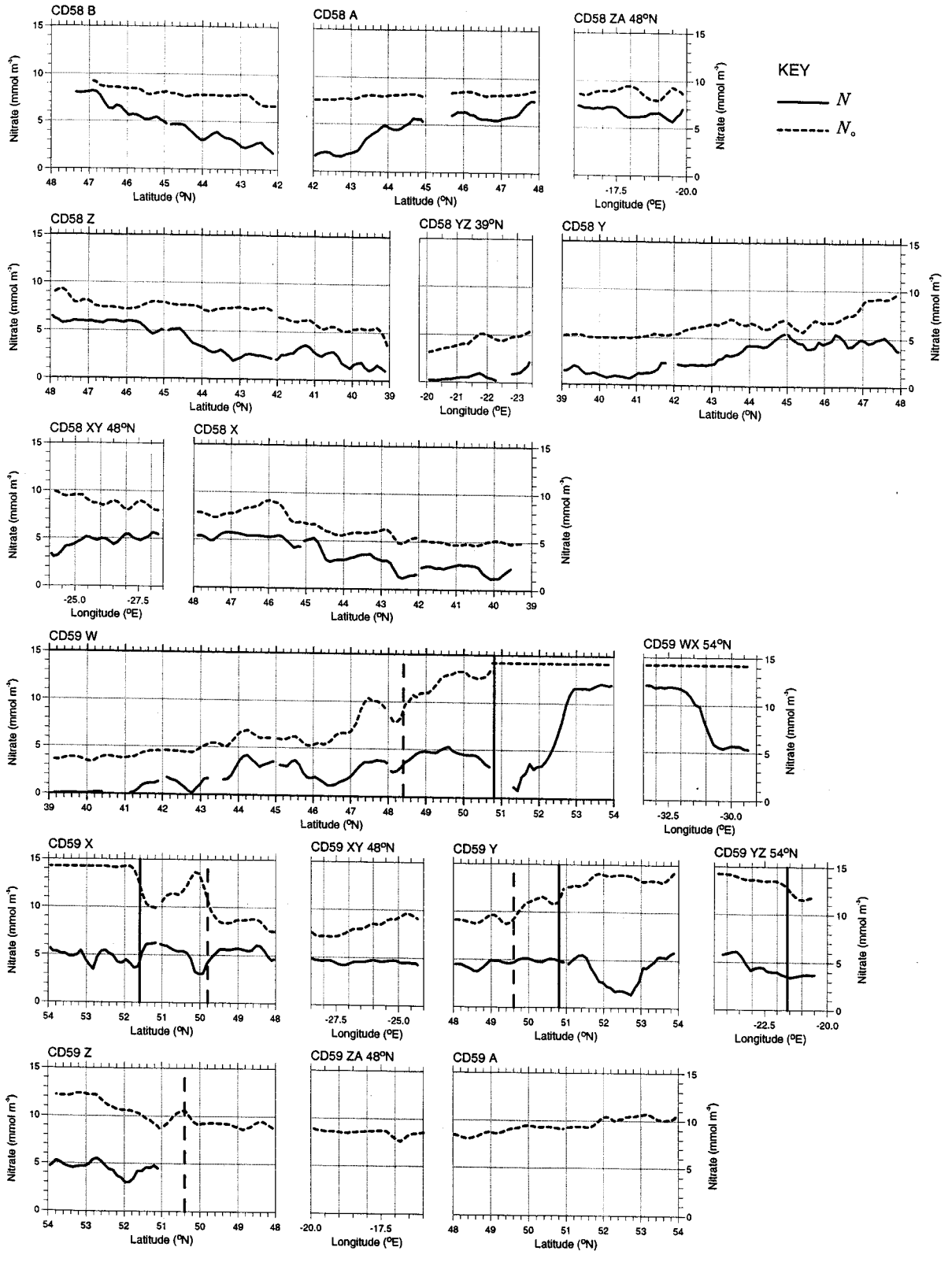

Figure 2.18. Surface nitrate N and estimated pre-bloom nitrate N_0. Reference lines show positions of the Polar Front (solid) and the weaker front associated with the southern branch of the NAC (dashed).

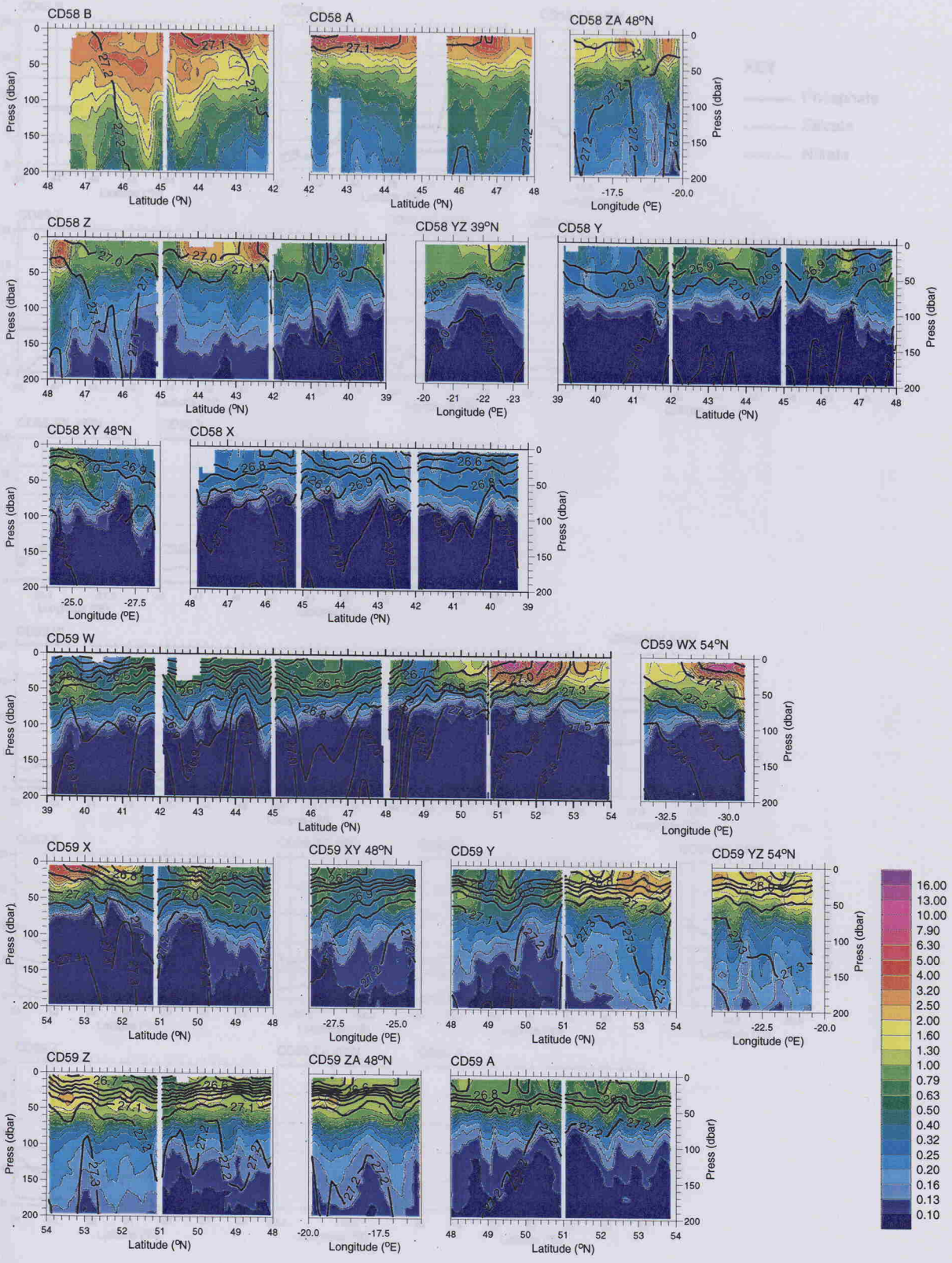

Figure 2.19. Vertical sections of chlorophyll a (mg m^{-3}). Isopycnals overlaid showing σ_θ (kg m^{-3}). Chlorophyll concentration is represented by a log colour scale.

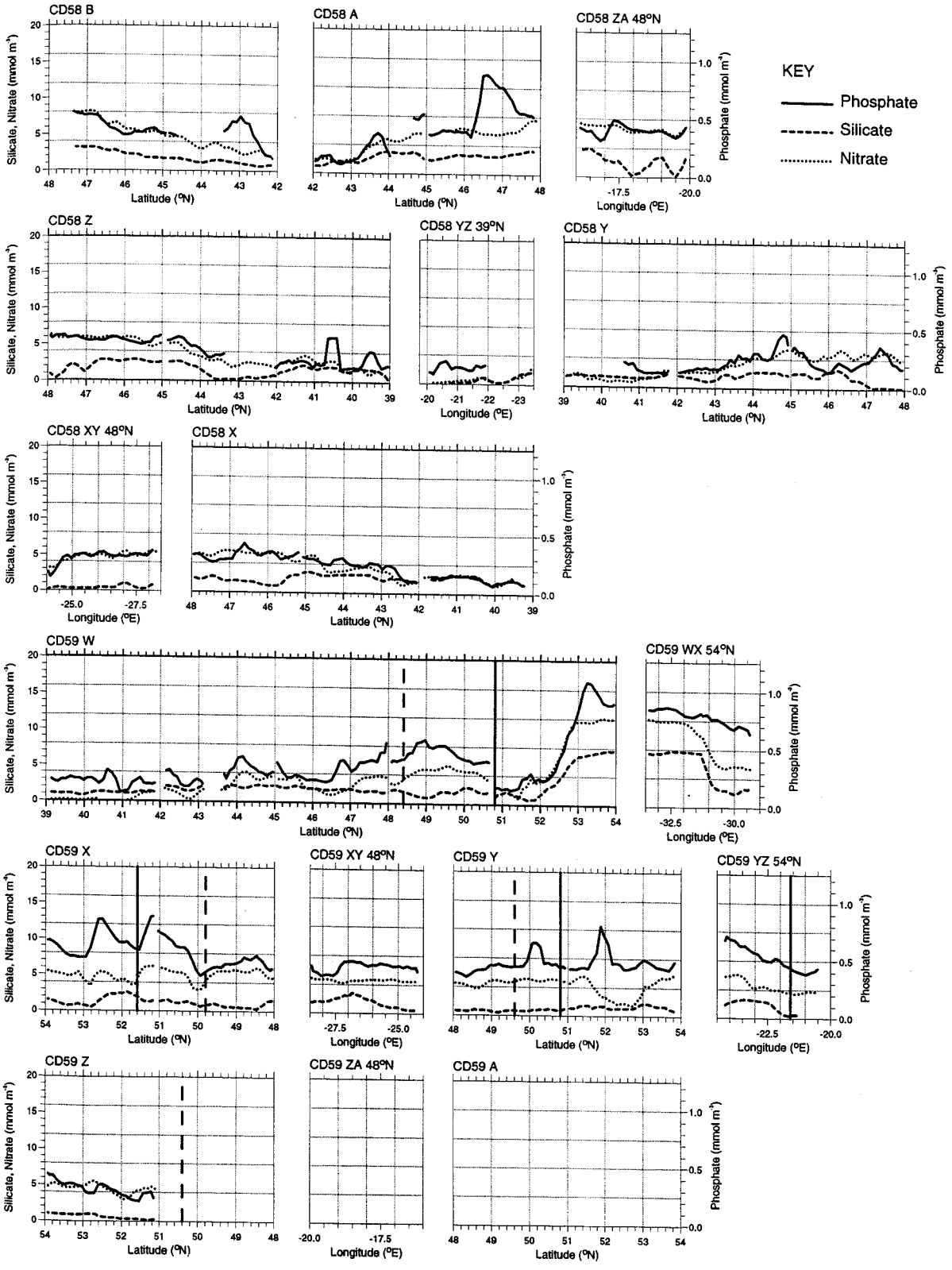

Figure 2.20. Surface phosphate, silicate and nitrate. Reference lines show positions of the Polar Front (solid) and the weaker front associated with the southern branch of the NAC (dashed).

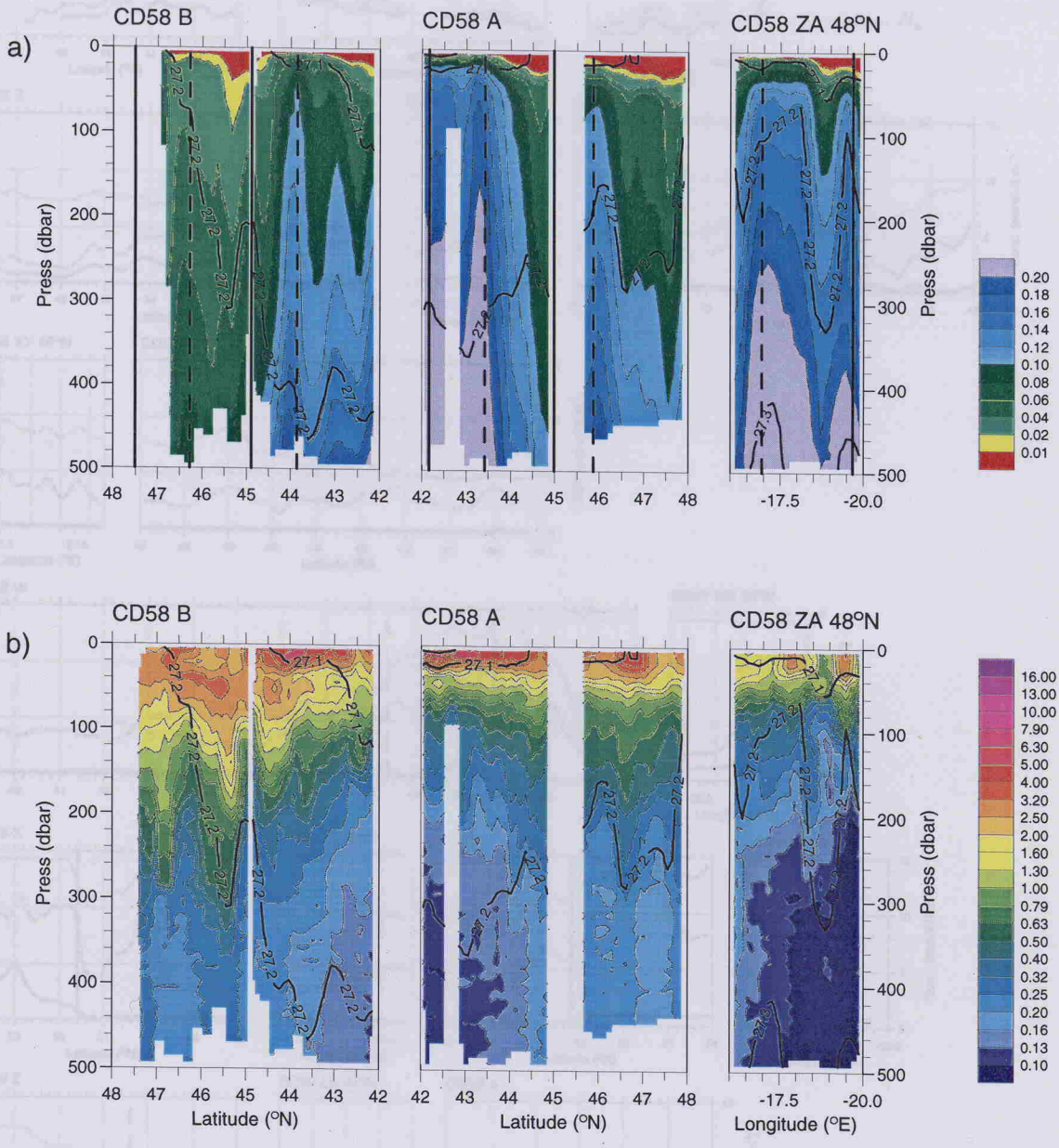

Figure 2.21. SeaSoar transect legs CD58 A and B. Vertical sections of (a) density relative to the sea surface (kg m^{-3}) and (b) chlorophyll a (mg m^{-3}). Isopycnals overlaid showing σ_θ (kg m^{-3}).

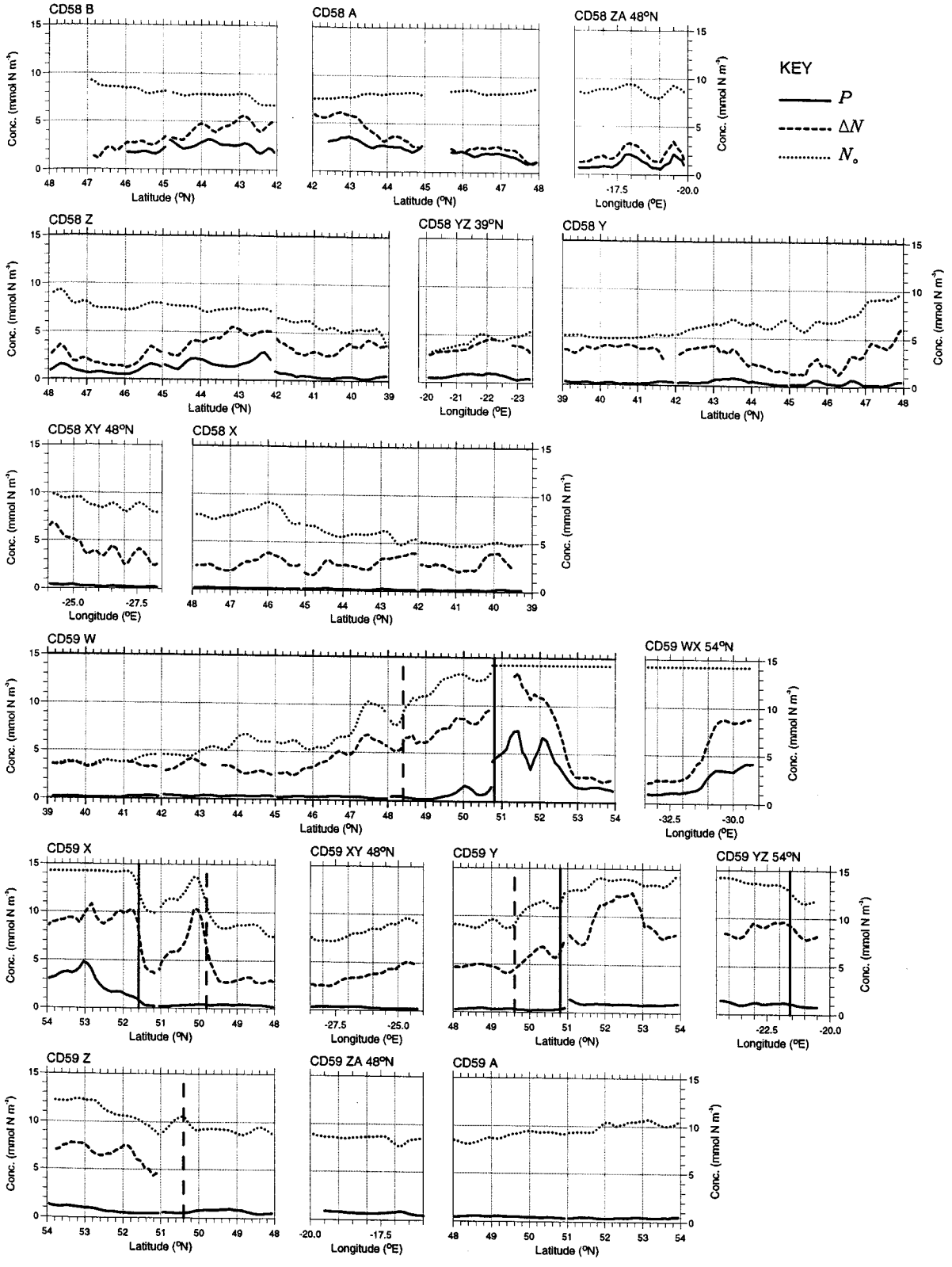

Figure 2.22. Estimated surface phytoplankton concentration P, nitrate utilisation ΔN and pre-bloom nitrate N_o. Reference lines show positions of the Polar Front (solid) and the weaker front associated with the southern branch of the NAC (dashed).

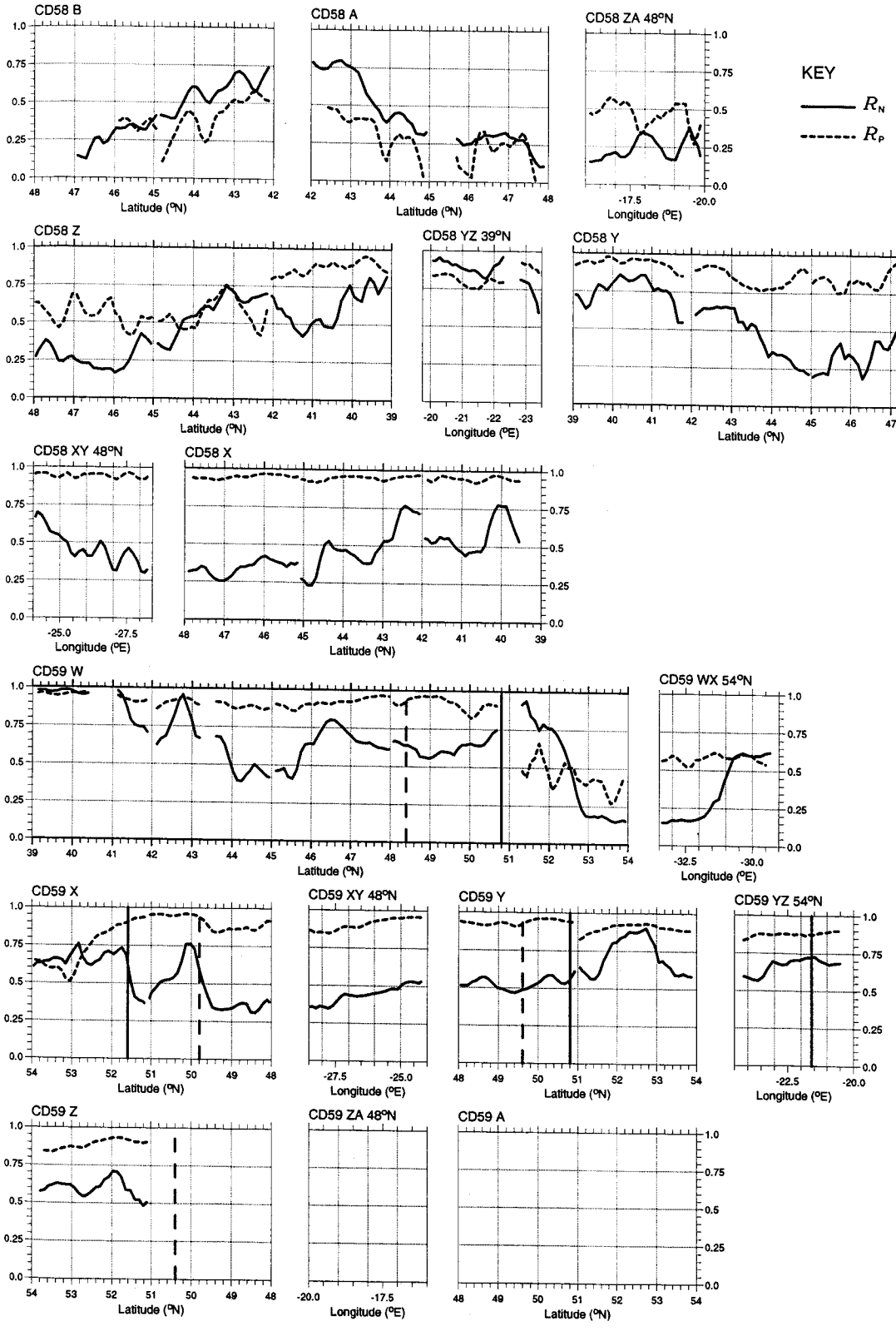

Figure 2.23. Fractional nitrate utilisation R_N and fraction of nitrate utilisation unaccounted for by standing stock R_P. Reference lines show positions of the Polar Front (solid) and the weaker front associated with the southern branch of the NAC (dashed).

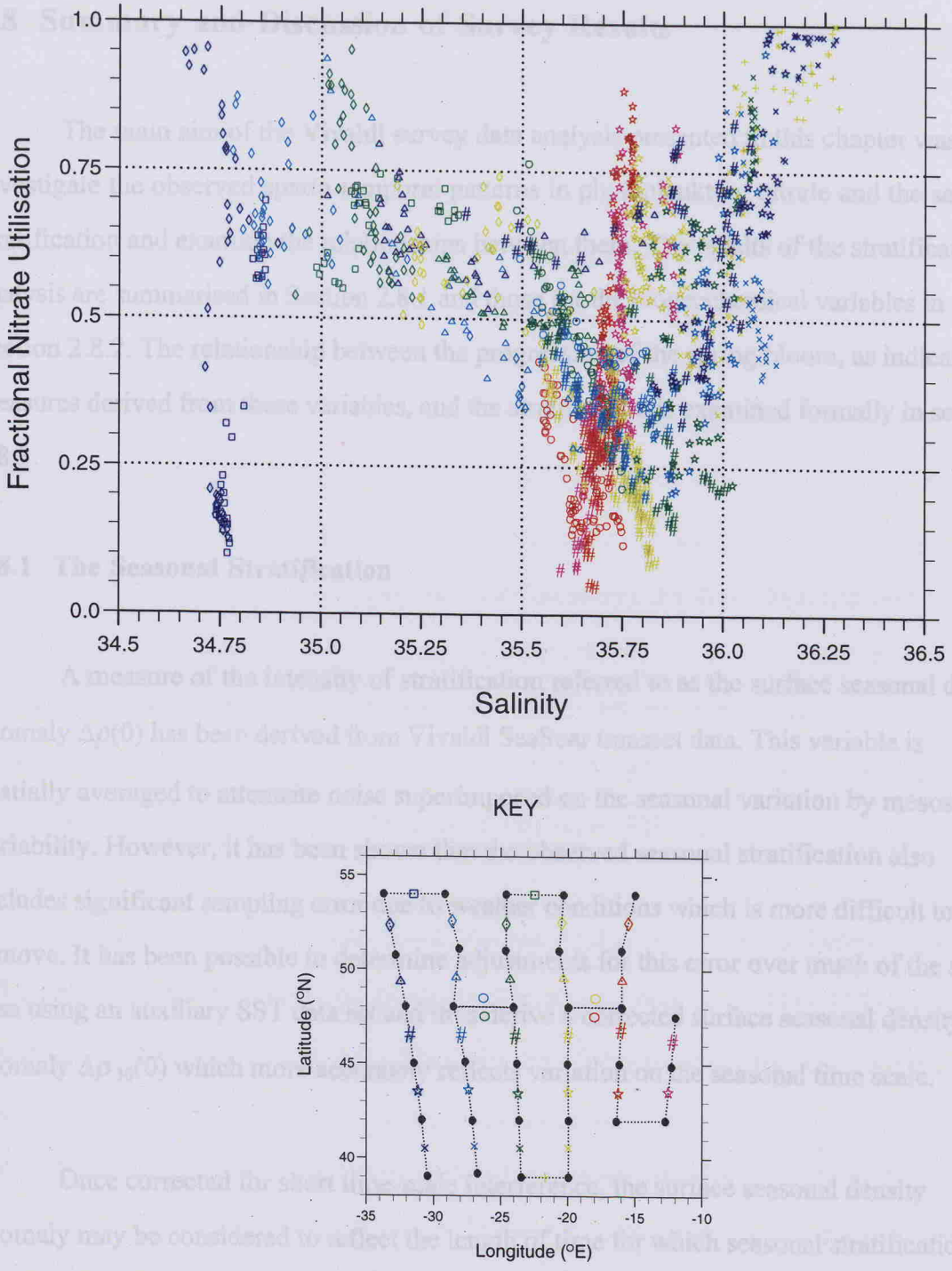

Figure 2.24. Distribution of fractional nitrate utilisation R_N against salinity for surface water samples taken during transects.

2.8 Summary and Discussion of Survey Results

The main aim of the Vivaldi survey data analysis presented in this chapter was to investigate the observed spatio-temporal patterns in phytoplankton, nitrate and the seasonal stratification and examine the relationships between them. The results of the stratification analysis are summarised in Section 2.8.1 and those for the biogeochemical variables in Section 2.8.2. The relationship between the progression of the spring bloom, as indicated by measures derived from these variables, and the stratification is examined formally in section 2.8.3.

2.8.1 The Seasonal Stratification

A measure of the intensity of stratification referred to as the surface seasonal density anomaly $\Delta\rho(0)$ has been derived from Vivaldi SeaSoar transect data. This variable is spatially averaged to attenuate noise superimposed on the seasonal variation by mesoscale variability. However, it has been shown that the observed seasonal stratification also includes significant sampling error due to weather conditions which is more difficult to remove. It has been possible to determine adjustments for this error over much of the survey area using an auxiliary SST data set and thus derive a corrected surface seasonal density anomaly $\Delta\rho_{30}(0)$ which more accurately reflects variation on the seasonal time scale.

Once corrected for short time-scale interference, the surface seasonal density anomaly may be considered to reflect the length of time for which seasonal stratification has been established, in the sense that it is expected to show a fairly steady monotonic increase in magnitude throughout the heating season. It is considered to be a more reliable variable than time for matching observations and ecosystem model results and potentially allows some information about the relative rates of bloom development to be gained from point-in-time biogeochemical data collected in different locations during the course of the survey. Such information must be interpreted with caution though as the rate at which the seasonal

density anomaly develops is likely to vary spatially as well as the time of initial stratification. Rates of stratification development based on $\Delta\rho_{30}(0)$ for the repeated transects ZA and XY were similar at 0.41 kg m^{-3} month^{-1} (0.45 in 33 days) and 0.36 kg m^{-3} month^{-1} (0.2 in 17 days) respectively. These two data points show little evidence then of spatial variation in stratification rates between about 18°W and 26°W at 48°N. However, we should expect meridional variation to be greater.

While the COADS SST time series $T_{30}(0)$ (Figure C.4) generally support the assumption that $\Delta\rho_{30}(0)$ shows a steady increase everywhere prior to the time of sampling, there is an indication of a levelling off towards the end of the survey which could be due to reductions in the rate of increase of air-sea heat flux and/or negative horizontal heat transport. If this pattern is reflected in $\Delta\rho_{30}(0)$ then the reliability of $\Delta\rho_{30}(0)$ as a proxy for elapsed time may be reduced. Fortunately the greatest effects of this apparent cooling seem to occur after the time of sampling. The worst affected SeaSoar runs for which $\Delta\rho_{30}(0)$ is available are probably 12014 on CD59 Z and 12016 on CD59 A.

The time series of seasonal density anomaly $\Delta\rho_{30}(0)$ is shown in Figure 2.25b. Where this variable is unavailable, due to insufficient coverage of COADS SST data, $\Delta\rho(0)$ is used as the best estimator of $\Delta\rho_{30}(0)$ and the confidence intervals are estimated from the sample variance of the event-scale density anomalies for CD59. The seasonal density anomaly shows a structure apparently dominated by temporal change in the early part of the survey with no obvious dependence on latitude (Figure 2.25a). Dependence on latitude appears to be greater in the later part of the survey as noted in Section 2.3. Some evidence was presented in section 2.3 for an influence of mesoscale heterogeneity in SST on the development of stratification. Evidence was also presented for enhancement of stratification in the south and south-western parts of the survey area by the action of vertical shear on pre-existing buoyancy structure in the winter-time mixed layer.

The mixed layer depth derived from the observations, using a density difference criterion of 0.1 kg m^{-3}, is summarised in Figure 2.25c. Very deep mixed layers and greater variance in mixed layer depth are associated with the weak stratification observed during the early part of the survey but very little variance is seen during the later part of the survey, showing stratification to be well established with the top of the seasonal pycnocline lying between about 20 and 50 m. Some evidence was found for a diel cycle in mixed layer depth, especially in the early part of the survey in the south-east.

2.8.2 The Spring Phytoplankton Bloom

An estimate of the pre-bloom nitrate concentration was constructed by deriving an empirical model of nitrate concentration as a function of salinity, based on the pre-formed nitrate concentration of water subducted prior to the bloom. This allowed nitrate utilisation during the bloom to be determined for water sampled at the surface. Comparison of nitrate utilisation with standing stock of phytoplankton estimated from chlorophyll *a*, shows the effect of loss processes on the phytoplankton bloom. The losses are thought to be largely due to zooplankton grazing, as the zooplankton bloom in response to the availability of food, and to sedimentation. These data are summarised in Figure 2.25d which effectively shows the division of the available nitrogen between three different ecosystem compartments.

A strong north-south gradient in nitrate utilisation was noted in the north-west corner on leg W which is believed to represent the northern edge of the main bloom as it progresses northward. Some evidence for weaker north-south gradients in nitrate utilisation was noted in the southern part of the survey area although this pattern may be partly due to the aliasing effect of deep mixing events after bloom initiation, possibly related to the diel cycle. Apart from the small area in the north-west corner there is no apparent north-south increase in nitrate utilisation in the northern part of the survey area and in fact the trend seems to be reversed to a large extent. In these areas, where the available nitrate before the

bloom was very high, the nitrate utilisation appears to be much more closely related to pre-bloom nitrate or salinity than to latitude or time.

Although nitrate concentrations are still generally high in the north, the effect of nitrate availability on phytoplankton growth rate cannot be ruled out as a causal factor of the observed heterogeneity in nitrate utilisation, as even small spatial variance in growth rate caused by differences in nitrate concentration can lead to large differences in nitrate utilisation if it is maintained for a period of several weeks. Additionally, nitrate uptake might be reduced in lower nitrate waters by ammonium inhibition if the balance between new and regenerated production is dependent on the relative concentration of the two nutrients. However, the apparent inverse relationship between nitrate utilisation and salinity is still evident after the nitrate utilisation is normalised to allow for spatial variance in pre-bloom nitrate, giving R_N, which suggests some other factor is at work. The main causal factor could be some other property, biogeochemical or physical, which tends to co-vary with salinity because its distribution is related to that of the water masses in the area as a result of longer time scale processes. For example, a highly plausible explanation might be that the dominant phytoplankton species in more eutrophic waters are adapted to more rapid growth and nitrate uptake than those which make up the assemblages in waters where less nitrate is generally available. It is clear that there are many possible explanations for the observed patterns, but very little information on which to base conclusions. Further speculation is not worthwhile at this stage.

2.8.3 Stratification and Bloom Development

Given that we expect a strong link between the progression of the bloom and the seasonal density anomaly $\Delta\rho_{30}(0)$ it is useful to examine the extent to which the latter might explain the measures of bloom progression defined in Section 2.7. The distribution of these variables against the surface seasonal density anomaly are shown in Figure 2.26. $\Delta\rho(0)$ data are used where $\Delta\rho_{30}(0)$ data is unavailable. These data points are shown in grey.

Just 16% of the variance in ΔN is explained by the seasonal density anomaly. If data points with N_o greater than 9 are excluded there is no clear relationship at all but there is some evidence of a good relationship for the higher pre-bloom nitrate waters. The relationship between ΔN and N_o for these waters stands out, with all N_o above 9 showing higher ΔN than the subset having lower N_o. Also, within the higher N_o, subset most of the low N_o points lie below the trend line shown by the observations with the highest N_o. R_N arguably shows a slightly more general trend, although it is still dominated by that for the higher N_o points which show very much the same pattern as they did before normalisation. The seasonal density anomaly explains only 11% of the variance in R_N. A more obvious trend is shown by R_P for which the density anomaly explains 56% of the variance.

These results show that, while the seasonal density anomaly gives a measure of elapsed time since initial stratification and is therefore potentially valuable in the interpretation of the biogeochemical observations, it does not in itself appear to be a very satisfactory predictor of the state of bloom development over a wide area, where numerous other factors are likely to contribute to the variability. Further progress requires a more sophisticated modelling approach and the remainder of this study is concerned with the application of a simple plankton ecosystem model to the description of the spring bloom in this part of the North Atlantic.

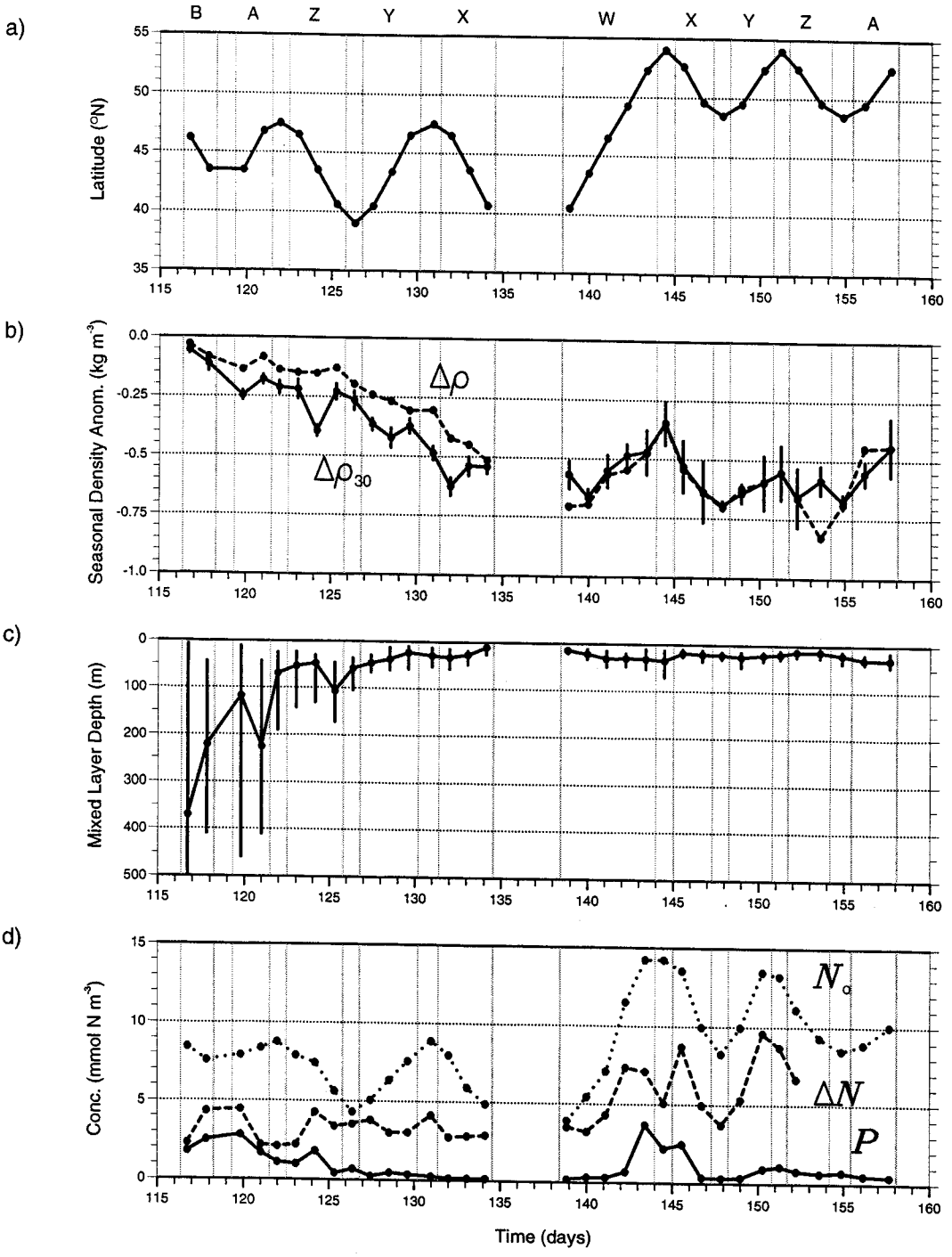

Figure 2.25. (a) Mean latitude of sampling. (b) 300 km mean surface seasonal density anomaly $\Delta\rho_{30}(0)$, showing 68% confidence intervals, and 300 km mean uncorrected seasonal density anomaly $\Delta\rho(0)$. $\Delta\rho(0)$ is plotted as an estimate of $\Delta\rho_{30}(0)$ where the latter is unavailable. (c) 300 km mean mixed layer depth, based on a density difference criterion of 0.1 kg m^{-3}, showing range for each 300 km transect. (d) 300 km mean estimated surface phytoplankton concentration P, nitrate utilisation ΔN and pre-bloom nitrate N_o.

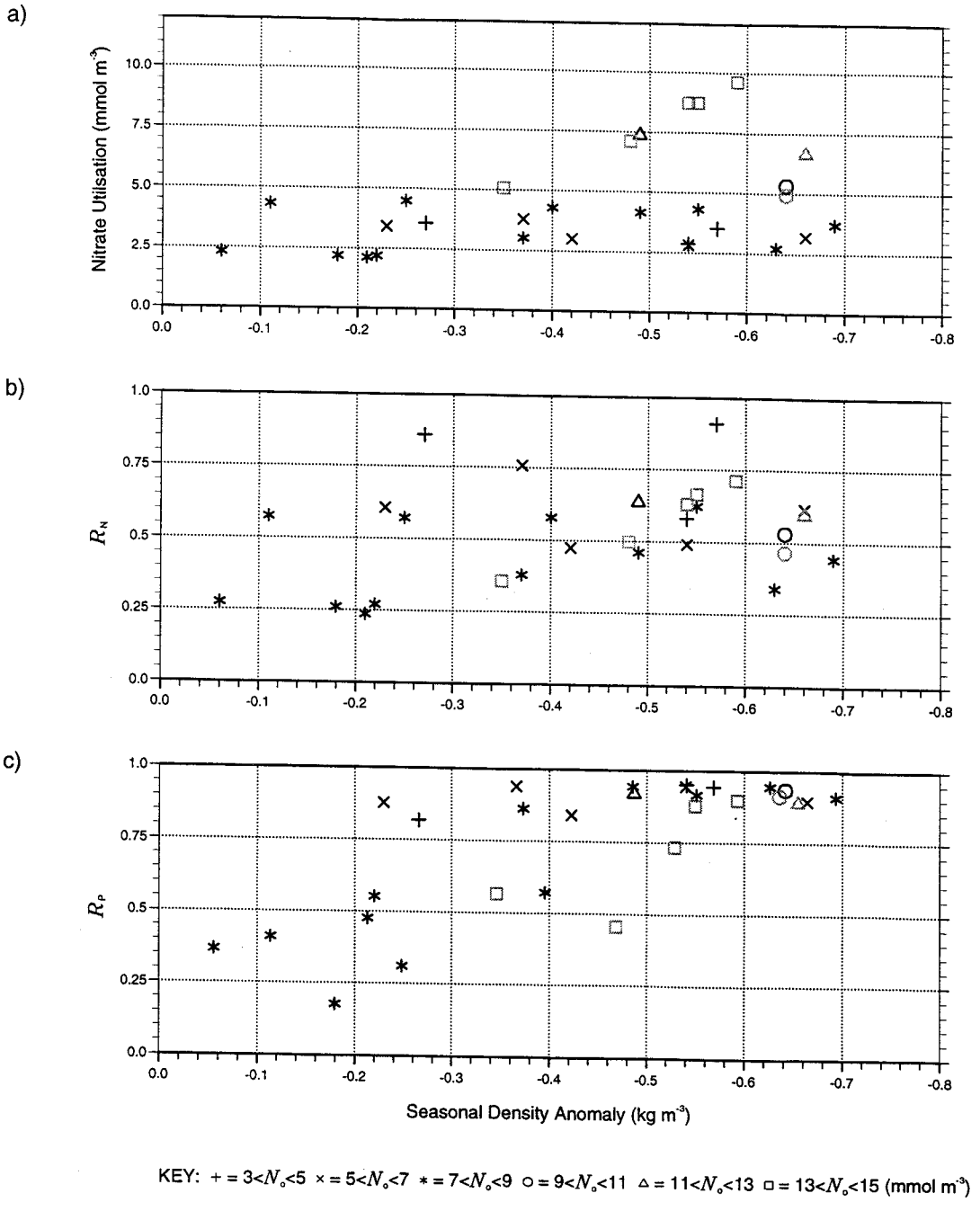

Figure 2.26. Distribution of (a) nitrate utilisation ΔN, (b) fractional nitrate utilisation R_N and (c) fraction of nitrate utilisation unaccounted for by standing stock R_P, against seasonal density anomaly $\Delta\rho_{30}(0)$. Data points in grey show observations with no event-scale anomaly correction.

Chapter 3

MODELLING THE 1991 SPRING BLOOM

3.1 Overview of Modelling Investigations

The primary aim of this study, as stated in Chapter 1, was to develop a method for fitting ecosystem models to wide area survey data and to investigate the practical problems involved in using data from this type of survey, which essentially consists of point-in-time observations. The motivation behind this goal is that the addition of such spatially distributed data to time series data already used in model calibration should help to reduce parameter bias, as well as increasing the size of the observational data set available. This is important with regard to the construction of generic models of the pelagic ecosystem response to physical variability for inclusion in global climate models. An effective method has been developed and tested by using the Vivaldi 1991 survey data to calibrate a simple candidate ecosystem model.

The main barrier to the use of point-in-time data is the absence of data regarding the history of physical conditions at the sampling location, from which forcing functions might be derived. Instead the forcing for the ecosystem model must be obtained either from climatological data or physical model output, both of which are likely to be less accurate than actual time series data. The applicability of the latter can also be questionable because of the effect of horizontal advection. At times in the annual cycle when rates of change in biological variables are relatively small these inaccuracies may not present significant problems, but during an event like the spring bloom, when biological variables tend to change very rapidly in response to the onset of seasonal stratification, any inaccuracy in the timing of stratification can cause very large differences in model values at the time of observation. One approach to overcoming this problem is to match the observations to the physical forcing using a measure of the stratification such as the seasonal density anomaly defined in

Chapter 2. This forms the basis of the method developed here for the purposes of fitting an ecosystem model to the Vivaldi nitrate and chlorophyll observations. The value of this method as a research tool in a wider context is discussed at the end of this chapter in Section 3.7.

The candidate physically forced ecosystem model used in this study, a 5 compartment model mixed layer nitrogen model (Fasham and Evans, 1995b), is described in detail in Section 3.2. Spatial variability over the study area is introduced by variance in the annual cycles of mixed layer depth and solar radiation and in the nitrate available below the mixed layer. While the available nitrate is a chemical rather than a physical environmental condition it is determined here purely from physical data, being modelled as a time invariant function of spatial position and salinity. The justification for this comes from the analysis of the relationship between nitrate and salinity in Chapter 2. Horizontal fluxes are not explicitly included in the model. It is assumed that the ecology of the region at the seasonal time-scale is dominated by vertical processes. At time scales which are long compared with the annual cycle, horizontal fluxes may be vital for the replenishment of nitrogen in the upper ocean in parts of the North Atlantic where Ekman pumping causes long term downwelling (Williams and Follows, 1998). This includes the southern part of the study area. The effect of these fluxes is included implicitly in the prescribed spatial model of available nitrate.

The application of the model to the study area and the methods used to compare the model results with the point-in-time data from the Vivaldi survey, for the purposes of parameter optimisation and model evaluation, are described in Section 3.3. The time series of mixed layer depth were taken from the output of a general circulation model (GCM) of the North Atlantic and the corresponding seasonal anomalies of density and salinity are validated against the observed stratification in Section 3.4. Section 3.5 presents the ecosystem model solutions for three different parameter sets. These are compared and evaluated against the Vivaldi observations, addressing another of the aims stated in Chapter 1: to assess the ability of a specific ecosystem model to explain the variance in the Vivaldi

spring bloom observations using a fixed parameter set. The annual production and particulate export implied by the different solutions are compared with estimates from the literature.

The final aim of this study was to identify processes which are potentially important in controlling patterns of bloom development in the eastern North Atlantic. This is addressed in Section 3.6 by means of a detailed analysis of the spatial variability in the simulated bloom over the study area, as represented by one of the model solutions. In particular, the factors controlling new production are investigated, in order to suggest possible explanations for the interesting patterns of nitrate utilisation exhibited by the Vivaldi survey data. The results of the modelling investigation are discussed, in Section 3.7, with reference to other observations of the North Atlantic spring bloom described in the literature.

3.2 The Mixed Layer Ecosystem Model

The 5 compartment ecosystem model used in this study is a simplified version of the widely adopted mixed layer nitrogen flow model of Fasham, Ducklow and McKelvie (1990), referred to hereafter as FDM90. FDM90 is a 7 compartment model of an ecosystem within a biogeochemically homogenous layer, each compartment representing a different nitrogen pool. The 7 compartment model includes 2 pools associated with the microbial loop (Azam *et al.*, 1983). As only nitrate and phytoplankton data were available from the survey, there were insufficient data to independently constrain parameters associated with this alternative nitrogen pathway and so it has been omitted for the purposes of this study. The 5 compartment version (Fasham and Evans, 1995b) retains the functional distinction between new and regenerated production of FDM90 and the export of nitrogen due to sinking of detrital material. The authors found that this version was able to fit data from the North Atlantic Bloom Experiment study site at 47°N 20°W equally well as the 7 compartment version.

The model structure is shown in Figure 3.1. The state variables are the mixed-layer concentrations (mmol N m^{-3}) of nitrate N, phytoplankton P, zooplankton Z, detritus D and Ammonium A. The FDM90 pools not included are bacteria and dissolved organic nitrogen (DON). New nitrogen enters the model via the supply of nitrate from below the mixed layer as a result of entrainment during mixed layer deepening and by diffusive mixing across the mixed layer base, parameterised by a constant mixing rate m (m day^{-1}). All concentrations other than nitrate are set to zero below the mixed layer. Nitrogen is exported as a result of detrainment, as the mixed layer shoals in the spring, by diffusive mixing of the non-nitrate components and by the sinking of particulate material. New primary production is balanced by non-nitrate export over the annual cycle. Following Evans and Parslow (1985), the asymmetry in the response of the ecosystem state variables to positive and negative changes in the mixed layer depth M (m) is handled by defining the term

$$h^+ = \max(h,0),$$

where h is the rate of change of the mixed layer depth dM/dt determined from the time series $M(x,y,t)$ at the model location, longitude x and latitude y.

The equations for each of the state variables are given in sections 3.2.1 to 3.2.5 and the differences from FDM90 are noted. Section 3.2.6 describes the spatial model which defines the nitrate concentration at the base of the mixed layer.

3.2.1 Phytoplankton

The rate of change of the phytoplankton concentration is given by

$$\frac{dP}{dt} = PJQ - G_P - \phi_P P - \frac{(m+h^+)P}{M}.$$

The first term is the primary production. The factor J is the light limited specific growth rate (d^{-1}) which is a function of PAR immediately below the sea-surface, mixed layer depth and the self-shading effect of phytoplankton biomass. Q is a nutrient limitation factor which is a non-dimensional function of nitrate and ammonium concentrations. The loss term G_P is the zooplankton grazing rate (mmol N m^{-3} d^{-1}) which is a function of zooplankton biomass and the biomass of their food sources. The remaining loss terms are the phytoplankton mortality, parameterised by a constant specific mortality rate ϕ_P (d^{-1}), which causes a nitrogen flow into the detritus pool, and the physical flux due to dilution as a result of vertical mixing processes. The equation differs slightly from that in the FDM90 model because of the removal of the exudation flux to the DON pool which was included in the 7 compartment version.

The light limited growth rate J at a given depth and time is defined by the Smith function (Smith, 1936) such that

$$J(z,t) = \frac{V_P \alpha I(z,t)}{\sqrt{V_P^2 + \alpha^2 I(z,t)^2}},$$

where V_P is the phytoplankton maximum growth rate (d^{-1}), α is the initial slope of the photosynthesis versus irradiance (P-I) curve (d^{-1} (W m^{-2})$^{-1}$) and $I(z,t)$ is the underwater light field (W m^{-2}). The light field is modelled in terms of the PAR directly below the sea surface $I_o(t)$, the attenuation of PAR due to water k_w (m^{-1}) and the specific attenuation of PAR due to phytoplankton k_p (m^2 (mmol N)$^{-1}$), the model taking the simple Beer's law form

$$I(z,t) = I_o(t) \exp[-(k_w + k_p P)z].$$

I_o is determined from the total solar radiation at the top of the atmosphere I_s using observational time series of fractional cloudiness $C(x,y,t)$ in conjunction with the cloud transmittance model of Evans and Parslow (1985):

$$I_o = 0.375\ (1.0 - 0.7C)\ I_s.$$

Evans and Parslow assumed that, for a clear sky, a fraction 0.375 of the solar radiation at the top of the atmosphere is available in the PAR waveband immediately below the surface. The transmittance model replaces the Smith and Dobson (1984) model used in FDM90.

While it is possible to simulate the diel cycle, in this implementation of the ecosystem model, as in FDM90, a daily averaged growth rate is used. For the purposes of integrating over the day the time of day is treated independently of the time of year t. A new time variable t_D is introduced which takes the value 0 at sunrise and τ (days) at noon. $I_o(t)$ is expressed as $I_o(t,t_D)$, $I(z,t)$ then becomes $I(z,t,t_D)$ and $J(z,t)$ becomes $J(z,t,t_D)$. The daily average light limited growth rate in the mixed layer is then given by

$$\bar{J}(t) = \frac{2}{M}\int_0^{\tau(t)}\int_0^{M} J(z,t,t_D)\mathrm{d}z\mathrm{d}t_D .$$

The variation of I_o with time of day is modelled as a triangular function $f_D(t,t_D)$ allowing an analytical integral to be obtained (Evans and Parslow, 1985).

$$I_o(t,t_D) = I_{on}(t)\, f_D(t,t_D),$$

where I_{on} is the noon value of PAR directly below the surface. f_D increases linearly from 0 to 1 between $t_D = 0$ and $t_D = \tau$ and decreases linearly from 1 to 0 between $t_D = \tau$ and $t_D = 2\tau$. Day length 2τ is a function of latitude and time and is calculated from standard astronomical formulae (e.g. Brock, 1981):

$$2\tau = \arccos(-\tan\delta(t)\tan y) / 180,$$

where δ, the declination or angle at solar noon between the sun and the equator (degrees), is given by

$$\delta = 23.45 \sin[360\,(284 + t) / 365],$$

t being expressed in days from the beginning of the year. I_{on}, the required noon value of I_o is determined from I_{sn}, the noon value of I_s. I_{sn} is a function of latitude and time, chosen such that the model integral over the day, $I_{sn}\tau$, corresponds to the daily integrated solar radiation at the top of the atmosphere as given by a standard formula. Thus

$$I_{sn} = \frac{R}{\pi\tau}(2\pi\tau(y,t)\sin y \sin\delta(t) + \sin[360\tau(y,t)]\cos y \cos\delta(t)),$$

where R is the solar constant (1353 W m^{-2}). τ is treated as a dimensionless fraction of a day in this expression.

The nutrient limitation factor in the phytoplankton equation is given by

$$Q(N,A) = \frac{N}{k_1 + N}\exp(-\psi A) + \frac{A}{k_2 + A},$$

after Wroblewski (1977). Here k_1 and k_2 are the Michaelis-Menten half saturation constants for nitrate and ammonium (mmol N m^{-3}) respectively and the parameter ψ ((mmol N m^{-3})$^{-1}$) determines the strength of ammonium inhibition of nitrate uptake.

3.2.2 Zooplankton

The zooplankton fluxes are given by the equation

$$\frac{dZ}{dt} = \beta(G_P + G_D) - \mu Z - \phi_Z Z^2 - \frac{hZ}{M},$$

In this 5 compartment model zooplankton feed on phytoplankton and detritus only. G_D is the equivalent term to G_P for grazing on detritus. β is the assimilation efficiency, μ is the zooplankton specific excretion rate (d^{-1}) and ϕ_Z is the zooplankton specific mortality parameter ((mmol N m^{-3} d)$^{-1}$). The final term in the zooplankton equation, which represents the physical flux, is different from that for phytoplankton because zooplankton are assumed to be able to swim sufficiently well to remain within the mixed layer. The form of the zooplankton equation differs from that in FDM90 in that, firstly, the assimilation efficiency is assumed to be identical for the different food sources and, secondly and more importantly, zooplankton mortality is density dependent. Steele and Henderson (1992) showed that the formulation of the zooplankton mortality term can have a major impact on the character of the model results and that a quadratic mortality term can improve model

stability, a conclusion supported by the work of Fasham (1995). This formulation is justified by interpretation of density dependent mortality as the result of "cannibalism" within the aggregation of species making up the zooplankton pool (Taylor and Joint, 1990) and/or as predation by a population of unmodelled higher predators having a distribution which is correlated with their prey (Steele and Henderson, 1981).

The model of zooplankton grazing allows for switching between food sources depending on their relative concentrations. The grazing rate of zooplankton on phytoplankton is given by

$$G_P = \frac{gZp_1P^2}{k_3(p_1P + p_2D) + p_1P^2 + p_2D^2},$$

where g is the maximum ingestion rate (d^{-1}), k_3 is the half saturation constant for zooplankton ingestion (mmol N m^{-3}) and p_1 and p_2 are the feeding preferences for phytoplankton and detritus respectively. The analogous expression for grazing on detritus is

$$G_D = \frac{gZp_2D^2}{k_3(p_1P + p_2D) + p_1P^2 + p_2D^2}.$$

These expressions are the two food source equivalents of those in FDM90.

The zooplankton excretion term represents a nitrogen flow from the zooplankton to ammonium pool. The mortality includes both natural mortality and predation by unmodelled higher predators which ultimately divides the nitrogen between ammonium, faecal pellets and dead predators. The carcasses and faecal pellets of the higher predators are assumed to have high sinking rates and this is reflected by an immediate export of a fraction Ω of the mortality from the system.

3.2.3 Detritus

The detritus equation is

$$\frac{\mathrm{dD}}{\mathrm{d}t} = \phi_{\mathrm{P}} P + (1-\beta) G_{\mathrm{P}} - \beta G_{\mathrm{D}} - \phi_{\mathrm{D}} D - \frac{(m + h^{+} + V) D}{M}.$$

The source terms reflect phytoplankton mortality and zooplankton faecal material (i.e. the fraction of grazing on both phytoplankton and detritus which is not assimilated). The sinks are zooplankton grazing, detrital breakdown to ammonium, parameterised by a constant specific breakdown rate ϕ_{D} (d^{-1}), and the physical fluxes. For detritus there is an additional physical flux of detrital material sinking out of the mixed layer at a rate V ($\mathrm{m\ d}^{-1}$).

3.2.4 Nitrate

The nitrate equation is

$$\frac{\mathrm{dN}}{\mathrm{d}t} = -PJ \frac{N}{k_1 + N} \exp(-\psi A) + \frac{m + h^{+}}{M} \max[N_{\mathrm{s}}(M) - N, 0].$$

The first term here represents the sink due to new production and the second represents the input of nitrate into the mixed layer from the ocean interior. N_{s} is the nitrate concentration immediately below the base of the mixed layer as defined by a simple model of the spatial variance in the sub-surface nitrate field described below. This replaces the constant sub-surface nitrate term in FDM90. Such a simple model with no temporal variation does result in sub-surface nitrate concentrations which are less than that those in the mixed layer when the mixed layer first shoals in the spring. This potentially causes negative nitrate fluxes which are simply artefacts of the model. Such fluxes are suppressed, as indicated in the nitrate equation, on the assumption that the nitrate concentration below the mixed layer is in

reality always at least as high as that within the mixed layer. Suppression of negative fluxes was not included in FDM90.

3.2.5 Ammonium

The final state variable equation, that for ammonium is

$$\frac{dA}{dt} = -PJ\frac{A}{k_2 + A} + \mu Z + \phi_Z Z^2(1-\Omega) + \phi_D D - \frac{(m+h^+)A}{M}.$$

The first term is the sink due to regenerated production. The source terms arise from zooplankton excretion, zooplankton mortality and detrital breakdown. The final term represents the physical flux due to dilution. In this 5 compartment version of the model all zooplankton excretion goes to ammonium, whereas in FDM90 a fraction of the nitrogen is excreted as DON. There is of course no sink due to bacterial uptake and, as the part played by bacteria in the breakdown of detritus is not explicitly modelled, the detrital breakdown flux goes directly to ammonium, replacing the bacterial excretion term in FDM90. The one other difference from the FDM90 equation is the density dependence of the zooplankton mortality already mentioned.

3.2.6 Spatial Model for Sub-surface Nitrate

Spatial variance in nitrate concentration below the mixed layer is defined by a logarithmic increase in nitrate with depth z of the form

$$N_s(z) = N_{ref} \ln(bz + 1).$$

N_{ref} is the nitrate concentration at reference depth (e - 1) / b modelled as a linear function of longitude x, latitude y and winter-time mixed layer salinity S_o:

$$N_{ref}(x,y,S_o) = a_o + a_x(x - x_{ref}) + a_y(y - y_{ref}) + a_S(S_o - S_{ref})$$

A reference point (x_{ref}, y_{ref}, S_{ref}) = (-20°, 47°, 35.6) is used which is fairly central within the survey area.

In previous studies (Fasham 1995; Fasham and Evans, 1995a,b) a linear variation of nitrate with depth has been used. A linear form was found to be inappropriate for this study because of the large spatial variance in the depth of the winter-time mixed layer over a range from about 200 to about 800 m. In preliminary trials, use of a linear form with realistic vertical gradients tended to push mixed layer nitrate very high in areas where winter mixing was especially deep, due to entrainment of water with unrealistically high concentrations.

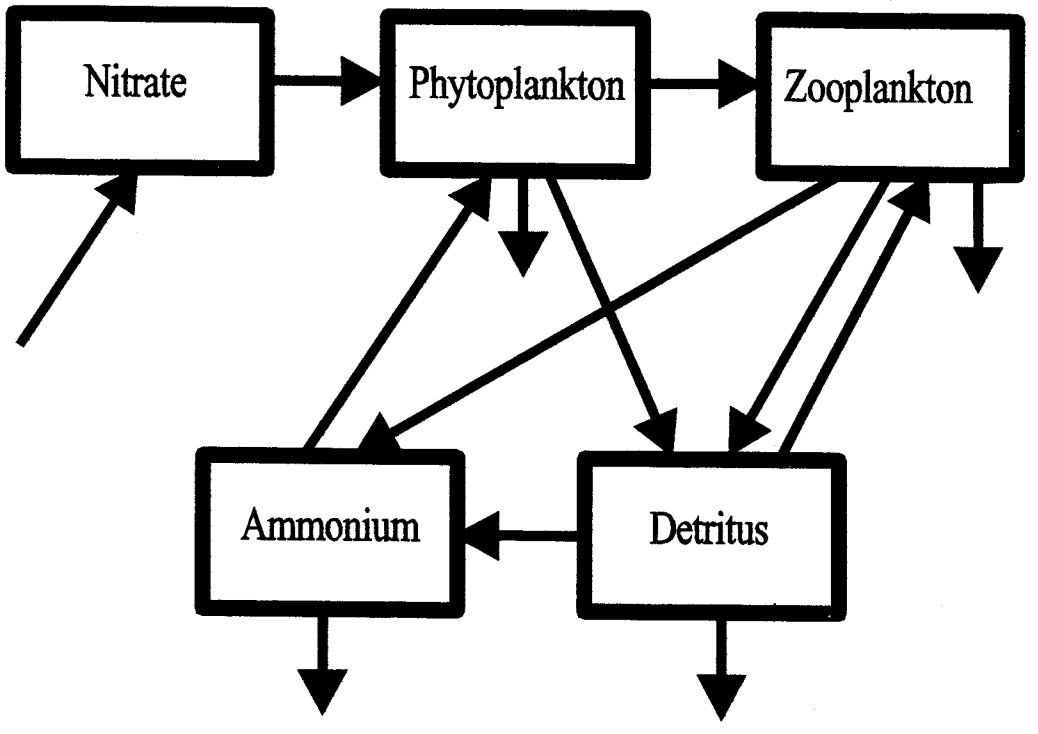

Figure 3.1. Schematic diagram of the mixed layer ecosystem model, showing nitrogen compartments, inter-compartmentmental flows and mixed layer imports and exports.

3.3 Method: Application of the Model to the Study Area

This section describes the application of the ecosystem model to the simulation of the annual cycle and the 1991 spring bloom at different locations within the study area. The physical forcing used to drive the annual cycle is presented in Section 3.3.1. The annual cycle of stratification in the model was found to give a poor fit to the seasonal stratification determined from the Vivaldi observations. However, a much better representation can be achieved by forcing the GCM, during the spring period, with surface meteorological fields derived in part from 1991 observational data. The method used is described in Section 3.3.2 and the results for both simulations are compared with the Vivaldi observations in the error analysis in Section 3.4. The surface seasonal density anomaly was used to adjust the time of the Vivaldi observations to match the observed and modelled stratification as described in Section 3.3.3. The optimisation method which was then used to determine the ecosystem model parameters is outlined in Section 3.3.4.

3.3.1 Physical Forcing

The external data required for determination of the ecosystem model forcing functions at each location are time series of mixed layer depth and fractional cloudiness. The latter is used to modify the noon PAR determined from astronomical formulae. A further requirement is a value for the local winter-time salinity S_0.

The GCM used to determine the mixed layer depth time series was an implementation of the Miami Isopycnic Co-ordinate Ocean Model (MICOM) (Bleck *et al.*, 1992) for the North Atlantic, described by Jia (submitted). This model was set up under the DYNAMO (Dynamics of North Atlantic Models) project which involved detailed inter-comparison of three different models (The DYNAMO Group, 1997). The output used in this study is taken from the final year of a 16 year integration of the coarse resolution (4/3°) version (Jia, pers. comm., 1997). The mixed layer in this model is of the vertically

homogenous Kraus-Turner formulation (Kraus and Turner, 1967). Mixed layer model parameters for this particular run were tuned to data collected during a subduction experiment conducted in the North Atlantic to the south of the Vivaldi survey, in the area from 18-33°N and 22-34°W (Moyer and Weller, 1997). The experiment was designed to investigate the process by which mixed layer waters are incorporated into the main pycnocline and involved the deployment of an array of buoys from June 1991 to June 1993. The differences between the model configuration for the present run and that described by Jia (submitted) are given in Appendix D (Jia, pers. comm. 1997).

The GCM has a time step of approximately one day (1/360 yr.). Mixed layer depth output fields at all time steps were processed in generating the time series for forcing the ecosystem model, in order to capture the details of the rapid changes in mixed layer depth during the development of spring stratification. Corresponding 'daily' profiles of temperature and salinity were used to calculate the seasonal density anomaly required for matching model results and observations. The model grid gives an isotropic spatial resolution, varying with latitude y, equivalent to 4/3° in longitude and 4/3° cos(y) in latitude. The output data were interpolated from this grid onto a 1° grid matching that for the COADS data used in this study. Mixed layer depth and seasonal density anomaly were then averaged over 5° boxes centred on the required locations. There are two reasons for this spatial averaging. The first is that the larger scale is more compatible with the processes modelled in the GCM. Fronts and eddies are not resolved and most of the smaller scale structure in the model output is an artefact of the discrete density layers in the model. Such patterns are removed by averaging over a scale which is large compared with the model grid. Secondly, the presence of horizontal advection affects the applicability of Eulerian time series to the water at a particular location. This was discussed in Chapter 2, in relation to the use of SST time series and it was argued that if a 5° SST field were used, advection on a time scale of 30 days could be ignored. Obviously we cannot expect the same to be true over the whole annual cycle and we must expect there to be differences between the annual cycle of mixed layer depth locally and that experienced by a particular water column. A 5° mean

may however be assumed to give a fair representation of the history of mixed layer depth for a moving water column over a period of a few months prior to the point at which the model is matched to observations. It is the variation in mixed layer depth during this period of shoaling to which we expect the bloom to be particularly sensitive.

The simulated patterns of variability in mixed layer depth shown by the annual cycle (Figure 3.2) are compared here with those presented by Lamb (1984) in the form of bi-monthly mean mixed layer depths, based on a 1°C temperature difference criterion (Figure 3.3). This data set has been chosen in preference to that compiled by Levitus (1982), which is more readily available in numerical form and has been used to define the annual cycle in a number of ecological modelling studies (Wroblewski *et al.*, 1988; Wroblewski, 1989; Fasham, 1995; Fasham and Evans 1995a,b). The reason for this is that it gives mean mixed layer depths based on individual profiles, rather than averaged profiles in which the vertical temperature gradient in the thermocline can be greatly reduced. Such a reduction makes the mixed layer depth more sensitive to the criterion chosen to define it and potentially less accurate.

The mixed layer depth patterns in the model are qualitatively similar to the patterns shown by the observations. The eastern extreme of the tongue of deep mixed layer depths noted by Lamb, to the south-east of the mean Gulf Stream position from late autumn through to early summer, is reproduced by the model in the western part of the study area, being evident from December through to April. The deepest winter mixing is found in the north-eastern part of the survey area, which is consistent with the March-April map presented by Lamb, although the mixing appears to be much deeper in the model. Unfortunately the observational data for these months only extend north to between 50 and 55°N. The coverage for January-February is even more limited, extending to between 45 and 50°N, with the bi-monthly mean mixed layer depth for some 5° boxes above 40°N being determined from less than 10 profiles. These data cannot therefore be used to validate the winter-time behaviour of the model in the far north of the study area but at 50°N 20°W, for

example, the March-April mixed layer depth is less than 300 m, whereas that in the model is about 400 m in April and more than 500 m in March. At 40°N there is less discrepancy between the model and observations. Here the January-February mean presented by Lamb is around 200 m. This is actually a little deeper than that in the model which is around 200 m by February but only around 130 m in January. The observed mean for March-April at 40°N is also typically around 200 m, dropping to about 150 m in the west at about 32°W. This is comparable with model values for this latitude of around 200 m and 160 m in March and April respectively.

While the model appears to over-estimate the depth of winter mixing over much of the study area, model mixed layer depths in both May and June are generally less than the observed May-June observations which vary between about 50 m in the south of the study area (37°N) and about 150 m in the north (58°N). The model therefore shows a more rapid stratification than is apparent from the observations. However, the slower shoaling of the mixed layer depth in the observational data set is likely to be an artefact of averaging over multiple years during which there is significant variance in the timing of stratification. A similar argument could also explain some of the discrepancy in the March-April depths. Quantitative agreement between the modelled and observed field is much improved from late summer through to early winter when changes in mixed layer depth are less sudden.

The cloudiness time series were determined from observational data from the COADS data set used in Chapter 2. Cloudiness for a particular day and location was interpolated linearly from 1° objectively analysed monthly mean fields at the nearest grid point to the required location. The objective analysis procedure, described by da Silva *et al.* (1994), has a broadly similar smoothing effect to the 5° averaging used for mixed layer depth. The annual cycle of fractional cloudiness over the study area is shown in Figure 3.4. From this it can be seen that the temporal variance in cloudiness is very small compared with that shown by the mixed layer depth and therefore has a much smaller effect on availability of light for phytoplankton growth in the mixed layer. Over most of the survey

area the maximum range is less than 0.1. The exception is in the south-west, where the skies are much clearer than elsewhere during the late summer and early autumn. In this region, the annual range is closer to 0.2, with the annual minimum in July being between 60 and 70% of the winter maximum. The spatial variance in cloudiness shows larger differences, particularly in late summer when minimum cloud cover in the south is about half that in the far north of the study area.

The winter-time salinity S_0 required for the nitrate model was, for the purposes of comparison with Vivaldi data (Section 3.5), taken to be the surface salinity S observed during the survey (Figure 3.5a). It was shown in Chapter 2 that salinity could be treated as a conservative tracer between the end of winter and the time of sampling such that $S \approx S_0$. For the analysis of bloom patterns over the wider study area (Section 3.6), S_0 is taken from the GCM. Values at locations on a 1° grid are extracted from the mid-March salinity field, spatially averaged over 5° boxes in the same way as the mixed layer depth (Figure 3.5b).

3.3.2 Modelling the Development of Seasonal Stratification in 1991

Comparisons between the stratification observed during the survey and that obtained from the GCM showed generally poor agreement, the simulated stratification being less developed at the time of sampling over the whole survey area. This is illustrated later in Section 3.4. In order to improve the simulation results the GCM was run with meteorological forcing based, in part, on 1991 data from February through to July. Initial conditions for this integration were taken from the 16 year climatologically forced run (Jia, pers. comm., 1997).

MICOM is forced by monthly mean surface fields of air-sea heat flux, friction velocity (used to determine the turbulent kinetic energy input to the ocean) and wind stress vectors (which determine the Ekman transport). The climatological forcing fields for the implementation used in this study (Jia, submitted) are from a 3 year climatology (1986-

1988) described by Barnier *et al.* (1995), based on 6 hourly records from the European Centre for Medium Range Weather Forecasting (ECMWF). The air-sea heat flux applied to the mixed layer includes a restoring term, dependent on the difference between the model mixed layer temperature and the climatological sea-surface temperature field. An equivalent term restores the sea surface salinity towards the Levitus climatology (Levitus, 1982).

Major differences were noted between the climatological heat fluxes driving the model and 1991 heat flux estimates for the survey area obtained from the COADS data set. This is illustrated by Figure 3.6 which shows time series of the integrated heat input to the ocean from the beginning of the heating season for both data sets. Also shown is the corresponding integral for the actual model forcing, which includes the restoring term. Over a large part of the study area and most of the area covered by the Vivaldi survey the 1991 flux estimates indicate a more rapid warming of the ocean which accounts for the observed stratification being more intense than that in the model. These differences therefore provided a strong motivation for using 1991 heat fluxes to force the model during the heating season.

Comparisons between the other ECMWF climatological forcing fields, which are derived from 6 hourly wind stress records, and the corresponding fields derived from COADS 1991 monthly mean wind data is less straightforward, as the relationship between mean wind stress and mean wind speed over periods of more than about 2 days depends very much on the fluctuations in the wind speed over the averaging period as well as the mean. Failure to take into account these fluctuations can lead to serious underestimation of the mean wind stress (Thompson *et al.*, 1983). A comparison between the friction velocities from the COADS climatology and the ECMWF fields for the study area showed the COADS values to be less than the ECMWF values, typically by a factor of 2, although the discrepancy tended to be less during the summer, when wind speeds are lower, particularly in the south. Although it is possible to correct for this effect to some extent using data for the variance in wind speeds, no attempt was made to do this in this study. Instead, the ECMWF field was retained for the friction velocity and the wind stresses during the heating season were given by uncorrected COADS 1991 data. The reason for using COADS data for

the latter is that, because the wind stress field used to calculate the Ekman transport is a vector field, averaging multiple years tends to reduce the magnitude of the vectors due to interannual variability in the wind direction. Comparison between the 3 year mean ECMWF Ekman transports for the study area (Figure 3.7) and those based on COADS 1991 (Figure 3.8) shows that the 1991 transports tend to be larger than those derived from the climatological wind stresses, despite the fact that they are determined from the lower bound estimates of the wind stress obtained when fluctuations in wind speed are ignored.

For the 1991 simulation then, the climatological forcing fields for heat flux and wind stress from February onwards were replaced by the equivalent objectively analysed 1991 fields from the COADS data set. The COADS 1° monthly means were interpolated onto the model grid over the model domain and the values, located at the mid point of each month, were adjusted (as in the climatological forcing) to preserve the monthly integrals when linear interpolating between months. One other important change was made to the forcing for 1991: the omission of the restoring terms. This modification is appropriate in the context of this study, where we are much more interested in accurately simulating the mixed layer depth and the surface properties relative to those at 150 m than in obtaining realistic absolute surface fields. The purpose for the restoring terms in the standard run is to compensate for drift due to errors in both the dynamics of the model and the air-sea fluxes. Compensation for the effects of model dynamics distorts air-sea buoyancy fluxes, which could contribute to errors in mixed layer depth. Such an effect was noted by New *et al.* (1995) in connection with inaccuracies in the position of the Gulf Stream. It is not possible to disentangle the effects of errors in the air-sea fluxes from those due to errors in the model dynamics and so it is assumed that the fluxes based on the 1991 observational data, with no restoration term, are the best estimates of the real air-sea fluxes.

In order to determine the required 1991 mixed layer depth and seasonal density anomaly fields, the full GCM was run from mid-January to mid-July with the modifications to the forcing fields detailed above. 1991 cloudiness data from the COADS data set were

also used in place of the climatological data from February onwards, affecting the cloudiness time series from mid-January. In the 1991 ecosystem simulation the biological model was run for two calendar years with climatological forcing, in order to obtain initial concentrations of the state variables representative of an approximately steady state annual cycle, before switching to 1991 forcing between January and February of the third year.

3.3.3 Matching Vivaldi Observations to the Model Stratification

For the purposes of comparing ecosystem model results with Vivaldi observations the observations are matched to the model output on seasonal density anomaly rather than time, as we are concerned more with the accuracy of the model response to the development of spring stratification than its ability to accurately reproduce the timing of the bloom. We expect the latter to be greatly affected by errors in the physical simulation as well as those in the biological model.

The 300 km corrected seasonal density anomaly data $\Delta\rho_{30}(0)$, derived in Chapter 2, are used as the best available estimate of the time-of-sampling seasonal density anomaly on time scales compatible with those resolved by the model. Observed biogeochemical properties, including both time-of-sampling concentrations and the pre-bloom or winter-time nitrate estimates, were also averaged over each 300 km SeaSoar run in order to attenuate the variance introduced by mesoscale variability and give values consistent with the stratification. The time attributed to the pre-bloom nitrate estimates is that of the maximum mixed layer depth obtained from the GCM output. Pre-bloom nitrates for the repeated zonal sections were averaged to give a single value. The observation data set thus obtained consists of records for 31 separate locations corresponding to the SeaSoar run mid-points and the co-ordinates of these points were used to extract the required time series of forcing data and seasonal density anomaly data from the relevant data sets.

The observation times were altered to match the observed seasonal density anomaly to that of the model. Because of uncertainty in the observed seasonal density anomaly it is inappropriate to specify an exact time for each observation. Instead a temporal window is defined based on the confidence intervals of the seasonal density anomaly estimate $\Delta\rho_{30}(0)$, derived in Chapter 2, and the modelled seasonal density anomaly time series. The times at which the model seasonal density anomaly matched the values at the upper and lower 68% $\Delta\rho_{30}(0)$ confidence intervals were determined, giving the start and end times respectively for the new temporally diffuse observations. There are a few cases where observed seasonal density anomaly values are greater in magnitude than the summer minimum in the model. In these cases the time of the minimum was used.

3.3.4 Optimisation of Ecosystem Model Parameters

The method for estimating suitable ecosystem parameters was essentially the same as that used by Fasham and Evans for fitting a version of the FDM90 model to data from the North Atlantic Bloom Experiment (Fasham and Evans, 1995a). It was also used in another study (Fasham and Evans, 1995b), in which the abilities of models of different complexity to explain these data were compared and the ability of the 5 compartment model to explain data sets from observations at Ocean Weather Station India (located at 59°N 19°W) and Ocean Weather Station Papa, in the north Pacific, was investigated. In the latter experiments, separate parameter sets were estimated for the two locations, although Fasham (1995) has shown that similar models are capable of reproducing the observed differences in the main characteristics of the annual cycle in the North Atlantic and North Pacific using a single parameter set.

The method involves the use of optimisation algorithms to find a point in the multi-dimensional parameter space which minimises some measure of misfit between model and observations. Fasham and Evans (1995a) defined a measure of misfit

$$T_{obs} = \Sigma\Sigma (\sqrt{x_{obs}} - \sqrt{x_{pred}})^2,$$

where x_{obs} and x_{pred} are observed and predicted values of variable x and the summation is over all variables and all observation times. This form, based on the assumption that the variance of the ensemble of possible values for $x(t)$ at time t increases as the square root of the mean, was proposed as a compromise between two alternative assumptions that, firstly, the variance and, secondly, the coefficient of variation were independent of the mean. The former implies a uniform distribution of absolute error for all x while the latter implies a uniform distribution of relative error.

The authors also defined a penalty function based on prior knowledge of intrinsic or acceptable parameter bounds and default values (referred to as "target" values) which would be accepted in the absence of evidence to the contrary from observational data. Given a target value T and upper and lower bounds U and L for a parameter with estimated variance v, the penalty function for a trial parameter value p is

$$P(p) = \frac{T - p}{(p - L)v} \qquad L < p \leq T,$$

$$P(p) = \frac{p - T}{(U - p)v} \qquad T < p \leq \mathrm{U}.$$

For each trial parameter set the penalty function is summed over all parameters and added to the observation misfit T_{obs}. Large values of v ensure that the penalty function is small, except close to the parameter bounds, so that most of the misfit comes from the data. Values of 10 were used for all parameters in the present study, as in the previous studies.

Some modifications to the way T_{obs} is calculated were necessary for this study. Firstly, it is necessary to introduce a further summation over all locations at which observations are available to get a global misfit measure. This means running the model for all locations for every trial parameter set. The second modification arises from the use of

temporally diffuse observations. For these the required misfit contribution is based on the smallest discrepancy between the predicted and observed values, over all predicted values within the observation window. In this context, it is undesirable to treat observations of different variables at the same time and location independently. Doing so would potentially cause the misfit to be evaluated at different times for the different variables. Instead a time within the window is chosen to minimise the misfit contribution of all variables making up the observation record. This means that valuable information about the relationship between the observed variables is not discarded. A final modification was made to reflect the uncertainty in the pre-bloom nitrates due to the error term in the nitrate-salinity model derived in Chapter 2. The misfit to these data is based on how far outside the 68% confidence intervals the model prediction lies, rather than how far from the estimated value. There is no contribution to the misfit where the model prediction is within the confidence interval.

The target values and bounds for most of the parameters were based on the work of Fasham (pers. comm., 1998). The version of the 5 compartment model used in this study includes a number of parameters which were not present in the version used by Fasham and Evans (1995b). These relate to the nitrate spatial variance model. In addition, the conversion factor between model phytoplankton concentration and chlorophyll *a*, assumed for simplicity to be constant over all observation times and locations, is treated as an additional model parameter to be estimated. The target value for this conversion factor was set to the reciprocal of the value of N:Chl *a* used in the analysis of the survey data in Chapter 2. Default values for the 5 sub-surface nitrate model parameters consistent with the rest of the default parameter set were determined by performing a preliminary optimisation with other parameters fixed. For this run the pre-bloom nitrate observations only were used. The parameter b was then fixed for the main optimisation, while the other sub-surface nitrate parameters were allowed to vary within fairly narrow bounds to compensate for other parameter changes. The target values and bounds used for all parameters are given in Table 3.1. The PAR attenuation coefficient for water k_w, while varying to some extent with the spectral properties of the underwater light field, is a comparatively well defined parameter

and so was fixed at the standard value used in FDM90. Because of the absence of zooplankton data in the Vivaldi data set, it was felt that at least some of the zooplankton parameters should be fixed. The assimilation efficiency β and the detrital fraction of mortality Ω were therefore also fixed at the standard values used in FDM90, on the recommendation of Fasham (pers. comm., 1998). Likewise, there is no data to constrain the detrital sinking rate V, so this parameter was also fixed. Its value was based on an analysis by Martin *et al.* (1993) in which sinking rate was derived by comparing observed PON fluxes with vertical profiles. 19 parameters were left as free parameters for optimisation.

The optimisation algorithm used was Powell's direction set method (Press *et al.*, 1992) as in the previous studies. Brent's linear minimisation method (Press *et al.*, 1992) was used for minimising the misfit contribution within the observation windows as well as for performing the linear minimisations in the Powell algorithm. The starting point for the search, hereafter referred to as the prior parameter set, is specified in this study by the default or target values. The Powell algorithm is not guaranteed to find a global minimum and so the solutions obtained must be treated only as improvements on the prior parameter set, with respect to the misfit. The existence of parameter sets which would give better fits than the one which corresponds to the minimum found by the algorithm is always a possibility. The successful location of a global minimum is a complex problem. While the algorithm of simulated annealing, which was applied to data from the Bermuda Atlantic Time-series Study site by Hurtt and Armstrong (1996), is more powerful in this respect, it was considered to be prohibitively expensive in computer time for the purposes of this study.

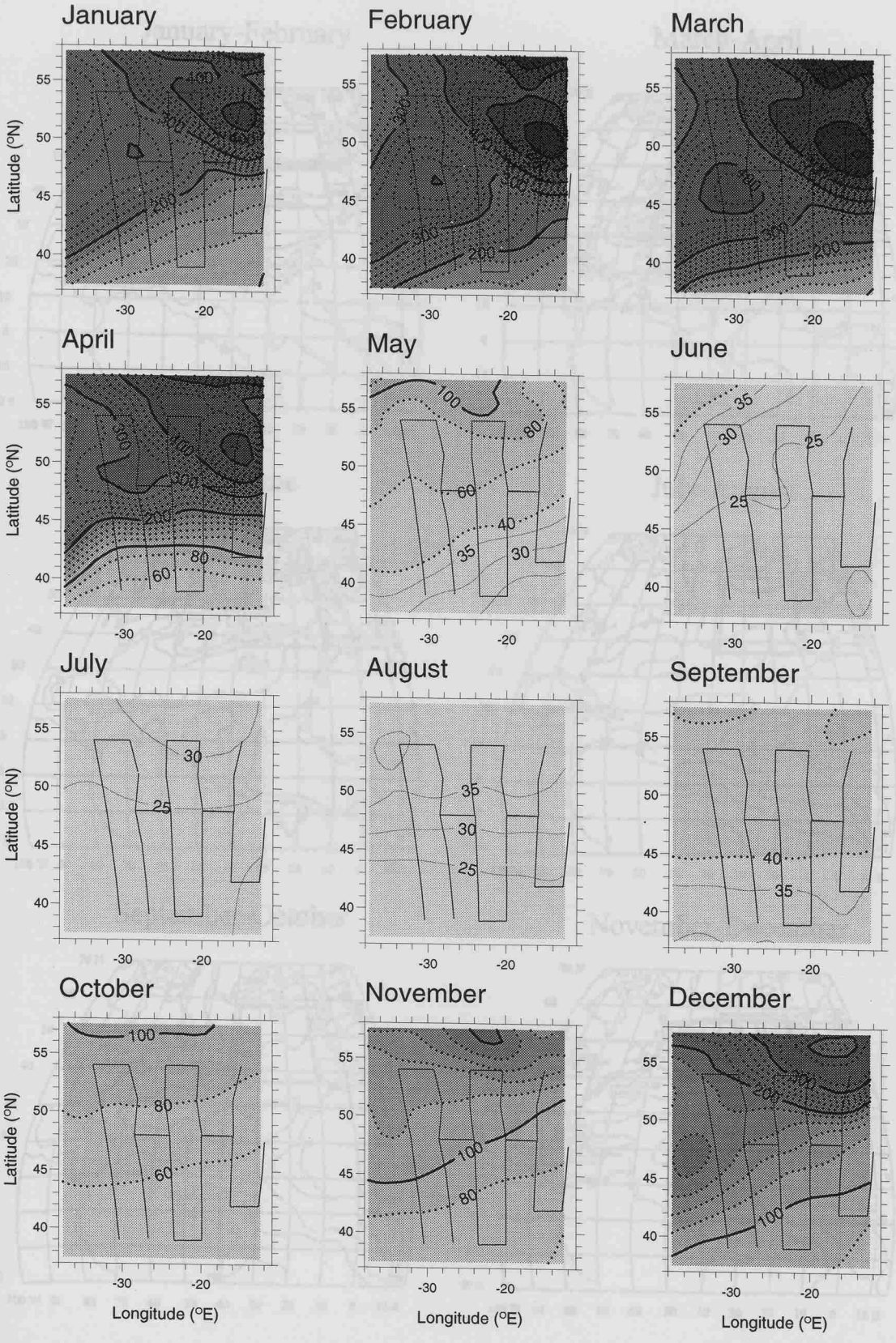

Figure 3.2. Model monthly mean mixed layer depth (m) for the climatological simulation.

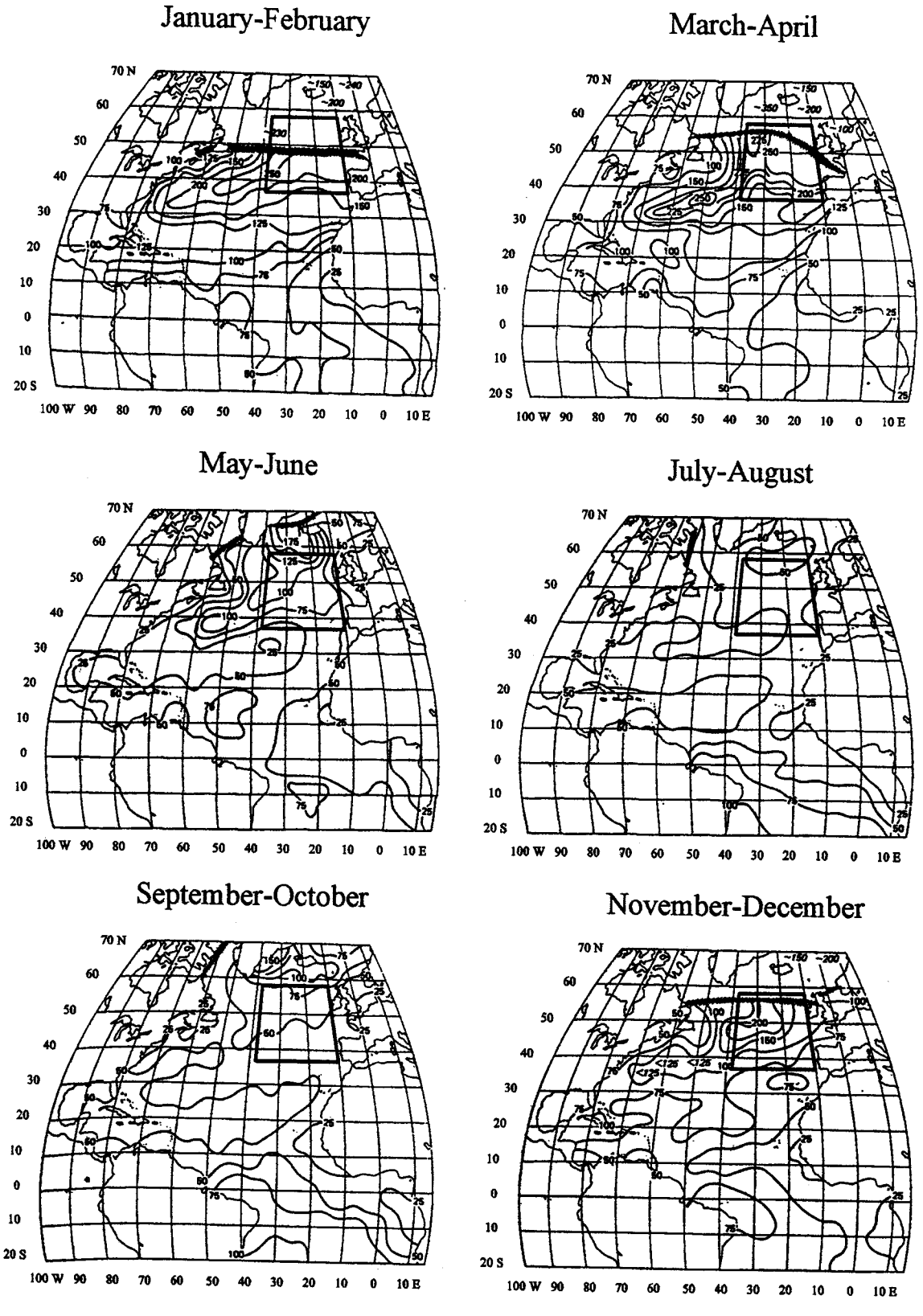

Figure 3.3. Climatological bi-monthly mean mixed layer depth (m) estimated from temperature profiles using a 1°C difference criterion. Maps reproduced from Lamb (1984). The box shows the present study area.

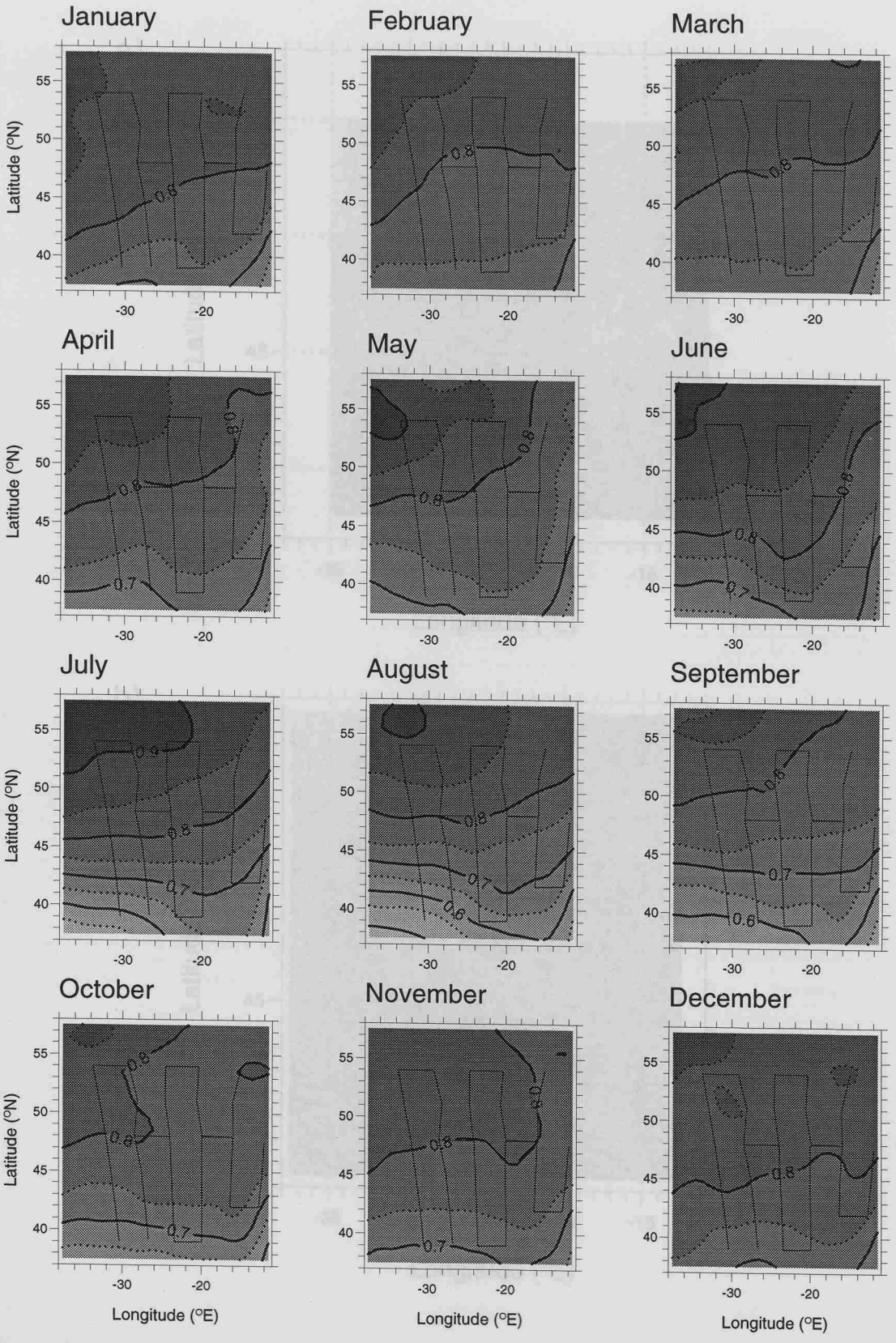

Figure 3.4. Climatological monthly mean fractional cloudiness (COADS).

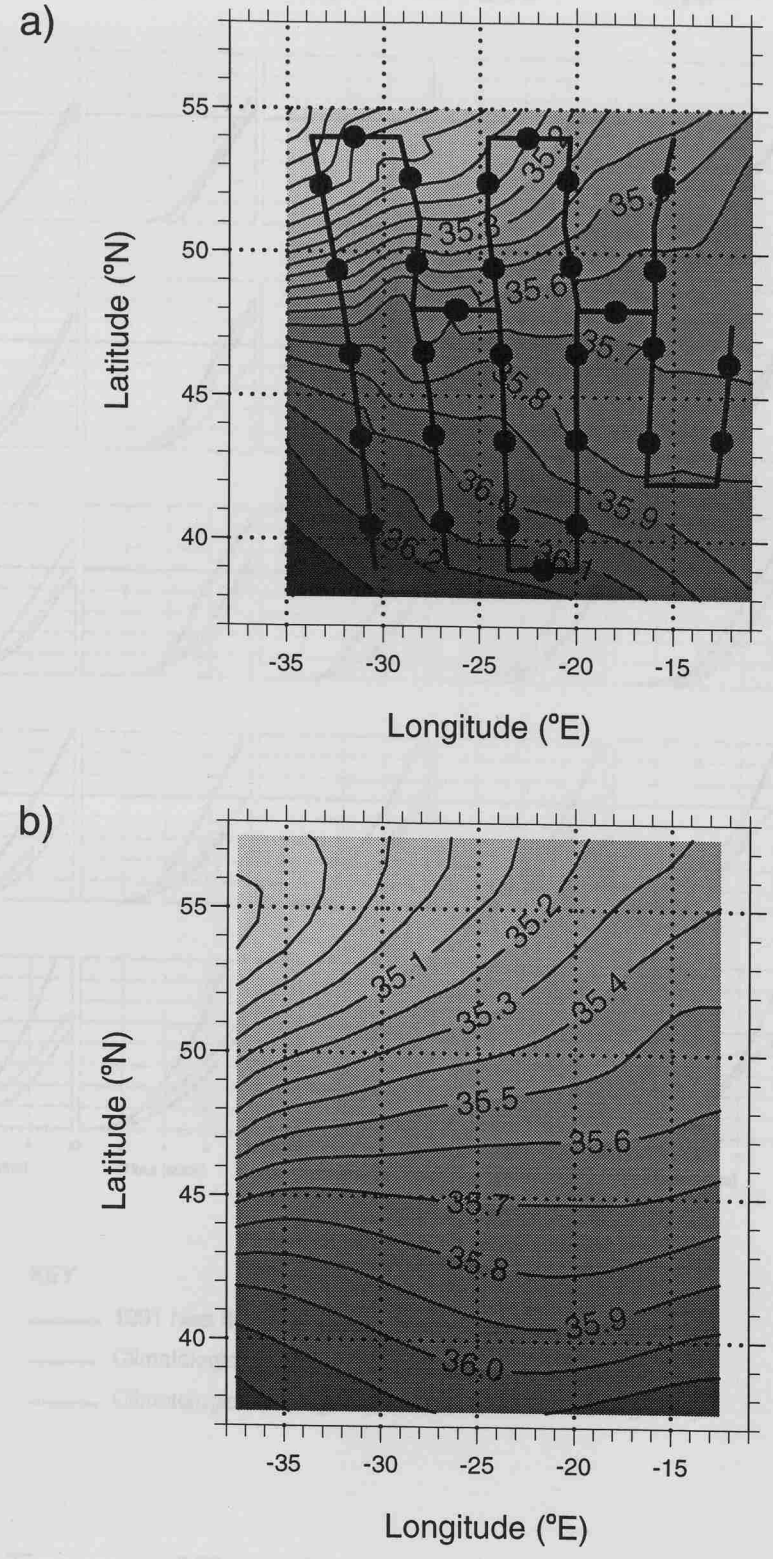

Figure 3.5. Salinity fields for the sub-surface nitrate model: (a) observed surface salinity, mapped from 300 km mean values for each Vivaldi SeaSoar run, and (b) model salinity in mid-March for the climatological simulation.

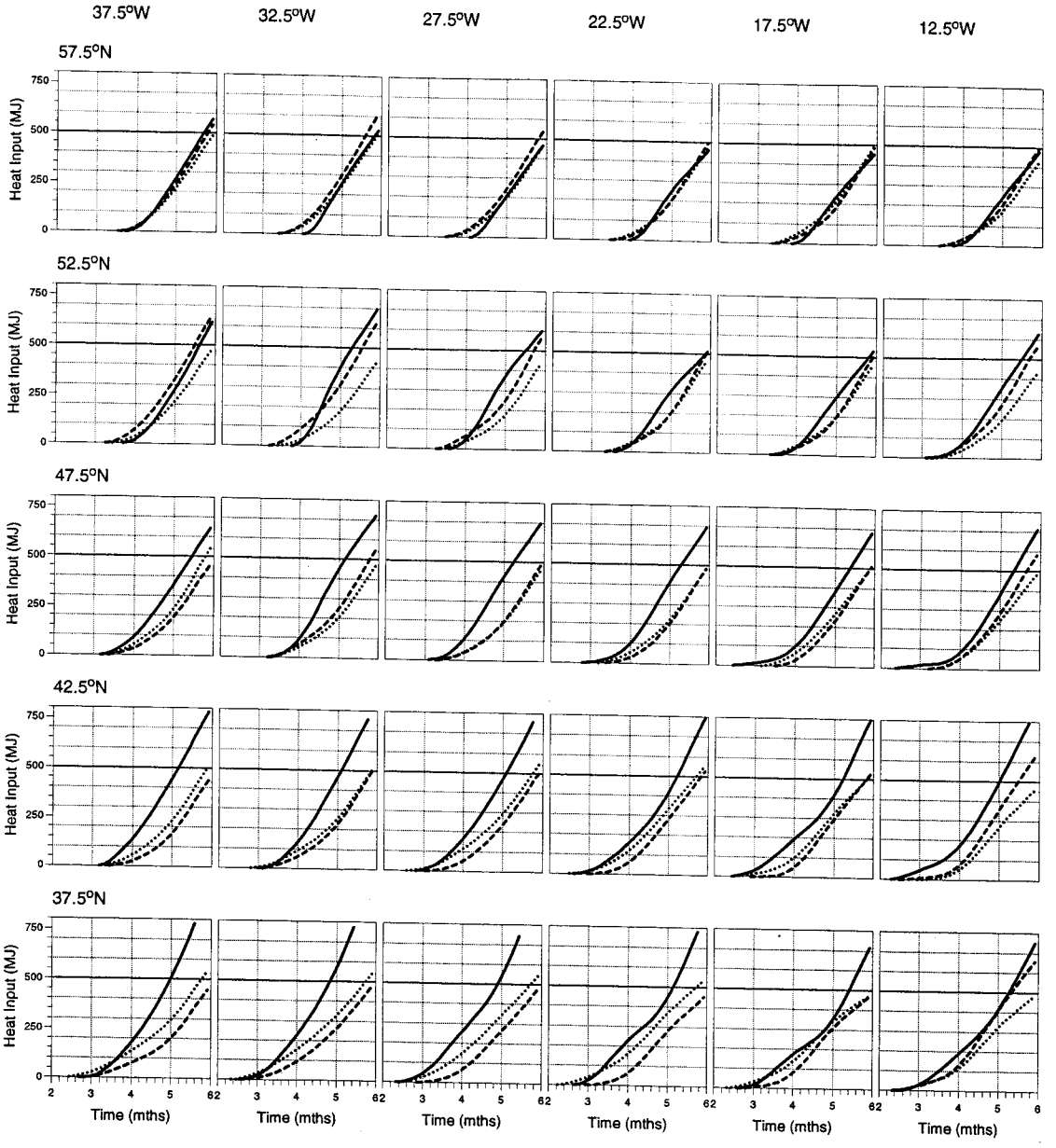

Figure 3.6. Time series of 5° mean heat input to the ocean for March to June, integrated from the beginning of the heating season.

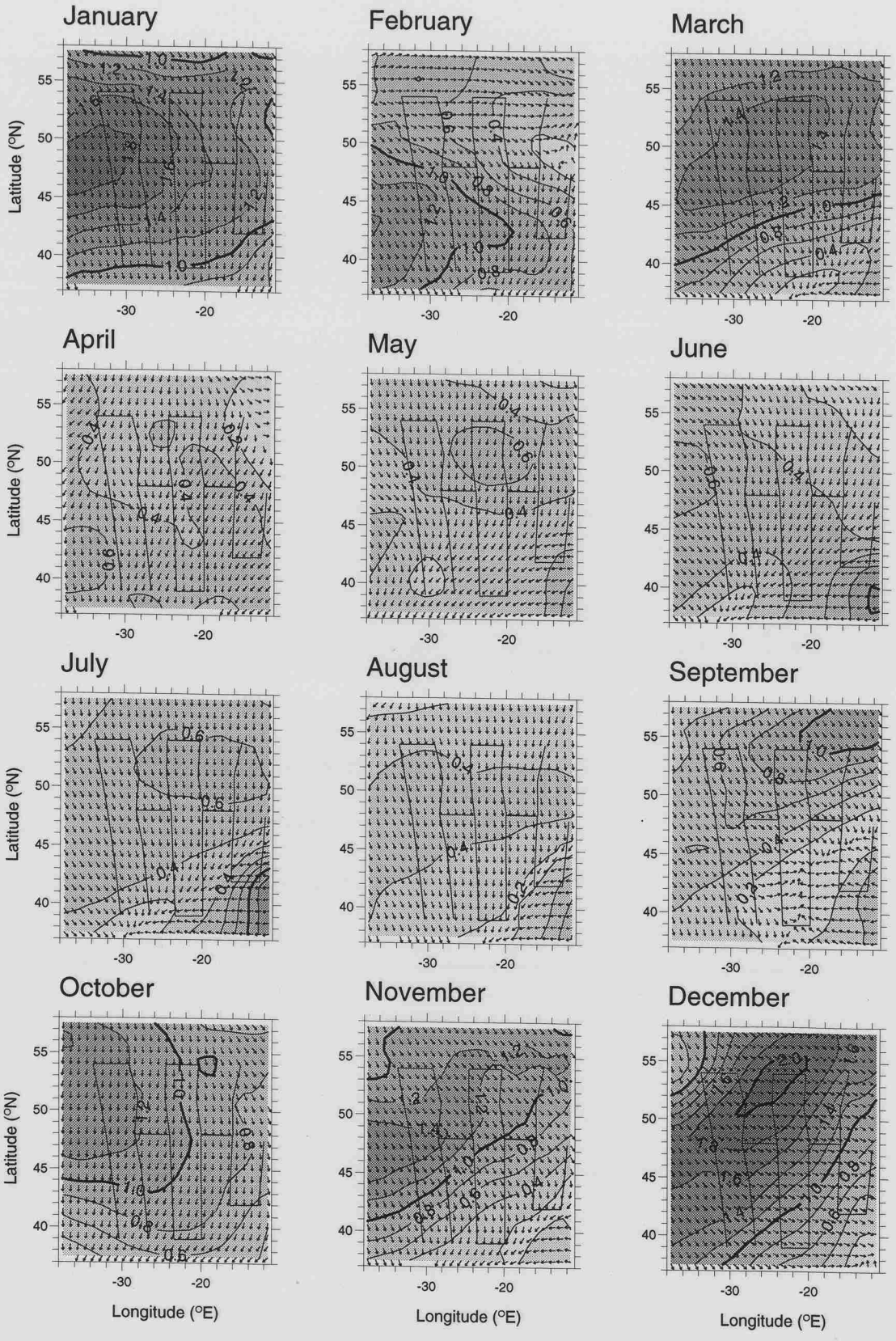

Figure 3.7. Model monthly mean Ekman transport ($m^2 s^{-1}$) for the climatological simulation.

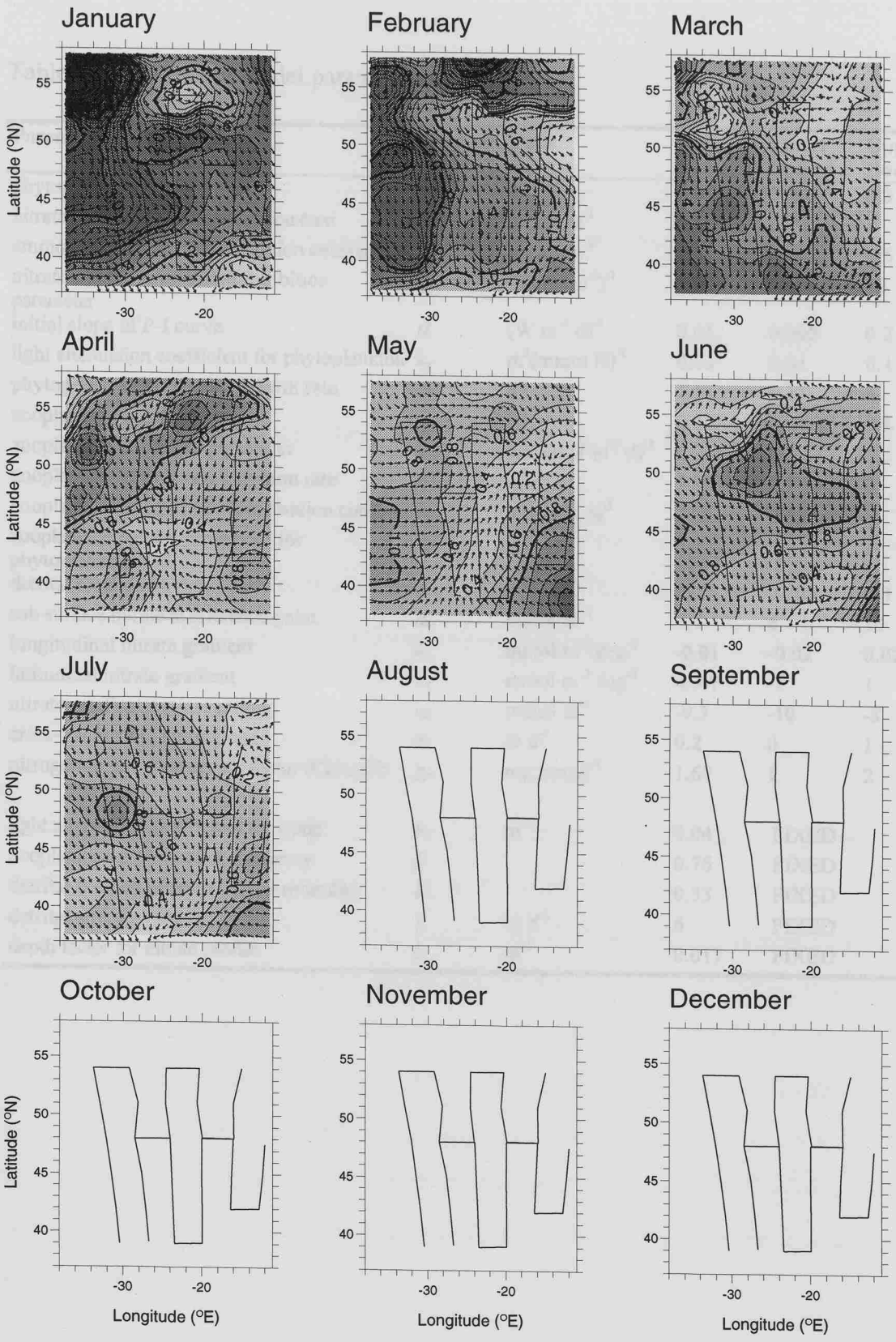

Figure 3.8. 1991 monthly mean Ekman transport ($m^2 s^{-1}$), for January to July, based on the COADS 1991 objectively analysed wind stress vectors.

Table 3.1. Ecosystem model parameters.

Parameter	Symbol	Units	Default Value	Lower Bound	Upper Bound
phytoplankton mortality rate	ϕ_P	d^{-1}	0.05	0.005	0.3
nitrate uptake half-saturation constant	k_1	mmol m^{-3}	0.5	0.05	1
ammonium uptake half-saturation constant	k_2	mmol m^{-3}	0.1	0.05	0.5
nitrate uptake ammonium inhibition parameter	ψ	$(mmol\ m^{-3})^{-1}$	1.5	0.15	10
initial slope of P-I curve	α	$(W\ m^{-2}\ d)^{-1}$	0.05	0.005	0.2
light attenuation coefficient for phytoplankton	k_p	$m^2(mmol\ N)^{-1}$	0.03	0.01	0.1
phytoplankton maximum growth rate	V_P	d^{-1}	1.5	0.15	4
zooplankton excretion rate	μ	d^{-1}	0.1	0.01	0.5
zooplankton mortality parameter	ϕ_Z	$(mmol\ N\ m^{-3}\ d)^{-1}$	0.2	0.02	0.5
zooplankton maximum ingestion rate	g	d^{-1}	1	0.1	3
zooplankton ingestion half-saturation constant	k_3	mmol N m^{-3}	1	0.05	3
zooplankton feeding preference for phytoplankton	p_1		0.5	0	1
detrital breakdown rate	ϕ_D	d^{-1}	0.05	0.005	0.3
sub surface nitrate at reference point	a_o	mmol m^{-3}	7.7	6	10
longitudinal nitrate gradient	a_x	mmol m^{-3} deg^{-1}	-0.01	-0.02	0.02
latitudinal nitrate gradient	a_y	mmol m^{-3} deg^{-1}	-0.47	-1	1
nitrate gradient against salinity	a_S	mmol m^{-3}	-9.3	-10	-8
cross-pycnocline mixing rate	m	m d^{-1}	0.2	0	1
nitrogen to chl. conversion factor (Chl *a*:N)	χ_c	mg $mmol^{-1}$	1.67	1	2
light attenuation coefficient for water	k_w	m^{-1}	0.04	FIXED	
zooplankton assimilation efficiency	β		0.75	FIXED	
detrital fraction of zooplankton mortality	Ω		0.33	FIXED	
detrital sinking rate	V	m d^{-1}	6	FIXED	
depth factor for nitrate profile	b	m^{-1}	0.017	FIXED	

3.4 Physical Model Results

Before examining the optimisation results for the ecosystem model, the physical model results for the development of stratification are evaluated against the Vivaldi observations in order to assess as far as possible the accuracy of the physical forcing applied to the ecosystem model. In Section 3.4.1, the differences between the development of stratification in the climatological and 1991 simulations are examined and the simulated surface seasonal density anomaly at the Vivaldi sampling time from each is compared. The time shifts required to match the Vivaldi seasonal density anomaly to that of the 1991 simulation are then discussed. Possible factors contributing to the seasonal density anomaly error are investigated in Section 3.4.2 and, finally, the differences between the observed and modelled mixed layer depths are examined in Section 3.4.3.

3.4.1 Seasonal Density Anomaly

The simulated development of the surface seasonal density anomaly between the beginning of March and the end of June is shown in Figure 3.9. It is immediately apparent that the 1991 simulation gives a more advanced seasonal stratification across the whole survey area, reflecting the greater heat inputs to the ocean in the 1991 meteorological forcing of the GCM. While it may be argued that much of the difference is due to a difference in timing of the initial stratification, rates of intensification of stratification also differ between the 1991 and climatological simulations, especially at some of the more southerly locations. In many areas, the difference in timing of stratification development by June is up to almost a month. This is a long time compared with the time scales involved in the dynamics of plankton blooms.

Inspection of the $\Delta\rho_{30}(0)$ observations plotted in Figure 3.9 shows that the surface seasonal density anomaly from the 1991 simulation gives a much better fit to the actual stratification at the time of sampling. This is shown more clearly in Figure 3.10 which

compares the values following the cruise track. Over large parts of the survey area the 1991 simulation comes within or close to the 68% confidence intervals. The main exceptions are areas where the model greatly underestimates the intensity of the stratification. These are towards the highest latitudes sampled on CD58, around times of 122 d and 131 d, and at 54°N on CD59, at 151 d, where the main branch of the North Atlantic Current flows northwards across the cruise track.

The observation time-shift δt required to match the observed seasonal density anomaly $\Delta\rho_{30}(0)$ to that of the 1991 simulation at each location is shown in Figure 3.11. The largest values, unsurprisingly, occur in the areas where the errors in the density anomaly at the time of sampling are greatest. Typically of order 5-10 days, these time shifts are still not small with respect to the time scales of bloom dynamics, despite the improved physical simulation. The difference between values of δt used and those which would have been obtained if no correction for event-scale variability had been applied illustrates the importance of applying this correction where possible. The larger the value of δt the more suspicious we should be about the accuracy of the physical forcing prior to the match time. This is particularly true for the large values, over 20 days, in the north of the survey area. At these locations, the observed density anomaly was below the model minimum as clearly seen in Figure 3.9 (SeaSoar runs 12011, 12012 and 12013). It was therefore not possible to get an exact match. Because there were insufficient SST data in this area to correct the observed seasonal density anomaly for event-scale variability, it is unclear whether this problem is due to inaccuracies in the physical simulation or whether it occurs because the observations are biased low due to calm and/or warm weather conditions. However, the time shift associated with the upper $\Delta\rho_{30}(0)$ 68% confidence interval is still greater than 20 days at two of these three locations.

Large temporal offsets present a problem because the phase shift with respect to the annual cycle of solar radiation could become a significant source of error in the forcing. In addition, if a large time-shift is required, particularly late in the season, it may be an

indication that the forcing function poorly represents the rate of intensification of the stratification, and, consequently, the elapsed time between the time at which the water column first stratified and the time at which the seasonal density anomaly reached a particular value. If the time of initial stratification is defined conceptually as that at which light limitation due to the depth of the mixed layer ceases to be the dominant factor controlling phytoplankton growth, then this elapsed time will be critical in determining the state of the bloom. Even if the only inaccuracy in the stratification used to force the model is in the timing of the initial water column stratification, the ecosystem is not expected to remain in a steady state over winter up until the mixed layer starts to shoal and so the distortion of the time axis before this point implied by a major time-shift is potentially serious.

3.4.2 Diagnostic Analysis of Seasonal Density Anomaly Error

Errors in the seasonal density anomaly obtained from the 1991 simulation are examined here with the aim of identifying causal factors which might suggest improvements to the physical model. Errors may be due to inadequate representation of vertical and/or horizontal processes. The most obvious source of error, inaccuracy in the air-sea heat flux, has been reduced as far as possible by the use of 1991 fluxes. The other relevant vertical processes are the air-sea flux of freshwater and those processes which determine the distribution of the seasonal buoyancy input in the water column (vertical advection and diffusion and absorption and scattering of solar radiation). No air-sea freshwater fluxes were applied in the 1991 simulation and it was argued in Chapter 2 that the contribution of air-sea fluxes was likely to be negligible on the time scales considered. The contribution of horizontal processes to stratification arises through the 'tilting' action of vertical shear on horizontal buoyancy gradients. The model's ability to reproduce this effect is assessed by comparing modelled and observed surface seasonal salinity anomalies, on the basis that salinity acts as a conservative tracer of winter-time buoyancy as discussed in Chapter 2. Further information is obtained by comparing vertical profiles of seasonal density anomaly.

The observed surface seasonal salinity anomaly is shown in Figure 3.12, together with the model values from the climatological and 1991 simulations at the time of sampling and the 1991 simulation at the match time. It is immediately obvious that the model values are much less in magnitude than the observed values, indicating an underestimate of the stabilising effect of buoyancy transport on the water column. The main reason for this is almost certainly the absence of a mesoscale eddy field in the model, in particular the absence of mesoscale fronts where higher resolution models show that ageostrophic shear should enhance stratification (Nurser and Zhang, in revision; Haine and Marshall, 1998; Lévy *et al.*, 1998). As discussed in Chapter 2, the main processes though to be responsible for the development of the seasonal salinity anomaly are the 'tilting' of density surfaces associated with baroclinic instability and Ekman drift. The former is not modelled in the GCM and the effect of the latter is expected to be much less than in reality because of the weak horizontal salinity gradients in the model. The maximum salinity gradient in the GCM over the study area is about 0.1 per degree of latitude or 0.001 km^{-1} (Figure 3.5b). This is found in the same region as the maximum observed salinity gradients, which are seen at mesoscale fronts on leg W, but the observed gradients are much greater. Examination of Figure 2.6 shows gradients of up to 0.5 per degree of latitude (0.005 km^{-1}). In fact, the fronts are likely to be steeper than shown by the transect data, firstly because the transects are not expected to be perpendicular to the fronts and, secondly, because of the attenuation of variance at length scales less than 36 km in the data processing. The evidence suggests something like an order of magnitude difference in maximum salinity gradients between the model and the real ocean. It is therefore unsurprising that the model salinity anomaly is so small in comparison to that observed.

Although the differences in magnitude are large, the general pattern is fairly well represented by both the climatological and 1991 simulations up until a time of about 145 d, with the high values in the south and south-west and the negative values at the north end of leg W being successfully reproduced. After this there are relatively large differences between the results for the climatological and 1991 simulations due to the differences in Ekman transport. The differences here between the two sets of 1991 simulation results, extracted at

different times, indicate a progressive change in salinity anomaly associated with eastward Ekman transport in May (Figure 3.8). Some of the largest differences, those occurring between times of 151 and 153 d, partly reflect the large time shifts here of between 20 and 30 days. The pattern after 145 d does not agree so well with that for the observed salinity anomaly. The sign of the simulated salinity anomaly is negative across the whole of the northern part of the survey area, whereas the observed anomaly is positive, although the peaks and troughs in the 1991 simulation at the time of sampling arguably show a rough match to those in the observational time series. We can make more sense of this by noting that the observed seasonal salinity anomaly at the surface in this area is less than the maximum in the depth profile between 0 and 150 m, suggesting an initial positive horizontal flux of salt, relative to 150 m, followed by a later negative flux, as mentioned in Chapter 2. Some degree of correspondence can be seen between the largest negative anomalies in the model and the largest differences between the observed maximum and surface values of the seasonal salinity anomaly. The pattern appears to reflect a reasonable simulation of the later negative fluxes, associated with the eastward Ekman transport, superimposed on a pattern arising from underestimation of the longer term positive flux as seen in the more southerly part of the survey area.

The observed vertical profiles of seasonal density anomaly are compared with those in the model at both the match time and the time of sampling in Figure 3.13. Two different 'observed' profiles are shown for each location. The observed 300 km mean $\Delta\rho$ profile is the greater in magnitude (the leftmost profile). The other profile shown is the estimated seasonal density anomaly due to air-sea fluxes only $(\Delta_L\rho)_Q$, the difference being the estimated transport component $(\Delta\rho)_T$. The observed profiles do not include any event-scale correction and so observed and modelled profiles do not normally match at the surface. It is more important, for the purposes of making inferences about the history of stratification development, to compare how well the profiles agree below the mixed layer or below the depth at which the observed density is say 0.1 kg m^{-3} greater than at the surface. Comparisons are not particularly useful for the early part of the survey in the south-east

where stratification is not well established and the observed profiles for this area are omitted.

One of the most important points to note is the lack of variability, both temporal and spatial, in the model profiles below the mixed layer, compared with the variance shown by the observed profiles. The form of the model profiles below about 50 m is partly an artefact of the density resolution in the model and so only the differences above 50 m will be discussed. All model profiles show a seasonal density anomaly of around 0.1 kg m^{-3} at 50 m and 0.2 kg m^{-3} between about 30 and 40 m (except where the surface value is less than 0.2 kg m^{-3}). In contrast, the observations show a definite increase in seasonal density anomaly at 50 m towards the west, up to a maximum of about 0.25 kg m^{-3} on most of leg W. This variation was discussed in Chapter 2, where an increase in the maximum depth of the seasonal pycnocline to the west was interpreted in terms of an enhanced contribution of buoyancy transport to the seasonal density anomaly in regions of stronger flow and steeper horizontal buoyancy gradients. The transport component is too small to account for all of the error and the increase from east to west is also seen in the signal due to air-sea fluxes only. However, this does not necessarily contradict the interpretation, as the transport component includes only the effect associated with pre-existing buoyancy gradients. We should expect the flow to have a similar effect on developing seasonal components of the horizontal structure.

The largest errors in the surface seasonal density anomaly at the time of sampling were not found in the same areas as the largest values of the transport component, which suggests that vertical buoyancy flux errors in the model may make a significant contribution. However, comparison between the observed profiles and the model profiles at the time of sampling shows that, in the majority of cases (with the exception of the locations in the south-east of the survey area where the observed profiles are omitted), the observed density anomalies are greater in magnitude over the whole depth range. This means that vertical redistribution of buoyancy cannot account for the discrepancy and a low bias in the air-sea buoyancy fluxes would be required if the errors were to be explained in terms of vertical

fluxes only. In general, the pattern of the error suggests that underestimation of the effect of horizontal processes is the more important factor and the absence of mesoscale fronts in the model provides a sound theoretical reason for this.

3.4.3 Mixed Layer Depth

The modelled and observed mixed layer depths at the matching time are shown in Figure 3.14. This shows that there are large differences for the early part of the survey where mixed layers between 100 and 400 m deep were observed. Mixed layer depth from the model is less than about 50 m throughout. Evidence was presented in Chapter 2 that observations of the seasonal development of stratification were affected by short-time scale variations associated with weather. No correction has been made to the observed mixed layer depth to compensate for this, and so much of the difference between the observed mixed layer depth and the model mixed layer depth, representing the seasonal variation, is likely to be due to weather conditions immediately before the time of sampling. Comparison between this observational mixed layer depth anomaly and the estimated event-scale SST anomaly, also plotted in Figure 3.14, shows no obvious correlation. However, there is some evidence of a possible connection in that both of the positive temperature anomalies which are significant at the 95% level (at times of 139 and 154 d) are associated with negative mixed layer depth anomalies and all significant negative temperature anomalies (11 out of 16 CD58 observations plus one CD59 observation at time 156 d) are associated with positive mixed layer depth anomalies (with the exception of one zero anomaly at time 129 d). The absence of a clear correlation is probably due to the non-linear relationship between the response of the mixed layer depth and SST to weather events.

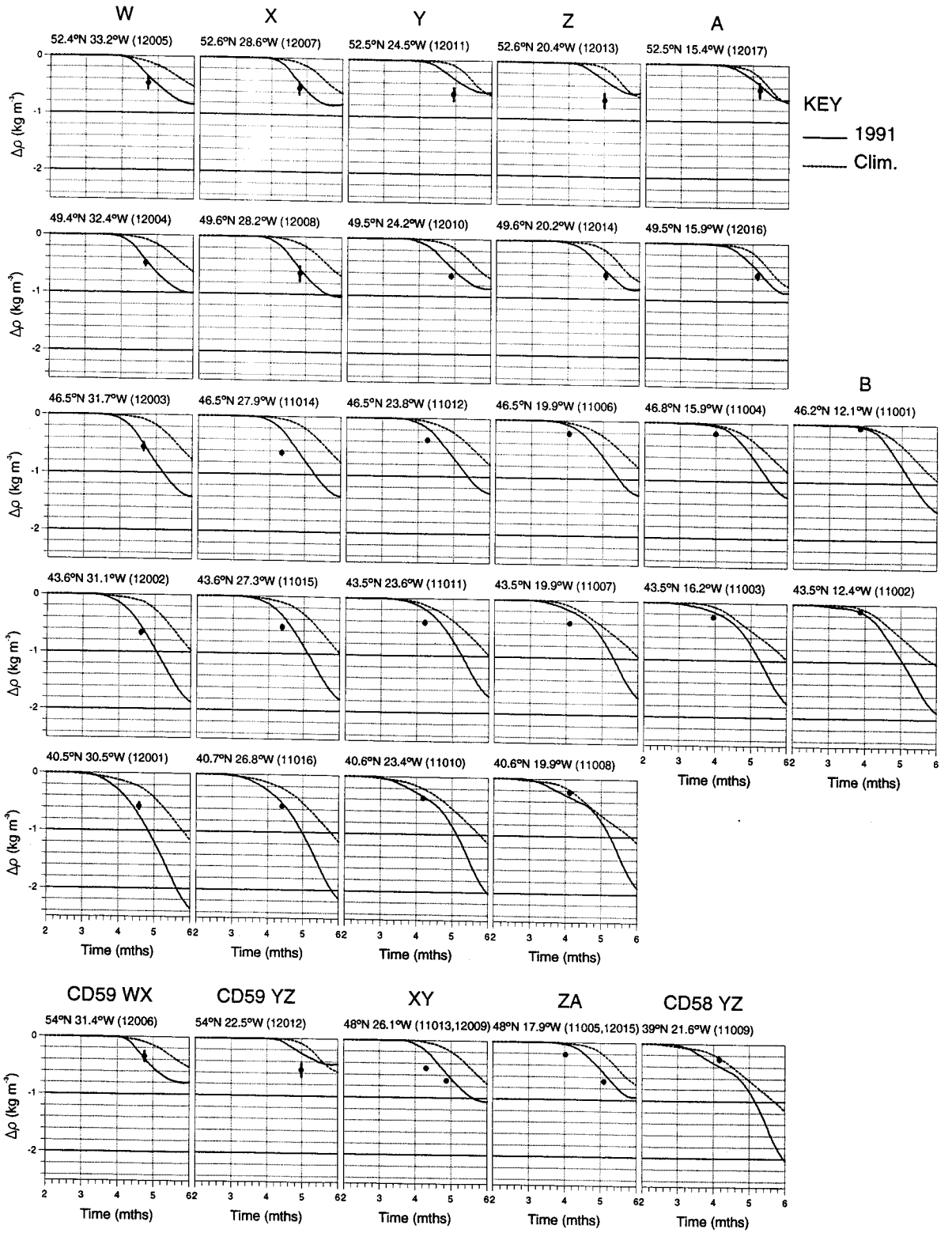

Figure 3.9. Model 5° mean time series of surface seasonal density anomaly, from March to June, at Vivaldi SeaSoar run locations. Results for the climatological and 1991 simulations are shown. The data points show the Vivaldi seasonal density anomaly estimate $\Delta\rho_{30}(0)$ with 68% confidence intervals.

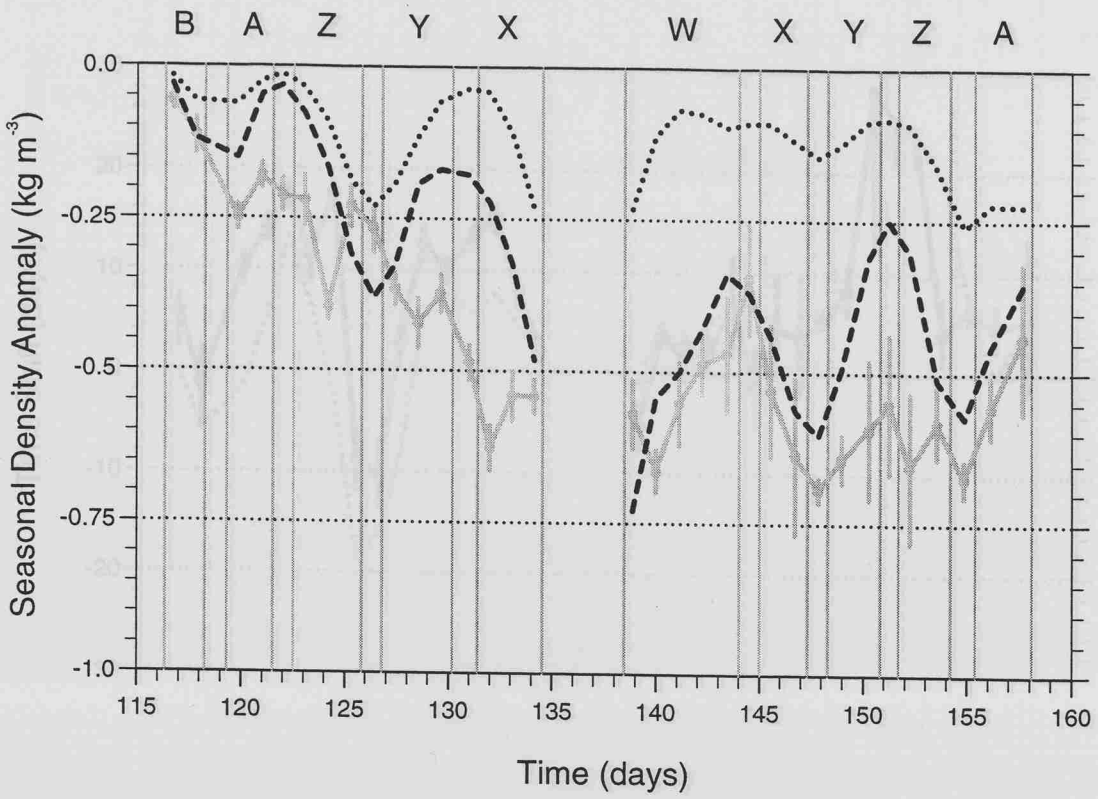

KEY

Observed $\Delta\rho(0)$

1991 Model $\Delta\rho(0)$

Climatological Model $\Delta\rho(0)$

Figure 3.10. Model 5° mean surface seasonal density anomaly at time and location of Vivaldi SeaSoar runs, compared with Vivaldi $\Delta\rho_{30}(0)$ estimate showing 68% confidence intervals.

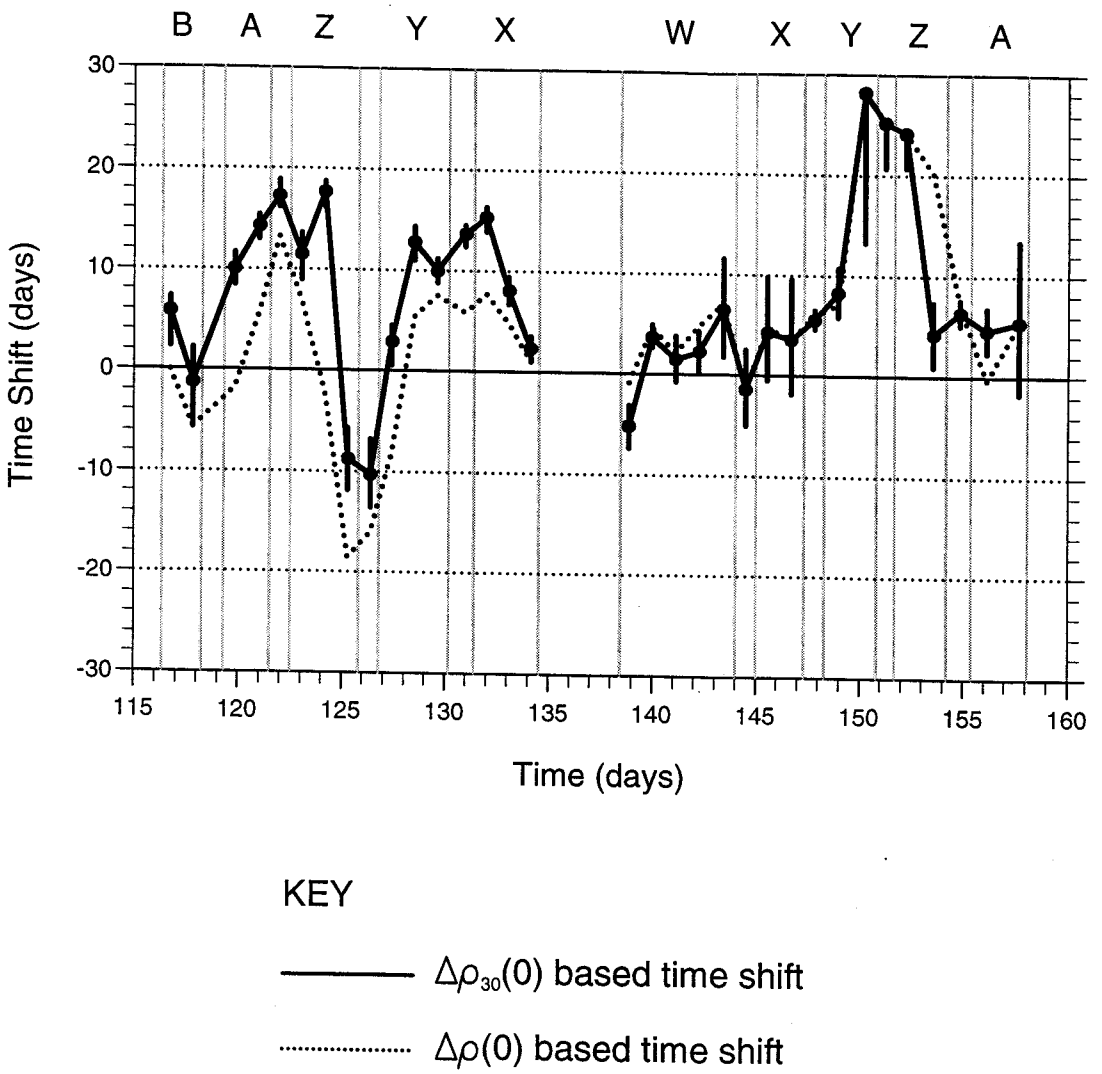

Figure 3.11. Time shift δt required for matching Vivaldi $\Delta\rho_{30}(0)$ to seasonal density anomaly for the 1991 simulation. 68% confidence intervals are shown, based on error in the $\Delta\rho_{30}(0)$ estimate. The time shift determined using the uncorrected seasonal density anomaly $\Delta\rho(0)$ is shown for comparison.

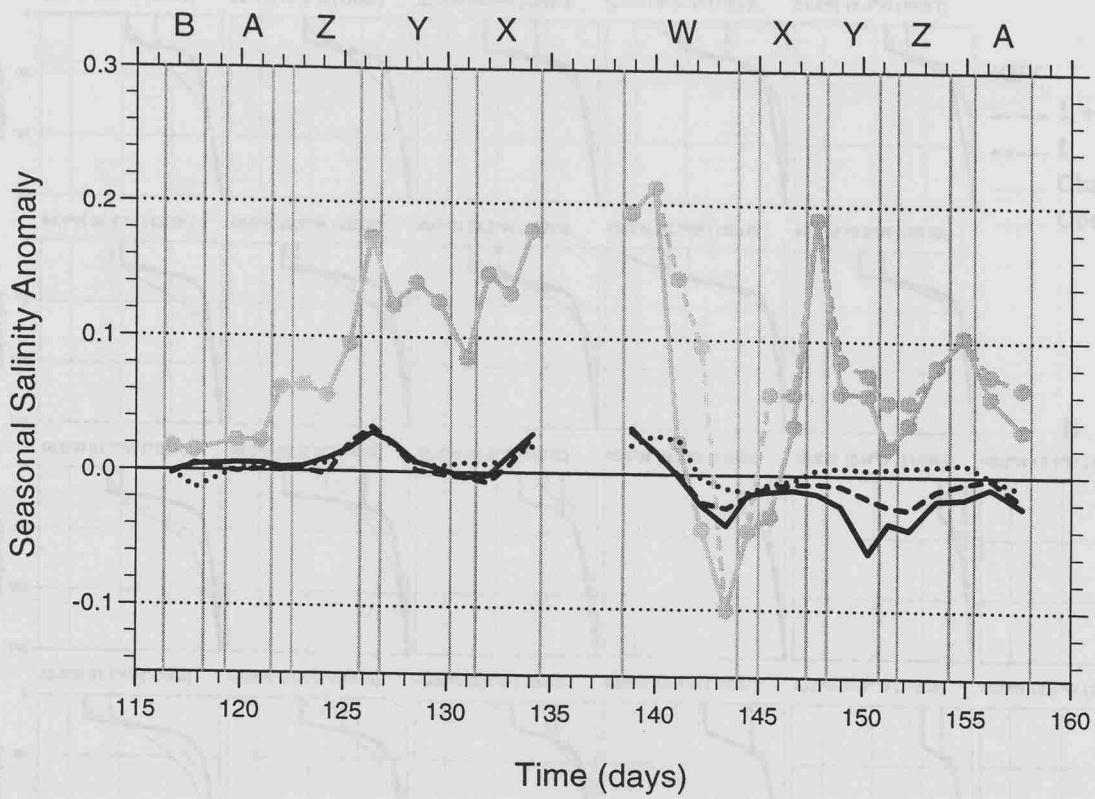

KEY

Observed $\Delta S(0)$

Observed ΔS max.

1991 Model $\Delta S(0)$ at $t_s + \delta t$

1991 Model $\Delta S(0)$ at t_s

Climatological Model $\Delta S(0)$ at t_s

Figure 3.12. Model 5° mean surface seasonal salinity anomaly at Vivaldi SeaSoar run locations, compared with the observed 300 km mean anomaly at the surface and maximum anomaly over the 0 - 150 m depth range. Results are shown for both simulations at the time of sampling t_s and for the 1991 simulation at $t_s + \delta t$.

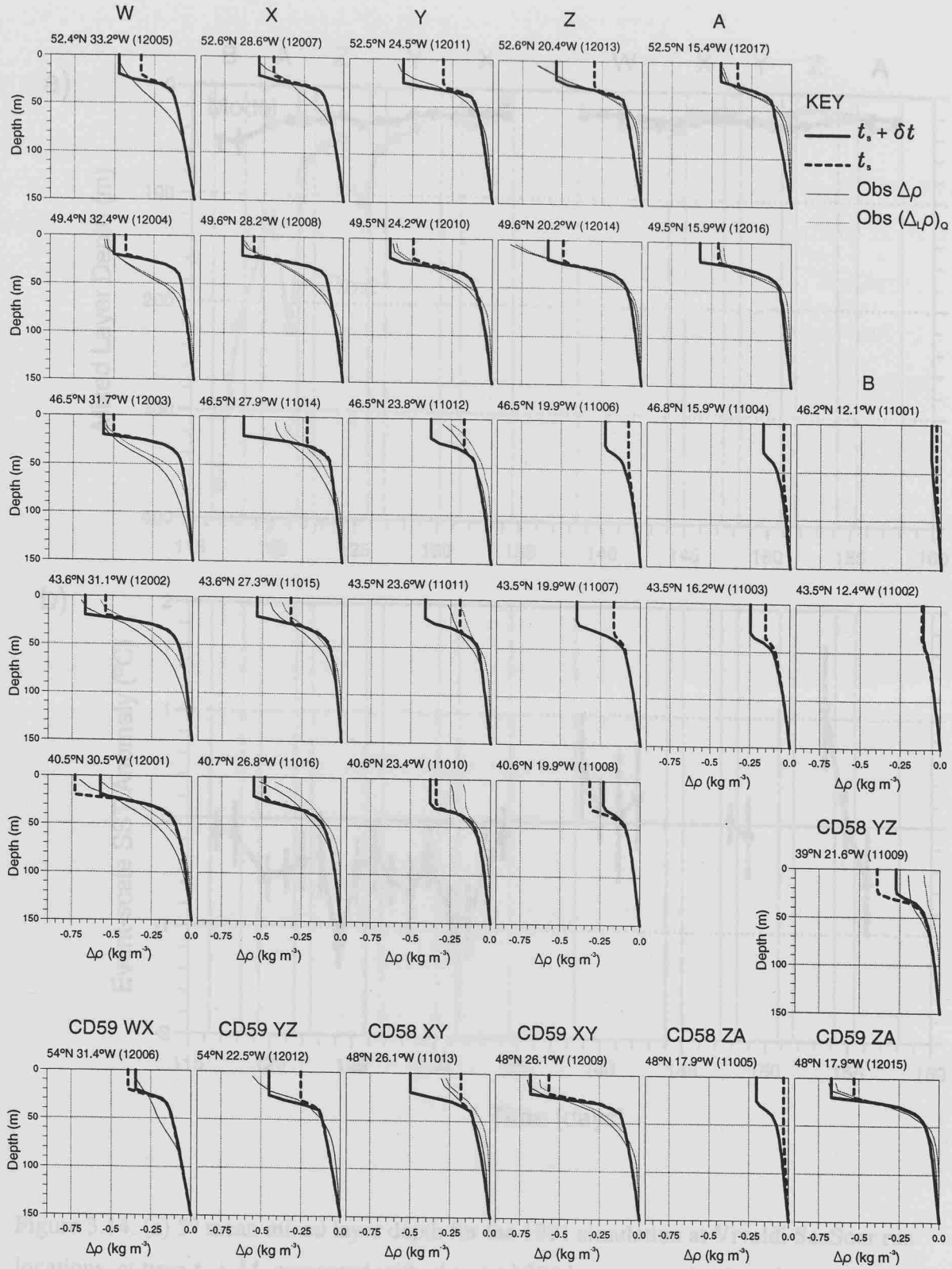

Figure 3.13. Profiles of 5° mean seasonal density anomaly against depth for the 1991 simulation, at Vivaldi SeaSoar run locations, at the time of sampling t_s and at $t_s + \delta t$. Observed 300 km mean profiles of $\Delta\rho$ and $(\Delta_L\rho)_Q$ are shown for comparison at locations where stratification is established.

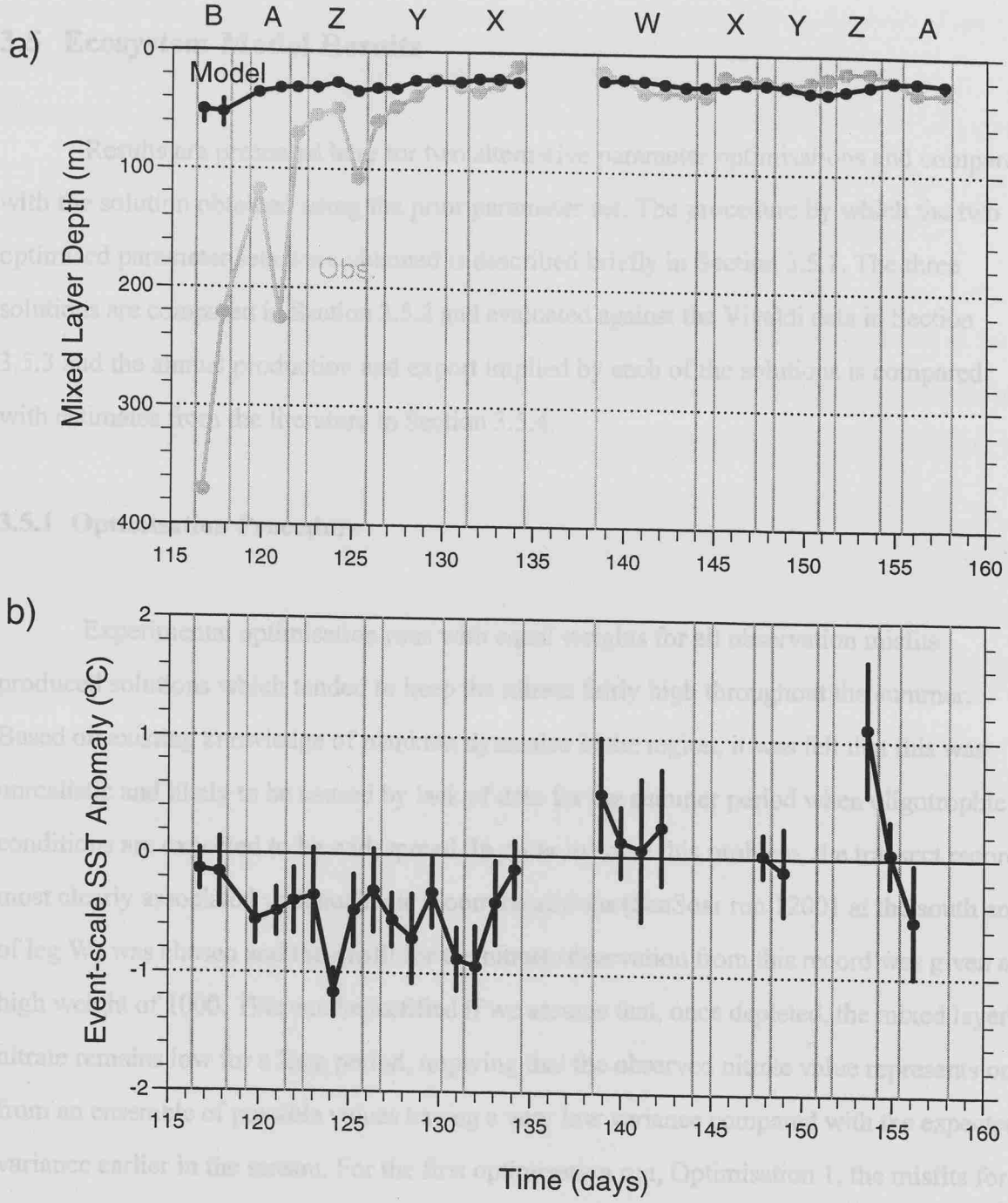

Figure 3.14. (a) 5° mean mixed layer depth for the 1991 simulation at Vivaldi SeaSoar run locations, at time $t_s + \delta t$, compared with observed 300 km mean value based on a density difference from the surface of 0.1 kg m^{-3}. Model 68% confidence intervals are shown based on error in the $\Delta\rho_{30}(0)$ estimate. (b) Observed event-scale SST anomaly $\delta T(0)$ with 95% confidence intervals.

3.5 Ecosystem Model Results

Results are presented here for two alternative parameter optimisations and compared with the solution obtained using the prior parameter set. The procedure by which the two optimised parameter sets were obtained is described briefly in Section 3.5.1. The three solutions are compared in Section 3.5.2 and evaluated against the Vivaldi data in Section 3.5.3 and the annual production and export implied by each of the solutions is compared with estimates from the literature in Section 3.5.4.

3.5.1 Optimisation Procedure

Experimental optimisation runs with equal weights for all observation misfits produced solutions which tended to keep the nitrate fairly high throughout the summer. Based on existing knowledge of plankton dynamics in the region, it was felt that this was unrealistic and likely to be caused by lack of data for the summer period when oligotrophic conditions are expected to be widespread. In order to solve this problem, the transect record most clearly associated with such late bloom conditions (SeaSoar run 12001 at the south end of leg W) was chosen and the misfit for the nitrate observation from this record was given a high weight of 1000. This can be justified if we assume that, once depleted, the mixed layer nitrate remains low for a long period, implying that the observed nitrate value represents one from an ensemble of possible values having a very low variance compared with the expected variance earlier in the season. For the first optimisation run, Optimisation 1, the misfits for all other observations were given an equal weighting of 1.

While the Optimisation 1 results gave a good fit to the nitrate data, they failed to simulate the large chlorophyll concentrations which were observed during the Vivaldi survey and another optimisation was carried out, Optimisation 2, with the addition of constraints that effectively forced the model to produce chlorophyll peaks at each location which were at least as high as those observed, although not at any particular time. These constraints

were specified by adding extra observations into the optimisation data set for each of the locations where observed chlorophyll was greater than 1 mg m^{-3}. These additional chlorophyll observations had the same values as the original observations but each was given a 3 month window covering the period from the beginning of April to the end of June. The misfits for these observations or constraints were given weights of 100. A preliminary optimisation run using the new constraints gave a very poor fit to the winter nitrate. The model tended to overestimate this in order to maintain reasonably high nitrate values at the observations times in the presence of larger blooms. The inherent variability in nitrate during the winter is expected to be much less than during the bloom and so it may be argued that it is more important to get a good fit to the pre-bloom nitrate, in a similar way that it is important to get a good fit during the summer period. In order to achieve this, higher weights of 100 were given to the pre-bloom nitrate misfits for Optimisation 2.

3.5.2 Comparison of Model Solutions

The three alternative parameter sets are shown in Table 3.2. In both of the optimisations, the nitrate is kept high by parameter settings which increase the ammonium inhibition of nitrate uptake. Optimisation 1 gave a very high ammonium inhibition parameter ψ, about 3.4 times greater than the prior value. For Optimisation 2, ψ is also increased but by a smaller factor of about 1.6. A 50% reduction in nitrate uptake is caused by an ammonium concentration of just 0.14 mmol m^{-3} in Optimisation 1 or 0.29 mmol m^{-3} in Optimisation 2, compared with 0.46 mmol m^{-3} if the prior parameter value is used. In the Optimisation 2 solution, much of the increase in ammonium inhibition is caused by higher concentrations of ammonium resulting from enhancement of the source terms: the zooplankton excretion is about 2.2 times higher than in the prior parameter set and the detrital breakdown is increased by a factor of about 5.6. While detrital breakdown is also increased in Optimisation 1, by 44%, zooplankton excretion in that optimisation is reduced to about half that in the prior parameter set. Uptake of ammonium is also reduced to some

extent, in both optimisations, by high half saturation constants: 0.40 in Optimisation 2 and 0.31 in Optimisation 1, as compared with 0.1 in the prior parameter set.

Other important features common to both optimised parameter sets are low phytoplankton mortality and high half saturation coefficients for nitrate. The former is reduced by 26% from the prior value in Optimisation 1 and by as much as 60% in Optimisation 2. The latter shows a similar increase in both optimisations: 86% in Optimisation 1 and 70% in Optimisation 2. Other notable changes from the prior parameter set seen in Optimisation 1 are a 37% increase in the initial slope of the P-I curve α, and a three-fold increase in the phytoplankton extinction coefficient k_p. These changes have opposing effects on phytoplankton growth rate. The significance of the high phytoplankton extinction coefficient, which is about 0.09 m^2 $(mmol\ N)^{-1}$, is appreciated if we consider that, for a phytoplankton concentration of 1 mmol N m^{-3}, it implies a change in the depth of the euphotic zone (defined by the 1% light level) from 65 m, using the prior parameter value, to 35 m. Such a high value for k_p is difficult to explain in terms of absorption by chlorophyll alone. Data compiled by Geider (1993) suggest a maximum specific absorption for chlorophyll of the order of 0.03 m^2 $(mg\ Chl)^{-1}$, occurring when phytoplankton cells are small with low intra-cellular chlorophyll concentrations (high C:Chl ratios), whereas the values of k_p and the nitrogen to chlorophyll conversion factor from Optimisation 1 give a chlorophyll *a* contribution to the attenuation coefficient for downward irradiance of 0.05 m^2 $(mg\ Chl)^{-1}$. This is not unrealistic if we consider that, in many situations, factors other than absorption by chlorophyll *a* make a major contribution to k_p. These include scattering of light and absorption by pigments other than chlorophyll *a* in phytoplankton cells, and by pigments present in other particles which tend to co-vary with phytoplankton biomass.

All other changes from the prior parameter set are less than 20%, with the exception of the horizontal nitrate gradients and the cross-pycnocline mixing rate *m*. Of these, a_x has only a small effect on nitrate availability and so is of minor importance. In Optimisation 1, the magnitude of a_y is reduced to about half that of the prior value. The sign of a_y is such as

to oppose the south to north increase in nitrate availability due to the salinity gradient and, while the reduction in a_y is offset slightly by the 8% reduction in the magnitude of a_S, these changes have a net effect of increasing the difference in nitrate availability at 50 m between the southern and northern ends of leg W from about 5.0 to 7.6 mmol m^{-3}. The pattern of nitrate availability in Optimisation 2 is very similar to that for the prior parameter set. Finally, we note that m is reduced to just 35% of its prior value in Optimisation 1 whereas in Optimisation 2 it is increased by 84%.

The solutions for nitrate and chlorophyll for each of the three parameter sets are shown in Figures 3.15 and 3.16. The solutions for the remaining state variables may be found in Appendix E. The rate of change in nitrate during the bloom differs greatly between the three solutions, with nitrate being depleted most quickly in the Prior solution (i.e. that for the prior parameter set) and least quickly in the Optimisation 1 solution. The picture is complicated though by the presence of 'ledges' at some locations where nitrate uptake is dramatically reduced for relatively short periods as a result of ammonium inhibition. These features are found only in the north-east where large peaks in ammonium concentration occur before the nitrate has been fully depleted (Figure E.6). They are more widespread in the Optimisation 1 solution because of the much higher ammonium inhibition parameter and the later depletion of nitrate.

Figure 3.16 shows clearly the absence of any major blooms for Optimisation 1, with the exception of those at 4 locations in the north-east part of the survey area. Elsewhere chlorophyll concentrations remain below 2 mg m^{-3} (equivalent to phytoplankton concentrations less than about 1 mmol N m^{-3}). The Prior solution tends to give very sharp blooms which are grazed away rapidly, which is consistent with the rapid depletion of nitrate in this solution. The magnitude of the blooms increases towards the north with the largest bloom in the far north-west (SeaSoar run 12006) reaching a chlorophyll concentration of 10 mg m^{-3} (6 mmol N m^{-3}). In Optimisation 2, the chlorophyll values before and after the bloom are comparatively high due to the low phytoplankton mortality. Ammonium is much more abundant and it inhibits uptake of nitrate, slowing its depletion. The persistence of

nitrate, along with the abundance of ammonium, allows production to remain relatively high for a longer period (Figure E.7). The blooms therefore appear much more spread out in time and double peaks also occur at a number of locations. Again the peak chlorophyll concentrations tend to increase towards the north, but in contrast to the Prior solution, by far the largest blooms are found in the north-east at locations on leg A, where the chlorophyll concentrations reach just over 16 mg m^{-3} (8 mmol N m^{-3}). Ammonium inhibition has a similar effect of slowing nitrate uptake and spreading the bloom out in time in Optimisation 1. However, in this parameter set, the phytoplankton mortality is nearly twice as great and pre-bloom populations are much lower. This, together with the strong self-shading effect due to the high phytoplankton extinction coefficient, reduces production throughout the bloom.

3.5.3 Evaluation of the Model Solutions Against Survey Data

The three model solutions are first evaluated against the Vivaldi data in terms of their misfit statistics and the extent to which they explain the observed variance in the state of bloom progression, as defined by the various measures introduced in Chapter 2. It is of course recognised that this is not a test of the model's predictive skill. Such a test can only be done against an independent data set not used in the parameter estimation procedure. In Chapter 2, evidence was presented which suggested higher rates of nitrate utilisation in the north of the survey area. A further more qualitative assessment of the model solutions is made with regard to their representation of such a phenomenon.

Figure 3.17a shows the model pre-bloom nitrate, defined as the winter-time maximum for each solution, compared with the observational estimate of pre-bloom nitrate at locations along the cruise track. It should be noted that the winter-time nitrate maximum is in some cases slightly different from the nitrate at the time of deepest mixing, which was the value compared with observed pre-bloom nitrate for optimisation purposes. The model nitrate and chlorophyll values corresponding to the observed nitrate and chlorophyll concentrations are shown in Figure 3.17b and 3.17c. These are the model values at the

optimum time within the observation window as described in Section 3.3. Misfit and correlation statistics are given in Tables 3.3 and 3.4. The mean misfit T_{obs}/n, where n is the number of observations, is shown for the whole data set and for each variable independently. The tabulated misfits are unweighted and are therefore directly comparable.

All three solutions give a good fit to the estimated pre-bloom nitrate at the sampling locations. The main differences between the solutions concern how well they fit the observations during the survey period. The Prior solution gives a very poor fit to the nitrate data, the nitrate being fully depleted in all but three locations, two on CD58 B at the beginning of the survey and the other corresponding to CD59 WX in the far north-west corner. Ironically though it gives the best fit to the chlorophyll data, both in terms of the mean misfit and the extent to which it explains the variance in these data. Optimisation 1 gives the best overall fit, giving a particularly good fit to the nitrate observations. 72% of the variance in observed nitrate is explained by this solution. However, it fails dramatically to reproduce the observed variance in chlorophyll. Just 3% is explained by the model solution. Optimisation 2 still gives a relatively good fit to nitrate and explains 54% of the variance in the observations. While the fit to chlorophyll is worse than that for Optimisation 1, being biased high over most of the survey, this solution does explain more of the variance (20%) as it manages to reproduce the peaks and troughs in the latter part of the survey. The main problem with the Optimisation 2 solution is its tendency to over-estimate chlorophyll throughout most of the survey, in particular in the areas in the south-east, in the middle part of the survey, where the observed values are very low.

In general, it appears that the model is capable of doing a better job of explaining the variance in nitrate than in chlorophyll. While there are many possible reasons for this, one of the most obvious sources of error is the use of a constant conversion factor between phytoplankton nitrogen and chlorophyll. A modelling study by Taylor *et al.* (1997), designed to show how the C:Chl *a* ratio might vary with latitude and season according to the physiological model of Geider *et al.* (1997), shows a doubling of the ratio between April and June at 47°N, while the increase further south at 35°N is about four-fold. Similar changes

might be expected in N:Chl *a* and are likely to make an important contribution to the observed variance in chlorophyll. Hurtt and Armstrong (1996) found the inclusion of a variable N:Chl *a* ratio to be important for the purposes of simulating the annual cycle at Bermuda.

The model results for each of the three bloom progression measures are shown in Figure 3.17d-f and the corresponding variance explained by each of the model solutions is given in Table 3.4. That explained by the observed seasonal density anomaly, as discussed in Chapter 2, is shown for comparison. The high correlation between nitrate utilisation in the Prior solution and the observed nitrate utilisation is a rather misleading result as it simply reflects the correlation between nitrate utilisation and pre-bloom nitrate in the observational data set. The correlation for the corresponding R_N is very low ($r^2 = 0.08$). It is encouraging that, with the exception of the Prior solution, the model explains more of the variance in the two measures of nitrate utilisation than is explained by the seasonal density anomaly. This is not so for R_P, but R_P was more closely correlated with the seasonal density anomaly than the other two variables. The comparison for nitrate utilisation shows some features which were not apparent in the nitrate comparison. In particular, we can see that Optimisation 1 underestimates nitrate utilisation by up to 50% or more in some areas, while Optimisation 2 tends to give an over-estimate. Optimisation 1 explains less of the variance in nitrate utilisation than in nitrate and it is interesting to note that, while this solution was the best at explaining the variance in nitrate, Optimisation 2 actually explains slightly more of the variance in nitrate utilisation than Optimisation 1.

The form of the variation in R_P which we might expect during the bloom is less intuitively obvious than for the measures of nitrate utilisation. The time series given by each of the model solutions are shown in Figure 3.18. We can see from this that our assumption that it increases monotonically is true for the model over most of the survey area but is violated at certain locations in the north and east, where as already noted the presence of high levels of ammonium tends to slow the nitrate uptake. At the same time regenerated production increases, leading to higher phytoplankton concentration without much of a

change in nitrate utilisation and so R_P drops. This highlights the necessity for caution when interpreting observational values of this particular measure of bloom progression.

As discussed in Chapter 2, the survey results show a clear south to north gradient in nitrate utilisation across the northern part of the survey area, possibly associated with that in the pre-bloom nitrate concentration. This appears to have developed while nitrate concentrations were still fairly high (more than about 3 mmol m^{-3}), assuming that the changes in mixed layer nitrate concentration prior to sampling were more or less monotonic, and was interpreted as possible evidence of a higher rate of nitrate utilisation in the north. It is useful then to investigate whether this feature occurs in the model solutions.

The rate of nitrate utilisation in the model ($-d\Delta N/dt$) is the difference between new production and the import of nitrate into the mixed layer due to physical processes. The latter is much smaller in the model than the new production, reaching a maximum of around 0.1 mmol m^{-3} d^{-1} in late June in Optimisation 2. During the bloom itself it is negligible, only starting to become important as nitrate is depleted. An approximate equivalence between nitrate utilisation rate and new production is therefore assumed and the spatial patterns of new production in each of the solutions are examined here. These patterns are presented in Figure 3.19, which also shows for comparison the corresponding patterns of pre-bloom nitrate, as represented by the winter nitrate maximum in the model simulations. The maps are based on model output for locations on a 1° grid and the mean and maximum values of new production are those for the period over which the model nitrate utilisation is between 1 and 6 mmol m^{-3}. This excludes the effect of nitrate limitation in the Liebig sense (i.e. limitation of stock as opposed to growth rate) for areas where the pre-bloom nitrate is greater than 6 mmol m^{-3}, including the whole of the region of interest which lies above about 45°N.

While the magnitude of the new production in the Optimisation 1 solution is generally rather less than that for Optimisation 2, the dominant spatial pattern is similar. In

both, the highest values of both mean and maximum new production are found in the far north, in the eastern half of the study area and a lesser spatial maximum is apparent between 50 and 52°N at about 32°W, although the maximum in mean new production for optimisation 2 lies a little to the north-east of this. New production is comparatively low in the south. The maps for the Prior solution however show that these latitudinal differences are not an entirely general feature of the model behaviour in response to the environmental forcing, but are more likely to be a consequence of the optimisation to the Vivaldi data. While the maximum values in the Prior solution are still found in the north, spatial maxima in the mean new production are more widely distributed, with a ridge running all the way down the western part of the study area, in addition to patches in the far north. Other features of interest in the mean new production patterns are a definite east to west increase in the south of the study area, seen in both the Prior and Optimisation 2 solutions, and a band of very low values from about 30°W in the far north to about 45°N in the far east, seen in all three solutions. These features are discussed in more detail in the next section. Evidence in the model solutions for association of high new production with high levels of pre-bloom nitrate, as suggested by the analysis of the survey data, is at best tenuous.

In conclusion, no single solution stands out as the best solution on all counts. With regard to assessing the ability of the 5 compartment mixed layer ecosystem model to successfully simulate the ecological variability across the survey area with a single parameter set, these results are rather inconclusive because it is unclear how much of the misfit to attribute to deficiencies in the model and how much to noise in the data and inaccuracies in the forcing. The observational data set is very limited for the purposes of such an evaluation, both because of its small size in relation to the number of parameters in the model and because of the absence of data for the inter-compartmental flows and for three out of the five state variables, causing zooplankton and detritus parameters to be rather poorly determined. In the context of statistical inference, the effective size of the data set is even smaller because any noise signal is likely to be autocorrelated along the cruise track, which means that individual observations cannot be regarded as independent.

The potential problems associated with noise in the data should not be underestimated. For example, in the early part of the survey, where the mixed layer is very deep and the mixed layer depth anomaly with respect to the physical simulation is large (Figure 3.14), it is particularly unclear how the concentrations of nitrate and chlorophyll observed at the surface relate to their variation at the seasonal time scale. If the deep mixed layers are a symptom of some short-term change in weather conditions as has been suggested, then we must suspect a distortion of the seasonal variation in mixed layer concentrations as a result, and the amplitude of the noise term could be very large. If, for example, we were to assume that the model mixed layer depth was a good representation of the seasonal variation and that the chlorophyll concentration below the mixed layer was negligible, then the observations of mixed layer depth around 6 times greater than those of the model might suggest a 6-fold dilution of mixed layer chlorophyll. In reality, the extent of the sampling error will depend on the vertical profile of each variable, immediately before the event, on which we have no information.

While it is very difficult to quantify the noise inherent in the biogeochemical observations, it may be inferred that event-scale variability is likely to cause a low bias to chlorophyll and a high bias to nitrate where the event-scale temperature anomaly is significantly negative (during most of CD58 and at the south end of CD59 A) and, conversely, a high bias to chlorophyll and a low bias to nitrate where it is significantly positive (at the south end of CD59 W and the south end of CD59 Z). The domination of the event-scale anomaly distribution by negative temperature anomalies suggests that short periods of relatively cool and/or windy weather may have occurred over much of the survey area prior to sampling, potentially biasing the optimisation results. This serves to underline the need for more independent data if unambiguous results are to be obtained.

3.5.4 Ecological Implications of the Model Solutions

In this section the ecological implications of the different model solutions are examined with regard to the annual cycles of primary production and the export flux of particulate organic nitrogen (PON). The results for each are compared with estimates for the study area from the literature, based on observational data.

Figure 3.20 shows maps of annually integrated areal primary production for each solution, together with the corresponding maps of new production and the *f*-ratio. The model estimate of areal production is the product of the production per unit volume and the mixed layer depth. In all solutions, total production and new production are both higher in the north, with maxima in the far north-west, where the nitrate availability is greatest. The *f*-ratio maps for each also show similar patterns with the highest annual *f*-ratios being found in the north-east where winter mixing is deepest. While the total production shown by the Prior and Optimisation 2 solutions is broadly similar, that implied by the Optimisation 1 solution is much lower, generally less than half that for the other solutions. New production is similarly low. This low productivity occurs as a result of light limitation, caused by the large value for the phytoplankton self-shading coefficient, and strong inhibition of nitrate uptake by ammonium, even at low concentrations. Some differences between the Optimisation 2 and Prior solutions are also noted, in particular the lower primary production minima in the east in the Prior solution and the generally lower new production and *f*-ratio in Optimisation 2.

The annual primary production cycles are shown at intervals on a 5° grid in Figure 3.21. All solutions show a gradual northward transition between the typical form for the westerlies biogeochemical domain and a form closer to that of the polar domain (Longhurst, 1995). The more southerly cycles show maxima associated with spring and autumn blooms with a nutrient limited period of low production during summer, while in the north-west, where nutrients are not seriously depleted and light limitation is the dominant control, the

optimised solutions show a summer maximum. In the Prior solution though, which generally shows much sharper spring peaks in production, there is a significant nutrient-limited summer-time low even here.

Sathyendranath *et al.* (1995) present annual primary production estimates for the North Atlantic Basin derived from 1979 Coastal Zone Colour Scanner data for phytoplankton biomass, using pigment profiles and P-I curves compiled from *in situ* data for different biogeochemical provinces in conjunction with surface PAR estimates. The pattern shown by their results for the area in this study is similar to the results presented here to the extent that it shows a clear maximum in the north-west, although there also appears to be an east to west gradient in the south which is not seen in Figure 3.20. The magnitude of the annual production in the north-west (50-55°N) is around 400 g C m^{-2} y^{-1}, equivalent to about 5 mol N m^{-2} y^{-1} (assuming carbon and nitrogen are assimilated at the Redfield ratio of 106:16). This is comparable with the values for the Prior and Optimisation 2 solutions. However, the decrease in the south and east is much more pronounced, with minimum values of around 120 g C m^{-2} y^{-1} (1.5 mol N m^{-2} y^{-1}) at about 40°N, closer to the Optimisation 1 productivity. Results determined by the same method from an 8 year CZCS climatology (Longhurst *et al.*, 1995) are similar to the 1979 results. The minimum values in the south appear to be a little higher though, between about 130 and 150 mol N m^{-2} y^{-1}, but this may be largely an artefact of the lower resolution used in the presentation. Sathyendranath *et al.* (1995) also present results based on their earlier method (Platt *et al.*, 1991b) where regions were determined according to latitude and ocean depth. These results show a similar maximum to that for the "biogeochemical provinces" method but a larger minimum, between 160 and 200 g C m^{-2} y^{-1} (2 and 2.5 mol N m^{-2} y^{-1}), which is closer to the Prior and Optimisation 2 results but still suggests they might be a little high, at between 3 and 4.5 mol N m^{-2} y^{-1}.

Primary production measured during the 1989 spring bloom at 47°N 20°W ranged from about 50 to 150 mmol C m^{-2} d^{-1} (Lochte *et al.*, 1993). This is equivalent to about 220 -

660 g C m^{-2} y^{-1}, the maximum being at least 3 times the annual mean estimated from CZCS data at this location. The equivalent nitrogen fluxes, for comparison with Figure 3.21, are 8 to 23 mmol N m^{-2} d^{-1}. This range is similar to that shown by Optimisation 2, which has a peak of about 30 mmol N m^{-2} d^{-1}. The maximum in the Optimisation 1 solution is rather low, compared with the 1989 data, at between 10 and 15 mmol N m^{-2} d^{-1}, while the Prior is over twice as high, at just over 60 mmol N m^{-2} d^{-1}.

Large scale estimates of new production are more problematical and are often based on total primary production estimates (e.g. Eppley and Peterson 1979). Strass and Woods (1991), however, estimated new production from transect data collected between 30 and 40°W from the Azores (39°N) to the polar front (52°N). These estimates were based on findings regarding the rate of deepening of the deep chlorophyll maximum, and therefore the nutricline, in the summer oligotrophic regime, which allowed the volume of nitrate depleted water at the end of summer to be estimated. This was then used in conjunction with estimates of winter-time nitrate concentration to determine new production integrated over the heating season to the end of August. Campbell and Aarup (1992) extended this approach, using CZCS data to provide basin scale estimates of annual new production which were independent of total primary production estimates. Strictly speaking, this method gives only the spring and summer production and therefore, as acknowledged by the authors, is almost certain to give low estimates for annual production. Their estimates and those of Strass and Woods do however provide a plausible lower bound for annual new production.

The Strass and Woods estimates are between 30 and 40 g C m^{-2} y^{-1} (0.4 and 0.5 mol N m^{-2} y^{-1}) for latitudes north of about 44°N, increasing gradually northward at about 0.6 g C m^{-2} y^{-1} per degree. South of 44°N the northward gradient is much steeper and at 39°N new production is only about 15 g C m^{-2} y^{-1} (0.2 mol N m^{-2} y^{-1}). A similar but less dramatic change in gradient is seen in all three model solutions presented here. The Campbell and Aarup values are about 10 to 15 g C m^{-2} y^{-1} higher than the Strass and Woods values at the

same latitude, this difference being explained by the different winter nitrate estimates used. Strass and Woods used the Glover and Brewer (1988) estimates, while Campbell and Aarup used an empirical relationship to derive winter nitrate from the annual maximum chlorophyll. These higher estimates for new production are equivalent to about 0.6 mol N m^{-2} y^{-1} in the middle of the western part of the study area, a little lower than the Optimisation 1 values and a factor of about 2 and 3 lower than Optimisation 2 and Prior values respectively.

Inspection of the annual cycles of new production for this part of the study area (Figure 3.22) shows that a significant amount of new production occurs during winter and for Optimisation 2 the April-August production is only about half the production for the whole year, implying that this solution is more or less compatible with the Campbell and Aarup estimate. In contrast, the Optimisation 1 solution gives rather low values and the values for the Prior solution are rather high to explain in this way. The Optimisation 2 values are also closest to values estimated by Yentsch (1990) for the 40°W meridian, just west of the study area, using a simple light-nutrient model. This gave values of about 0.6 mol N m^{-2} y^{-1} at 40°N, increasing to a maximum of about 1.4 mol N m^{-2} y^{-1} at 50°N and then decreasing slightly to about 1.2 mol N m^{-2} y^{-1} at 60°N. The annual cycles of *f*-ratio (Figure 3.23) for all solutions exhibit a high degree of variability, indicating a rather unstable balance between new and regenerated primary production, especially in the north where some particularly dramatic changes in *f*-ratio occur in spring.

Figure 3.24 shows the annual export flux of particulate organic nitrogen (PON) for each of the model solutions. This is very similar to the new production, especially for the Optimisation 1 solution, which is unsurprising as total export must equal new production in a steady state annual cycle and the only other export flux in the model is that due to the detrainment and diffusive mixing of ammonium. For the other solutions, the particulate export is up to 20% less than the new production in some areas, due to the accumulation of higher concentrations of ammonium than in Optimisation 1. The particulate export is much

higher in these solutions than in Optimisation 1, reflecting the differences in production already noted. Comparison between the Optimisation 2 and Prior solutions shows a 50% higher export flux in the south for the Prior solution, while the values in the north are very close. The difference in the south is more pronounced than the difference in new production.

Data from sediment traps deployed during the 1989 bloom at 47°N 20°W indicate average PON export rates from the upper 35 m for the study period (late April to the beginning of June) of 6.8 mmol N m^{-2} d^{-1} (Martin *et al.*, 1993). The Optimisation 1 solution shows export fluxes closest to this during the bloom. Those for the other solutions are a little higher but certainly of the same order of magnitude. Comparison between the 1989 export fluxes and primary production (Lochte *et al.*, 1993) suggested an *f*-ratio for the study period of about 0.45, which is a little higher than that shown by all the model solutions during most of the bloom period (Figure 3.23).

The comparisons presented in this section show that the production and export fluxes for all of the model solutions are within reasonable bounds, given the level of uncertainty in the observational estimates. While it was concluded in the previous section that none of the solutions could be considered obviously better than the others, there are clearly important differences in the ecology implied by the different model parameter sets and so, before such a model could be used to make useful ecological predictions, further evaluation work would be necessary using a more comprehensive data set.

Table 3.2. Parameter sets for each of the model solutions.

Parameter	Symbol	Units	Prior	Opt. 1	Opt. 2
phytoplankton mortality rate	ϕ_P	d^{-1}	0.05	0.037	0.019
nitrate uptake half-saturation constant	k_1	mmol m^{-3}	0.5	0.93	0.85
ammonium uptake half-saturation constant	k_2	mmol m^{-3}	0.1	0.31	0.4
nitrate uptake ammonium inhibition parameter	ψ	$(mmol\ m^{-3})^{-1}$	1.5	5.1	2.4
initial slope of P-I curve	α	$(W\ m^{-2}\ d)^{-1}$	0.05	0.069	0.05
light attenuation coefficient for phytoplankton	k_p	$m^2(mmol\ N)^{-1}$	0.03	0.09	0.031
phytoplankton maximum growth rate	V_P	d^{-1}	1.5	1.72	1.37
zooplankton excretion rate	m	d^{-1}	0.1	0.054	0.223
zooplankton mortality parameter	ϕ_Z	$(mmol\ N\ m^{-3}\ d)^{-1}$	0.2	0.205	0.167
zooplankton maximum ingestion rate	g	d^{-1}	1	1	1
zooplankton ingestion half-saturation constant	k_3	mmol N m^{-3}	1	1	0.95
zooplankton feeding preference for phytoplankton	p_1		0.5	0.5	0.43
detrital breakdown rate	ϕ_D	d^{-1}	0.05	0.073	0.278
sub surface nitrate at reference point	a_o	mmol m^{-3}	7.7	6.8	7.5
longitudinal nitrate gradient	a_x	mmol m^{-3} deg^{-1}	-0.01	0.012	0.005
latitudinal nitrate gradient	a_y	mmol m^{-3} deg^{-1}	-0.47	-0.225	-0.47
nitrate gradient against salinity	a_S	mmol m^{-3}	-9.3	-8.5	-9.5
cross-pycnocline mixing rate	m	m d^{-1}	0.2	0.071	0.367
nitrogen to chl. conversion factor (Chl *a*:N)	χ_c	mg $mmol^{-1}$	1.67	1.82	1.96

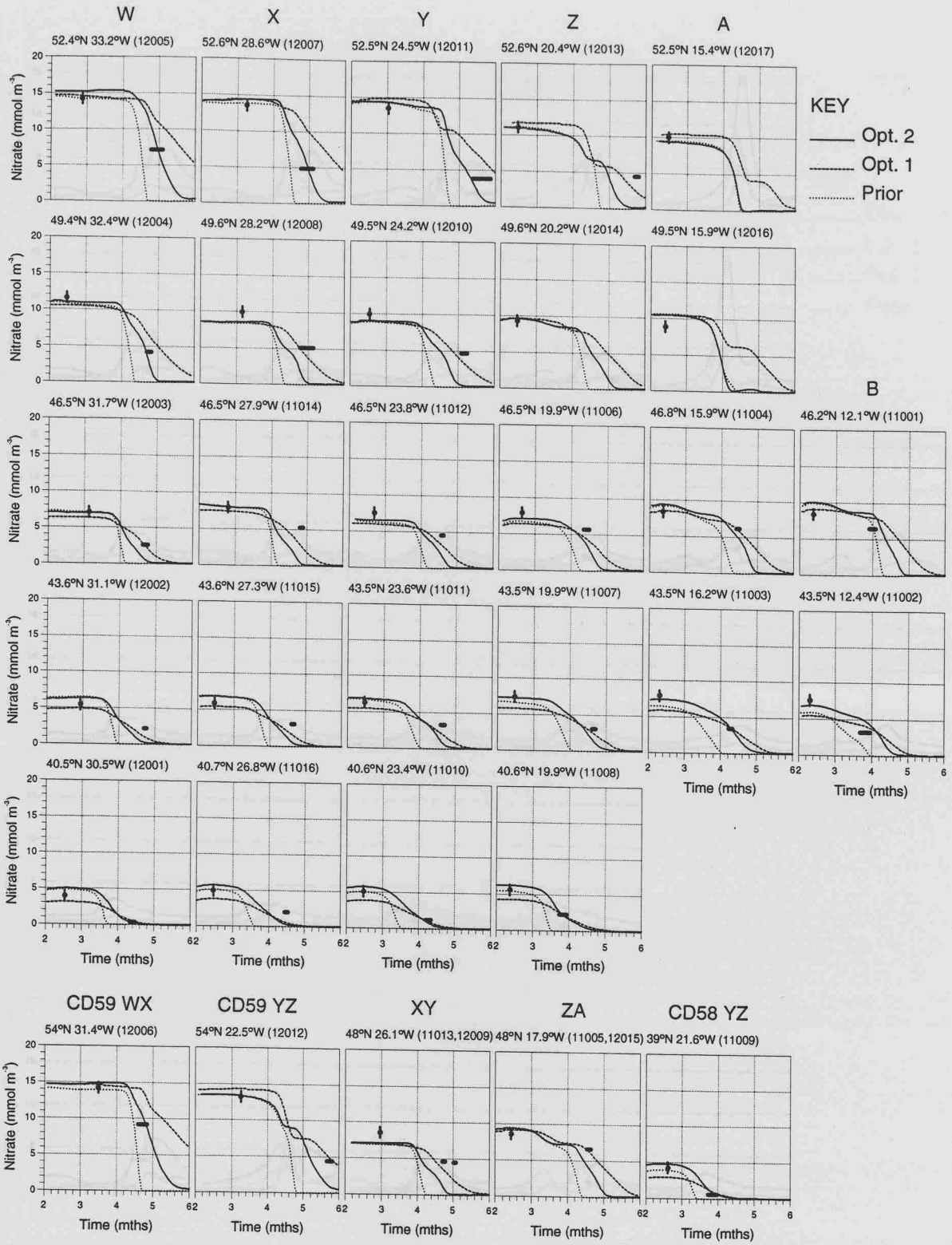

Figure 3.15. Model solutions for nitrate, from March to June 1991, at Vivaldi SeaSoar run locations, showing observations used in the parameter optimisations. Temporal windows for time-of-sampling observations reflect 68% confidence intervals for $\Delta\rho_{30}(0)$ estimate. Error bars for pre-bloom nitrate estimates also show 68% confidence intervals.

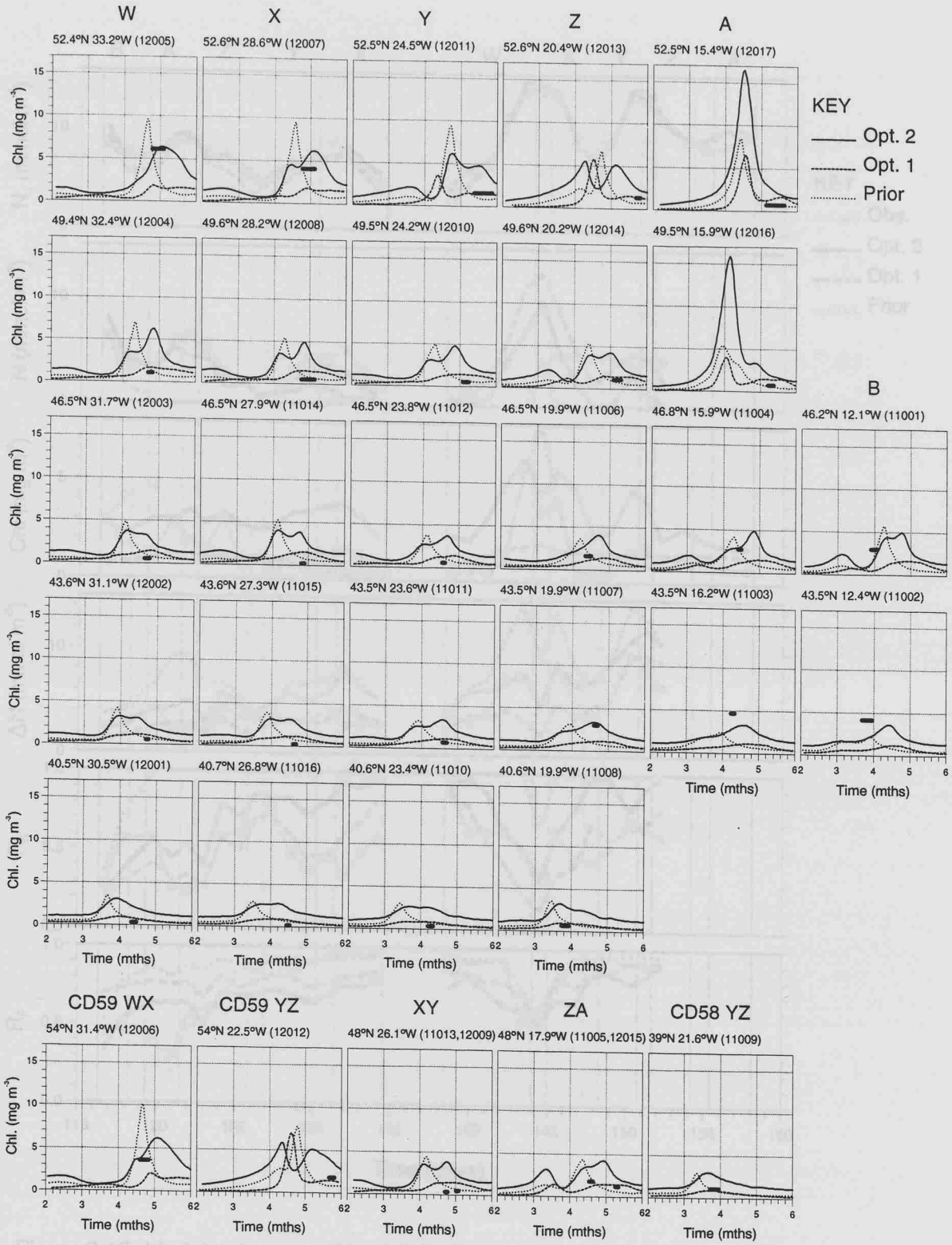

Figure 3.16. Model solutions for chlorophyll a, from March to June 1991, at Vivaldi SeaSoar run locations, showing observations used in the parameter optimisations. Temporal windows for time-of-sampling observations reflect 68% confidence intervals for $\Delta\rho_{30}(0)$ estimate.

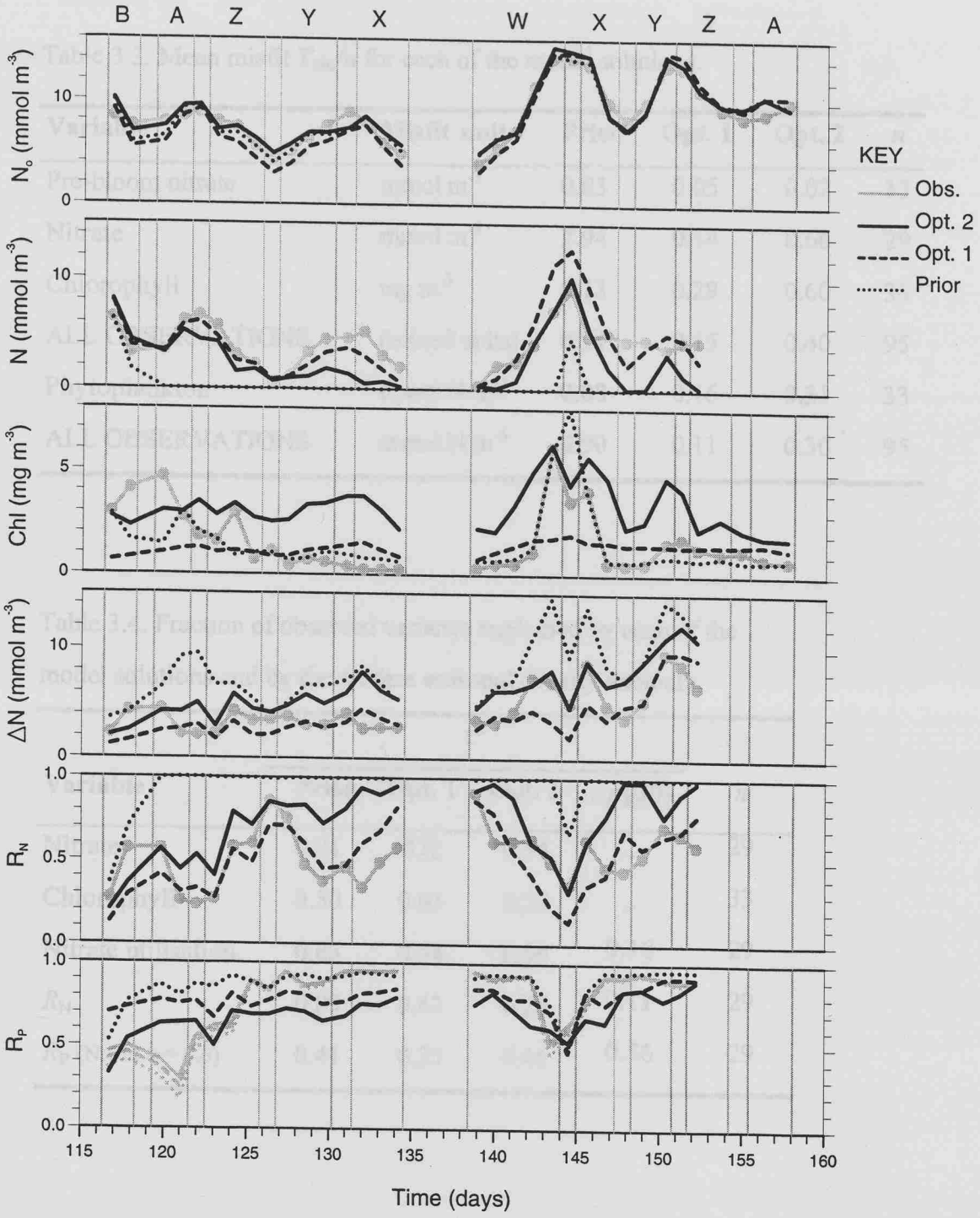

Figure 3.17. Model solutions at Vivaldi SeaSoar run locations for (a) pre-bloom nitrate N_o, (b) nitrate, (c) chlorophyll a and model derived values for (d) nitrate utilisation ΔN, (e) fractional nitrate utilisation R_N and (f) fraction of nitrate utilisation unaccounted for by standing stock R_P. Observed 300 km mean values are shown for comparison. With the exception of pre-bloom nitrate, the model values are those at the time of least misfit (to nitrate and chlorophyll) within the observation windows.

Table 3.3. Mean misfit T_{obs}/n for each of the model solutions.

Variable	Misfit units	Prior	Opt. 1	Opt. 2	*n*
Pre-bloom nitrate	mmol m^{-3}	0.03	0.05	0.02	33
Nitrate	mmol m^{-3}	2.94	0.14	0.66	29
Chlorophyll	mg m^{-3}	0.13	0.29	0.60	33
ALL OBSERVATIONS	(mixed units)	0.91	0.15	0.40	95
Phytoplankton	mmol N m^{-3}	0.08	0.16	0.31	33
ALL OBSERVATIONS	mmol N m^{-3}	0.90	0.11	0.30	95

Table 3.4. Fraction of observed variance explained by each of the model solutions and by the surface seasonal density anomaly.

	r^2				
Variable	**Prior**	**Opt. 1**	**Opt. 2**	$\Delta\rho_{30}(0)$	*n*
Nitrate	0.21	072	0.54	–	29
Chlorophyll	0.50	0.03	0.20	–	33
Nitrate utilisation	0.63	0.54	0.59	0.16	29
R_N	0.09	0.42	0.25	0.11	29
R_P (N:Chl a = 0.6)	0.41	0.25	0.45	0.56	29

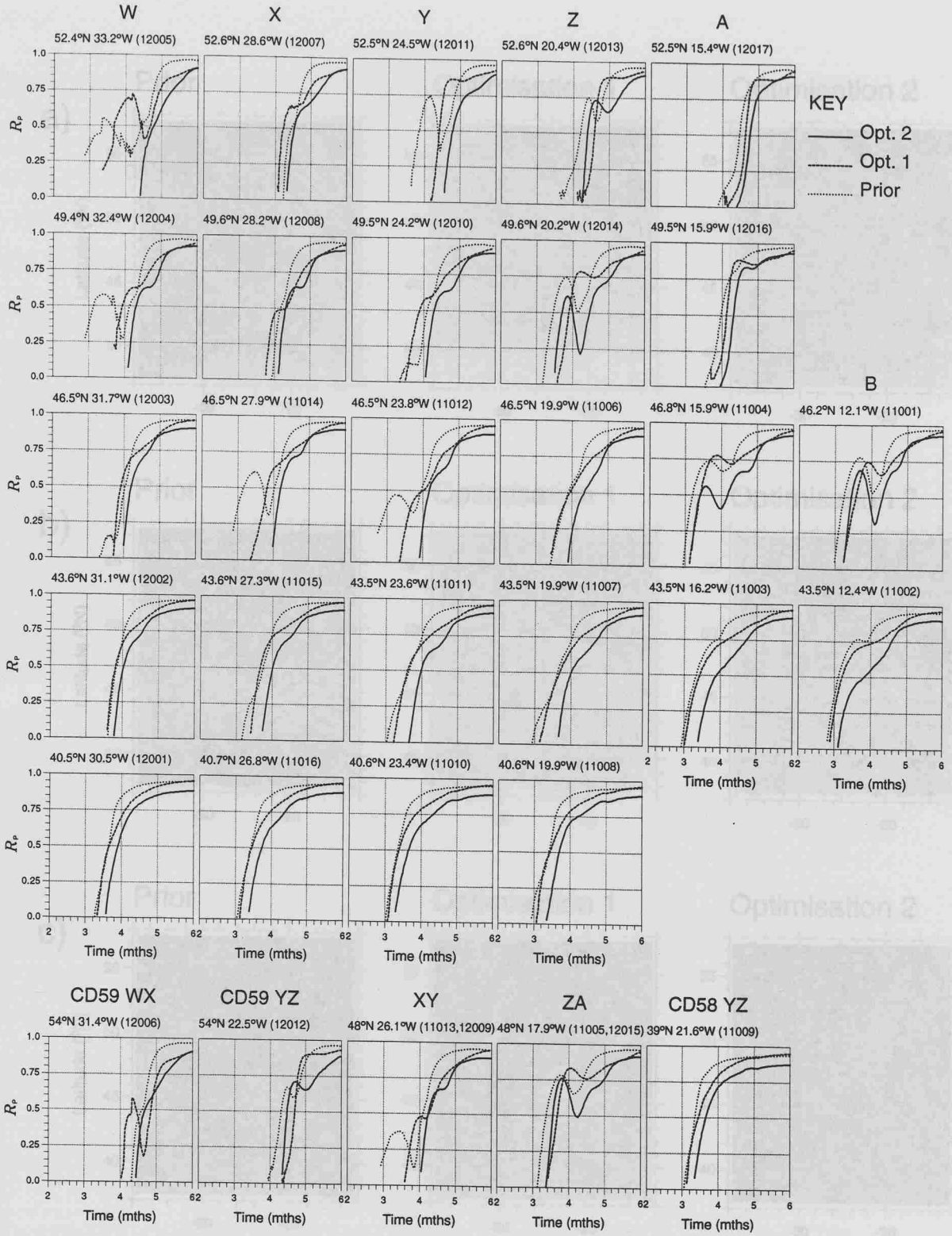

Figure 3.18. Model time series of R_P, the fraction of nitrate utilisation unaccounted for by standing stock, from March to June 1991, at Vivaldi SeaSoar run locations.

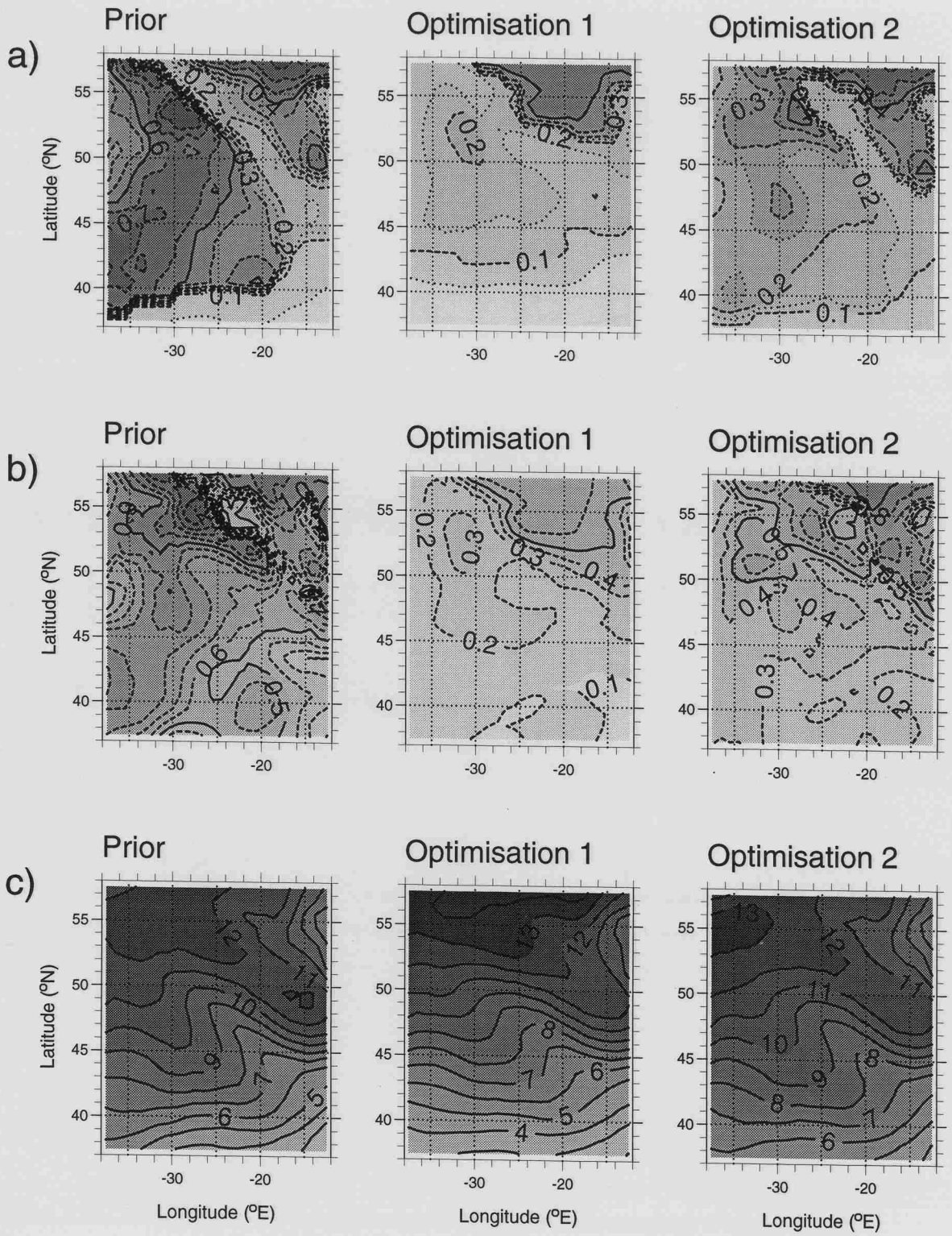

Figure 3.19. (a) Mean and (b) maximum new production (mmol N m^{-3} d^{-1}) for each of the 1991 model solutions over the period during which nitrate utilisation is between 1 and 6 mmol m^{-3}. (c) Model pre-bloom nitrate (mmol m^{-3}).

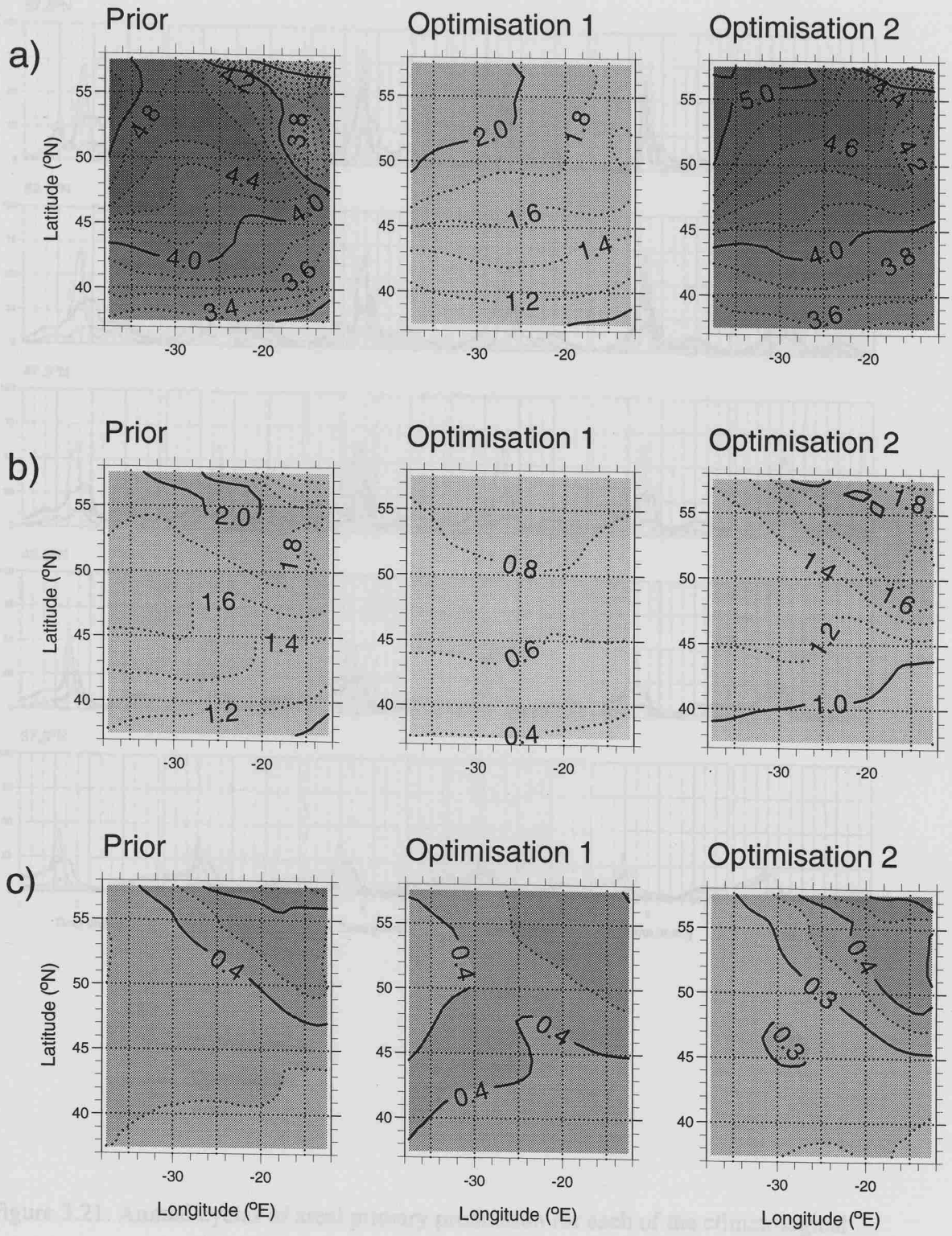

Figure 3.20. (a) Annual areal primary production and (b) new production (mol N m^{-2} y^{-1}) and (c) annual f-ratio for each of the climatological model solutions.

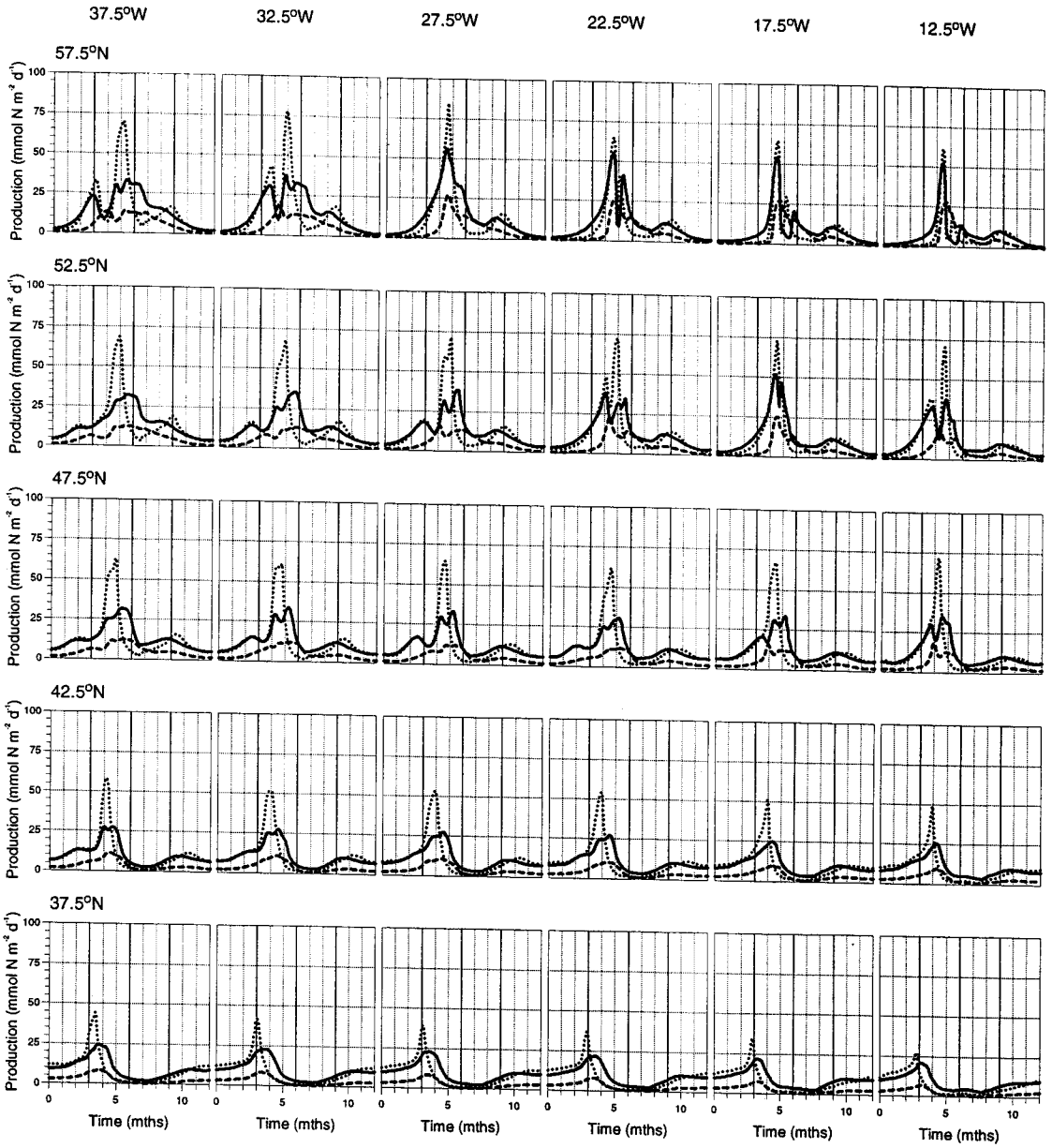

Figure 3.21. Annual cycles of areal primary production for each of the climatological model solutions at 5° intervals.

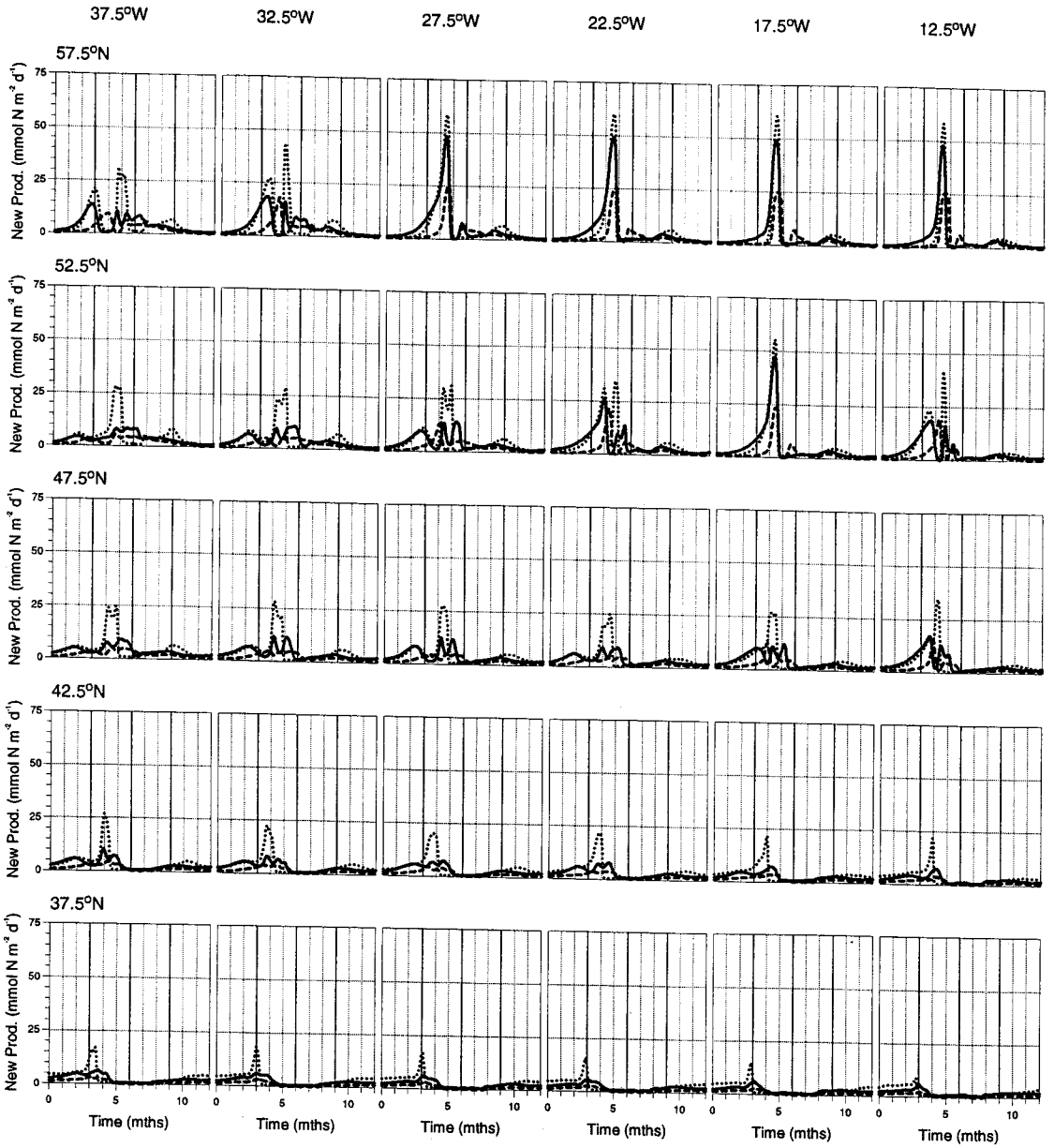

Figure 3.22. Annual cycles of areal new production for each of the climatological model solutions at 5° intervals.

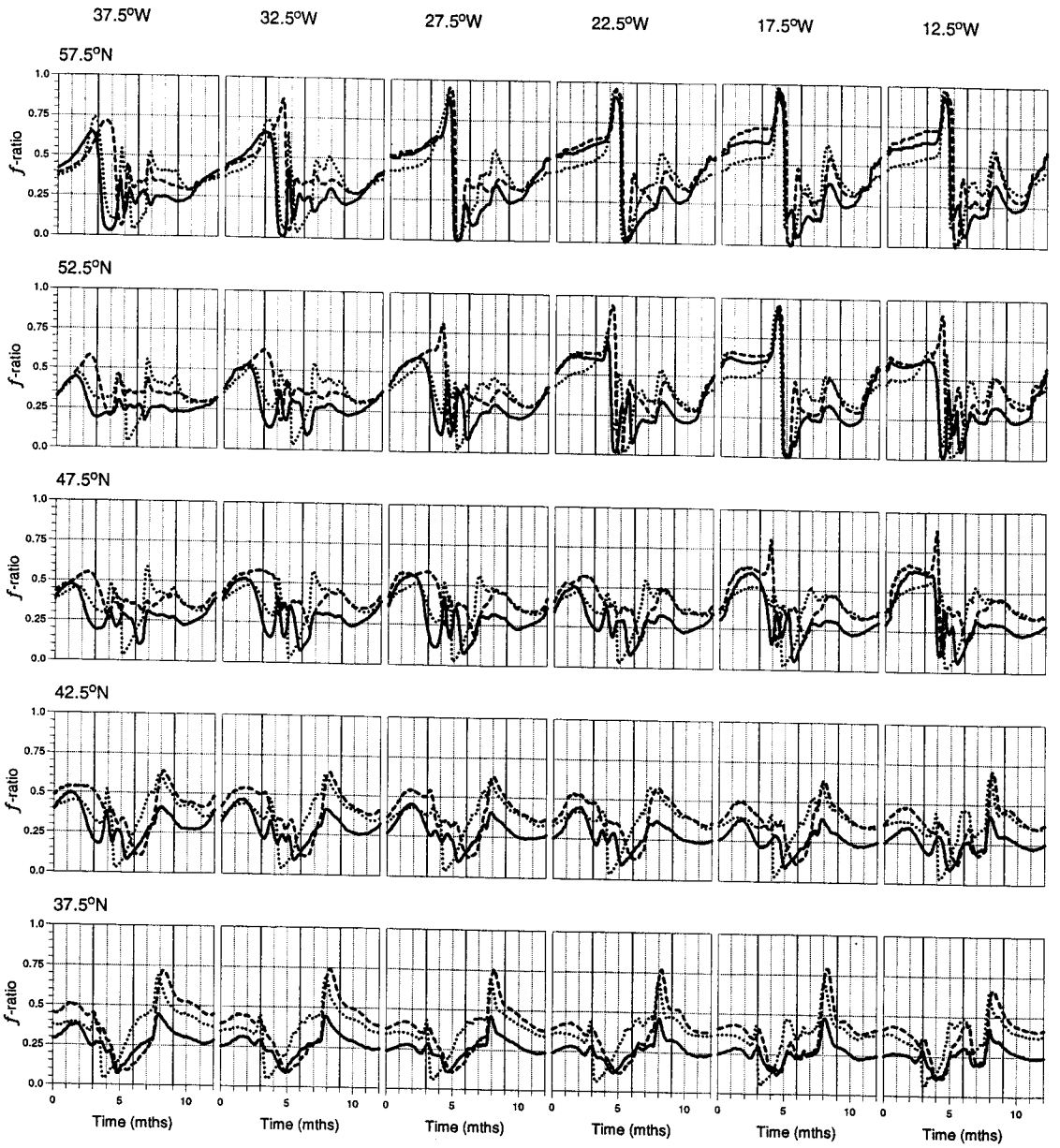

Figure 3.23. Annual cycles of f-ratio for each of the climatological model solutions at 5° intervals.

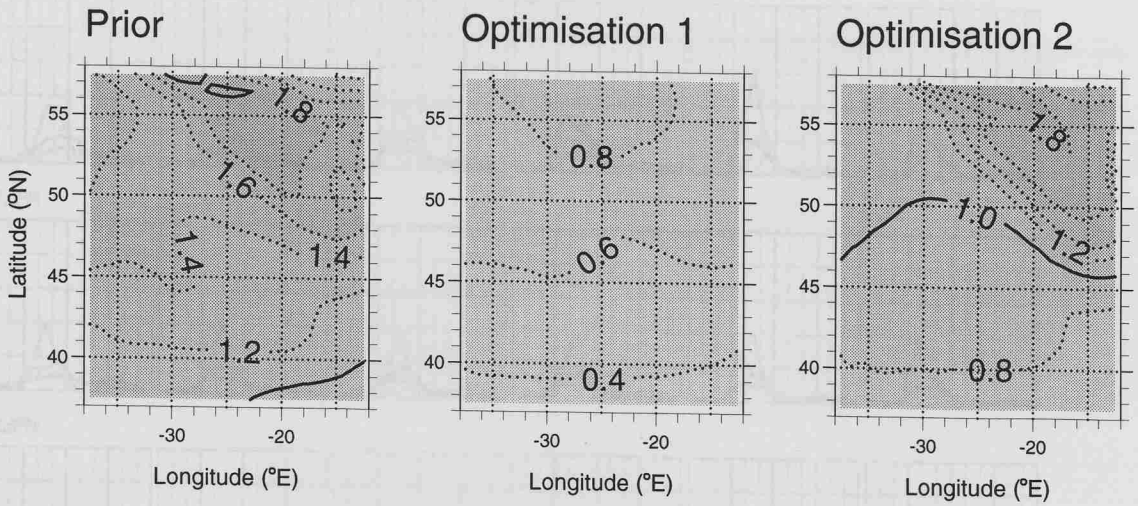

Figure 3.24. Annual PON export (mol N m^{-2} y^{-1}) for each of the climatological model solutions.

Figure 3.25. Annual cycles of PON export for each of the climatological model solutions at 5° intervals.

3.6 Spatial Pattern of Bloom Development

In this section, the spatial variability of the phytoplankton bloom in the model is examined over the four month period from March to June, using results from the 1991 simulation with the Optimisation 2 parameter set. This parameter set was chosen as the preferred of the two optimised parameter sets because of the absence of large blooms in the Optimisation 1 solution and its extremely poor performance with regard to explaining the variance in the Chlorophyll observations. While we hope to gain some insight from this analysis into factors of potential importance in controlling spatial variability in the spring bloom, it must be interpreted as the response of a notional ecosystem to the variability in environmental conditions within the study area, rather than a realistic simulation of the 1991 bloom.

The patterns of plankton populations in the winter-time mixed layer, before bloom initiation, are discussed in Section 3.6.1, before going on to examine the development of the bloom itself, in Section 3.6.2. In order to aid interpretation of the nitrate utilisation patterns in the survey data, the importance of different factors in the determination of new production and nitrate utilisation is further investigated in Section 3.6.3.

3.6.1 Over-wintering Plankton Populations

Deepening of the mixed layer in winter causes a drop in phytoplankton concentrations, both directly as water is entrained from the ocean interior and indirectly as light limitation causes a drop in the average production in the deeper mixed layer. The consequences of low phytoplankton concentration for over-wintering zooplankton populations can be determined from the zooplankton equation. Concentrations of detritus are an order of magnitude less than phytoplankton in the model over-winter and so the equation can be simplified for this purpose by ignoring detritus as a food source. If we also ignore the dilution term, considering a situation in the later part of the winter when the dilution rate is small, the zooplankton equation becomes

$$\frac{dZ}{dt} = \left(\frac{\beta g P}{k_3 + P} - (\mu + \phi_Z Z) \right) Z,$$

showing that a steady state phytoplankton concentration P can maintain a zooplankton population at a concentration given by

$$Z = \frac{1}{\phi_Z} \left(\frac{\beta g P}{k_3 + P} - \mu \right).$$

Using the Optimisation 2 parameter values, a threshold value of P of about 0.4 mmol N m^{-3} is determined which "supports" a zero zooplankton population, while a phytoplankton concentration of 0.5 mmol N m^{-3} will support zooplankton at a concentration of 0.2 mmol N m^{-3}.

A phytoplankton concentration can only be maintained at a steady state if there is sufficient growth to offset losses due to grazing, mortality and mixing. During the winter nitrogen is plentiful and primary production is controlled by light limitation. A steady state analysis is presented here to show the maximum mixed layer depths which will allow maintenance of the required phytoplankton concentrations at low light levels such as those found in the north of the study area in winter.

The phytoplankton equation is simplified by setting $Q = 1$ (i.e. no nutrient limitation) and, as for the zooplankton equation, ignoring detritus and treating the mixed layer depth as fixed. This gives

$$\frac{dP}{dt} = P \left(J - \frac{gZ}{k_3 + P} - \phi_P - \frac{m}{M} \right).$$

The appropriate value of J is the daily average growth rate over the mixed layer $\bar{J}$, expressed in Section 3.2 as an integral over depth and time. The value of this integral is given by

$$\bar{J} = \frac{2V_P}{Mk}\left[F(\gamma e^{kM},\tau) - F(\gamma,\tau) - F(\gamma e^{kM},0) + F(\gamma,0)\right],$$

where

$$F(a,b) = (a^2+b^2)^{\frac{1}{2}} - b\ln\frac{b+(a^2+b^2)^{\frac{1}{2}}}{a},$$

$$\gamma = \frac{V_P\tau}{\alpha I_{on}}$$

and

$$k = k_w + k_p P$$

(Evans and Parslow, 1985). Since $F(a,0) = a$ and $F(a,b) \approx a$ for $a >> b$, a good approximation for the daily average growth rate during winter when M is large is given by

$$\bar{J} \approx \frac{2V_P\lambda}{Mk},$$

where

$$\lambda = \gamma - F(\gamma,\tau).$$

With this approximation applied and dP/dt set to zero the phytoplankton equation is rearranged to give an expression for the mixed layer depth:

$$M = \frac{2V_P\lambda - km}{k\left(\phi_P + \frac{gZ}{k_3+P}\right)}.$$

In the north of the study area (57.5°N), at the winter solstice, the noon PAR immediately below the ocean surface I_{on} is only 43 W m^{-2} (assuming 85% cloud, see Figure

3.4) and there are just 6.3 hours of daylight. When the mixed layer reaches its maximum depth, around the end of March, I_{on} has increased to 153 W m^{-2} and the daylength is 12.8 hours. In each case, the maximum mixed layer depth which can maintain given plankton concentrations is presented in Table 3.5. Optimisation 2 parameter values are used.

Table 3.5. Maximum mixed layer depths at which the specified plankton concentrations can be maintained at 57.5°N.

Zooplankton (mmol N m^{-3})	**Phytoplankton (mmol N m^{-3})**	**Mixed Layer Depth (m)**	
		At winter solstice	**At end of March**
0	0+	300	1502
0+	0.4	225	1142
0.2	0.5	26 (-8)	130 (-0.2)

0+ indicates a vanishing concentration at the tabulated mixed layer depth.
The values in brackets show the error term associated with the daily average growth rate approximation, evaluated at the tabulated mixed layer depth.

The values determined for M at the solstice are about 5 times less than those at the end of March. In contrast, the model mixed layer depths in the north of the study area are only about twice as shallow in December as in March (Figure 3.2). It is clear therefore that the period around the winter solstice is far more critical than the period at the end of winter when the mixed layer is deepest. In December, mixed layer depths greater than the threshold value for phytoplankton of 300 m are found in the north-east, implying that the light available here around the solstice is insufficient to support a non-zero concentration of phytoplankton at steady state. The table also shows that, while a steady state phytoplankton concentration of 0.5 mmol N m^{-3} is sufficient to support a 0.2 mmol N m^{-3} concentration of zooplankton, an unrealistically shallow mixed layer would be required in the north to maintain such a phytoplankton concentration, given the implied grazing pressure.

Having explored the winter-time requirements of the model plankton under steady state conditions, their response to physical forcing varying in space and time is now

examined. The winter-time minimum phytoplankton concentration in the mixed layer over the study area is shown in Figure 3.26a. While phytoplankton concentrations remain comparatively high everywhere throughout the winter in the Optimisation 2 solution because of the low phytoplankton mortality, they do drop much lower in the north than in the south, particularly in the north-east where winter mixing is deepest. The light limitation effect associated with deep mixed layers is exacerbated here by the high latitude. The drop in phytoplankton concentration is sufficient to cause zooplankton populations to crash in the north-eastern part of the study area, falling to nanomolar concentrations and below (Figure 3.26b).

The dynamics are shown in more detail in Figure 3.27. The phytoplankton minimum tends to occur much earlier than the zooplankton minimum and in many cases we see a slow recovery in phytoplankton concentrations for much of the period before the onset of spring stratification, as the days lengthen after the winter solstice and solar elevation increases. The potential for recovery depends also on a relatively slow rate of mixed layer deepening and low grazing pressure during the late winter period. Signs of recovery are much more obvious in the north where zooplankton concentrations are lowest, while in the south the winter-time conditions are much closer to a steady state. Zooplankton populations also begin to recover before the mixed layer starts to shoal, as phytoplankton concentrations rise above the threshold value (0.4 mmol N m^{-3}). The end-of-winter zooplankton populations at the beginning of the heating season (defined by the time of the mixed layer depth maximum) are shown in Figure 3.28. The areal zooplankton concentrations are plotted here. Because zooplankton are able to swim to remain within the mixed layer as it shoals this gives a better indication of the potential grazing pressure at the beginning of the bloom.

3.6.2 Spatial Variability in the Simulated Bloom

Time series showing spatial pattern in the progression of the bloom are presented in Figure 3.29. If we define bloom initiation as the first appearance of phytoplankton concentrations greater than 1 mmol N m^{-3} (Figure 3.29c), we can see that the bloom appears to spread from two separate areas in such a way that the study area is divided into two distinct "cells": one in the north-east corner, which corresponds to the area of low end-of-winter zooplankton populations, and one covering the remainder of the study area. In the more southerly cell the bloom starts in the south-east where the mixed layer first shoals to less than 100 m. In the north-eastern cell it starts in a band stretching from the north-west corner to between 45 and 50°N in the east and it actually occurs slightly in advance of that further south. While bloom initiation in the southern cell is always associated with mixed layer depths of less than 100 m (Figure 3.29a), in the north-eastern cell bloom initiation occurs while the mixed layer is still rather deep, in some cases well over 300 m. This is possible, despite the relatively strong light limitation, because of the low grazing pressure. Because of the absence of zooplankton in the north-eastern cell, ammonium concentrations here at the beginning of the bloom are low and this is reflected in the high *f*-ratios (Figure 3.29f). In contrast the *f*-ratios in the southern cell are very low, less than 0.3, indicating that only a small amount of the production occurring in response to the increase in light availability is actually new production.

Following its initiation, the bloom in each area spreads generally northwards and the two blooms merge in early May (t = 126 d), by which time the bloom at 50°N in the north-east has intensified sharply, reaching nearly 10 mmol N m^{-3}. Nitrate concentrations here are already depleted by this time (Figure 3.29b), well in advance of anywhere else at the same latitude. The bloom in the southern cell reaches the far north-west corner of the study area in mid to late May, just over a month after its initiation in the south-west. This is equivalent to a mean northward progression of 15-20° per month, although the progression appears rather irregular. At 20°W the southern bloom appears to progress more slowly at a mean

rate of between 10° and 15° per month. In both cases, progression seems to be more rapid in the south. A strong south to north gradient in phytoplankton concentration starts to develop as stocks fall in response to nitrate depletion in the middle of May and this feature follows the line of nitrate depletion, marked by the 1 mmol m^{-3} nitrate contour, northwards and westwards during the rest of May and June at a rate of around 10° per month over the main part of the survey area. In general, the zooplankton bloom shows a steadier northward progression (Figure 3.29d), although there is a tendency for some interesting small scale patterns to develop in the north-eastern corner during May.

The relationship between phytoplankton concentration and nitrate utilisation is shown in Figure 3.30 which gives the time series of each at 5 degree intervals. The pre-bloom nitrate level is shown for reference. This illustrates how the exceptionally large blooms develop in the north-east with negligible phytoplankton losses. The mismatch here between net primary production and loss due to grazing can be clearly seen in Figure 3.31. In the far north of the eastern half of the study area, there is very little loss of biomass until the mixed layer nitrate concentration falls below about 1 mmol m^{-3}. This pattern is very different from that elsewhere, where a large fraction of the phytoplankton stock is consumed long before the nitrate becomes depleted.

Figure 3.30 shows a number of locations where blooms start to develop slowly but are cut short by sudden losses, before recovering again. This feature is seen at 47.5°N 17.5°W, 47.5°N 12.5°W, 52.5°N 22.5°W and 52.5°N 12.5°W. There is also a similar feature at 32.5°W and 37.5°W in the far north and it is also present but less obvious in other locations in the north-west above 45°N. The areas where this feature is seen most clearly are areas where the phytoplankton start to bloom while the mixed layer is still much deeper than 100 m, but they lie outside the region of exceptionally low end-of-winter zooplankton populations. In these areas the winter zooplankton populations fall low enough to allow the phytoplankton bloom to start early but remain high enough to respond rapidly. In the more easterly of these areas, the effect of this response on phytoplankton concentration tends to

be more dramatic as zooplankton density is increasing at the same time due to mixed layer shoaling. At the locations in the far north-west the situation is rather different. Here, because of the relatively shallow winter mixed layer, phytoplankton concentrations rise earlier to a level which allows zooplankton recovery. In the far north-west phytoplankton concentration reaches values between 1 and 2 mmol N m^{-3} well before the mixed layer begins to shoal, which it does here around the beginning of April. The zooplankton response also occurs before the mixed layer shoals and it is this that causes the high end-of-winter zooplankton populations seen in the north-west in Figure 3.28. The balance between production and consumption (Figure 3.31) swings back again as the mixed layer either starts to shoal or, in the east, becomes shallower still, and light limitation decreases. It is the effect of large spatial gradients in mixed layer depth on the relative phase of these patterns in the bloom dynamics which leads to the small scale patterns noted earlier in this section. We might expect similar dynamics to contribute towards patchiness at the mesoscale at times when there is a large variance in mixed layer depth associated with a mesoscale eddy field.

The patterns of 10 day mean primary production in Figure 3.29e show generally higher production in the north. The highest production of over 40 mmol N m^{-2} d^{-1} occurs during May and is associated with the high phytoplankton biomass in the north-east. The differences in production between the north-east and north-west are less dramatic than the corresponding differences in standing stock though. One of the main reasons for this is the effect of self-shading in the large blooms. The *f*-ratio (Figure 3.29f) is highly variable over the northern part of the study area. The north-eastern maximum for example intensifies during the bloom in April and then drops dramatically in May as nitrate is depleted and large amounts of ammonium are produced by zooplankton excretion and detrital breakdown during the bloom's demise. Patterns of PON export (Figure 3.29g) show a major contribution from the north-eastern bloom, the highest exports of over 50 mmol N m^{-2} d^{-1} being seen here in early May. This is a time when high phytoplankton biomass has accumulated but the mixed layer is continuing to shoal and the high export is due mainly to the detrainment of particles formed during the bloom. Similar highs, associated with detrainment can be seen from late March through April.

3.6.3 Factors Controlling Patterns of Nitrate Utilisation

In Chapter 2, various factors were put forward speculatively as possible causes of the observed south to north gradient in nitrate utilisation. Two of these were suggested by the observed correlation between nitrate utilisation and pre-bloom nitrate concentration. The first was the cumulative effect over time of small differences in the nitrate limitation of growth rate, due to spatial variance in nitrate concentration. The second was spatial variance in the ammonium inhibition of nitrate uptake for a specific ammonium concentration, under an assumption that inhibition depends on the relative concentrations of the two nutrients. Both offered an explanation in terms of rates of nitrate uptake and a south to north gradient in nitrate uptake rate was obtained in the simulation, as demonstrated by the new production maps for Optimisation 2 in Figure 3.19. The possible effect of relative concentrations of nitrate and ammonium cannot be investigated using the present model, as inhibition in the model is a function of ammonium concentration only. However, the contribution of spatial variance in nitrate limitation to this model result is of interest. The effect is investigated here by comparing the standard model run for 1991 with a run in which the nitrate concentration is adjusted to a high, spatially uniform value (1000 mmol m^{-3}) at the time of the mixed layer depth maximum. The results are presented in Figure 3.32.

A change in nitrate concentration potentially affects the model in two ways, via the phytoplankton growth rate and via the import flux. We are only interested in the sensitivity to the former and the timing of the adjustment was chosen to minimise the effect on the import flux. There is no import due to entrainment after this time and nitrate is sufficiently high already for its limiting effect on growth rate to be negligible, so transients associated with the large step change are minimal. There is however a small import due to diffusive mixing which is effectively switched off by the nitrate adjustment. The effect of this flux in the standard run is negligible during the bloom but does cause a noticeable deviation from the nitrate utilisation in the "high nitrate" run before the main bloom at some locations. The worst case is seen at 52.5°N 37.5°W. While the difference between the two solutions does

not perfectly represent the difference due to the effect on growth rate, it does give an upper bound. With the exception of the location noted, we can see from these results that the greatest difference in nitrate utilisation occurring while the nitrate remaining is greater than 3 mmol m^{-3}, is about 1 mmol m^{-3}. In many cases it is much less. This is small compared with observed differences of about 5 mmol m^{-3} over 6 degrees of latitude. The model therefore provides little support for the hypothesis that the observed south to north gradient in nitrate utilisation is the result of variance in nitrate limitation of growth rate.

Progress can be made towards identifying more likely causes of the observed nitrate utilisation patterns by examining the relationship between patterns of new production and the factors which define new production in the model. These are shown, for the standard run, in Figure 3.33. Values are plotted at 10 day intervals after the initial stratification, defined here as the time t_0 when the mixed layer depth has shoaled to 150 m. Plotting the patterns in this way removes most of the structure due to phase differences across the study area so that spatial patterns related to bloom development can be seen more clearly.

By time t_0 the phytoplankton biomass (Figure 3.33b) in the north-east of the survey area is already more than 2 mmol N m^{-3} and the pattern of new production (Figure 3.33a) reflects this. In general, new production remains spatially correlated with phytoplankton biomass until nitrate limitation starts to take effect. This occurs much more quickly in the north-east than anywhere else in the study area because of the high new production there. The nitrate limitation factor, $N / (k_1 + N)$ (Figure 3.33e), shows that nitrate limitation has started to have a major effect in the north-east by $t_0 + 20$ days. Elsewhere, the effect is not obvious until about $t_0 + 40$ days. By that time, the nitrate limitation factor is less than 0.7 over large parts of the study area and both new production per unit volume and biomass specific new production are seen to be correlated with this pattern.

The importance of the other factors is best investigated with reference to spatial pattern in specific new production (Figure 3.33c). The maps of the light limited specific growth rate J (Figure 3.33d) show clearly the importance of self-shading in the large blooms

in the north-east which reduces the potential growth rate by a factor of about 3 compared with that in areas of low biomass. Despite this, until nitrate limitation (Figure 3.33e) starts to become significant, the greatest effect is that of ammonium inhibition of nitrate uptake, indicated by low values of the ammonium inhibition factor $\exp(-\psi A)$ (Figure 3.33f). In fact, at $t_0 + 10$ the large effect of self-shading in the intense bloom area is outweighed by the effect of the comparatively low ammonium concentrations in this area. The band of high ammonium inhibition (low ammonium inhibition factor) stretching south-eastward from 30°W at the northern edge of the study area is matched by a band of low specific new production and the low ammonium inhibition around 30°W 48°N and that to the north of this are matched by local maxima in specific new production. By $t_0 + 20$, all these patterns of ammonium inhibition are largely reversed, except in the area where the bloom is most intense in the east at 50°N. The reversal is reflected in the specific new production pattern, although the picture is starting to become more complicated as nitrate limitation comes into play. By $t_0 + 30$ the pattern of ammonium inhibition in the band from 30°W and to the west of this has undergone a further reversal, being now fairly well correlated with that seen at $t_0 + 10$. Again the pattern in specific new production reflects this, although the effect of nitrate limitation now dominates the eastern area.

Another feature shown by the J maps is reduced light availability in the south-east between about 40 and 45°N from $t_0 + 10$ up until about $t_0 + 40$ days. This reflects the slower shoaling of the mixed layer in this area and contributes to the east-west gradient in mean new production seen in Figure 3.19. Some evidence can be seen of this pattern in the specific new production maps when longitudinal variation in ammonium is low, (e.g. at $t_0 + 20$) but in general it is of much lesser importance than ammonium inhibition.

In general, it is concluded that the timing of the bloom in the model is determined by a combination of light availability and end-of-winter grazing pressure, that the end of the bloom period is determined by nitrate limitation and that the patterns of new production, and therefore nitrate utilisation, in-between are strongly affected by patterns of zooplankton

grazing. This effect occurs in two ways: by the removal of standing stock and by the inhibition of nitrate uptake as ammonium increases due to zooplankton excretion and mortality.

Finally, we can interpret the south to north gradient in new production in the light of this analysis. The high new production in the north-east in Figure 3.19 is easily explained by the fact that large blooms are allowed to develop as a result of low grazing pressure. However, this figure also shows areas of relatively high new production in the north-west where the end-of-winter zooplankton populations are high. This seems to be linked to a generally greater accumulation of phytoplankton biomass than in the south, which can be explained by the more complicated zooplankton dynamics associated with early zooplankton blooms. Examples are shown by the time series at 47.5°N 32.5°W, 47.5°N 27.5°W, the same longitudes 5 degrees to the north and at 57.5°N 37.5°W and 57.5°N 32.5°W. A predator-prey cycle occurs, leading to low areal zooplankton concentrations (Figure 3.34) and reduced grazing pressure (Figure 3.31) during the early phase of the main bloom. High ammonium concentrations develop during the demise of the early zooplankton bloom from zooplankton excretion and mortality, while phytoplankton are still low. This inhibits nitrate uptake, delaying significant nitrate utilisation until a large amount of biomass has accumulated as a result of regenerated production. When new production takes over, as ammonium concentrations fall, the rate of nitrate utilisation is therefore greater than in areas where significant new production starts earlier when the biomass is low. Similar dynamics occur a little later in the east at 47.5°N 12.5°W, 52.5°N 12.5°W, 52.5°N 22.5°W and 57.5°N 32.5°W. Here the main period of high ammonium inhibition occurs after a significant period of new production and it is this which is responsible for the band of low average new production in Figure 3.19.

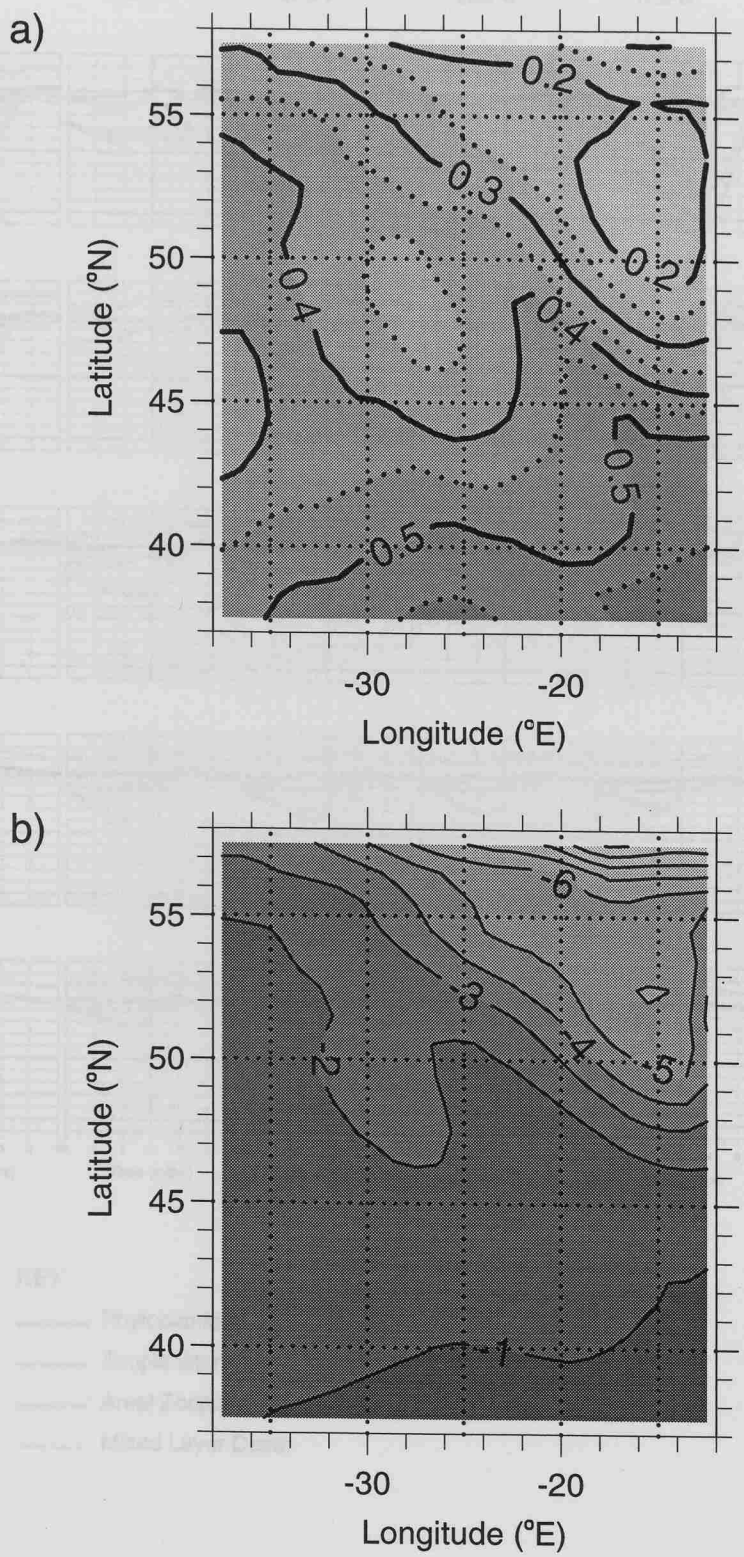

Figure 3.26. Winter-time minima of (a) phytoplankton and (b) $\log_{10}$(zooplankton) concentrations (mmol N m^{-3}).

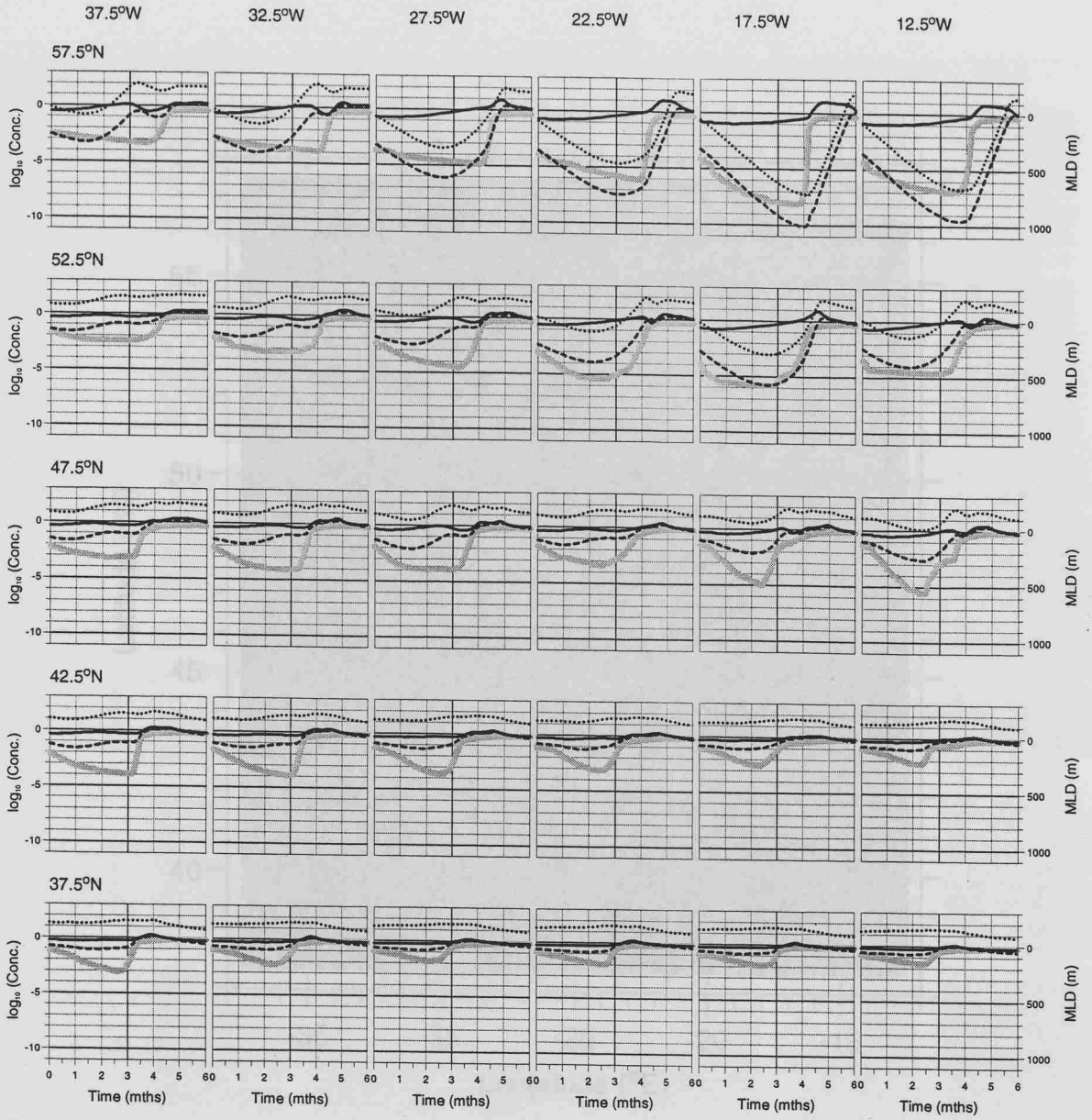

Figure 3.27. Time series of phytoplankton and zooplankton concentrations (mmol N m^{-3}), areal zooplankton concentration (mmol N m^{-2}) and mixed layer depth from January to June at 5° intervals.

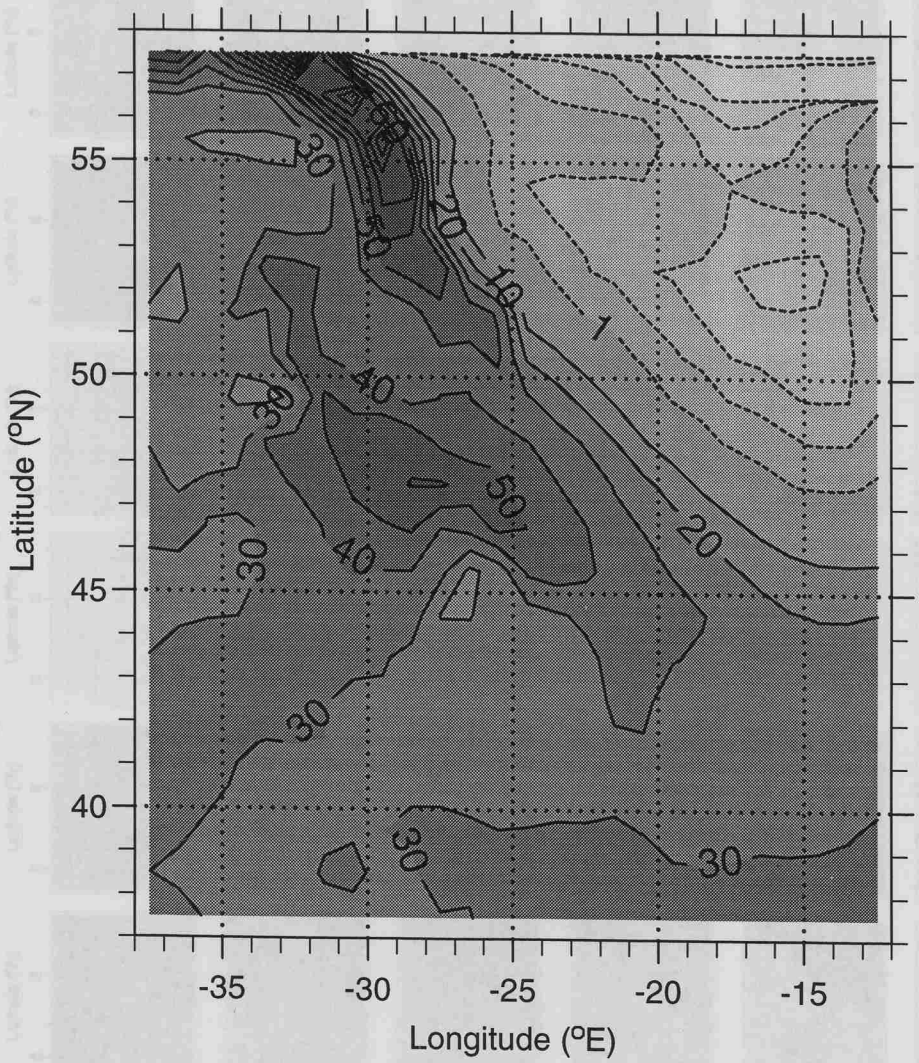

Figure 3.28. End-of-winter areal zooplankton concentration (mmol N m^{-2}). Broken contour lines indicate order of magnitude steps from 1 to 10^{-6} in the extreme NE.

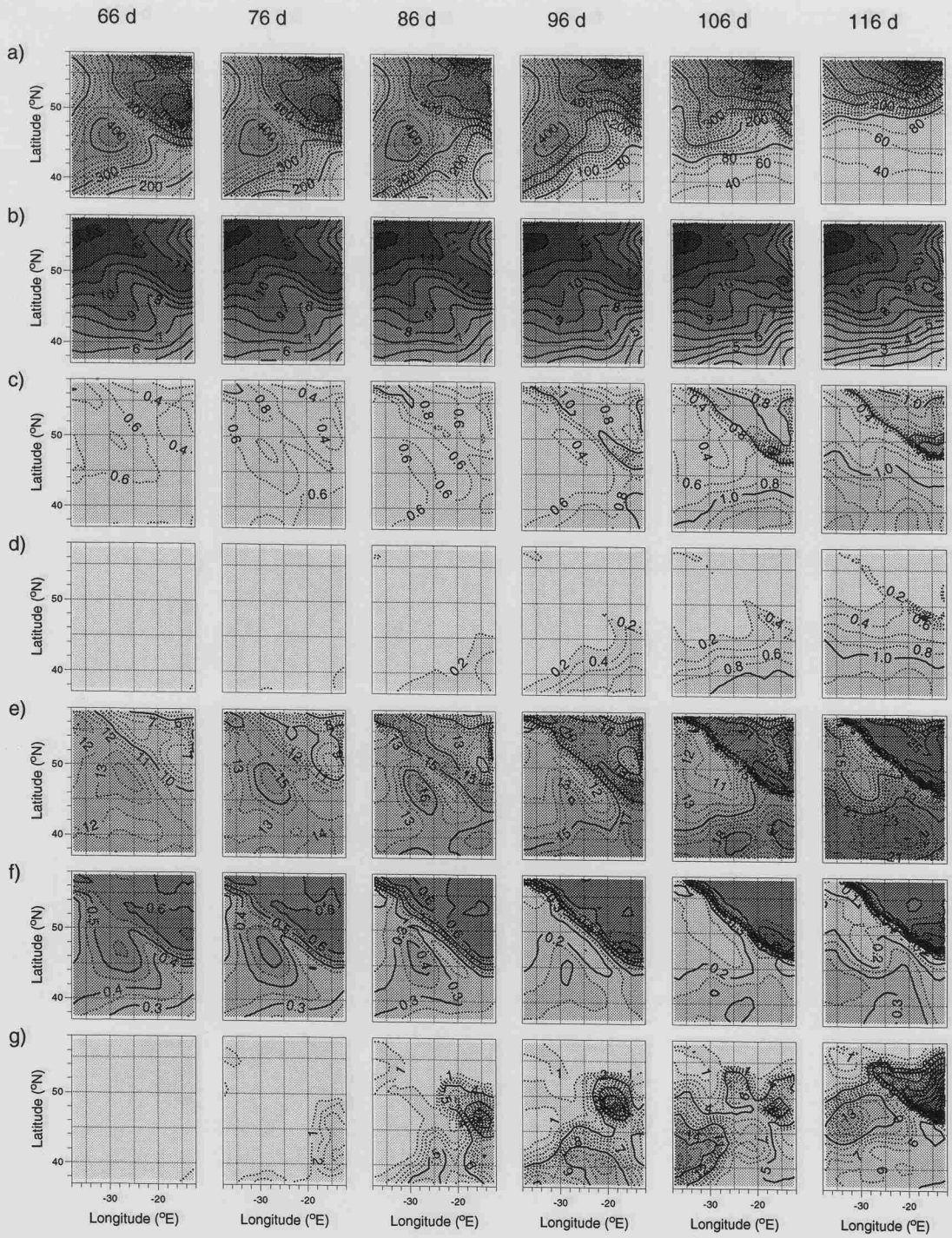

Figure 3.29. 10 day interval time series from March to June. (a) Mixed layer depth (m). (b) Nitrate (mmol m^{-3}). (c) Phytoplankton (mmol N m^{-3}). (d) Zooplankton (mmol N m^{-3}). (e) 10 day mean areal primary production (mmol N m^{-2} d^{-1}). (f) 10 day f-ratio. (g) 10 day mean PON export (mmol N m^{-2} d^{-1}). Figures (a) to (d) show point-in-time values. Figures (e) to (g) show values for the preceding 10 day periods.

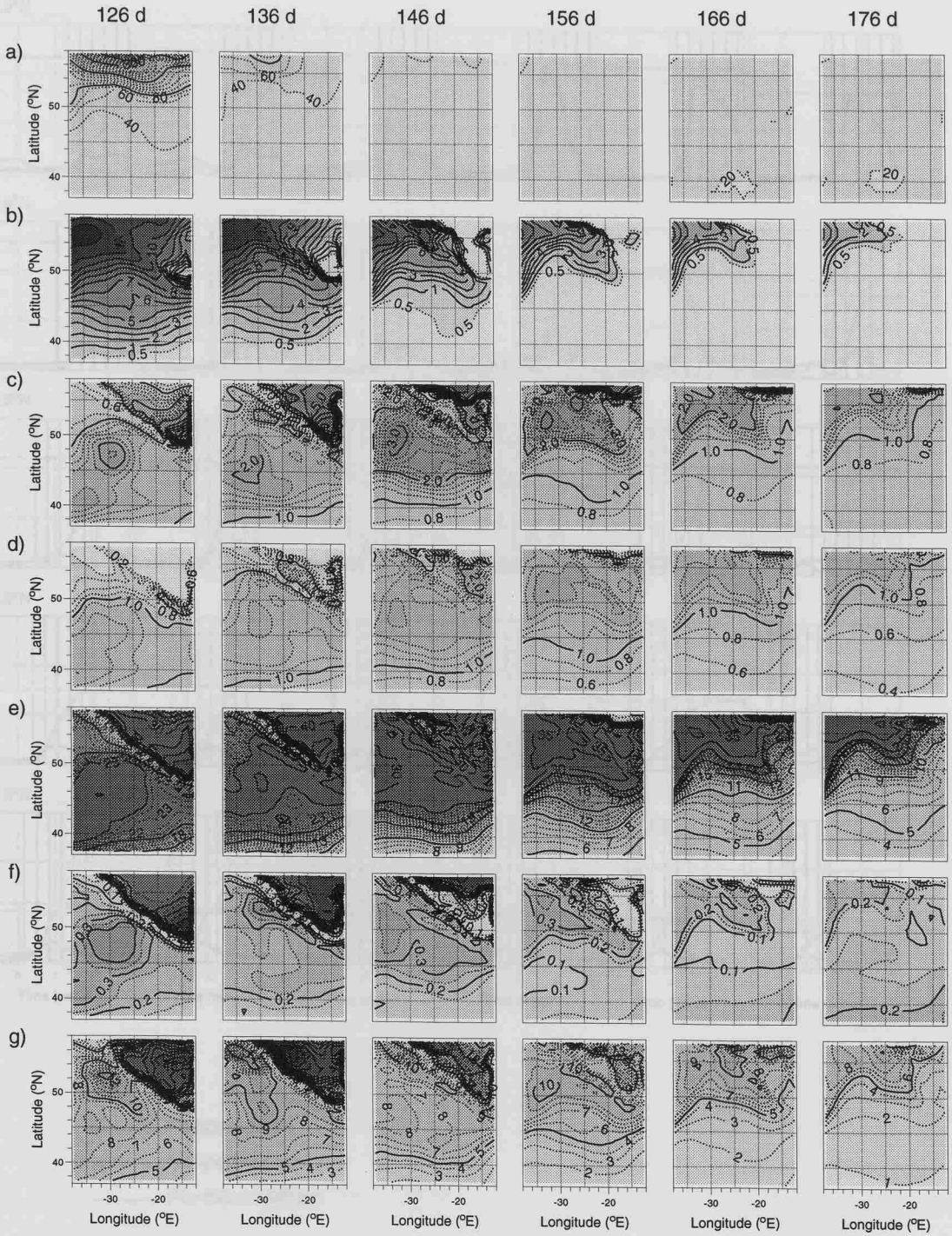

Figure 3.29 continued.

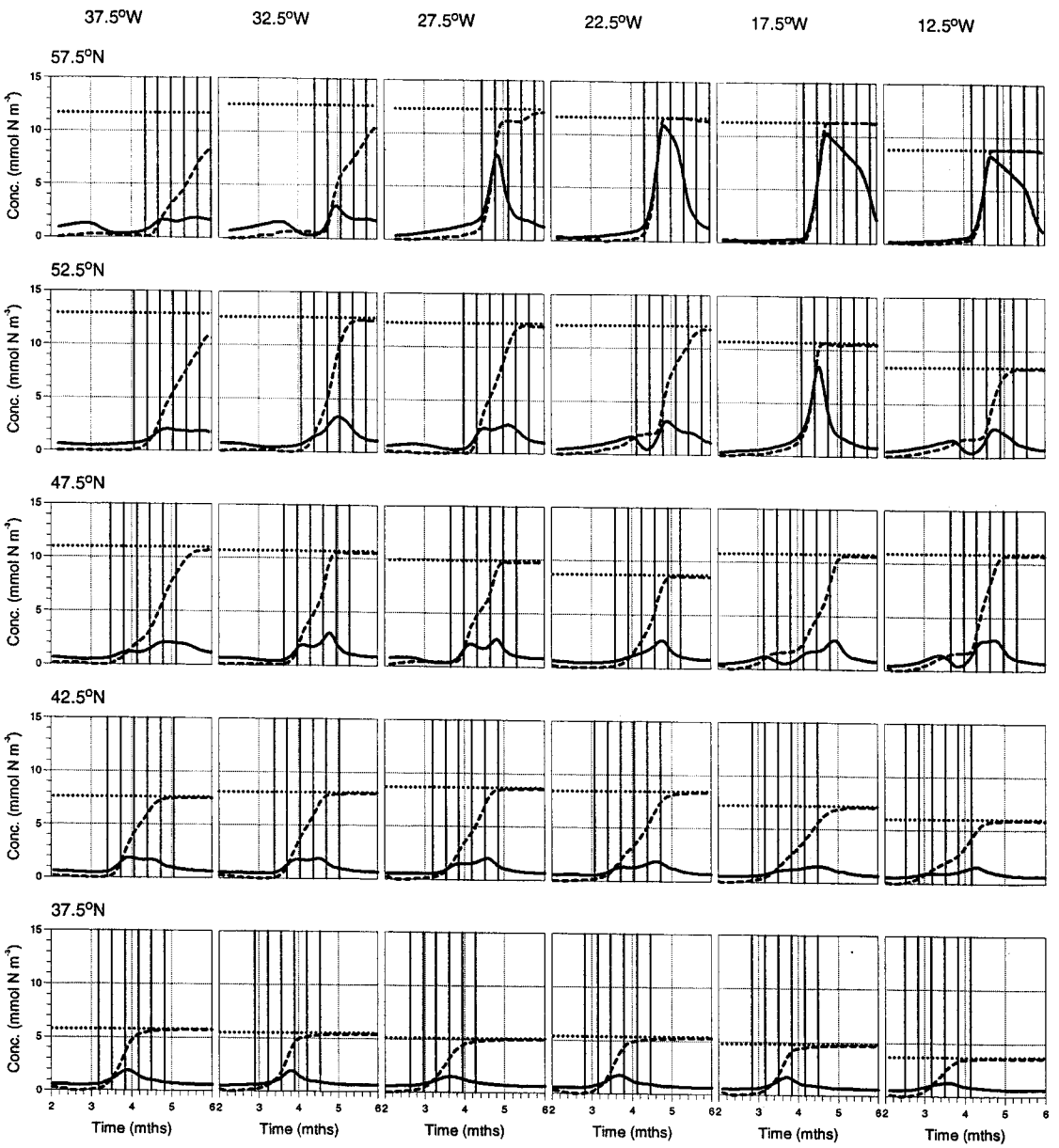

Figure 3.30. Time series of nitrate utilisation and phytoplankton from March to June at 5° intervals. The pre-bloom nitrate level is shown for reference. Vertical reference lines show 10 day intervals from time of initial stratification for cross-reference with Figure 3.33.

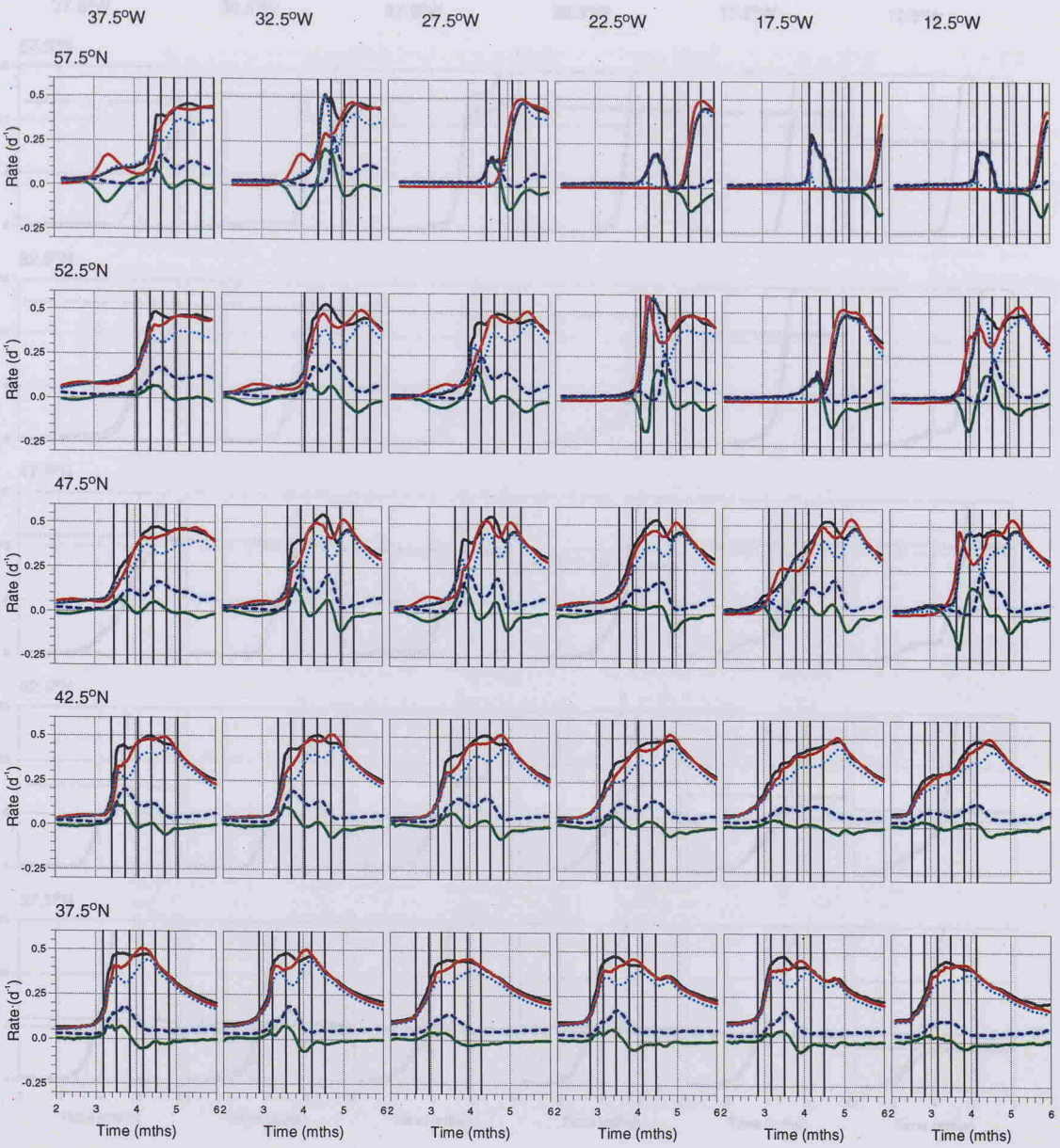

Figure 3.31. Time series of biomass specific phytoplankton fluxes, from March to June, at 5° intervals. Vertical reference lines show 10 day intervals from time of initial stratification for cross-reference with Figure 3.33.

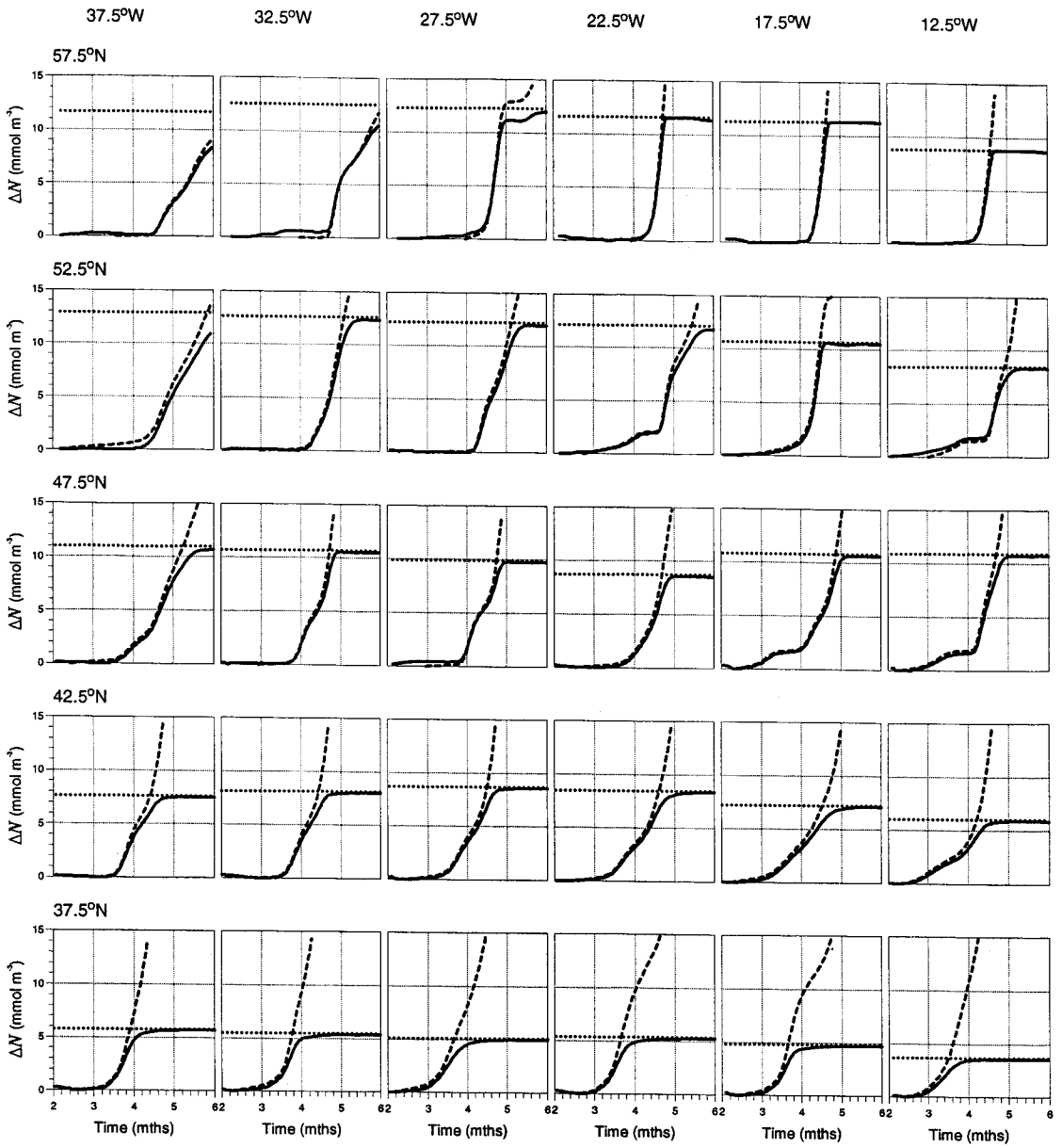

Figure 3.32. Nitrate utilisation for the adjusted winter nitrate run compared with the standard run. The pre-bloom nitrate level is shown for reference.

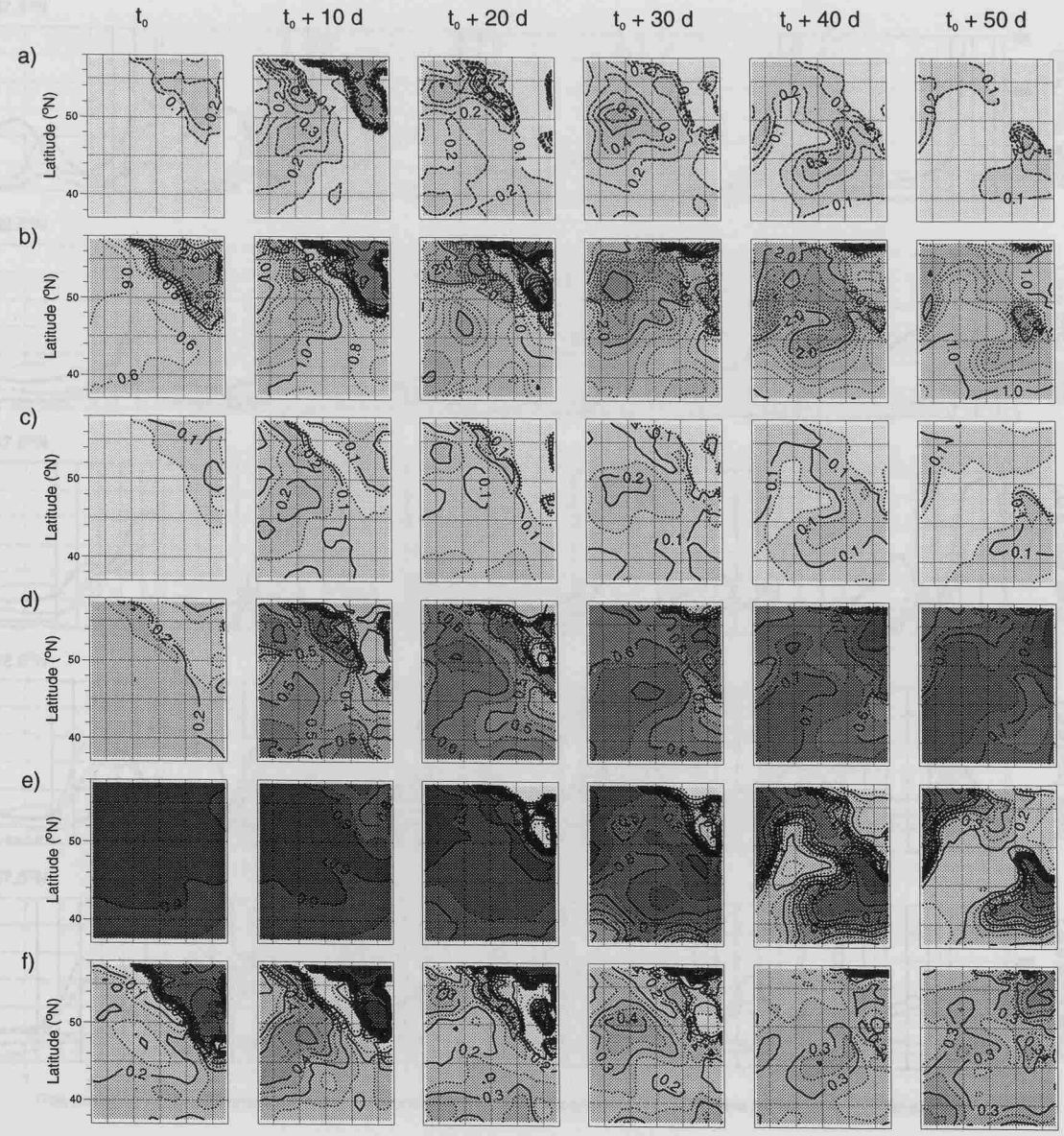

Figure 3.33. Spatial pattern at time of initial stratification above 150 m and at 10 day intervals thereafter. (a) New production (mmol N m^{-3} d^{-1}). (b) Phytoplankton (mmol N m^{-3}). (c) Specific new production (d^{-1}). (d) Light limited specific growth rate (d^{-1}). (e) Nitrate limitation factor. (f) Ammonium inhibition factor.

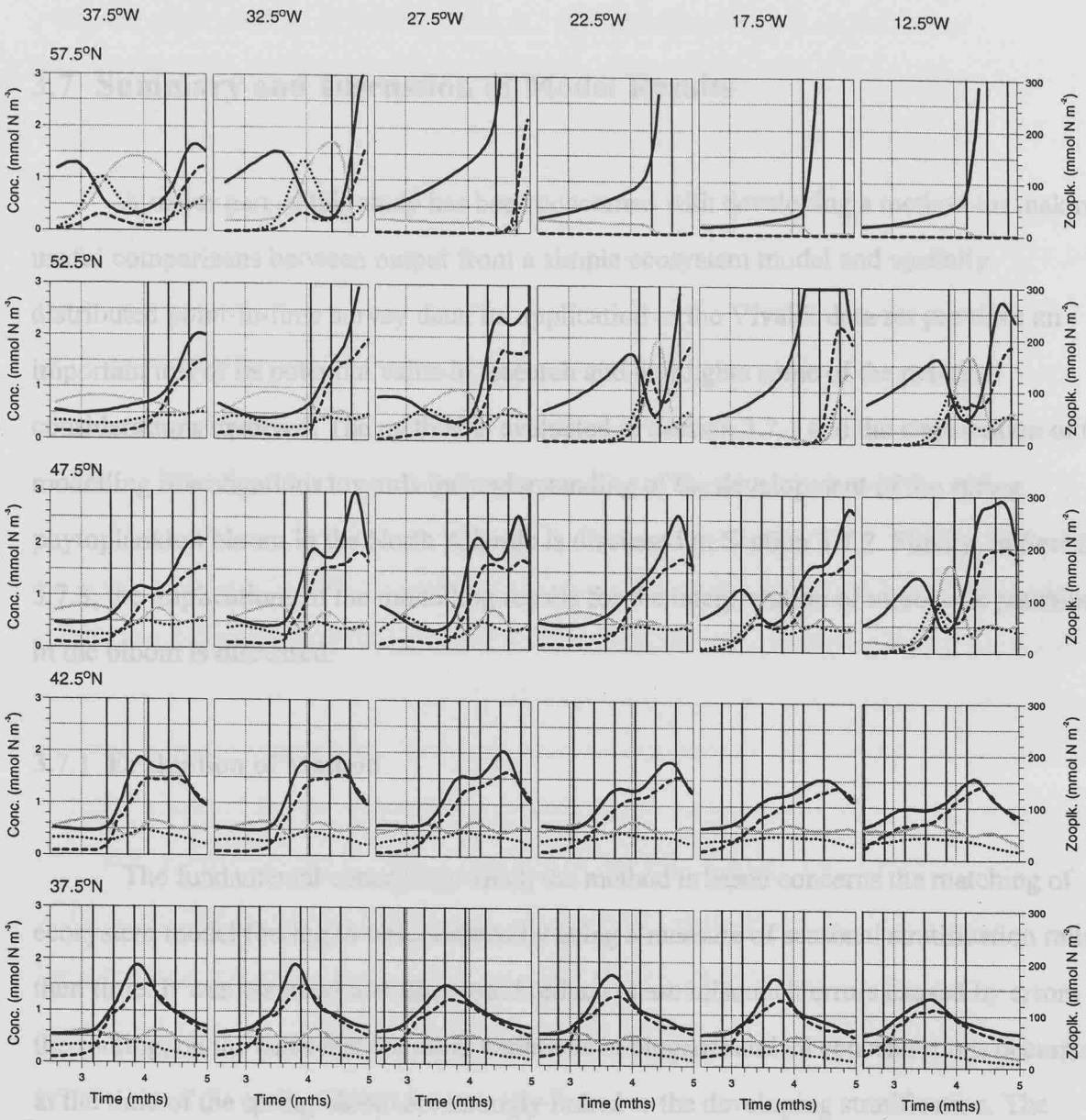

Figure 3.34. Time series of phytoplankton, zooplankton and ammonium concentrations and areal zooplankton concentration from mid-March to the end of May at 5° intervals. Vertical reference lines show 10 day intervals from time of initial stratification for cross-reference with Figure 3.33.

3.7 Summary and Discussion of Model Results

A major part of this study has been concerned with developing a method for making useful comparisons between output from a simple ecosystem model and spatially distributed point-in-time survey data. Its application to the Vivaldi data set provides an important test of its potential value in research and highlights some of the practical considerations involved. The method is evaluated in Section 3.7.1 and the contribution of the modelling investigations towards the understanding of the development of the spring phytoplankton bloom in the North Atlantic is discussed in Section 3.7.2. Finally, in Section 3.7.3, the implications of the modelling results for the interpretation of mesoscale patchiness in the bloom is discussed.

3.7.1 Evaluation of Method

The fundamental concept on which the method is based concerns the matching of ecosystem model forcing to observations by using a measure of seasonal stratification rather than time. It was assumed that this would reduce phase mismatch errors caused by errors in the forcing, on the basis that the rapid variations in biogeochemical concentrations occurring at the time of the spring bloom are strongly linked to the developing stratification. The method is more complicated than matching by time and therefore a more objective test of its effectiveness is required if its application in future work is to be justified. Such a test can be performed by making use of the two alternative solutions obtained with 1991 and climatological forcing. The Optimisation 2 parameter set is used for this purpose.

If we treat the 1991 forcing functions and model solution as 'reality' and the climatological solution as an attempt to reproduce the 1991 biogeochemical time series using the climatological forcing functions as estimates of the 1991 forcing functions, then the difference between the two solutions is a measure of the error due to the inaccuracy in the forcing. In most parts of the study area the development of stratification is slower in the

climatological version, so this test is biased towards situations where the rate of stratification development is underestimated. It will be referred to as Scenario A. An alternative test, Scenario B, which assesses the method for situations where it is overestimated, may be performed by reversing the forcing functions so that the 1991 solution represents an estimate of the 'reality' defined by the climatology. We therefore have two hypothetical scenarios with which to test the method, each being a plausible example taken from the ensemble of situations which could arise in practice.

Results for Scenario A are shown in Figures 3.35 and 3.36. The nitrate and chlorophyll solutions obtained using climatological forcing are shown in relation to the 1991 solutions with time matching and seasonal density anomaly matching. The latter is achieved by shifting the climatological solutions in time such that their density anomaly matches that for the 1991 solution. The seasonal density anomalies for the two alternative forcing data sets are shown in Figure 3.37. Only density anomalies between zero and the minimum at the end of the heating season are used and data are omitted where no match is possible. We can see that in most cases the solutions matched by density anomaly are closer to the 1991 solution but this is not true everywhere. In particular, the time match gives a better result for some locations in the north-east, especially 52.5°N 17.5°W, and a better result in the south in terms of the nitrate error, although the form of the solution here is more closely approximated by the density anomaly match.

A more objective comparison is provided by averaging the nitrate errors over time and location. It is not useful to do this for the phytoplankton solutions because they are not monotonic. Each of the 30 locations on the 5° grid is included and the errors for both methods are averaged over the periods for which a density anomaly match is possible. In addition, periods during which all three nitrate values are less than 0.5 are ignored. This has little effect on the relative errors for the two methods but avoids biasing both errors low by the inclusion of an arbitrary length of time for which errors are approximately zero. The

mean errors obtained are thus more representative of the magnitude of error which might be obtained during the bloom.

For Scenario A, in which the 1991 forcing represents reality, the r.m.s. error over a total time period of 68 months is 1.11 mmol m^{-3} for the density anomaly match, compared with 1.80 mmol m^{-3} for the time match, an improvement of 38%. For Scenario B, where the climatological forcing represents reality, the r.m.s. error over a total time period of 90 months is 1.22 mmol m^{-3} for the density anomaly match, compared with 1.63 mmol m^{-3} for the time match, an improvement of 25%. Combining the results for both scenarios, weighted according to the respective time periods, gives an r.m.s. error of 1.17 mmol m^{-3} for the density anomaly match and an r.m.s. error of 1.71 mmol m^{-3} for the time match. The overall improvement obtained by density anomaly matching according to this test is 32%.

Another novel and important aspect of the method developed in this study was the introduction of temporal windows for comparing observations and model output. These have the effect of reducing the information content of individual observations to a more realistic level for the context in which they are being used, thus preventing the optimised model from being over-constrained. The windows used here were based on the level of uncertainty in the event-scale correction made to the observed seasonal density anomaly. However, they also compensate to some extent for errors in the forcing. Temporal windows could potentially be introduced in future studies specifically for the purpose of allowing for uncertainty in forcing estimates. Determining appropriate window sizes in this case may not be trivial though. From Figure 3.35 we can see that a typical phase offset for the nitrate solution matched by density anomaly is of the order of 10 days so, for this scenario, a 20 day window would remove most of the error in nitrate due to the forcing. This is rather large, compared with the time scale of the bloom, and implies a very low information content for each observation in such a scenario.

The introduction of seasonal density anomaly matching and temporal windows is no substitute for improving the accuracy of the physical forcing. Although nitrate errors are

generally reduced by the seasonal density anomaly matching, mean errors of the order of 1 mmol m^{-3} are still rather high and Figure 3.35 shows that errors of more than 2 mmol m^{-3} are not uncommon in Scenario A. This, combined with the large phase shift between the solutions in some locations, even after density anomaly matching, suggests that the errors due to the forcing in any similar scenario would be highly significant. In the present study, Figure 3.10 shows that the error in the seasonal density anomaly from the climatological simulation was mostly greater than the difference between the seasonal density anomaly fields for the climatological and 1991 simulations. This suggests that the nitrate errors which would have been incurred if climatological forcing had been used in this study would have been at least as great as those in Scenario A. The error in the seasonal density anomaly given by the 1991 simulation is still rather large in some locations and, together with the large time shifts (greater than 10 days) which were sometimes required in order to achieve the density anomaly matches (Figure 3.11), this provides a strong incentive for improving our ability to accurately model the development of the stratification.

Analysis of the model errors in stratification showed that a major source of inaccuracy in the forcing was poor simulation of the contribution of horizontal buoyancy transport to the development of seasonal stratification in the GCM. This can be accounted for by the absence of strong buoyancy fronts in the model. High resolution process modelling studies of mesoscale fronts (Nurser and Zhang, in revision; Haine and Marshall, 1998; Lévy *et al.*, 1998) show that the ageostrophic velocity field associated with baroclinic instability contributes to stratification by 'tilting' horizontal buoyancy gradients. Ekman drift across the fronts may also make a significant contribution to the stratification early in the season, when it is likely to have an asymmetric effect. The present study provides observational evidence that buoyancy transport, probably due to these mesoscale processes, makes an important contribution to the mean rate of seasonal stratification development at larger scales. The biological effects are less easily quantified. However, in their modelling investigation of the onset of a spring bloom during the sinking and spreading phase of a convective chimney, Lévy *et al.* (1998) showed that primary production in a non eddy-resolving control experiment, was underestimated by up to a factor of 4. In that experiment,

mesoscale processes were crudely parameterised by a second order diffusion operator, as in the GCM in the present study. Lévy *et al.* (1998) propose two alternative approaches to improving the accuracy of physical forcing in large scale ecosystem models: either the use of computationally expensive eddy-resolving general circulation models (EGCMs) should be considered or some more realistic parameterisation of mesoscale processes should be found, the Gent and McWilliams (1990) scheme being a possible candidate.

One of the aims of this study was to evaluate a simple ecosystem model according to the extent to which it could explain the variance in the Vivaldi observations with a single parameter set. In any evaluation of a model with free parameters it must be recognised that the "best" area of the parameter space may be missed. Even once a parameter set is chosen, the issue of model evaluation is a complex one. This is partly because the degree of misfit between the model and observations depends on the criteria chosen to define it, but also, more fundamentally, because this misfit arises from noise in the biogeochemical observations and inaccuracy in the physical forcing as well as deficiencies in the model. Before any useful evaluation may be achieved, steps must be taken to reduce the misfit contribution arising from these other factors as far as possible by increasing the effective sample size of the observational data set (allowing for spatial autocorrelation) and/or by improving the forcing estimates.

Noise in the observational data can arise from two sources. One of these, which was discussed in some detail with reference to the Vivaldi observations in section 3.5, is a modification of the response at the seasonal time-scale by shorter time-scale variations. The other source of noise, which applies to time series data as well as point-in-time data, is the inherent variability in the response of the mixed layer ecosystem to specific physical forcing on the seasonal time-scale. This depends on spatial and temporal variance in the biological parameters and structure of the real ecosystem and also on physical variability at shorter time-scales. These factors together determine the infinite ensemble of possible seasonal time-scale responses to the actual seasonal forcing. While errors in the physical forcing have been put forward as a separate factor contributing to the misfit, if we are evaluating the

ability of ecosystem models to give a 'correct' response to prescribed physical forcing, then it is perhaps more useful to view the differences between the real forcing and the prescribed forcing as a third source of noise in the biogeochemical observations.

The evaluation of the 5 compartment model used in this study was inconclusive, largely because of the limited size of the Vivaldi data set and the small number of model variables represented. The potential for bias in a data set of this size is great. Clearly, for practical evaluation of different models, a larger more comprehensive database is required, ideally comprising data from many independent sources, including time-series data as well as data from wide-area surveys. The question of how large is difficult to answer. This depends on the magnitude of the various noise sources. The most difficult of these to quantify is the inherent variability in the ecosystem response to physical forcing and this problem is intimately linked with that of determining the feasibility of successfully simulating the ecology of the world ocean with generic models.

3.7.2 Bloom Development in the Eastern North Atlantic

Patterns of bloom progression shown by the Optimisation 2 solution in response to 1991 forcing were investigated. On the assumption that the model captures the real dynamics to some degree, this analysis of the model response to environmental variability allows some of the features of that variability which are potentially important in determining the characteristics of the bloom to be identified. This provides an aid in the interpretation of features exhibited by the Vivaldi '91 survey data and other survey and satellite data from the same region, as well as providing hypotheses which might usefully be tested by future research. In this section, the main results are summarised and compared with evidence from observational data in the literature.

The major implications of this analysis concern the role of zooplankton grazing as the most important factor controlling patterns of bloom development in the model, prior to nutrient depletion. The sensitivity of bloom development to grazing pressure has been

demonstrated by previous modelling work (e.g. Fasham *et al.*, 1983, Frost, 1987; McGuillicuddy *et al.*, 1995a) and this study shows how spatial pattern in grazing pressure might arise in the eastern North Atlantic, as a consequence of spatial variability in the physical environment, and examines the implications for development of the spring bloom over a large area.

In the simulation, patterns of grazing pressure strongly affect the critical depth of the mixed layer at which bloom initiation can occur, as suggested by Platt *et al.* (1991a), and grazing pressure and ammonium inhibition of nitrate uptake, as a result of the ammonium produced in zooplankton blooms, are the major factors affecting its pattern of development once seasonal stratification is established. Deep critical depths associated with low grazing pressure could offer an alternative or complementary explanation of the high chlorophyll concentrations found at depths of several hundred metres at the beginning of the Vivaldi survey, which were interpreted in Chapter 2 as the results of short-time scale variations in mixed layer depth.

The potential effect of the depth of winter-time mixing on the magnitude of the phytoplankton bloom is highlighted by the simulation. The mechanism, in which the size of the over-wintering zooplankton population supported by the reduced mean primary production over the winter-time mixed layer strongly influences the dynamics of the plankton ecosystem in spring, was put forward by Evans and Parslow (1985) to explain the different characteristics of the annual cycle in the North Atlantic and the North Pacific. In the North Pacific, where deep winter mixing is inhibited by a strong halocline between 100 and 150 m, large spring blooms are not observed and nitrate is not depleted during the summer. Their hypothesis was strongly supported by a sensitivity analysis carried out by Fasham (1995).

The present study illustrates how the same mechanism can potentially cause large pseudo-latitudinal differences in the scale of the phytoplankton bloom over the temperate zone in the eastern North Atlantic. Satellite data do show that larger phytoplankton blooms

occur in the northern part of the study area than in the south. Campbell (1989), for example, showed in an analysis of 1979 CZCS data that the peak in phytoplankton biomass at 50°N on the 20°W meridian was about twice as high as that at 40°N. However, comparison of the temporal patterns of chlorophyll at each location indicates that this larger bloom may have been the result of a longer bloom period in the north, rather than accelerated accumulation from the beginning of the bloom, suggesting earlier nutrient limitation in the south as a more likely cause than spatial variance in grazing pressure. In reality, both are probably important. The interaction of these two factors is illustrated in Figure 3.38, which shows the effect of both winter-time nitrate and zooplankton concentrations on the magnitude of the bloom in the simulation. Here, the winter-time minimum zooplankton concentration has a very large variance and is the major factor controlling the peak phytoplankton concentration. While the bloom is grazing limited over much of the area, the effect of nitrate availability is evident where over-wintering zooplankton populations are low. Much work remains to be done before the dominant factors in the real ecosystem are established.

The largest blooms in the simulation, with peak chlorophyll concentrations of over 15 mg m^{-3} are seen in the north-east, where the winter mixing in the GCM was much deeper than elsewhere. These are, however, unsupported by observational evidence from the local area. The highest surface chlorophyll concentrations observed during Vivaldi were in the north-west (6 mg m^{-3} when averaged over 300 km or about twice this when averaged over 36 km), the north-eastern area being sampled after the main bloom according to the timing given by the simulation. While there is insufficient hydrographic data to discount the exceptional winter-time mixed layer depths shown by the model in the north-east as unrealistic, it was noted, in Section 3.3, that the available observational data suggests they could be over-estimated. If we were to assume this to be the case, we should interpret the dramatic behaviour of the ecosystem model in the north-east as an artefact of the physical model. The less extreme behaviour in the north-west might perhaps be more typical. The magnitude of the bloom here is still greater than further south because of grazing patterns. However, the dynamics are a little more complicated.

The difference between the two versions of this grazing hypothesis depends on the extent of the reduction in zooplankton populations during winter and the timing of the zooplankton recovery. If zooplankton populations fall low enough such that they cannot exert significant grazing pressure early in the bloom, then high new production occurs, producing exceptionally large phytoplankton blooms. This is seen where the winter mixing is very deep. Where the winter mixing is less deep and the winter reduction in primary production is less extreme, but still enough to cause a drop in zooplankton populations, then the reduction in grazing pressure allows sufficient primary production to occur between the winter solstice and the onset of stratification to fuel an earlier recovery, leading to the occurrence of pre-stratification instabilities in the form of predator-prey cycles. These affect the balance between production and consumption, causing phytoplankton blooms which are larger than those in the south where production and consumption are relatively well matched.

The simulation results presented in this study show that spatial variance in grazing pressure might lead to deviations from the traditional model of northward progression of the phytoplankton bloom in the eastern North Atlantic (Strass and Woods, 1988; Weeks *et al.*, 1993b). The northward progression of the spring bloom in 1989 on the 20°W meridian was mapped by Weeks *et al.* (1993b) using data from a series of NABE transects between about 45 and 60°N carried out in mid-April, late May, late June and early August. While the simulated phytoplankton bloom occurs in advance of the observed 1989 bloom, it is consistent with the 1989 pattern in that phytoplankton stocks reach fairly high concentrations everywhere between 47°N and 54°N within a month of bloom initiation. Weeks *et al.* (1993b) interpret the absence of chlorophyll concentrations greater than 1 mg m^{-3} in April, combined with the presence of a bloom as far north as 57°N in May, as a northward progression of 10° per month. However, the model results suggest that this feature of the observations should not necessarily be viewed in the context of a steady progression. A steadier northward progression was seen in the simulation for nitrate

depletion. Weeks *et al.* (1993b) concluded that nitrate depletion, based on the 0.5 mmol m^{-3} nitrate contour, showed a northward progression of about 8° per month, which is very similar to the rate shown by the simulation, between early May and early June, of about 10° per month. Both estimates are much greater than the 3.5° per month estimated by Strass and Woods 1988, based on comparisons between surveys made in different years.

With regard to nitrate utilisation patterns, the model analysis provides support for the hypothesis that the observed south to north gradient in nitrate utilisation is the result of higher new production rates during the bloom in the north. It is not therefore necessary to invoke the alternative explanation of earlier bloom initiation. However, in the light of the results implicating mesoscale dynamics in frontal regions as an important factor contributing to the development of stratification, early bloom initiation as a consequence of early stratification in the region of the North Atlantic Current is seen as an interesting possibility worthy of investigation in future surveys.

In the model, the cause of higher new production in the north, prior to nitrate depletion, is related to zooplankton dynamics rather than nitrate availability and is essentially the greater accumulation of phytoplankton biomass in the north. However, the pre-stratification instabilities in the form of predator-prey cycles, which occur in certain areas, cause a pre-stratification accumulation of ammonium as well as leading to greater accumulation of biomass. The former has a destabilising effect on the balance between new and regenerated production. Resulting fluctuations in the *f*-ratio increase the peaks in new production associated with the high levels of standing stock. Evidence for large fluctuations in the *f*-ratio on time scales of days to weeks has been presented by Sambrotto *et al.* (1993) based on observations during the 1989 North Atlantic Bloom Experiment at 59.5°N 21°W, when a sudden drop in nitrate uptake was apparently compensated for by an increase in regenerated production, keeping total primary production fairly constant. The *f*-ratio dropped from 0.46 to 0.20 during this period.

The 1989 NABE data do not support the idea of more rapid utilisation of nitrate in the north as a general principle. In contrast with the results of this study, the data of Weeks *et al.* (1993b) show a more rapid utilisation of nitrate between about 45 and 49°N, where nitrate decreases at about 4 mmol m^{-3} mth^{-1} (0.13 mmol m^{-3} d^{-1}) during late April and early May, than further north where the rate was generally about half this. More accurate results are available from the time series at 47°N 20°W (Lochte *et al.*, 1993), showing a faster rate of about 6 mmol m^{-3} mth^{-1} (0.20 mmol m^{-3} d^{-1}). At 60°N nitrate was observed to decrease more or less linearly from about 14 mmol m^{-3} in early April to 2.5 mmol m^{-3} in August (Sambrotto *et al.*, 1993) a change of between 2.5 and 3 mmol m^{-3} per month (0.08 and 0.10 mmol m^{-3} d^{-1}). Overall, these rates are similar to mean new production values over much of the 20°W meridian for both of the optimised model solutions (Figure 3.19), but, in both, the new production above about 52°N is much higher due to the low grazing pressure, reaching values of about 0.50 mmol m^{-3} d^{-1}.

Although the high rates suggested by the model are not seen in the NABE data, observational evidence is available from Ocean Weather Station India in 1972 which directly supports the occurrence of such high rates in certain years. Data from that year, used in the optimisation experiments of Fasham and Evans (1995b), show a drop in nitrate of about 10 mmol m^{-3} within a period of about 3 weeks (approximately equivalent to 0.5 mmol m^{-3} d^{-1}). The location of OWS India is within 1° of the NABE 60°N 20°W study site and, although the possibility of an advective contribution to the nitrate reduction cannot be ruled out, the contrast between the two data sets suggests a large inter-annual variability in average new production during the spring bloom period, perhaps linked to the over-wintering success of zooplankton populations.

3.7.3 Mesoscale patchiness

A feature of the Vivaldi survey data and those from other spring bloom surveys is a marked mesoscale patchiness in chlorophyll and nitrate distributions. While this modelling

investigation has focused on larger scales, the results regarding the ecological response to variability in the depth of winter-time mixing, stratification development and pre-bloom nitrate availability are applicable at the mesoscale too. It is difficult to obtain reliable information regarding mesoscale heterogeneity in winter-time mixed layer depth from the survey data. However, the data presented in Chapter 2 (Figures 2.2 & 2.3) certainly shows large variations in seasonal stratification at scales between 36 km (the width of the averaging window) and 300 km (the length of the SeaSoar runs) and mesoscale patchiness is also evident in the pre-bloom nitrate data (Figure 2.15).

Much of the observed patchiness in chlorophyll and nitrate utilisation is likely to be due to differences in timing of the initial stratification, leading to phase differences in bloom development. The potential effect of this can be appreciated if we note that on survey leg W, between 39°N and the Polar Front near 51°N, that the amplitude of the mesoscale patchiness in the surface seasonal density anomaly (Figure 2.4), varies between about 0.2 and 0.4 km m^{-3} (peak to peak). This is a variation of similar magnitude to the trend over 10 degrees of latitude or more. Model rates of stratification development for this area, from the 1991 simulation, are of the order of 1 kg m^{-3} mth^{-1} (Figure 3.9), suggesting that mesoscale patchiness in stratification development on leg W might have caused phase differences of a week or more. The ecological simulation shows that phase differences can also be introduced by spatial variability in winter-time physical conditions via their effect on zooplankton populations. Smith *et al.* (1996) obtained results consistent with this from an investigation of the response of the FDM90 model to mesoscale variability: mesoscale patchiness in biogeochemical variables during the bloom was found to be largely dependent on heterogeneity in over-wintering plankton populations. This strong dependence on relatively long-term dynamics makes it difficult to relate biological patchiness to contemporary physical conditions.

As demonstrated in this study and that of Smith *et al.* (1996), relationships between patterns of biogeochemical and physical fields change during the course of the bloom as

different factors become important. This is seen in observational data too. Weeks *et al.* (1993b) found temporal reversals in the correlation between mesoscale distributions of chlorophyll and temperature during the period of the NABE study. Because of this complication and the dependency on winter-time dynamics we do not, and should not, expect to find clear relationships between biogeochemical and physical variables over the time and space scales of a wide area survey such as Vivaldi. Only limited progress towards understanding the ecological effects of mesoscale variability can therefore be made by such a statistical approach.

While Smith *et al.* (1996) found mesoscale variability to have a only a minor effect on spatially averaged annual primary production, their physical model was a relatively simple quasi-geostrophic model in which frontal dynamics were not represented. In contrast, an enormous effect on spatially averaged primary production was found in the primitive equation modelling study of Lévy *et al.* (1998), although their simulation was limited to a period of about a month so is not directly comparable. As indicated in Chapter 1, there is a significant body of work suggesting that the spatially averaged effects of mesoscale variability could be very important. The present study has provided supporting observational evidence for this hypothesis by quantifying the contribution of buoyancy transport, presumably associated with mesoscale frontal dynamics, to the development of seasonal stratification. Further understanding of the effects of mesoscale variability on bloom development requires intensive mesoscale surveys, combined with mesoscale modelling studies. Data assimilation techniques developed at Harvard University (Robinson, 1996) have recently been used to produce near real time forecasts of mesoscale physical (Robinson *et al.*, 1996; Srokosz *et al.*, 1997) and biological fields (Srokosz *et al.*, 1997) and provide a promising approach to this problem.

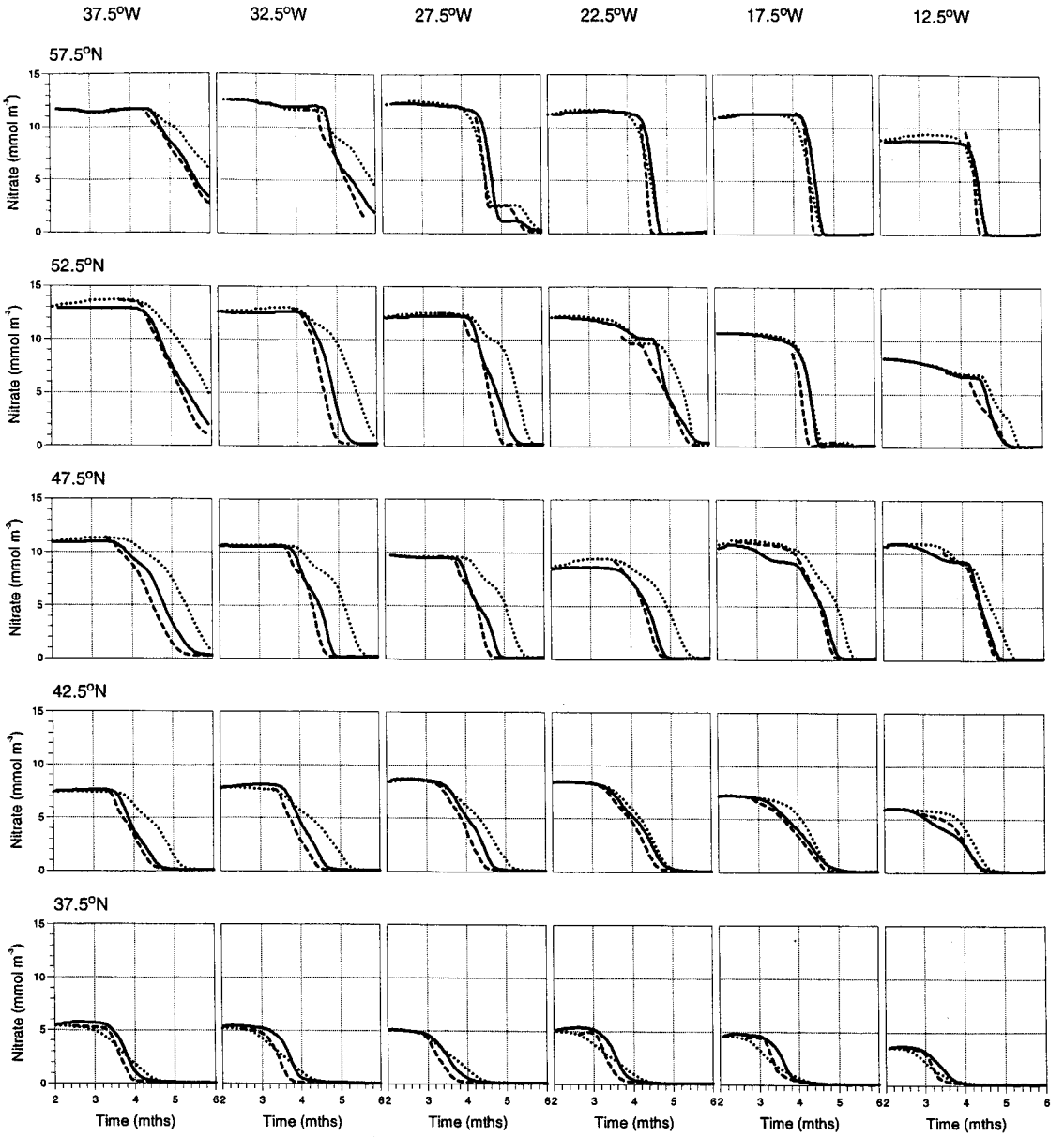

Figure 3.35. Time series of nitrate, from March to June at 5° intervals, for the 1991 and climatological simulations and for the climatological simulation matched to the 1991 simulation by seasonal density anomaly.

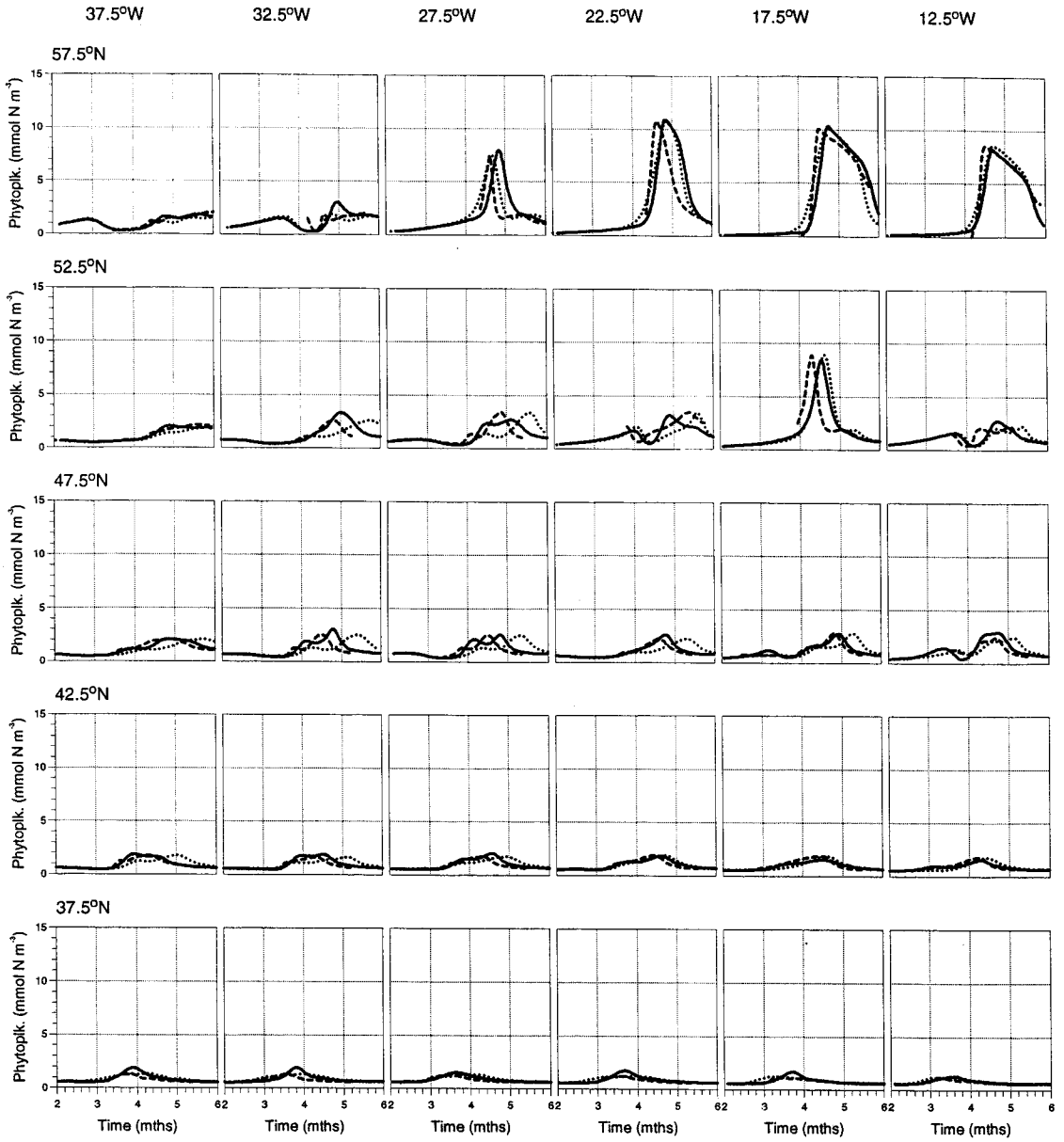

Figure 3.36. Time series of phytoplankton, from March to June at 5° intervals, for the 1991 and climatological simulations and for the climatological simulation matched to the 1991 simulation by seasonal density anomaly.

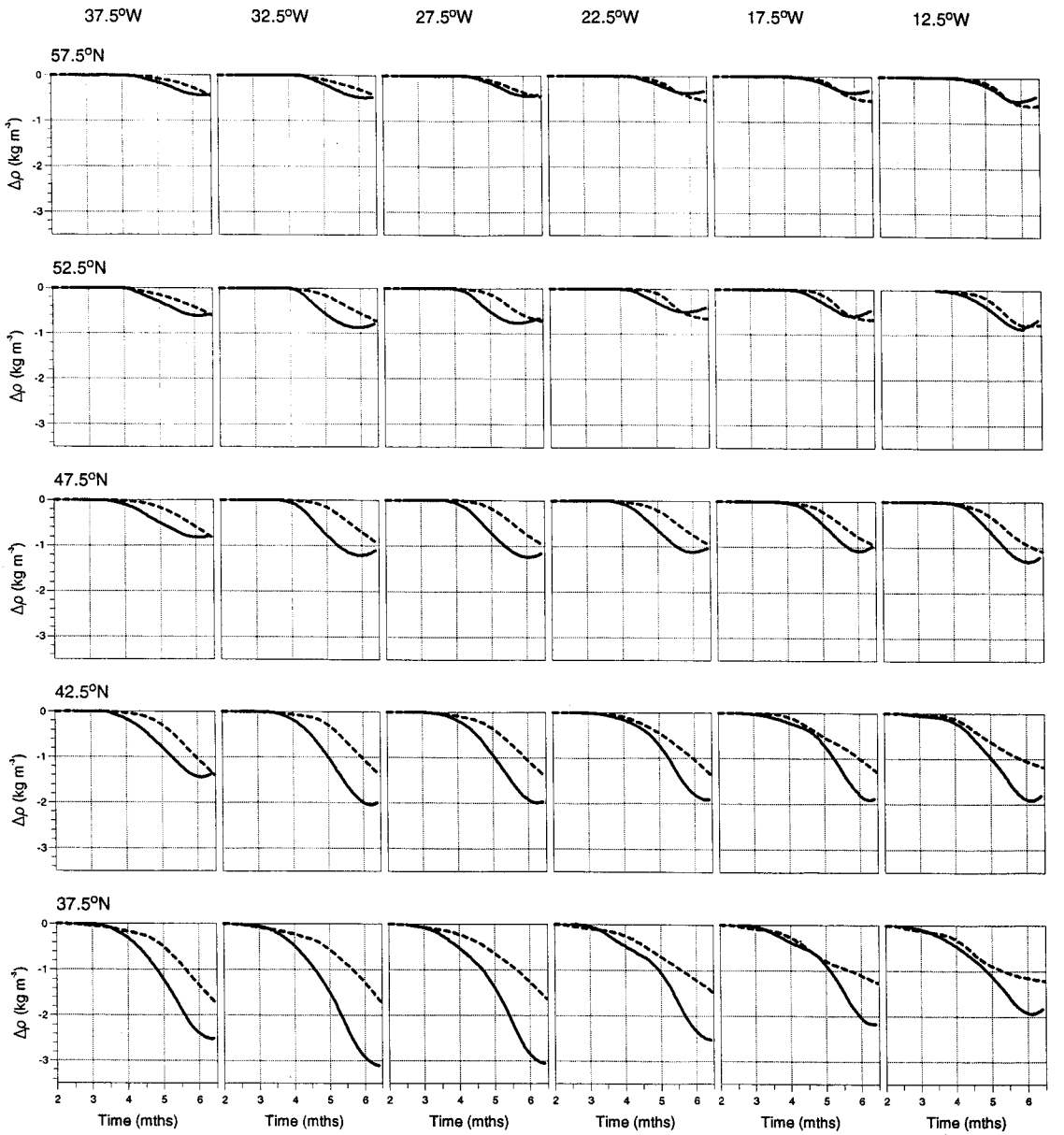

Figure 3.37. Time series of surface seasonal density anomaly, from March to June at 5° intervals, for the 1991 and climatological simulations.

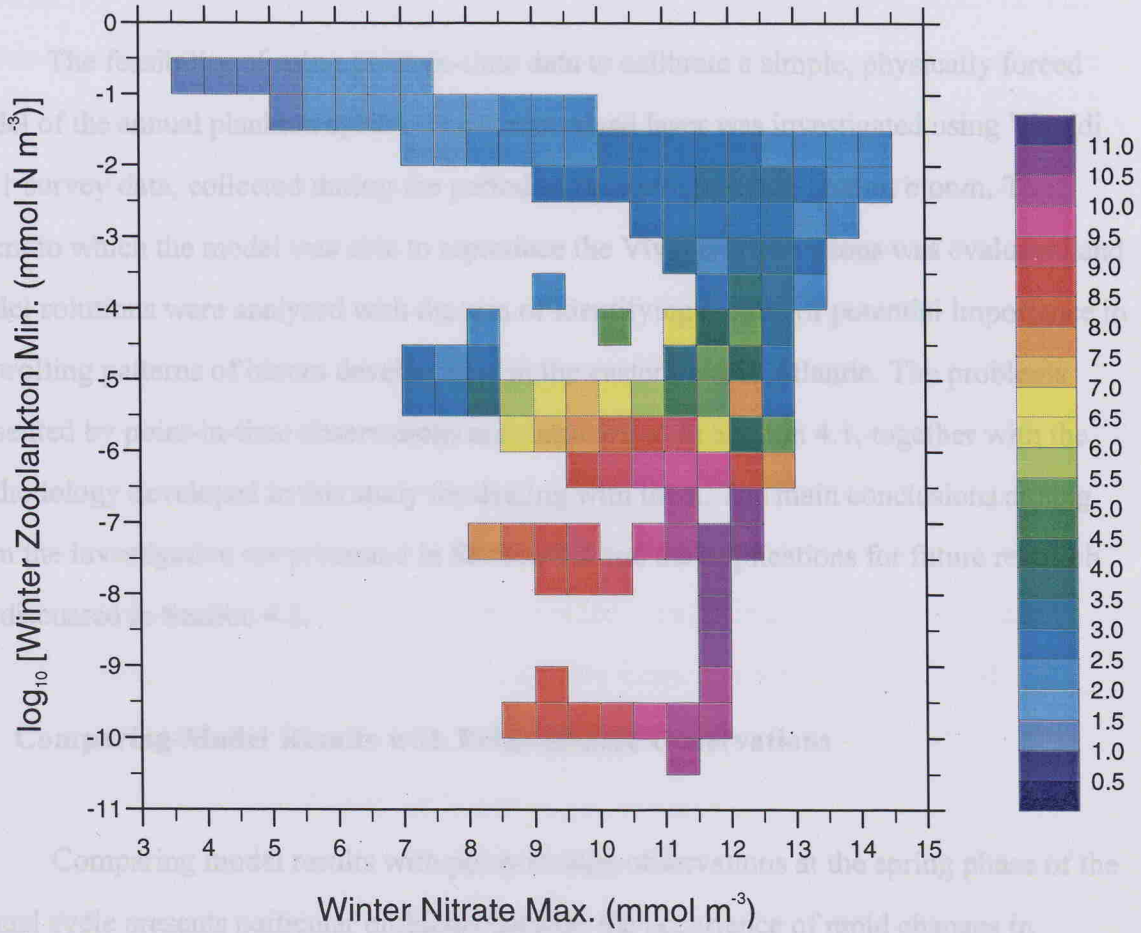

Figure 3.38. Temporal maximum in phytoplankton concentration (mmol N m^{-3}) as a function of the winter-time nitrate maximum and the winter-time zooplankton minimum.

Chapter 4
CONCLUSIONS

The feasibility of using point-in-time data to calibrate a simple, physically forced model of the annual plankton cycle in the ocean mixed layer was investigated using Vivaldi 1991 survey data, collected during the period of the spring phytoplankton bloom. The extent to which the model was able to reproduce the Vivaldi observations was evaluated and model solutions were analysed with the aim of identifying factors of potential importance in controlling patterns of bloom development in the eastern North Atlantic. The problems presented by point-in-time observations are summarised in Section 4.1, together with the methodology developed in this study for dealing with them. The main conclusions arising from the investigation are presented in Section 4.2 and the implications for future research are discussed in Section 4.3.

4.1 Comparing Model Results with Point-in-time Observations

Comparing model results with point-in-time observations at the spring phase of the annual cycle presents particular problems because the occurrence of rapid changes in ecosystem variables at this time makes timing critical. Forcing functions for the ecosystem model must be based on physical simulations or climatological data, which may be out of phase with the seasonal variation in the physical forcing of the real ecosystem. Significant inaccuracies are therefore inevitable and, if useful comparisons are to be made, some allowance must be made for these. The introduction, in this study, of temporal windows over which misfit measures are minimised provides an effective way of achieving this.

The information content of point-in-time observations tends to be low due to both uncertainties in timing and the inherent variability of the ecological response to physical forcing at the seasonal time-scale. The latter is increased by the presence of short time-scale

variability in the physical environment which cannot be resolved by forcing function estimates, but can affect the seasonal dynamics because the ecosystem responds non-linearly to physical forcing. In addition, short time-scale variability introduces noise which can cause observations to misrepresent the seasonal variation in biogeochemical properties. Significant progress has been made in this study towards solving the timing problem. The remaining problems are best tackled by increasing the number of independent observations.

One way of reducing timing errors is to improve the accuracy of the forcing functions, in particular the function representing the development of seasonal stratification (mixed layer depth in the present study). It was demonstrated that year specific stratification time series for forcing an ecosystem model can be obtained from a general circulation model (GCM), spun up under climatological forcing, by using meteorological data for the appropriate spring period to extend the integration. The resulting simulated time series can be partially validated by comparing the modelled and observed seasonal anomalies of density and salinity. The salinity anomaly is used to provide information regarding advective contributions to the stratification development. The application of 1991 meteorological data in this study made a dramatic improvement to the simulated stratification at the time of Vivaldi sampling.

Matching observations to the stratification forcing by the surface seasonal density anomaly was proposed as a method of reducing the discrepancy between modelled and observed biogeochemical fields due to forcing function errors. This approach was evaluated for hypothetical scenarios using two alternative solutions for nitrate, obtained with 1991 and climatological forcing. First one solution and then the other were treated as estimates of the time series given by the alternate solution. Matching by seasonal density anomaly, rather than by time, reduced the error of the nitrate estimate by an average of 32%.

The seasonal anomalies in density and salinity were estimated from observed density profiles by the property differences between the surface and a fixed depth below the seasonal pycnocline. Because mesoscale processes can cause relatively rapid changes in

these property differences for a particular water column, any observational record to be matched by seasonal density anomaly must include a set of vertical profiles averaged over a length scale which is reasonably large compared with the ocean mesoscale. The technique is therefore particularly suited to data obtained from towed undulating platforms such as SeaSoar.

The effect of fluctuating weather conditions on the observed seasonal density anomaly can lead to errors in timing of a week or more, as shown by the analysis of the 1991 survey data. However, this effect can be corrected for by use of a contemporary sea surface temperature (SST) data set, derived from voluntary observing ship records or satellite imagery, provided the coverage of such an auxiliary data set is sufficient to define the variation of SST at the seasonal time-scale.

The application of the methodology developed here to the Vivaldi 1991 survey data provides a good test of its potential value in research. However, the Vivaldi data set contains insufficient independent observations to satisfactorily evaluate a specific ecosystem model, partly because of spatial autocorrelation in the error due to short time-scale variability. Useful progress towards the development of generic ecosystem models requires a larger data set, ideally comprising data from many different surveys and different years, which is more comprehensive with respect to the number of ecosystem variables represented. Despite the limitations of the Vivaldi data set, optimisation results using this data produced a parameter set which gave plausible solutions for the survey area.

4.2 Main Conclusions

Four main conclusions arise from the present study. The first two relate to modelling methodology and the third and fourth contribute to our understanding of the seasonal development of stratification and the phytoplankton bloom respectively.

(1) Point-in-time observations made during the spring bloom can be usefully compared with output from physically forced ecosystem models of the annual plankton cycle, for purposes of parameter estimation and model evaluation, provided allowances are made for phase errors in the physical forcing. These can be greatly reduced, firstly by forcing the ecosystem model with a year specific stratification time series covering the heating season and, secondly, by matching observations to the forcing data by seasonal density anomaly. The effect of weather fluctuations on the observed seasonal density anomaly can be corrected for using a suitable contemporary SST data set, if one is available.

(2) There exists an approximately linear relationship between pre-formed nitrate and salinity over a large section of the eastern North Atlantic, roughly corresponding to the North Atlantic Drift biogeochemical province defined by Longhurst (1995). A model of this relationship has been empirically derived from Vivaldi observations below the seasonal pycnocline. The model can be used to estimate the nitrate concentration of the mixed layer at the end of the winter from spring-time salinity observations, with an accuracy in the order of 1 mmol m^{-3}, because salinity acts largely as a conservative tracer over the heating season. Estimates of nitrate concentration before the spring bloom provide an important constraint for the optimisation of ecosystem model parameters, as well as contributing valuable information to the interpretation of observations made during the bloom.

(3) Vertical shear in the ageostrophic velocity field makes an important contribution to the development of seasonal stratification by virtue of its 'tilting' action on horizontal buoyancy gradients. That part of the contribution associated with pre-existing horizontal buoyancy structure in the winter-time mixed layer was shown to account for up to 50% of the observed surface seasonal density anomaly in some parts of the study area, although the effect was more typically around 20%. The effect was severely underestimated by the GCM and the absence of sharp density fronts and the associated mesoscale dynamics in the model seems the most likely explanation for the discrepancy.

(4) Analyses of the patterns of bloom development implied by the ecosystem model strongly support the hypothesis that spatial variance in zooplankton grazing is one of the dominant factors determining spatial pattern in the spring phytoplankton bloom. The results suggest that variance in the depth and/or duration of winter mixing in the eastern North Atlantic is likely to lead to major differences in grazing pressure in the spring. Such differences could explain the spatial variance in nitrate utilisation rates in 1991 implied by the Vivaldi observations and might also be a major factor contributing to interannual variability in the characteristics of the bloom. The simulation indicates that spatial variance in grazing pressure could strongly distort patterns of northward progression in the phytoplankton bloom.

4.3 Implications for Future Research

The demonstration here of theoretical mechanisms by which bloom development in the eastern North Atlantic is controlled by grazing patterns provides useful working hypotheses which can be tested by future research. Further progress might be made by examining satellite data for features similar to those shown in the simulation. Ocean colour data would ideally be used in conjunction with thermal imagery in order to investigate the possibility of alternative physical explanations. *In situ* data would, however, be required to provide proper evidence of causality and this study serves to underline the need for good quality zooplankton data.

While the insight provided by a single ecosystem model is useful, true advances in the understanding of the processes occurring in nature will require the analysis of a suite of alternative generic ecosystem models, varying in complexity and formulation. These would be tested according to their ability to reproduce observations, given good quality physical forcing data. Probably the most important contributions of this work are therefore those concerned with the improvements in methodology for comparing models and observations. These improvements make it feasible to augment the time series data currently used for parameter estimation and model validation (Fasham and Evans, 1995a,b) with transect data

from wide-area surveys. As well as increasing the size of the observational data set, this would increase spatial coverage, potentially reducing bias in model parameters. Removal of local bias is important if generic models which can simulate the main features of pelagic ecosystems at basin scales, or ultimately anywhere in the global ocean, are to be developed.

The sensitivity of ecosystem model error to physical forcing provides a strong motivation for improving the accuracy of the physical forcing used in model development. The observational evidence presented for major advective contributions to seasonal stratification supports a number of recent mesoscale modelling studies, which predict a shoaling effect of frontal dynamics on the spatially-averaged mixed layer depth (Nurser and Zhang, in revision; Haine and Marshall, 1998; Lévy *et al.*, 1998). Together, this work suggests that the accuracy of ecosystem model forcing functions could be greatly improved either by the use of eddy resolving GCMs or by improved parameterisation of sub-grid scale dynamics.

Finally, as Lévy *et al.* (1998) remind us, averaging the physical forcing over scales of 100s of km may prove to be an over-simplistic approach if the interactions between biogeochemical and physical processes at the mesoscale are shown to have important consequences at larger scales. The salinity-based method of winter-time nitrate estimation provides a potentially important contribution to the ongoing research addressing this problem, because it allows mesoscale patchiness to be resolved. This gives it an important advantage over the Glover and Brewer (1988) method and it could be used to remove much of the mesoscale variance which has hitherto confounded interpretation of observations.

Appendix A
Calibration of Chlorophyll Fluorescence Data

When measured *in vivo*, chlorophyll fluorescence yield (the fluorescence per unit pigment) varies dramatically. This variation is caused by physiological factors associated with light adaptation and nutrient stress and by differences in the phytoplankton taxa present in the sample (e.g. Strass, 1990). Frequent water samples for *in vitro* determination of chlorophyll *a* are therefore vital for calibration purposes. Surface water samples were taken from the ship's pumped sea-water supply at intervals of approximately 1 hour during each of the Vivaldi transects. These observations were used to calibrate chlorophyll *a* fluorescence measured by fluorometers attached to the SeaSoar and the pumped sea-water supply. Measurements from the latter instrument are used to derive the surface chlorophyll variable used in this study. The two instruments had different characteristics and during hours of daylight they were presumed to measure the fluorescence of phytoplankton cells in different photo-adaptive states as the pumped water was in darkness for about two minutes prior to measurement, whereas the fluorometer on the SeaSoar measured the water *in situ*. They were therefore calibrated independently.

Correction for fluorescence quenching, the reduction in fluorescence yield which occurs while photosynthesis is taking place, requires concurrent measurements of Photosynthetically Available Radiation (PAR). These were provided by hemispherical sensors, measuring scalar irradiance, mounted on the SeaSoar and on the ship, the latter being used in the calibration of the fluorescence signal for the pumped water.

A.1 Method

The sampling was timed to coincide with times when the SeaSoar was at the minimum depth in its cycle. For comparison with surface water samples, SeaSoar fluorescence and PAR data collected within 3 minutes of the sampling time were extracted

and averaged over a 2 dbar pressure band, centred on the pressure at the sampling depth (about 4 dbar). Where these restrictions resulted in data gaps of more than 3 hours, top 10 m averages were taken instead with a 5 minute cut-off. This applies to less than 10% of the data points. Fluorescence yield, in arbitrary, instrument dependent units, was determined for surface and SeaSoar measurements after a crude offset correction. The correction was based on a preliminary examination of the relationships between chlorophyll and measured fluorescence and, in the case of the SeaSoar data, an average of measurements at the maximum depth of the SeaSoar cycle (~500 m) where chlorophyll concentration was assumed to be negligible.

Observed surface fluorescence yield and PAR were used to derive an empirical model which defines an estimate of reciprocal yield R (chlorophyll per unit fluorescence) for the complete time and depth range of the fluorescence data collected. This is then used to derive a chlorophyll estimate

$$C_f = Rf,$$

where f is the measured fluorescence (arbitrary units). The model for R is the product of two components: the dark or unquenched yield reciprocal R_n and a quenching factor Q. Both of these are assumed to vary with time t and the latter also varies with PAR I, having a minimum value of 1 during the night. This is expressed by

$$R = R_n(t) \,.\, Q(I, b(t)),$$

where $b(t)$ is a scaling factor which defines the magnitude of the quenching response relative to a long-term mean. The quenching factor is modelled by

$$Q = 1 + b(t)K_1(1 - e^{-K_2 I}),$$

where K_1 and K_2 are constants. Variation of yield with depth is treated as a function of PAR only, this function being derived purely from surface data. However, physiological characteristics of phytoplankton assemblages in the pycnocline, other than their photo-adaptive state, may differ significantly from those in the mixed layer. Sub-surface chlorophyll estimates must therefore be considered much less reliable than those for surface waters.

A first approximation to $R_n(t)$ was given by linearly interpolating the mean observed yield reciprocal for each night of the survey. Observational estimates of Q were then given by the ratio of observed R to R_n and values of K_1 and K_2 were determined for each of the two cruises by fitting a reference quenching model $Q(I,1)$ to all available day-time data (with the exception of data for pumped water from CD59 section YZ onwards which was omitted because of instrument changes). Daily values of b were determined by linear regression of Q against $Q(I,1)$ for each day, with the restriction that $Q = 1$ when $Q(I,1) = 1$. Day-time values for R_n were then obtained by dividing R by $Q(I,b)$ to correct for quenching. A final estimate of $R_n(t)$ was formed by applying a 12 hour running mean to all day-time and night-time observations. $R_n(t)$ and $b(t)$ were linearly interpolated between data points for use in calibrating the fluorescence signal.

A.2 Results

Figure A.1 shows the time series $R_n(t)$. Fluorescence for the pumped water was calibrated separately for two sequences of 3 SeaSoar runs at the end of CD59 (sections YZ - Z and ZA - A). This was necessary because of instrument changes affecting fluorescence yield and the yield reciprocal data for these two sequences is not directly comparable with the earlier data. The data for the pumped water show a 5-fold variation in unquenched fluorescence yield over the survey domain. Those for the *in situ* water show a 9-fold variation. The difference may be due to an underestimate of the offset correction for the pumped water fluorescence. This offset is difficult to estimate because of the absence of near zero chlorophyll concentrations at the surface. The offset correction for the

fluorescence measured by the SeaSoar is expected to be more accurate and the larger 9-fold variation is therefore probably a better reflection of the true changes in yield. Figure A.1 also shows the observed yield reciprocal R for comparison with R_n.

The reference quenching model was fitted to data from CD58 and CD59 separately, defining two independent long-term mean quenching responses for each fluorometer. The coefficients obtained are shown in Table A.1. The reference quenching factor at a PAR level of 100 W m^{-2}, $Q(100,1)$, is also given. The quenching factors as a function of PAR are shown in Figure A.2.

Table A.1. Quenching function parameters with 68% confidence intervals.

Fluorescence measurement	**Cruise**	K_1	K_2 (W^{-1} m^2)	$Q(100,1)$
Pumped water	CD58	7.19 ± 9.84	0.00048 ± 0.00088	1.34
	CD59	1.23 ± 0.18	0.0049 ± 0.0018	1.48
In situ water (SeaSoar)	CD58	3.96 ± 1.20	0.0072 ± 0.0033	3.03
	CD59	2.34 ± 0.32	0.017 ± 0.005	2.91

It is immediately obvious that the fluorescence measured *in situ* is quenched to a much greater extent then the pumped water fluorescence, presumably because of dark adaptation of phytoplankton cells in the pipeline carrying the pumped supply. The extent of the day-to-day variation in the magnitude of the quenching response at a given light level is illustrated by the time series of $Q(100,b)$ (Figure A.3).

The accuracy of the calibration is indicated by the statistics given in Table A.2, which summarise the relationship between C_f and observed chlorophyll C in terms of the mean modulus of the relative deviation $(C_f - C) / C$, and the Pearson correlation coefficient for the two variables.

Table A.2. Fluorescence calibration statistics.

Fluorescence measurement	**Cruise / Section**	$\left(\left\|\frac{C_f - C}{C}\right\|\right)$	r^2
Pumped water	CD58	0.17	0.93
	CD59 W - Y	0.16	0.92
	CD59 YZ & Z	0.21	0.80 (0.72*)
	CD59 ZA & A	0.14	0.60 (0.47*)
In situ water (SeaSoar)	CD58	0.21	0.87
	CD59	0.19	0.83

* Bracketed coefficients are those obtained when a zero offset restriction is applied. The range of C is rather limited for these sections and linear regressions of C_f against C with no restriction give slopes less than 1 and positive offsets. Applying the restriction gives slopes approximately equal to 1.

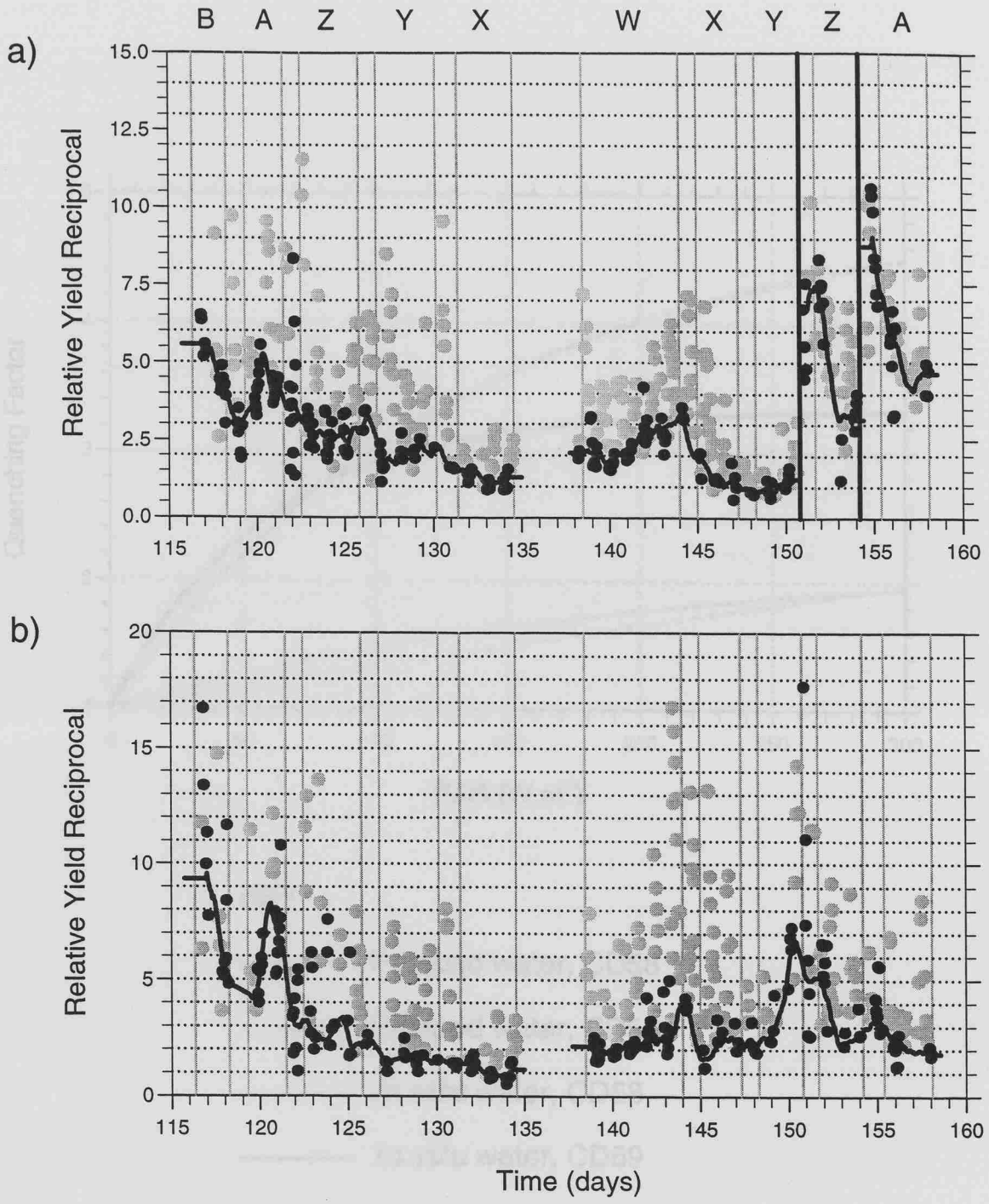

Figure A.1. Estimated 12 hour mean unquenched fluorescence yield reciprocal R_n for (a) pumped water and (b) *in situ* water. The data points show the yield reciprocal R for night-time observations (black) and day-time observations (grey). Units are arbitrary and not directly comparable between the two figures or between the 3 segments delineated by the heavy vertical lines in Figure (a). These indicate the times of instrument changes affecting fluorescence yield.

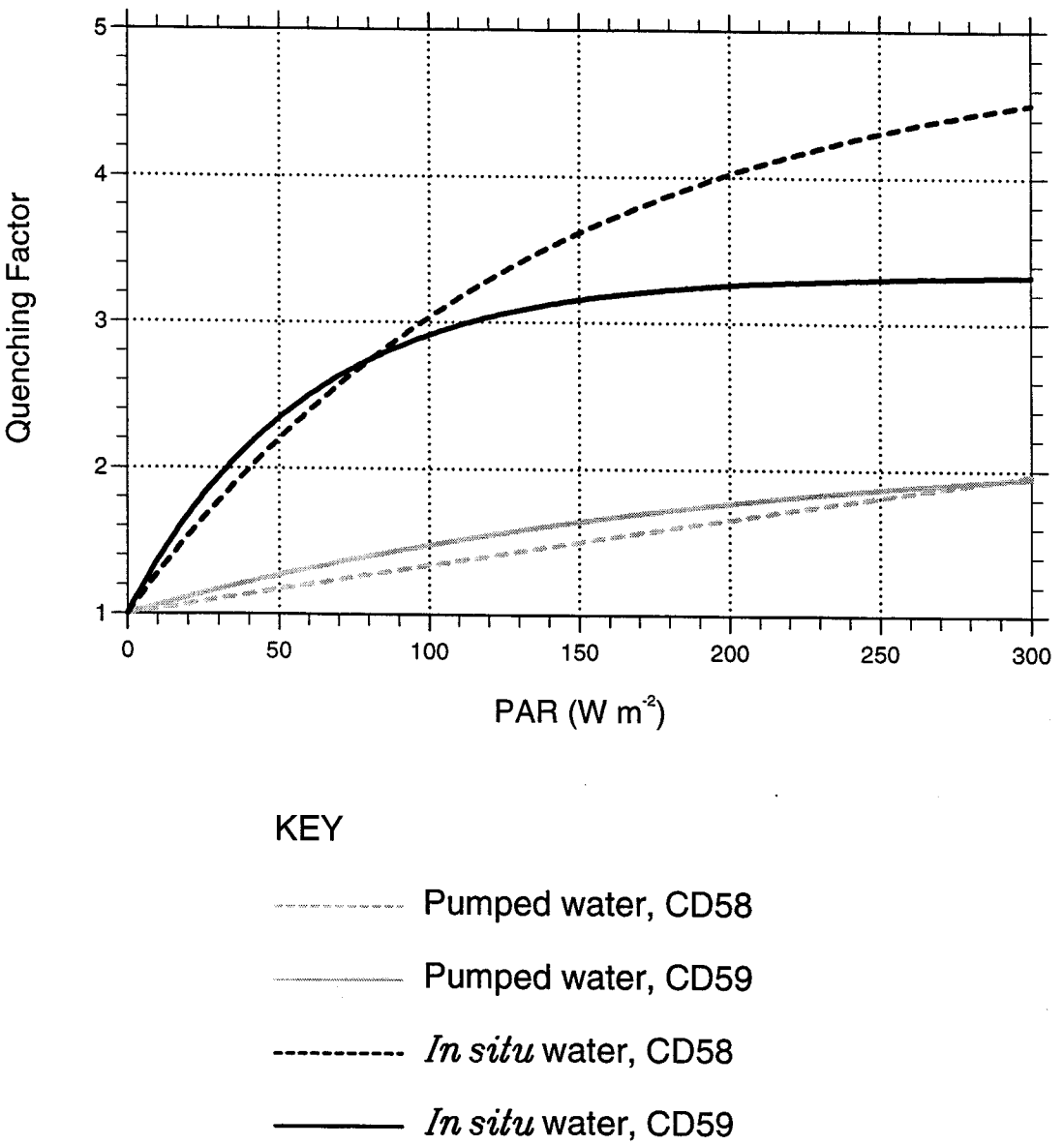

Figure A.2. Variation of estimated reference quenching factor $Q(I,1)$ with PAR I. The curves represent long-term mean responses for each cruise.

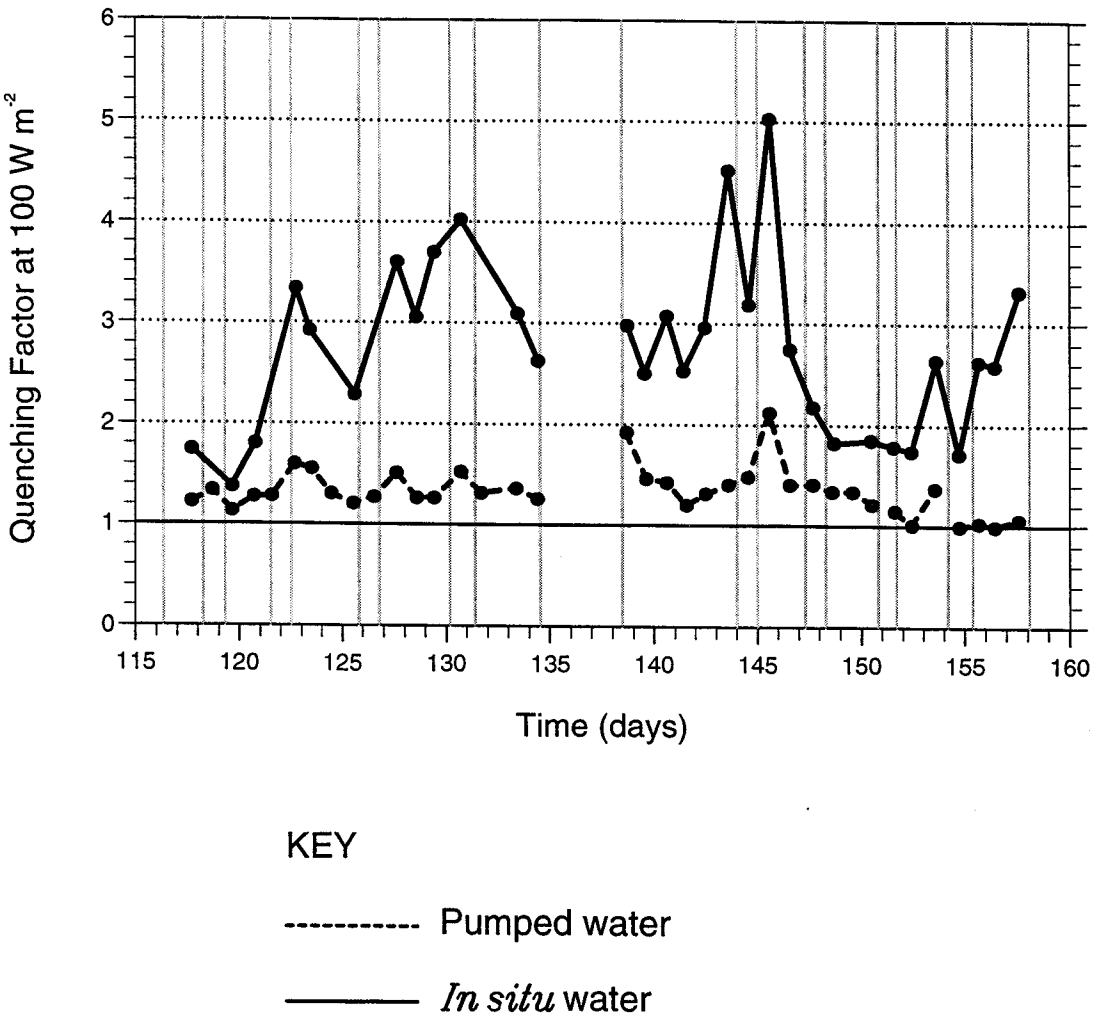

Figure A.3. Estimated quenching factor at a PAR level of 100 W m^{-2}, $Q(100,b)$.

Appendix B
The Extent of Winter-time Mixed Layer Water

B.1 Vivaldi '91 Stability and AOU Data

Figure B.1 shows the water column stability ($-\rho^{-1}\, d\rho/dz$) for each of the survey legs. This has been calculated from the 4 km gridded σ_θ data after applying a 20 m running mean to smooth the vertical profiles before differentiating, as for the temperature gradient. In order to show stability minimum layers more clearly a 300 km running mean has then been applied to smooth out the effects of mesoscale dynamics.

The corresponding AOU field for the Vivaldi survey legs is shown in Figure B.2. Oxygen data is unfortunately only available at the CTD stations on a 300 km grid so the spatial resolution is limited to a minimum of 600 km according to the Nyquist criterion. In order to reduce the sampling error due largely to mesoscale variability, the AOU data has been smoothed by averaging across adjacent stations to give a 900 km mean. The procedure for deriving the AOU field from the deep CTD survey data was as follows. Data for each station profile were divided into 50 m bins and any multiple data points averaged. Then for each station position, subject to availability of data, a 5 station average was calculated. The sample of profiles used in the calculation was made up of the local profile (averaged between the two cruises for repeated stations) and the neighbouring station profiles 300 km to the north, south, east and west. To avoid bias in cases where a data point from a neighbour was not balanced by one on the opposite side those data were excluded from the sample. This means that most of the field in the interior of the survey area is derived from 5 data points and at the edges of the area only 3 data points were used.

B.2 Upper Bound of Winter-time Mixed Layer Water

The upper bound of water retaining the temperature and salinity properties of the winter-time mixed layer is defined by the base of the seasonal pycnocline. In, general the pycnocline is well defined with the stability maximum tending to increase from east to west in the southern part of the survey area and from west to east in the northern part. This is largely a temporal effect reflecting the evolution of spring stratification. Super-imposed on this pattern, if we look at the water column as a whole down to 500 m, we can see there is a tendency for the stability increase towards the west. This is probably due to the effects of vertical shear on the buoyancy transport in regions of stronger mesoscale eddy activity, a hypothesis which is discussed in some detail in Section 2.4.

The apparent effect of vertical shear makes it difficult to determine the vertical extent of the seasonal pycnocline on some parts of leg W where there does not appear the be a well defined stability minimum. However, over most of the survey area there is no evidence of seasonal heating below about 150 m and the enhancement of seasonal stratification by vertical shear would make it less likely for seasonally heated water to be mixed down to this depth so it is probably reasonable to assume that a depth of 150 m is safely below the seasonal pycnocline everywhere. Vertical velocities associated with mesoscale eddy activity in areas of strong flow can advect seasonally heated water to greater depths but the features caused by this process are small, typically in the order of 10 km in diameter, and are unlikely to have a major effect on the larger scale averages used in this study.

B.3 Lower Bound of Winter-time Mixed Layer Water

The lower bound of water which was in the surface boundary layer during the last winter is marked by an increase in the vertical gradient of AOU. Strong vertical gradients in AOU can be seen at two distinct levels. The shallower level is immediately below the surface. Here, negative values are observed indicating supersaturation as a result of

photosynthesis. The deeper level lies between about 200 and 800 m. Climatological data indicates winter mixed layer depths in this range for the region and it is therefore reasonable to interpret the AOU gradient as a separation between water ventilated during the last winter and much older water. The relatively homogenous region above this level is the signature of the most recently formed water. Its deepest extent is from a minimum of about 200 m in the west to a maximum of between 600 and 700 m in the east. This depth is safely below the seasonal thermocline as determined from the stability data, with the possible exception of leg W, providing good evidence for the existence of a band of 'pure' winter-time mixed layer water below the seasonal thermocline.

The 900 km resolution of the AOU data is rather limited and we cannot exclude the possibility of fairly large areas where the lower bound of ventilated water could lie above that indicated by these data. It is therefore important to examine the stability field for independent evidence of the deepest extent of winter mixing. Over most of the survey area there is a broad stability minimum which extends below the 200 m depth indicated as the shallowest limit of older water by the AOU field so in general the stability does not show evidence of older water above this depth. There are however a few exceptions, notably a fairly pronounced stability minimum at around 150 m, to the south of about 42°N on legs Y and Z and also to the north of about 52°N on leg X and 51°N on leg Y. The latter lies to the north of the Polar Front and appears to correspond to the colder Atlantic Subarctic Intermediate Water in this region, although it is not apparent on leg W. In these areas evidence for the existence of a significant layer of water retaining the properties of the winter-time mixed layer is therefore rather less conclusive than elsewhere.

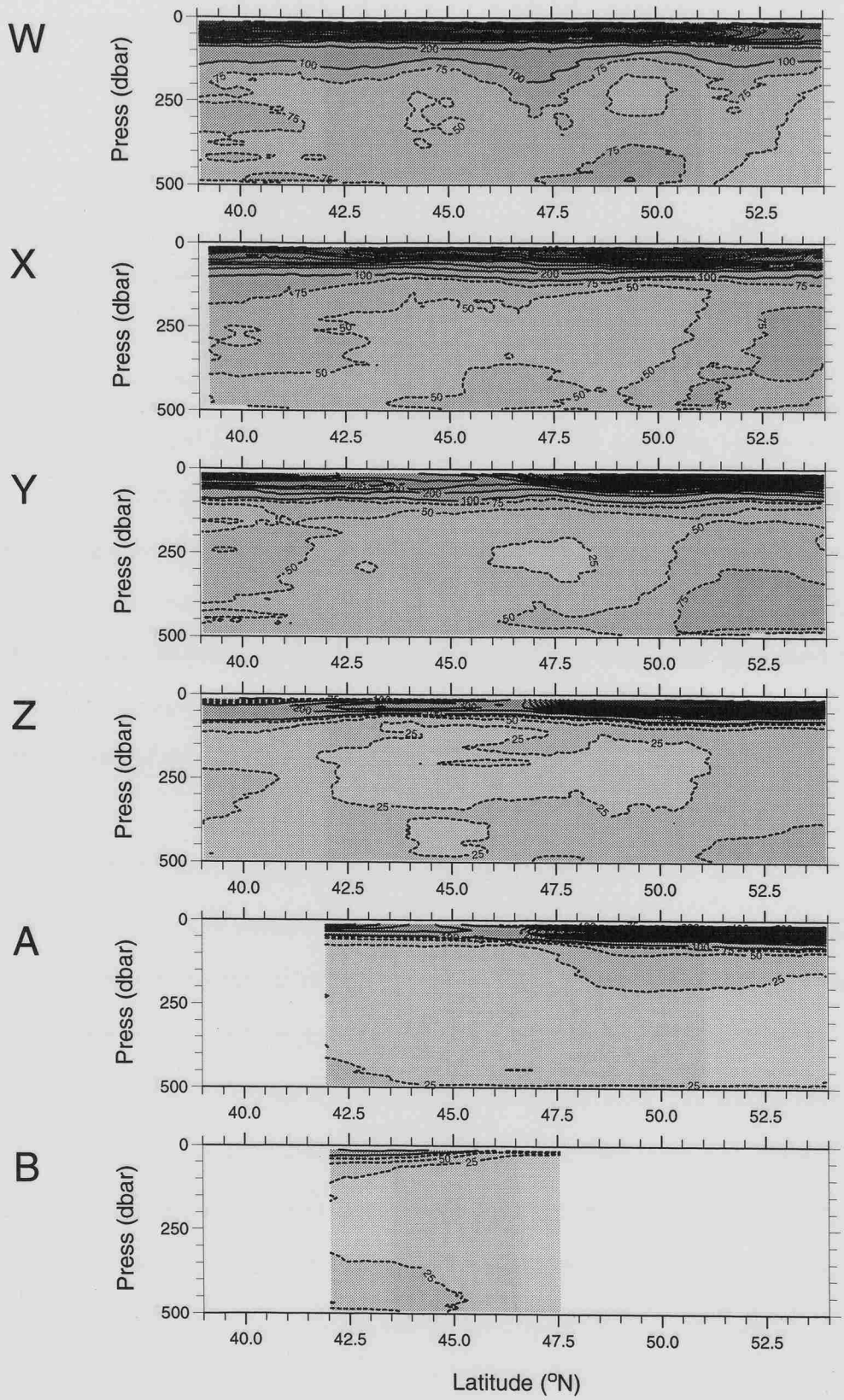

Figure B.1. Vertical sections of 300 km mean stability for Vivaldi transect legs (10^{-8} m^{-1}).

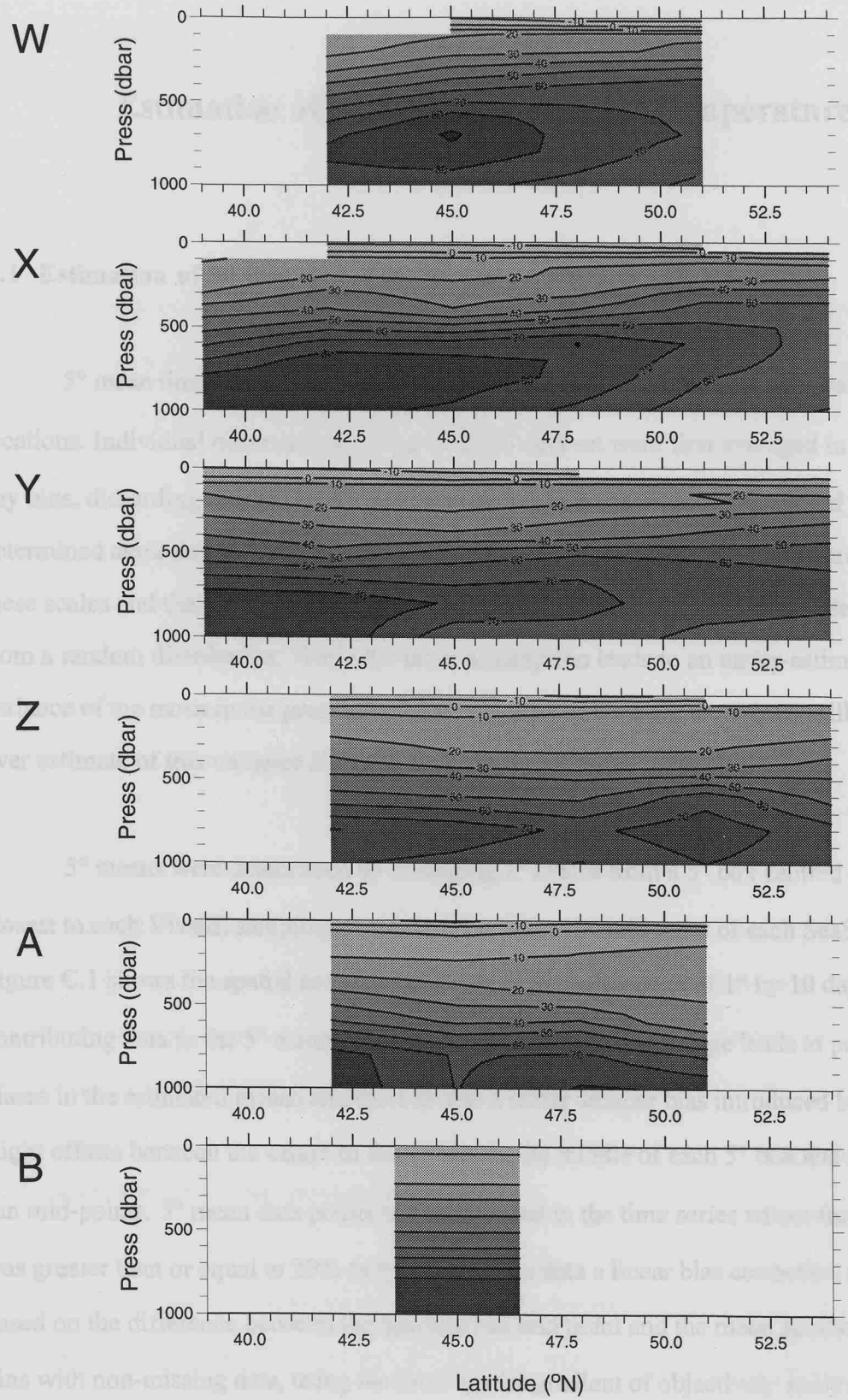

Figure B.2. Vertical sections of 900 km mean AOU for Vivaldi transect legs (mmol m^{-3}).

Appendix C
Estimation of 5° Mean Sea Surface Temperature

C.1 Estimation of 30 Day SST Time Series

5° mean time series of SST from March to June were determined at Vivaldi sampling locations. Individual observations in the COADS data set were first averaged in $1° \times 1° \times 10$ day bins, discarding means for any bins with less than 3 observations. Standard errors were determined assuming that random errors dominated over temporal and spatial trends on these scales and that observations within each bin could be treated as independent samples from a random distribution. While the latter assumption leads to an under-estimation of the variance of the mean in the presence of dependencies in the data, the former will lead to an over estimate of this variance if trends are actually present.

5° means were determined by averaging 1° means from a 5° box centred on the bin closest to each Vivaldi sampling position, taken to be the mid point of each SeaSoar run. Figure C.1 shows the spatial coverage in terms of the percentage of 1° by 10 day bins contributing data to the 5° mean SST estimates. Incomplete coverage leads to positional biases in the estimated means and there is also a rather smaller bias introduced because of slight offsets between the centre of the 1° bins in the middle of each 5° box and the SeaSoar run mid-points. 5° mean data points were only used in the time series where the coverage was greater than or equal to 20% ($n = 5$). For these data a linear bias correction was made, based on the difference between the SeaSoar run mid point and the mean position of all 1° bins with non-missing data, using the local spatial gradient of objectively analysed monthly mean SST data (Figure C.2), linearly interpolated between monthly mid-points. The objective analysis method is described by da Silva and Levitus (1994) and has the effect of a

filter with a response function which heavily damps out wavelengths smaller than 770 km and has values of 0.95 at 1980 km, 0.49 at 1100 km and 0.23 at 880 km. Time series of the estimated bias for the data points used are shown in Figure C.3. A three point running mean was applied to the 10 day SST time series data and the resulting 30 day mean interpolated linearly to the Vivaldi sampling time.

Standard errors for the 5° means were determined from the 1° errors, assuming that samples from different 1° bins were independent, according to the Gaussian law of error propagation. For a linear function of random variables

$$g(X_i) = \sum_{i=1}^{n} w_i X_i$$

this gives

$$\mathrm{var}(\overline{g}) = \sum_{i=1}^{n} w_i^2 \, \mathrm{var}(\overline{X}_i).$$

Errors were likewise propagated during the time series processing assuming independence between adjacent 10 day bins. Although it is difficult to determine confidence intervals for the bias corrections the biases themselves are in most cases small compared with the confidence intervals for the SST estimates so this is not a major problem.

C.2 Estimation of Point-in-time SST

Vivaldi SST observations for each SeaSoar run are treated as a sample from a 5° mean SST field at a point in time and the 300 km mean for the transect is taken as an estimate of the 5° mean SST at the mean time of sampling. This estimate is expected to have a small bias wherever the second derivative of the large scale SST field is non-zero due to

the limited coverage of the 5° box. Spatial biases in the 300 km means due to variation in large scale gradients were estimated and corrected for as far as possible using the 1° objectively analysed SST fields (Figure C.2) by comparing 1° by 3° means with 5° by 5° means at time of sampling. The 4 km data for each SeaSoar run were first averaged in latitude/longitude bins equivalent to 12 km to ensure even coverage.

Confidence intervals were determined allowing for autocorrelation in the data using the expression for the variance of the sample mean given by Priestly (1981):

$$\mathrm{var}(\bar{x}) = \frac{\sigma^2}{\kappa n},$$

where κ can be written in terms in the normalised population spectrum at zero frequency $f(0)$ as

$$\kappa = \frac{1}{2\pi f(0)}.$$

$f(0)$ is estimated using the method described by Challenor and Carter (1994) by fitting an order 1 autoregressive model (AR(1) model) to the residuals obtained after removal of linear trends in latitude/longitude. Least squares regression was used throughout.

C.3 Results

Table C.1 gives the time-of-sampling 5° mean SST estimates $T_{30}(0)$ and $T(0)$ for each SeaSoar run for which sufficient COADS SST data were available, together with the resulting event-scale SST anomaly estimates $\delta T(0)$. $T_{30}(0)$ time series are shown in Figure C.4. The term κn in the table is the estimated effective sample size for each Vivaldi transect, used in the determination of the $T(0)$ standard error, which allows for dependency arising

from autocorrelation in the data. The Vivaldi sampling bias is the bias due to the limited coverage of the 5° box by the 300 km transect, estimated from the COADS objectively analysed SST data (Figure C.2). $T(0)$ includes a correction for this bias term.

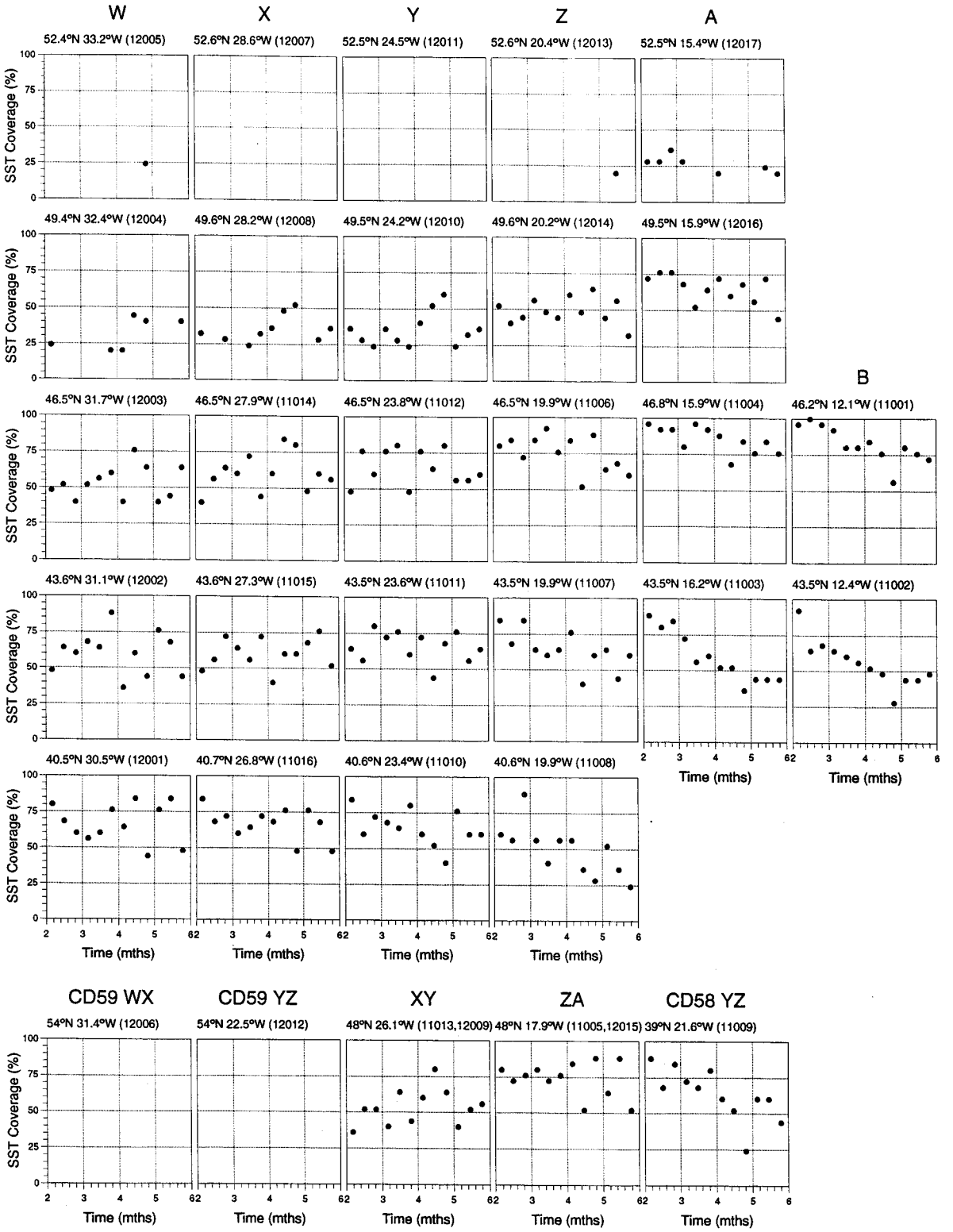

Figure C.1. COADS SST coverage: percentage of the 25 one degree bins contributing to the 5° mean SST $T_{30}(0)$, centred on Vivaldi SeaSoar run mid-points.

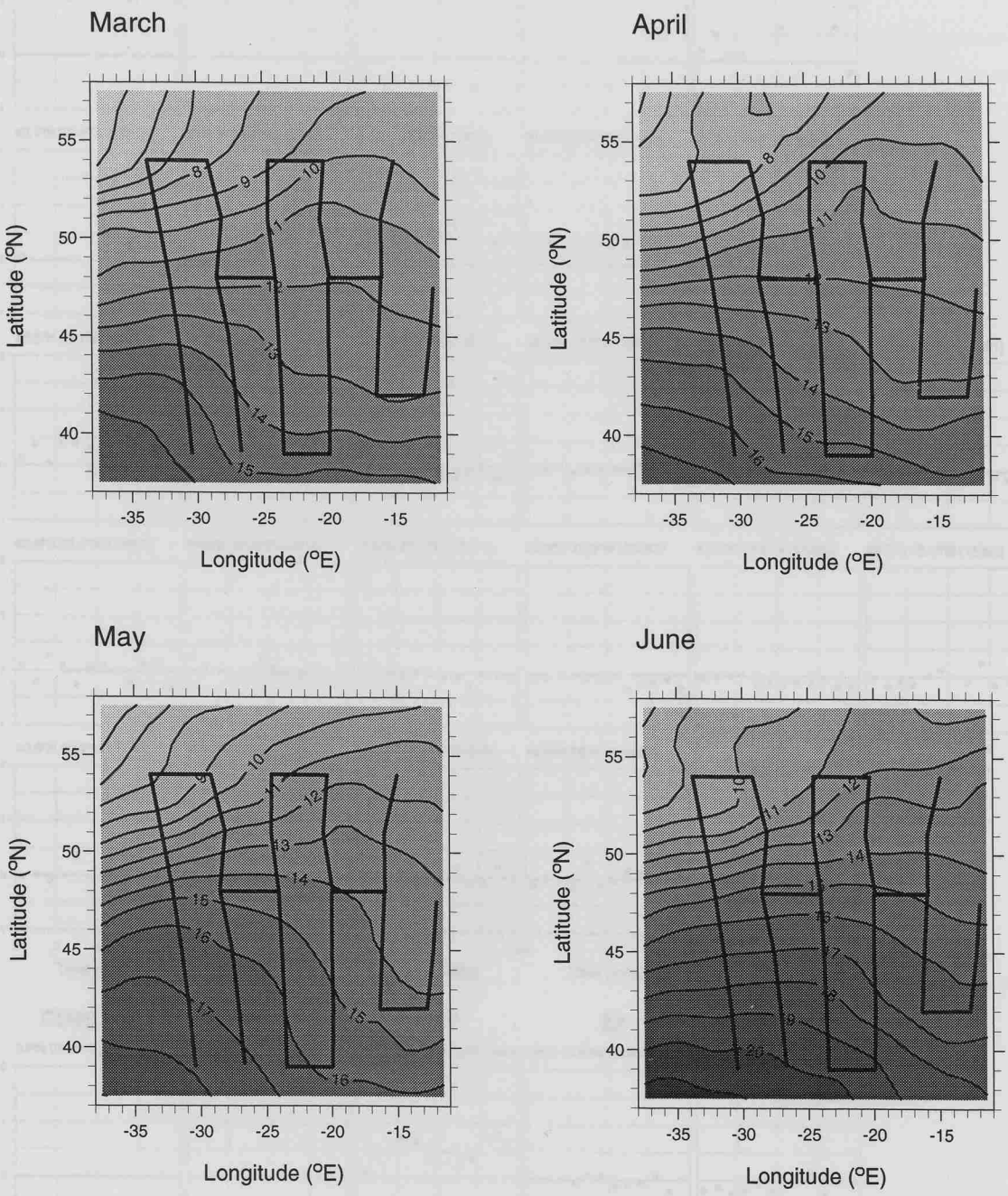

Figure C.2. Objectively analysed COADS monthly mean SST (°C) for March to June 1991.

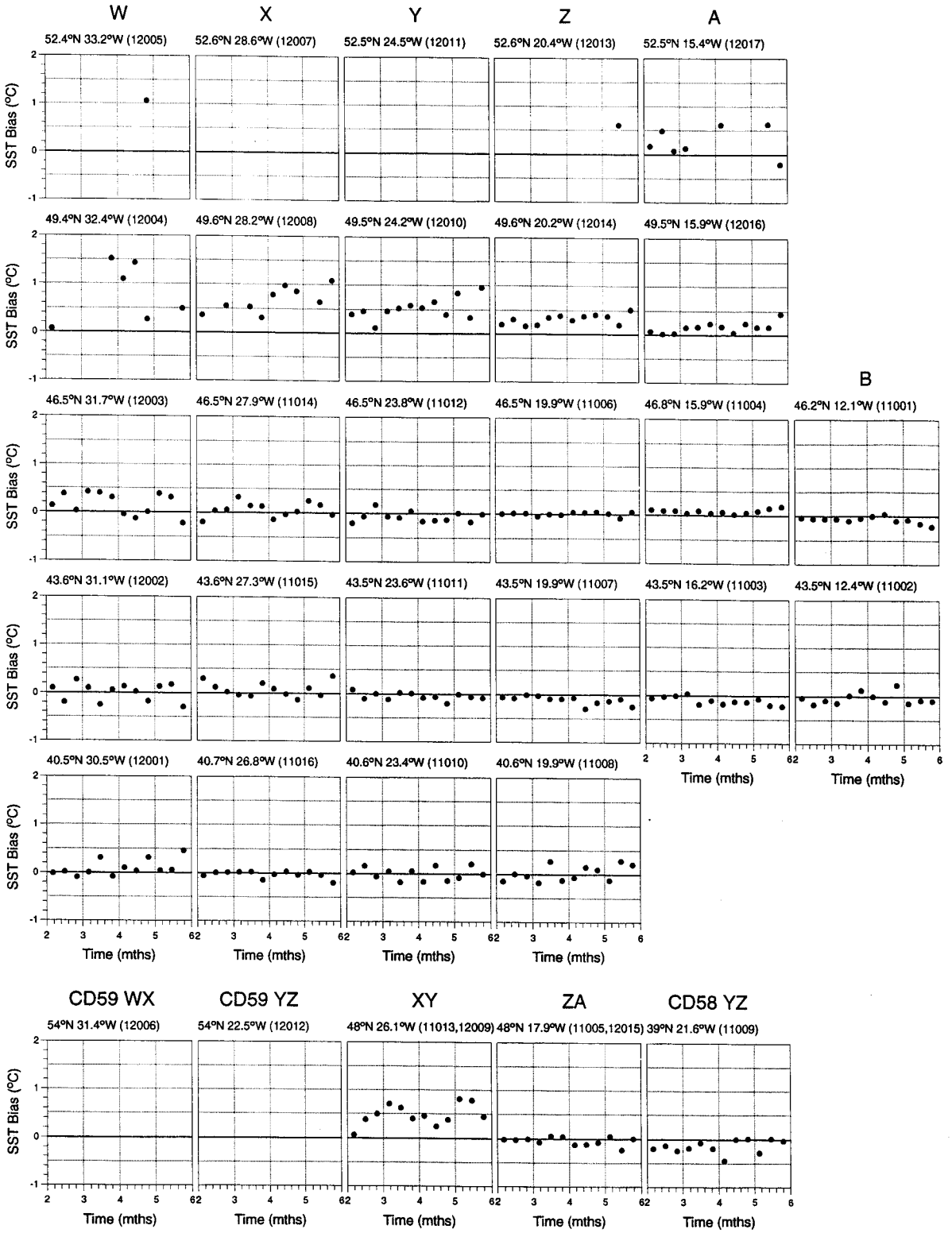

Figure C.3. Positional bias for COADS 5° mean SST with respect to Vivaldi SeaSoar run mid-points.

Table C.1 Event-scale temperature anomalies.

Section	SS run	$T_{30}(0)$		$T(0)$				$\delta T(0)$	
		mean	SE	mean	SE	κn	samp. bias	mean	SE
CD58 B	11001	11.96	0.08	11.83	0.03	10.8	-0.01	-0.13	0.09
	11002	13.04	0.10	12.89	0.11	2.7	-0.12	-0.15	0.15
CD58 A	11003	13.37	0.09	12.81	0.05	5.7	-0.03	-0.55	0.10
	11004	12.67	0.05	12.19	0.09	1.3	0.01	-0.48	0.10
CD58 ZA	11005	12.63	0.05	12.24	0.13	4.1	0.04	-0.39	0.14
CD58 Z	11006	13.33	0.07	12.99	0.18	2.4	0.03	-0.34	0.20
	11007	14.41	0.10	13.24	0.02	11.4	-0.04	-1.17	0.10
	11008	14.93	0.14	14.45	0.07	13.1	-0.07	-0.47	0.15
CD58 YZ	11009	15.70	0.10	15.40	0.14	2.7	-0.05	-0.30	0.18
CD58 Y	11010	15.77	0.09	15.22	0.06	4.1	0.03	-0.55	0.11
	11011	15.23	0.08	14.53	0.17	3.7	0.03	-0.70	0.19
	11012	14.39	0.06	14.08	0.13	4.4	-0.01	-0.32	0.15
CD58 XY	11013	14.07	0.09	13.20	0.10	3.9	0.02	-0.88	0.13
CD58 X	11014	15.11	0.08	14.17	0.15	3.3	0.03	-0.94	0.17
	11015	16.16	0.07	15.76	0.16	2.9	-0.02	-0.40	0.18
	11016	16.95	0.09	16.83	0.08	5.3	-0.01	-0.11	0.12
CD59 W	12001	17.61	0.07	18.14	0.23	2.2	0.01	0.53	0.24
	12002	16.90	0.08	17.03	0.12	3.8	0.01	0.13	0.15
	12003	15.90	0.07	15.97	0.29	2.3	0.05	0.06	0.30
	12004	12.66	0.11	12.92	0.22	6.9	0.08	0.25	0.24
CD59 XY	12009	15.16	0.07	15.18	0.06	9.4	0.09	0.02	0.09
CD59 Y	12010	14.20	0.11	14.09	0.15	4.1	-0.01	-0.11	0.18
CD59 Z	12014	14.35	0.08	15.46	0.27	2.8	0.06	1.10	0.28
CD59 ZA	12015	14.87	0.07	14.91	0.12	4.0	0.11	0.05	0.14
CD59 A	12016	14.21	0.07	13.70	0.23	1.3	0.02	-0.52	0.24

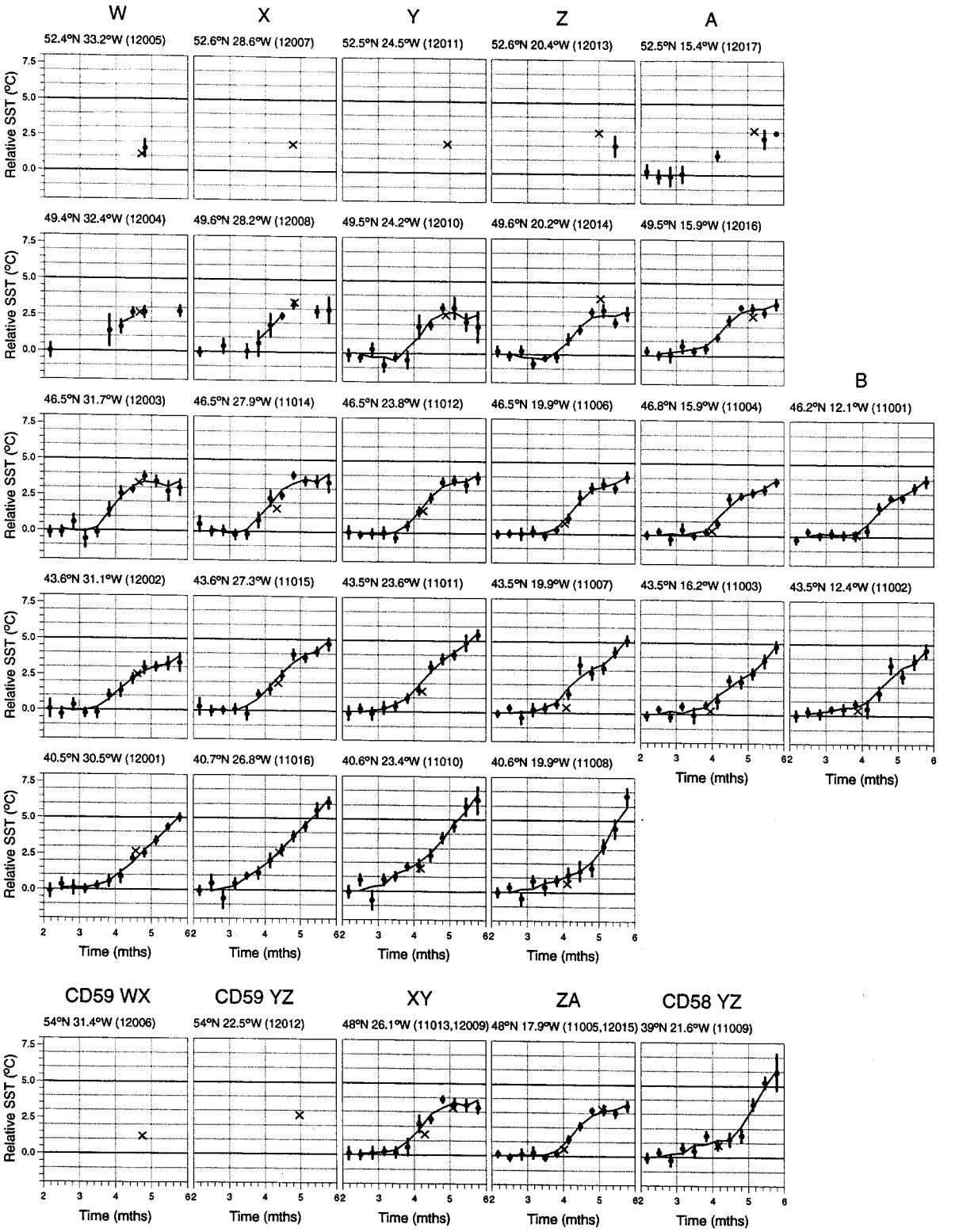

Figure C.4. Time series of COADS 5° mean SST $T_{30}(0)$, from March to June 1991, centred on Vivaldi SeaSoar run mid-points. Temperature scales are offset for each location to give the temperature difference relative to the local March value. The data points show the means for each 10 day bin with 95% confidence intervals. Crosses show the Vivaldi 300 km mean SST $T(0)$.

Appendix D
Physical Model Configuration

For the purposes of the present study, time series representing seasonal variation in stratification were provided by a 16 year North Atlantic integration of the MICOM general circulation model (version 2.6) as described in Chapter 3. The model configuration for this run was based on the 4/3° model described by Jia (submitted) with the differences outlined below (Jia, pers. comm, 1997).

The surface referenced potential densities defining the discrete model layers are given in Table D.1. Layer 1 is the surface boundary layer which is implemented as a vertically homogenous Kraus-Turner formulation mixed layer (Kraus and Turner, 1967) having a temporally and spatially varying density distribution.

Table D.1. MICOM layer densities.

Layer	σ_θ	Layer	σ_θ
1	Variable	11	27.00
2	24.70	12	27.20
3	25.28	13	27.45
4	25.77	14	27.74
5	26.18	15	27.82
6	26.40	16	27.88
7	26.55	17	27.92
8	26.70	18	28.00
9	26.80	19	28.09
10	26.90	20	28.12

Kraus-Turner turbulence energy dissipation parameters m and n were chosen to optimise the fit of the mixed layer model to mixed layer depth data from the subduction experiment described by Moyer and Weller (1997). Their values are are given by:

$$m = 0.8 \exp(-h/50)$$
$$n = 0.4 \exp(-h/50),$$

where h is the mixed layer depth.

Diffusion velocities are 2 cm s^{-1} for layer thickness, 1 cm s^{-1} for temperature and 2 cm s^{-1} for velocity, as used in DYNAMO. The horizontal diffusion coefficients are the products of the diffusion velocities and the grid spacing which decreases with increasing latitude.

Appendix E
Ecosystem Model Solutions

The ecosystem model solutions covering the period from March to June 1991 at the Vivaldi SeaSoar run locations are presented here for each of the three parameter sets used in Chapter 3 (Table 3.2), together with the physical forcing functions at each location. The forcing comprises annual climatological cycles of mixed layer depth (Figure E.1) and cloudiness (Figure E.2) each succeeded by functions specific to 1991 for the months February to July. Figures E.3 to E.6 show the solutions for each of the state variables, with the exception of nitrate which was presented in Figure 3.15. Model time series are also given for total volumetric primary production (Figure E.7) and the *f*-ratio (Figure E.8).

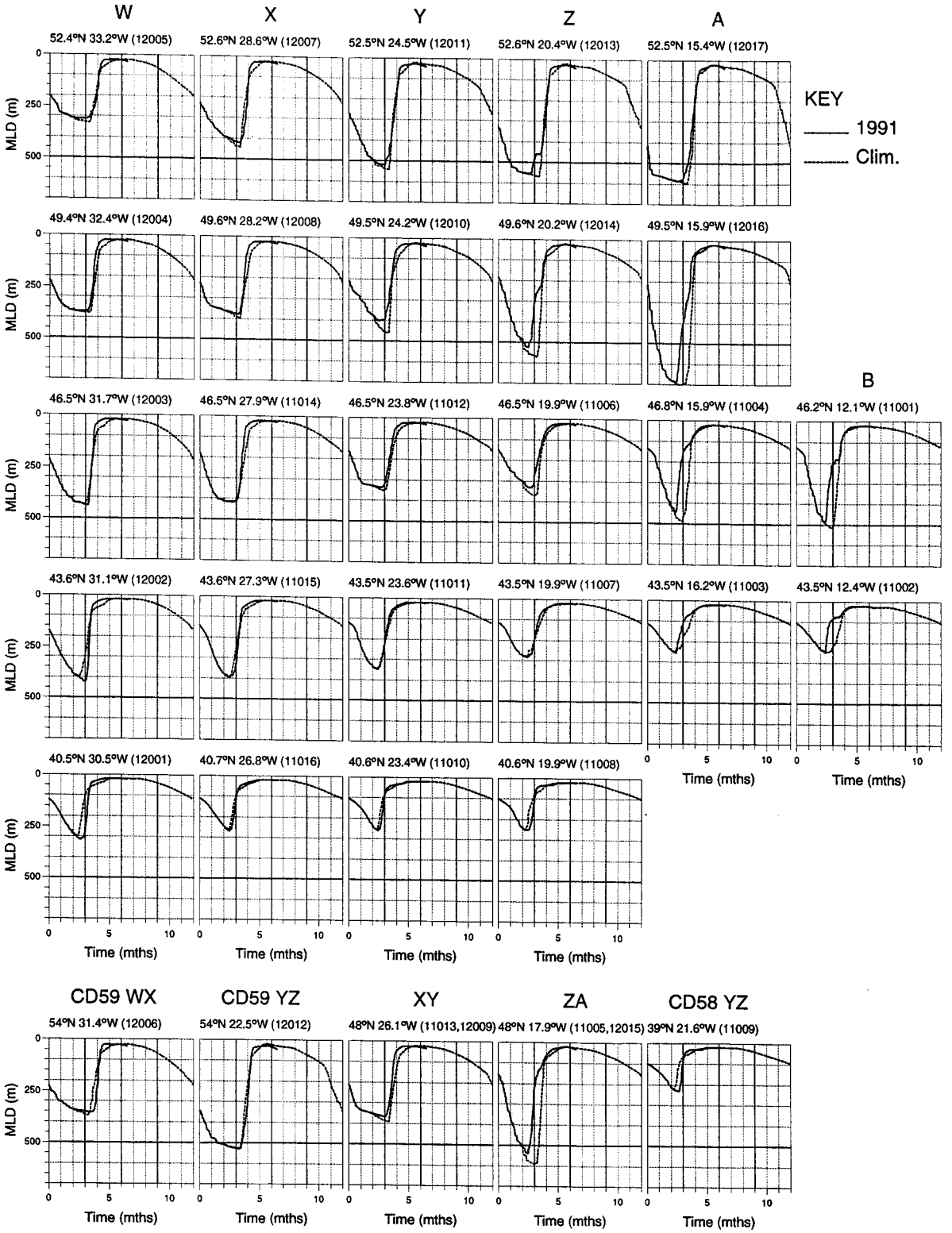

Figure E.1. Model 5° mean time series of mixed layer depth at Vivaldi SeaSoar run locations for the climatological and 1991 simulations.

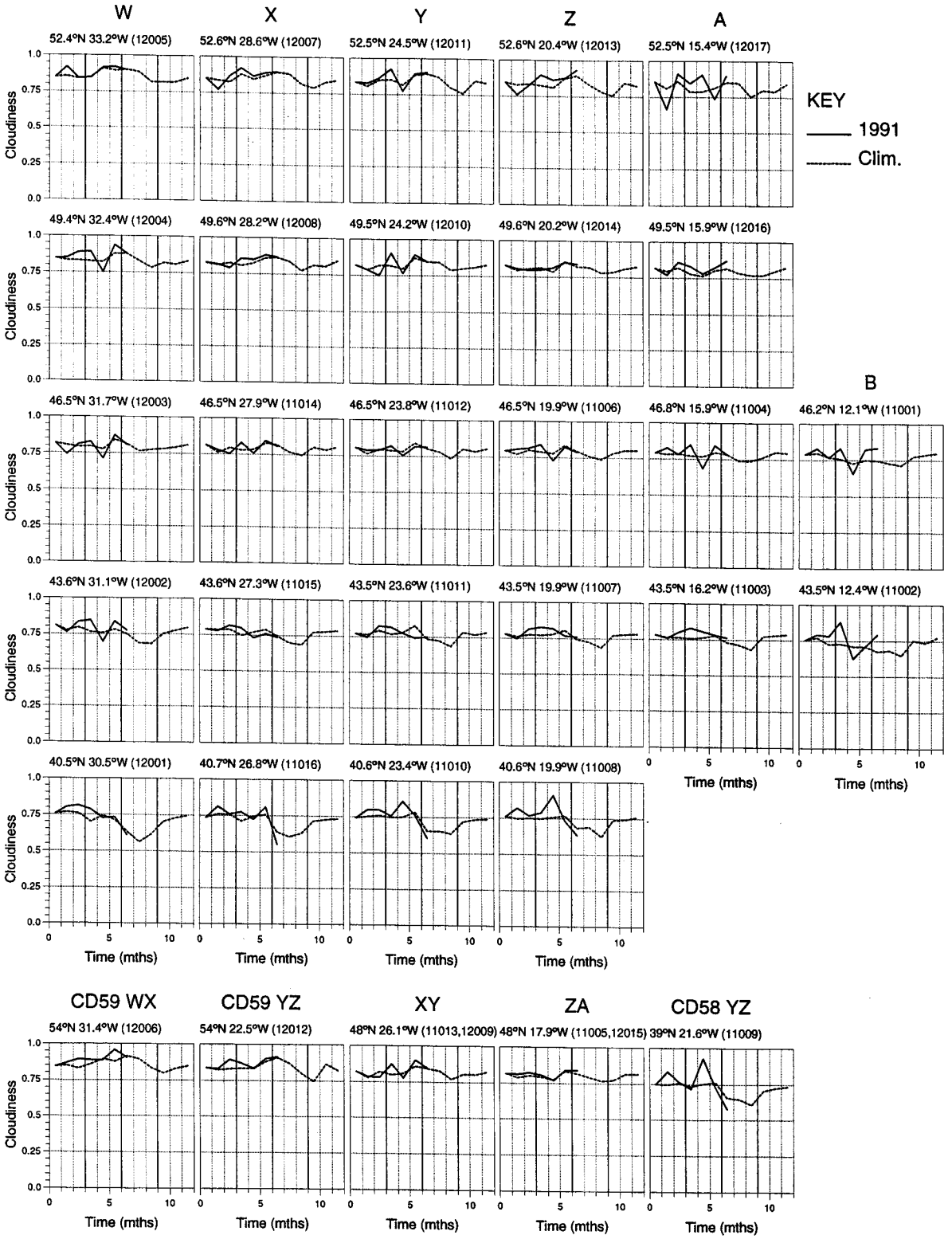

Figure E.2. Time series of COADS objectively analysed fractional cloudiness, at Vivaldi SeaSoar run locations, from climatological and 1991 data sets.

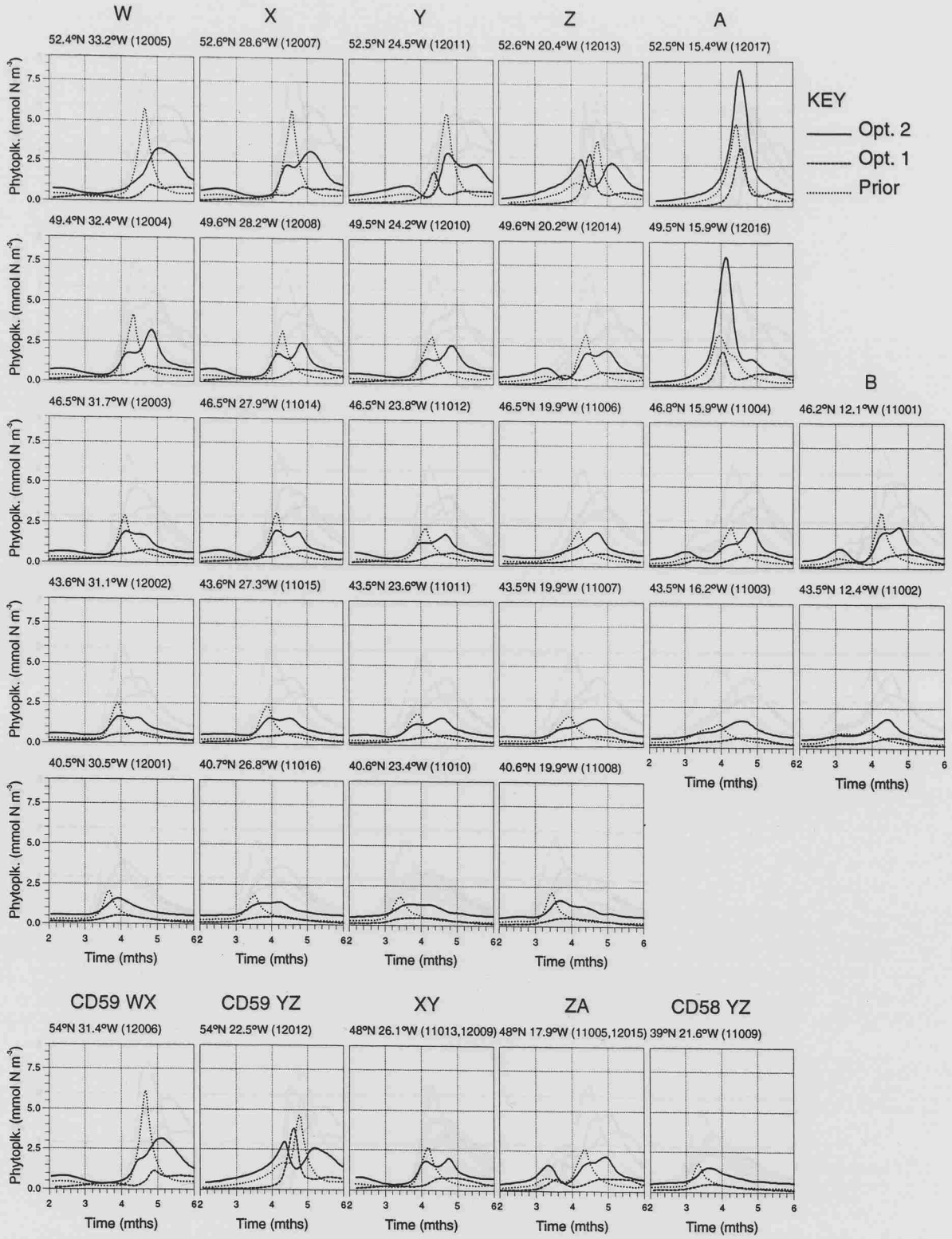

Figure E.3. Model solutions for phytoplankton, from March to June 1991, at Vivaldi SeaSoar run locations.

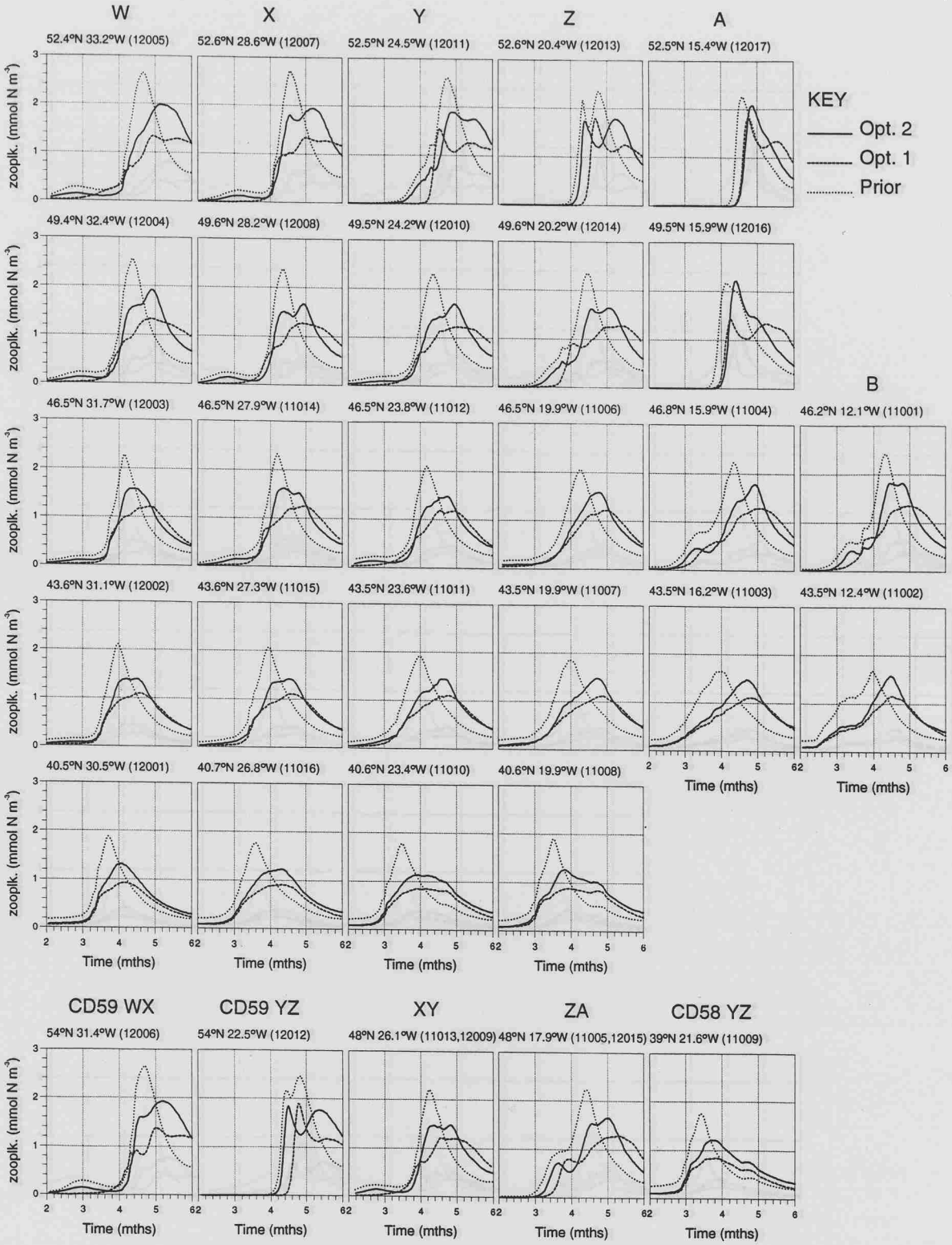

Figure E.4. Model solutions for zooplankton, from March to June 1991, at Vivaldi SeaSoar run locations.

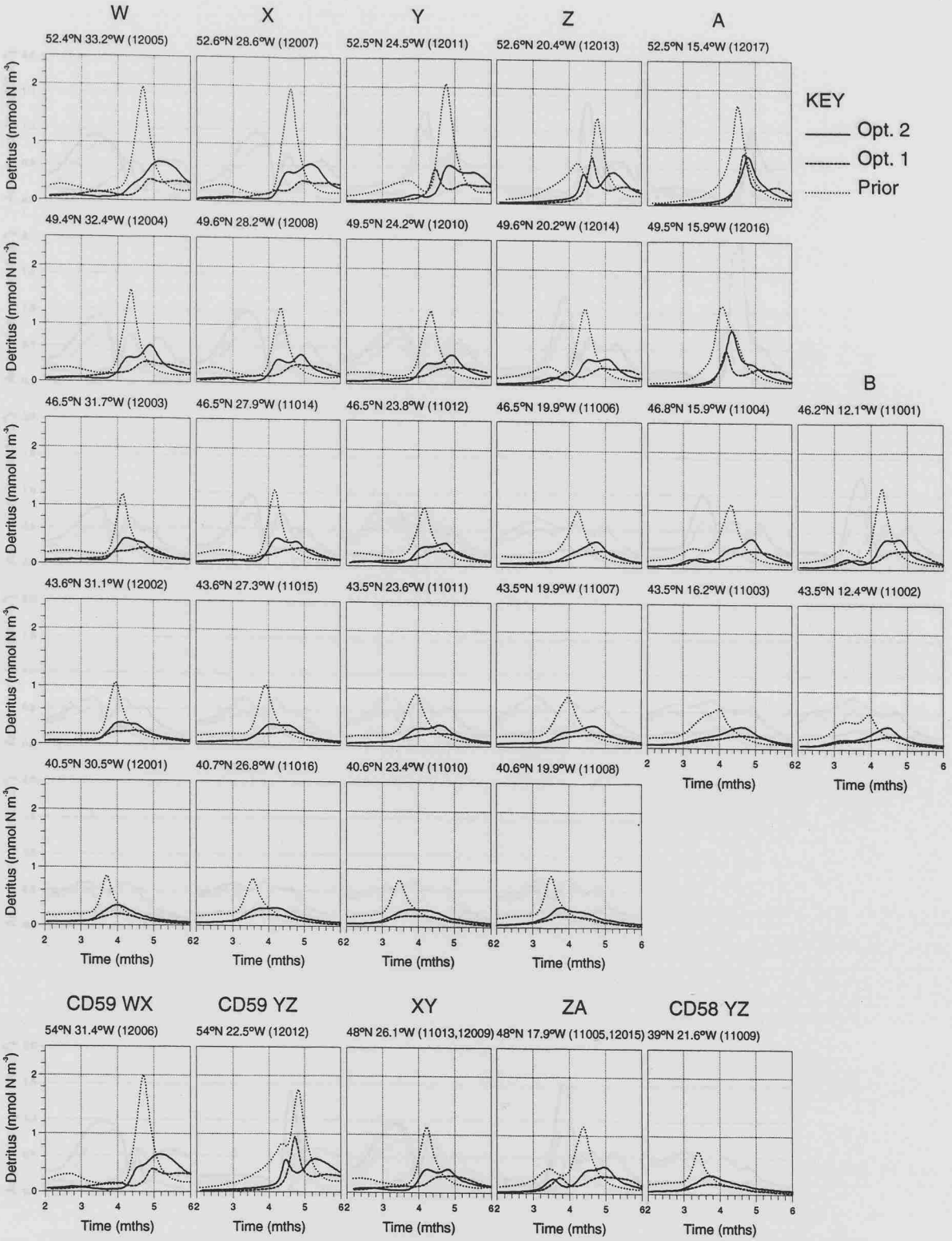

Figure E.5. Model solutions for detritus, from March to June 1991, at Vivaldi SeaSoar run locations.

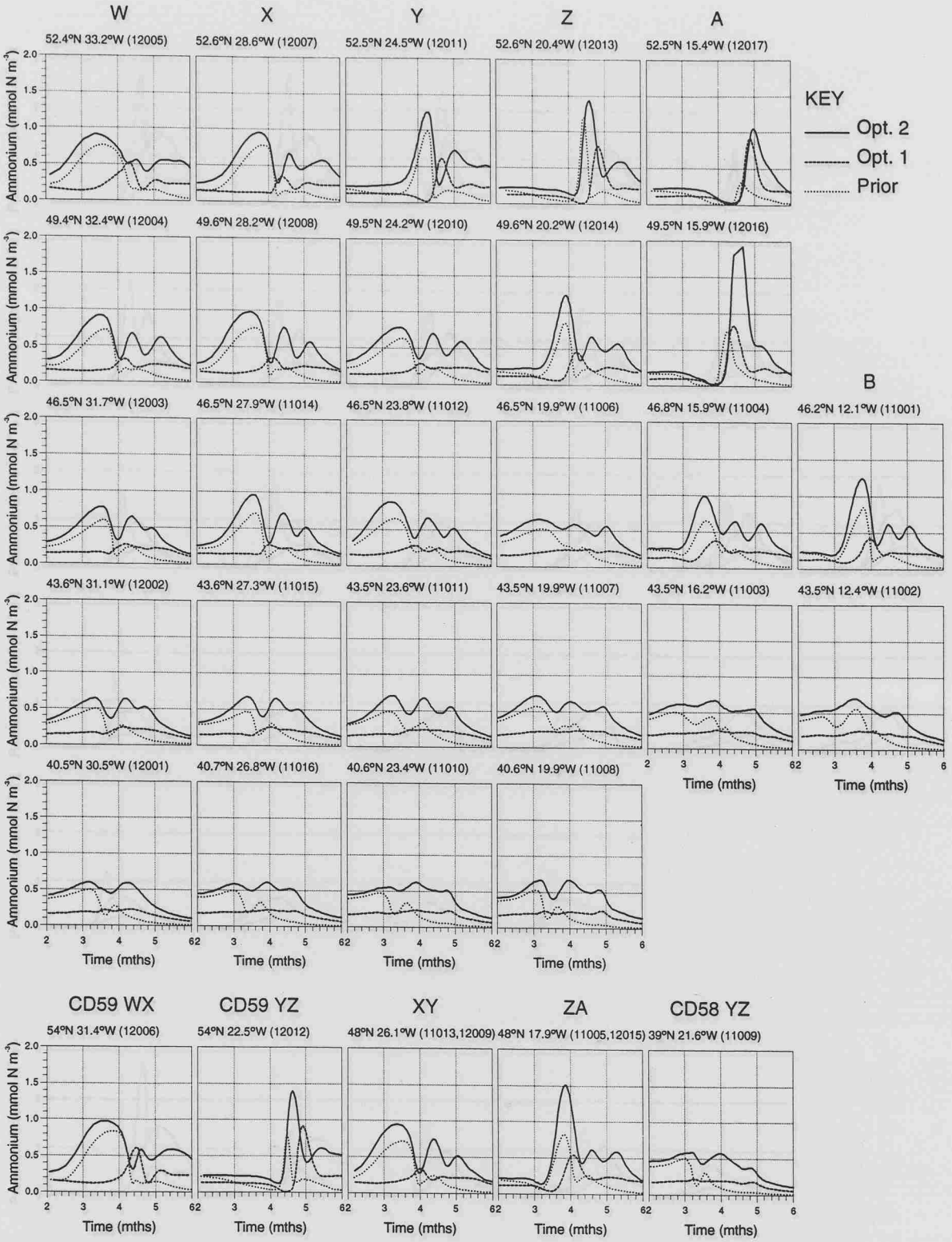

Figure E.6. Model solutions for ammonium, from March to June 1991, at Vivaldi SeaSoar run locations.

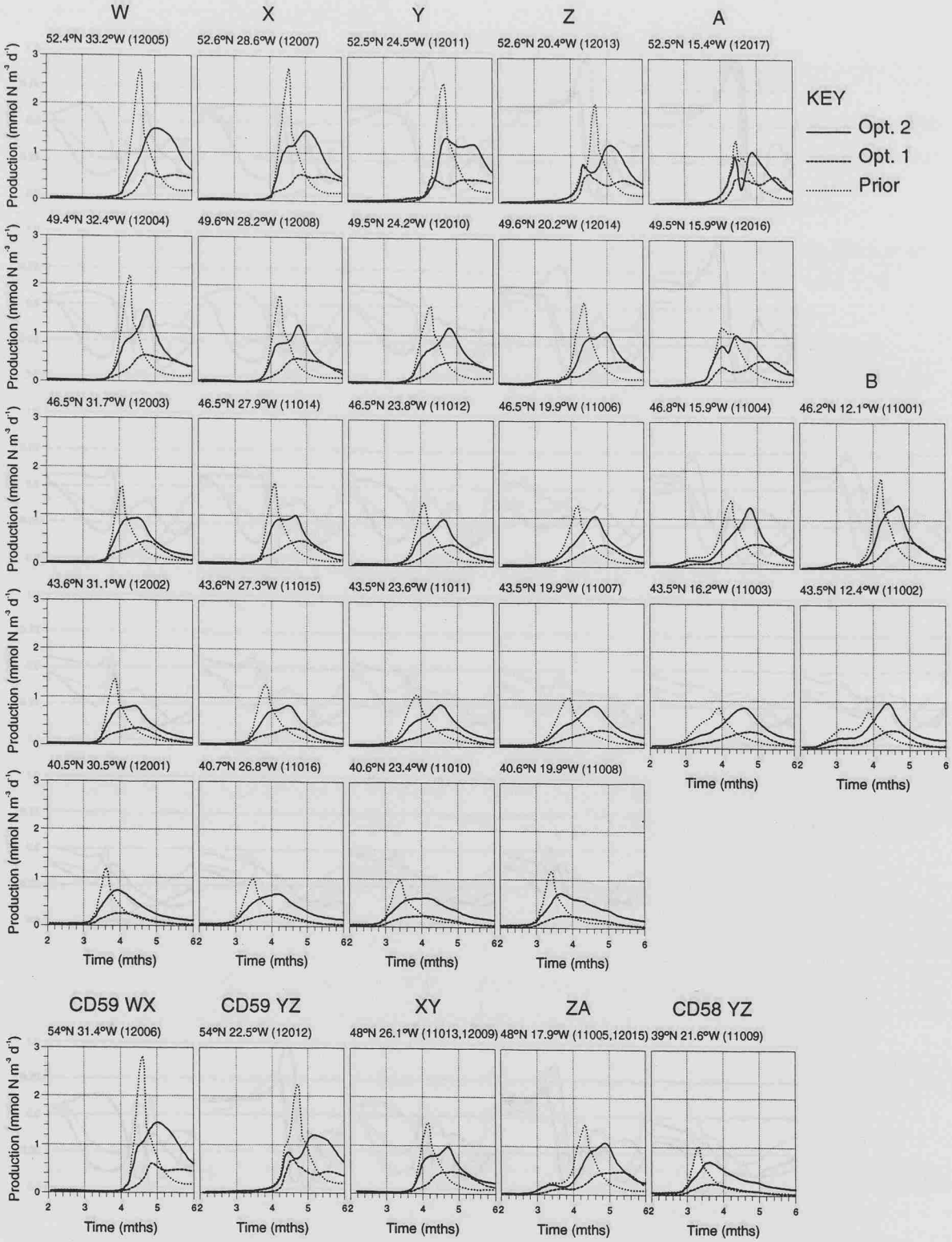

Figure E.7. Model solutions for primary production, from March to June 1991, at Vivaldi SeaSoar run locations.

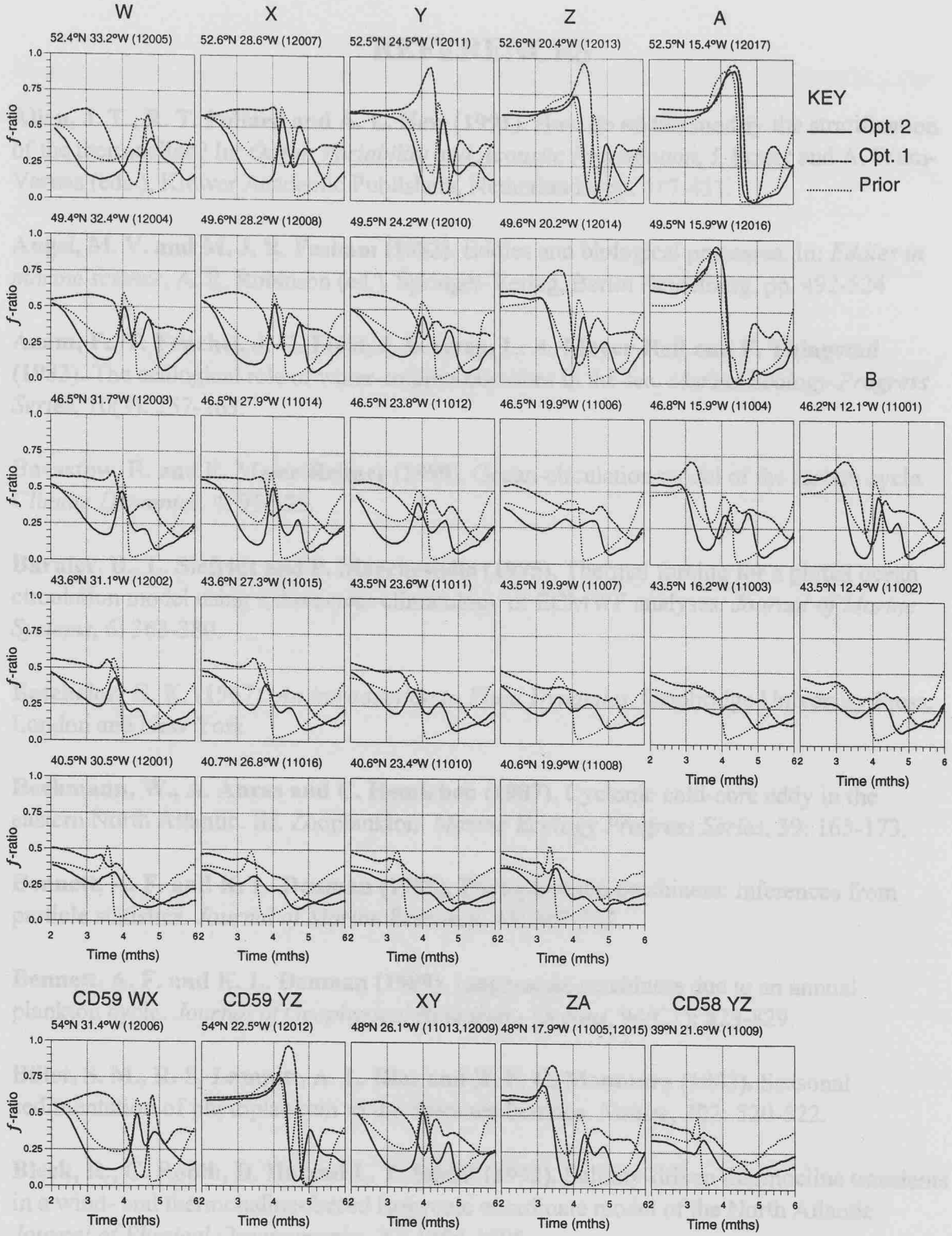

Figure E.8. Model solutions for f-ratio, from March to June 1991, at Vivaldi SeaSoar run locations.

REFERENCES

Allen, J. T., R. T. Pollard and A. L. New (1991). How do eddies modify the stratification of the thermocline? In: *Ocean Variability and Acoustic Propagation*, J. Potter and A. Warn-Varnas (eds.), Kluwer Academic Publishers, Netherlands, pp. 417-431.

Angel, M. V. and M. J. R. Fasham (1983). Eddies and biological processes. In: *Eddies in marine science*, A. R. Robinson (ed.), Springer-Verlag, Berlin Heidelburg, pp. 492-524

Azam, F., T. Fenchel, J. G. Field, J. S. Gray, L. A. Meyer-Reil and F. Thingstad (1983). The ecological role of water-column microbes in the sea. *Marine Ecology-Progress Series*, 10(3): 257-263.

Bacastow, R. and E. Maier-Reimer (1990). Ocean-circulation model of the carbon cycle. *Climate Dynamics*, 4: 95-125.

Barnier, B., L. Siefridt and P. Marchesiello (1995). Thermal forcing for a global ocean circulation model using a three-year climatology of ECMWF analyses. *Journal of Marine Systems*, 6: 363-380.

Batchelor, G. K. (1967). *An Introduction to Fluid Dynamics*, Cambridge University Press, London and New York

Beckmann, W., A. Auras and C. Hemleben (1987). Cyclonic cold-core eddy in the eastern North Atlantic. III. Zooplankton. *Marine Ecology Progress Series*, 39: 165-173.

Bennett, A. F. and K. L. Denman (1985). Phytoplankton patchiness: inferences from particle statistics. *Journal of Marine Research*, 43: 307-335.

Bennett, A. F. and K. L. Denman (1989). Large-scale patchiness due to an annual plankton cycle. *Journal of Geophysical Research - Oceans*, 94(C1): 823-829.

Billet, S. M., R. S. Lampitt, A. L. Rice and R. F. C. Mantoura (1983). Seasonal sedimentation of phytoplankton to the deep-sea benthos. *Nature*, 302: 520-522.

Bleck, R., C. Rooth, D. Hu and L. T. Smith (1992). Salinity-driven thermocline transients in a wind- and thermohaline-forced isopycnic coordinate model of the North Atlantic. *Journal of Physical Oceanography*, 22: 1486-1505.

Boggs, P. T. and J. E. Rogers (1990). Orthogonal distance regression. *Contemporary Mathematics*, 112: 183-194.

Boyd, P. W., D. L. Muggli, D. E. Varela, R. H. Goldblatt, R. Chretien, K. J. Orians, P. J. Harrison (1996). In vitro iron enrichment experiments in the NE subarctic Pacific. *Marine Ecology-Progress Series*, 136(1-3), 179-193.

Brainerd, K. E. and M. C. Greg (1995). Surface mixed and mixing layer depths. *Deep-Sea Research I*, 42(9): 1521-1543.

Brock, T. D. (1981). Calculating solar radiation for ecological studies. *Ecological Modelling*, 14(1/2): 1-19.

Broecker, W. S. and T. H. Peng (1982). *Tracers in the Sea*, Lamont-Doherty Geological Observatory, New York.

Brzezinski, M. A. (1985). The Si:C:N ratio of marine diatoms: interspecific variability and the effect of some environmental variables. *Journal of Phycology*, 21: 347-357.

Buesseler, K. O., M. P. Bacon, J. K. Cochran and H. D. Livingston (1992). Carbon and nitrogen export during the JGOFS North Atlantic bloom experiment estimated from ^{234}Th:^{238}U disequilibria. *Deep-Sea Research*, 39(7A/8A): 1115-1137.

Burkill, P. H., E. S. Edwards, A. W. G. John and M. A. Sleigh (1993). Microzooplankton and their herbivorous activity in the northeastern Atlantic Ocean. *Deep-Sea Research II*, 40: 479-494.

Campbell, J. W. (1989). Temporal patterns of phytoplankton abundance in the North Atlantic. *Advances in Space Research*, 9(7): 453-460.

Campbell, J. W. and T. Aarup (1992). New production in the North Atlantic derived from seasonal patterns of surface chlorophyll. *Deep-Sea Research*, 39(10A): 1669-1694.

Challenor, P. G. and D. J. T. Carter (1994). On the accuracy of monthly means. *Journal of Atmospheric and Oceanic Technology*, 11(5), 1425-1430.

Charlson, R. J., J. E. Lovelock, M. O. Andreae and S. G. Warren (1987). Oceanic phytoplankton, atmospheric sulphur, cloud albedo and climate. *Nature*, 326: 655-661.

Chavez, F. P., K. R. Buck, K. H. Coale, J. H. Martin, G. R. Ditullio, N. A. Welschmeyer, A. C. Jacobson and R. T. Barber (1991). Growth-rates, grazing, sinking and iron limitation of equatorial Pacific phytoplankton. *Limnology and Oceanography*, 36(8), 1816-1833.

Colebrook, J. M. (1982). Continuous plankton records: seasonal variations in the distribution and abundance of plankton in the North Atlantic Ocean and the North Sea. *Journal Plankton Research*, 4(3): 435-462.

Cunningham, S. A., M. J. Griffiths, J. Hemmings, S. G. Alderson, G. Griffiths, R. T. Pollard, J. C. Donlan, P. Lancaster, H. Leach, R. K. Lowry, M. W. Stirling, P. Smith, T. J. P. Gwilliam, J. Smithers, S. Keene, R. Pearce, T. R. Anderson, S. Bowerman

and D. Grohmann (1992). SeaSoar CTD, fluorescence and scalar irradiance data from RRS Charles Darwin Cruises 58/59, NE Atlantic (Vivaldi 91). Institute of Oceanographic Sciences Deacon Laboratory, Report No. 299.

Dam, H. G., C. A. Miller and S. H. Jonasdottir (1993). The trophic role of mesozooplankton at 47°N during the North Atlantic Bloom Experiment. *Deep-Sea Research II*, 40: 197-212.

Denman, K. L. and M. R. Abbott (1988). Time evolution of surface chlorophyll patterns from cross-spectrum analysis of satellite color images. *Journal of Geophysical Research - Oceans*, 93(C6): 6789-6798.

Denman, K. L. and M. R. Abbott (1994). Time scales of pattern evolution from cross-spectrum analysis of Advanced Very High Resolution Radiometer and Coastal Zone Color Scanner imagery. *Journal of Geophysical Research - Oceans*, 99(C4): 7433-7442.

Denman, K. L. and T. M. Powell (1984). Effects of physical processes on planktonic ecosystems in the coastal ocean. *Oceanography and Marine Biology Annual Review*, 22: 125-168.

da Silva, A. M., C. C. Young and S. Levitus (1994). Atlas of surface marine data 1994. Volume 1: algorithms and procedures. NOAA Atlas NESDIS 6, U. S. Government Printing Office, Washington D. C.

Ducklow, H. W., C. A. Carlson, N. R. Bates, A. H. Knap, A. F. Michaels and T. Takahashi (1995). Dissolved organic carbon as a component of the biological pump in the North Atlantic ocean. *Philosophical Transactions of the Royal Society of London*, B348: 161-167.

Ducklow, H. W. and R. P. Harris (1993). Introduction to the JGOFS North Atlantic Bloom Experiment. *Deep-Sea Research II*, 40: 1-8.

Dugdale, R. C. and J. J. Goering (1967). Uptake of new and regenerated forms of nitrogen in primary production. *Limnology and Oceanography*, 12: 196-206.

Emery, W. J. and J. Meincke (1986). Global water masses: summary and review. *Oceanologica Acta*, 9: 383-391.

Eppley, R. B. (1972). Temperature and phytoplankton growth in the sea. *Fishery Bulletin*, 70(4): 1063-1085.

Eppley, R. W. and B. J. Peterson (1979). Particulate organic matter flux and planktonic new production in the deep ocean. *Nature*, 282: 677-680.

Ertel, H. (1942). Ein neuer hydrodynamischer Wirbelsatz. *Meteorol. Z.*, 59: 271-281.

Esaias, W. E., G. C. Feldman, C. R. McClain and J. A. Elrod (1986). Monthly satellite-derived phytoplankton pigment distribution for the North Atlantic Ocean basin. *EOS*, 67: 835-837.

Evans, G. T. and J. S. Parslow (1985). A model of annual plankton cycles. *Biological oceanography*, 3(3): 327-347.

Falkowski, P. G., D. Ziemann, Z. Kolber and P. K. Bienfang (1991). Role of eddy pumping in enhancing primary production in the ocean. *Nature*, 352: 55-58.

Fasham, M. J. R. (1993). Modelling the marine biota. In: *The Global Carbon Cycle*, M. Heimann (ed.), Springer-Verlag, Berlin Heidelberg, pp. 457-504.

Fasham, M. J. R. (1995). Variations in the seasonal cycle of biological production in subarctic oceans: A model sensitivity analysis. *Deep-Sea Research I*, 42(7): 1111-1149.

Fasham, M. J. R., H. W. Ducklow and S. M. McKelvie (1990). A nitrogen-based model of plankton dynamics in the oceanic mixed layer. *Journal of Marine Research*, 48: 591-639.

Fasham, M. J. R. and G. T. Evans (1995a). The use of optimisation techniques to model marine ecosystem dynamics at the JGOFS station at 47°N 20°W. *Philosophical Transactions of the Royal Society of London B*, 348: 203-209.

Fasham, M. J. R. and G. T. Evans (1995b). How good are our ecosystem models? GLOBEC Numerical Modelling WG meeting, Nantes (unpublished manuscript).

Fasham, M. J. R., P. M. Holligan and P. R. Pugh (1983). The spatial and temporal development of the spring phytoplankton bloom in the Celtic Sea April 1979. *Progress in Oceanography*, 12: 87-145.

Fasham, M. J. R., T. Platt, B. Irwin and K. Jones (1985). Factors affecting the spatial pattern of the deep chlorophyll maximum in the region of the Azores front. *Progress in Oceanography*, 14: 129-165.

Fasham, M. J. R., J. L. Sarmiento, R. D. Slater, H. W. Ducklow and R. Williams (1993). Ecosystem behaviour at Bermuda Station "S" and Ocean Weather Station "India", a general circulation model and observational analysis. *Global Biogeochemical Cycles*, 7: 379-415.

Franks, P. J. S. and L. J. Walstad (1997). Phytoplankton patches at fronts: A model of formation and response to wind events. *Journal of Marine Research*, 55(1), 1-29.

Frost, B. W. (1987). Grazing control of phytoplankton stock in the open subarctic Pacific Ocean: a model assessing the role of mesozooplankton particularly the large calanoid copepods Neocalanus spp. *Marine Ecology Progress Series*, 39: 49-68.

Frost, B. W. (1991). The role of grazing in nutrient rich areas of the open sea. *Limnology and Oceanography*, 36(8): 1616-1630.

Frost, B. W. (1993). A modelling study of processes regulating plankton standing stock and production in the open subarctic Pacific. *Progress in Oceanography*, 32: 17-56.

Geider, R. J. (1993). Quantitative phytoplankton ecophysiology: implications for primary production and phytoplankton growth. ICES Marine Science Symposium 197: 52-62.

Geider, R. J., H. L. MacIntyre and T. M. Kana (1997). A dynamic model of phytoplankton growth and acclimation: responses of the balanced growth rate and the chlorophyll *a*:carbon ratio to light, nutrient-limitation and temperature. *Marine Ecology Progress Series*, 148: 187-200.

Gent, P. and J. McWilliams (1990). Isopycnal mixing in ocean circulation models. *Journal of Physical Oceanography*, 20: 150-155.

Gill, A. E. (1982). *Atmosphere-ocean dynamics*. Academic Press Inc., San Diego, California.

Glover, D. M. and P. G. Brewer (1988). Estimates of winter-time mixed layer nutrient concentrations in the North Atlantic. *Deep-Sea Research*, 35(9): 1525-1546.

Gower, J. F. R., K. L. Denman and R. J. Holyer (1980). Phytoplankton patchiness indicates the fluctuation spectrum of mesoscale oceanic structure. *Nature*, 288: 157-159.

Gran, H. H. and T. Braarud (1935). A quantitative study on the phytoplankton of the Bay of Fundy and the Gulf of Maine including observations on hydrography, chemistry and morbidity. *Journal of the Biological Board, Canada*, 1: 219-467.

Griffiths, G., S. Cunningham, M. Griffiths, R. T. Pollard, H. Leach, S. Holley, R. Paylor, T. W. N. Haine, A. Ríos, S. G. Alderson, R. K. Lowry, P. Smith, M. Preston, T. J. P. Gwilliam, J. Smithers, S. Keene, J. Hemmings and T. R. Anderson (1992). CTD oxygen, tracer and nutrient data from RRS Charles Darwin Cruises 58/59 in the NE Atlantic as part of Vivaldi '91. Institute of Oceanographic Sciences Deacon Laboratory, Report No. 296.

Haine, T. W. N. and J. Marshall (1998). Gravitational, symmetric and baroclinic instability of the ocean mixed layer. *Journal of Physical Oceanography*, 28(4): 634-658.

Harris, G. P. (1980). Temporal and spatial scales in phytoplankton ecology. Mechanisms, methods, models, and management. *Canadian Journal of Fisheries and Aquatic Science*, 37: 877-900.

Harris, G. P. (1986). Phytoplankton ecology: structure, function and fluctuation. *London, Chapman and Hall*

Harrison, W. G., E. J. H. Head, E. P. W. Home, B. Irwin, W. K. W. Li, A. R. Longhurst, M. A. Paranjape and T. Platt (1993). The western North Atlantic Bloom Experiment. *Deep-Sea Research II*, 40(1/2): 278-305.

Haury, L. R., J. A. McGowan and P. H. Wiebe (1978). Patterns and processes in the time-space scales plankton distributions. In: *Spatial pattern in plankton communities*, J. H. Steele (ed.). Plenum Press, New York, pp. 277-327.

Holligan, P. M., E. Fernández, J. Aiken, W. M. Balch, P. Boyd, P. H. Burkill, M. Finch, S. B. Groom, G. Malin, K. Muller, D. A. Purdie, C. Robinson, C. C. Trees, S. M. Turner and P. V. D. Wal (1993). A biogeochemical study of the coccolithophore, *Emiliania huxleyi*, in the North Atlantic. *Global Biogeochemical Cycles*, 7(4): 879-900.

Hurtt, G. C. and R. A. Armstrong (1996). A pelagic ecosystem model calibrated with BATS data. *Deep-Sea Research II*, 43(2-3): 653-683.

Hutchinson, G. E. (1953). The concept of pattern in ecology. *Proceedings of the Academy of Natural Sciences, Philadelphia*, 105: 1-12.

Intergovernmental Panel on Climate Change (1990). Climate change: the IPCC scientific assessment. Report prepared for IPCC by Working Group I, J. T. Houghton, G. J. Jenkins and J. J. Ephraums (eds.), Cambridge University Press.

Intergovernmental Panel on Climate Change (1996). Climate change 1995 - The science of climate change: contribution of Working Group I to the second assessment report of the Intergovernmental Panel on Climate Change, J. T. Houghton, L. G. Meira Filho, B. A. Callander, N. Harris, A. Kattenberg and K. Maskell (eds.), Cambridge University Press.

Jia, Y. (submitted). On the formation of an Azores current due to Mediterranean overflow in a modelling study of the North Atlantic. *Journal of Physical Oceanography.*

Joint, I., A. Pomroy, G. Savidge and P. Boyd (1993). Size-fractionated primary production in the northeast Atlantic in May-July 1989. *Deep-Sea Research II*, 40: 423-440.

Josey, S. A., E. C. Kent and P. K. Taylor (in press). New insights into the ocean heat budget closure problem from analysis of the SOC air-sea flux climatology. *Journal of Climate.*

Kent, E. C., P. K. Taylor, B. S. Truscott and J. S. Hopkins (1993). The accuracy of voluntary observing ships' meteorological observations - results of the V.S.O.P. *North American Journal of Atmospheric and Oceanic Technology*, 10(4): 591-608.

Kirk, J. T. O. (1988). Solar heating of water bodies as influenced by their inherent optical properties. *Journal of Geophysical Research - Atmospheres*, 93(D9): 10897-10908.

Kishi, M. J. (1994). Prediction of phytoplankton growth in a warm-core ring using three dimensional ecosystem model. *Journal of Oceanography*, 50: 489-498.

Klein, P. and B. L. Hua (1988). Mesoscale heterogeneity of the wind-driven mixed layer: Influence of a quasigeostrophic flow. *Journal of Marine Research*, 46: 495-525.

Klepper, O., B. J. D. Haan and H. V. Huet (1994). Biochemical feedbacks in the oceanic carbon cycle. *Ecological modelling*, 75/76: 459-469.

Kraichnan, R. H. (1967). Inertial ranges in two-dimensional turbulence. *Physical Fluids*, 10: 1417-1423.

Kraichnan, R. H. (1971). Inertial range transfer in two- and three-dimensional turbulence. *Journal of Fluid Mechanics*, 47: 525-535.

Kraichnan, R. H. and D. Montgomery (1980). Two-dimensional turbulence. *Reports in Progress in Physics*, 43: 547-619.

Kraus, E. B. and J. S. Turner (1967). A one-dimensional model of the seasonal thermocline: II. The general theory and its consequences. *Tellus*, 19: 98-106.

Lamb, P. J. (1984). On the mixed-layer climatology of the north and tropical Atlantic. *Tellus*, 36A: 292-305.

Lee, M.-M., D. P. Marshall and R. G. Williams (1997). On the eddy transfer of tracers: Advective or diffusive? *Journal of Marine Research*, 55, 483-505.

Le Traon, P. Y. (1991). Time scales of mesoscale variability and their relationship with space scales in the North Atlantic. *Journal of Marine Research*, 49: 467-492.

Lenz, J., A. Morales and J. Gunkel (1993). Mesozooplankton standing stock during the North Atlantic spring bloom in 1989 and its potential grazing pressure on phytoplankton: a comparison between low, medium and high latitudes. *Deep-Sea Research II*, 40(1/2): 559-572.

Levitus, S. (1982). *Climatological atlas of the world ocean.* National Oceanic and Atmospheric Administration, Rockville, Maryland.

Lévy, M., L. Mémery and G. Madec (1998). The onset of a bloom after deep winter convection in the northwestern Mediterranean Sea: mesoscale process study with a primitive equation model. *Journal of Marine Systems*, 16(1-2): 7-21.

Lewin, J. C. (1962). Silicification. In: *Physiology and biochemistry of the algae*, R. E. Lewin (ed.), Academic Press, pp. 445-455.

Lochte, K., H. W. Ducklow, M. J. R. Fasham and C. Stienen (1993). Plankton succession and carbon cycling at 47°N 20°W during the JGOFS North Atlantic Bloom Experiment. *Deep-Sea Research II*, 40: 91-114.

Lochte, K. and O. Pfannkuche (1987). Cyclonic cold-core eddy in the eastern North Atlantic. II. Nutrients, phytoplankton and bacterioplankton. *Marine Ecology Progress Series*, 39(2): 153-164.

Longhurst, A. (1995). Seasonal cycles of pelagic production and consumption. *Progress in Oceanography*, 36: 77-167.

Longhurst, A., S. Sathyendranath, T. Platt and C. Caverhill (1995). An estimate of global primary production in the ocean from satellite radiometer data. *Journal of Plankton Research*, 17(6): 1245-1271.

Longhurst, A. R. and W. G. Harrison (1989). The biological pump: profiles of plankton production and consumption in the ocean. *Progress in Oceanography*, 22(1): 47-123.

Marra, J. and C. Ho (1993). Initiation of the spring bloom in the northeast Atlantic (47°N, 20°W): a numerical simulation. *Deep-Sea Research II*, 40: 55-74.

Martin, J. H. and S. E. Fitzwater (1988). Iron deficiency limits phytoplankton growth in the northeast Pacific subarctic. *Nature*, 331, 341-343.

Martin, J. H., S. E. Fitzwater, R. M. Gordon, C. N. Hunter and S. J. Tanner (1993). Iron, primary production and carbon-nitrogen flux studies during the JGOFS North Atlantic Bloom Experiment. *Deep-Sea Research II*, 40(l/2): 115-134.

McClain , C. R., M. L. Cleave, G. C. Feldman, W. W. Gregg, S. B. Hooker and N. Kuring (1998). Science quality SeaWiFs data for global biogeochemical research. *Sea Technology*, 39(9): 10-16.

McClain, C. R. and J. Firestone (1993). An investigation of Ekman upwelling in the North Atlantic. *Journal of Geophysical Research - Oceans*, 98(C7): 12327-12339.

McCulloch, M. E. (1996). Heat content changes inferred from single hydrographic sections. Ocean Modelling, S.C.O.R. newsletter (unpublished manuscript), 113, 1-3 (& Figures pp13-14).

McCulloch, M. E. and H. Leach (1997). Seasonal heat and freshwater budgets of the upper ocean in the north-east Atlantic. *Quarterly Journal of the Royal Meteorological Society*, 123(539A): 767-784.

McGillicuddy, D. J. and A. R. Robinson (1997). Eddy-induced nutrient supply and new production in the Sargasso Sea. *Deep Sea Research I*, 44: 1427-1450.

McGillicuddy Jr., D. J., J. J. McCarthy and A. R. Robinson (1995a). Coupled physical and biological modeling of the spring bloom in the North Atlantic (I): model formulation and one dimensional bloom processes. *Deep-Sea Research*, 42(8): 1313-1357.

McGillicuddy Jr., D. J., A. R. Robinson and J. J. McCarthy (1995b). Coupled physical and biological modeling of the spring bloom in the North Atlantic (II): three dimensional bloom and post-bloom processes. *Deep-Sea Research*, 42(8): 1359-1398.

Miller, C. B., B. W. Frost, P. A. Wheeler, M. R. Landry, N. Welschmeyer and T. M. Powell (1991). Ecological dynamics in the subarctic Pacific, a possibly iron-limited ecosystem. *Limnology and Oceanography*, 36(8): 1600-1615.

Mills, E. L. (1989). *Biological Oceanography, An Early History, 1870-1960.* Cornell University Press.

Mitchell, G. B., E. A. Brody, O. Holm-Hansen, C. McClain and J. Bishop (1991). Light limitation of phytoplankton biomass and macronutrient utilization in the Southern Ocean. *Limnology and Oceanography*, 36(8): 1662-1677.

Mittelstaedt, E. (1987). Cyclonic cold-core eddy in the eastern North Atlantic. I. Physical description. *Marine Ecology Progress Series*, 39: 145-152.

Mooney, K. (1992). The role of the oceans in climate. *Marine Technology Society Journal*, 25(4): 55-56.

Moore, B. (1992). The changing global carbon cycle: dust to dust. *Marine Technology Society Journal*, 25(3): 19-24.

Morales, C. E., A. Bedo, R. P. Harris and P. R. G. Tranter (1991). Grazing of copepod assemblages in the north-east Atlantic: the importance of the small size fraction. *Journal of Plankton Research*, 13(2): 455-472.

Moyer, K. A. and R. A. Weller (1997). Observations of surface forcing from the subduction experiment: A comparison with global model products and climatological datasets. *Journal of Climate*, 10(11): 2725-2742.

Nelson, D. M., J. J. McCarthy, T. M. Joyce and H. W. Ducklow (1989). Enhanced near-surface nutrient availability and new production resulting from the frictional decay of a Gulf Stream warm core ring. *Deep-Sea Research*, 36(5A): 705-714.

Nelson, D. M. and W. O. Smith Jr (1991). Sverdrup revisited: Critical depths, maximum chlorophyll levels, and the control of Southern Ocean productivity by the irradiance-mixing regime. *Limnology and Oceanography*, 36(8): 1650-1661.

New, A. L., R. Bleck, Y. Jia, R. Marsh, M. Huddleston and S. Barnard (1995). An isopycnic model study of the North Atlantic. Part I: model experiment. *Journal of Physical Oceanography*, 25(11): 2667-2699.

Nurser, A. J. G. and J. W. Zhang (in revision). Eddy-induced mixed layer shallowing and mixed-layer/thermocline exchange. *Journal of Geophysical Research.*

Onken, R. (1992). Mesoscale upwelling and density finestructure in the seasonal thermocline - a dynamical model. *Journal of Physical Oceanography*, 22: 1257-1273.

Passow, U. and R. Peinert (1993). The role of plankton in particle flux: two case studies from the northeast Atlantic. *Deep-Sea Research II*, 40(1/2): 573-585.

Platt, T., B. Bird and S. Sathyendranath (1991a). Critical depth and marine primary production. *Proceedings of the Royal Society of London B*, 246: 205-217.

Platt, T., C. Caverhill and S. Sathyendranath (1991b). Basin-scale estimates of oceanic primary production by remote sensing: the North Atlantic. *Journal of Geophysical Research - Oceans*, 96(C8): 15147-15159.

Pollard, R. T., M. J. Griffiths, S. A. Cunningham, J. F. Read, F. F. Pérez and A. F. Ríos (1996). Vivaldi 1991 - A study of the formation, circulation and ventilation of Eastern North Atlantic Water. *Progress in Oceanography*, 37: 167-192.

Pollard, R. T., H. Leach and G. Griffiths (1991). RRS Charles Darwin Cruises 58 & 59, 25 Apr-16 May; 18 May-10 Jun 1991. VIVALDI '91. Institute of Oceanographic Sciences Deacon Laboratory Cruise Report No. 228.

Pollard, R. T. and L. Regier (1990). Large variations in potential vorticity at small spatial scales in the upper ocean. *Nature*, 348(6298): 227-229.

Pollard, R. T. and L. A. Regier (1992). Vorticity and vertical circulation at an ocean front. *Journal of Physical Oceanography*, 22: 609-625.

Press, W. H., B. P. Flannery, S. A. Teukolsky and W. T. Vetterling (1992). Numerical recipes in C: the art of scientific computing, 2nd edition, Cambridge University Press.

Price, N. M., B. A. Ahner, F. M. M. Morel (1994). The equatorial Pacific Ocean: Grazer controlled phytoplankton in an iron-limited ecosystem. *Limnology and Oceanography*, 39(3), 520-534.

Priestly, M. B. (1981). *Spectral Analysis and Time Series*. Academic Press, London and San Diego.

Redfield, A. C. (1934). *On the proportions of organic derivatives in sea water and their relationship to the composition of plankton.* James Johnstone Memorial Volume (Liverpool).

Redfield, A. C. (1942). The processes determining the concentration of oxygen, phosphate and other organic derivatives within the depths of the Atlantic Ocean. *Papers in Physical Oceanography and Meteorology*, 9: 1-22.

Rhines, P. B. (1979). Geostrophic turbulence. *Annual Review of Fluid Mechanics*, 11: 401-441.

Riebesell, U., D. A. Wolf-Gladrow and V. Smetacek (1993). Carbon dioxide limitation of marine phytoplankton growth rates. *Nature*, 361: 249-251.

Ríos, A. F., T. R. Anderson and F. F. Pérez (1995). The carbonic system distribution and fluxes in the NE Atlantic during spring 1991. *Progress in Oceanography*, 35(4): 295-314.

Robertson, J. E., C. Robinson, D. R. Turner, P. Holligan, A. J Watson, P. Boyd, E. Fernandez and M. Finch (1994). The impact of a coccolithophore bloom on oceanic carbon uptake in the northeast Atlantic during summer 1991. *Deep-Sea Research I*, 41(2), 297-314.

Robertson, J. E., A. J. Watson, C. Langdon, R. D. Ling and J. W. Wood (1993). Diurnal variation in surface pCO_2 and O_2 at 60°N, 20°W in the North Atlantic. *Deep-Sea Research II*, 40(1/2): 409-422.

Robinson, A. R. (ed.) (1983). *Eddies in marine science*. Springer-Verlag, Berlin Heidelburg.

Robinson, A. R. (1996). Physical processes, field estimation and an approach to interdisciplinary ocean modeling. *Earth-Science Reviews*, 40: 3-54.

Robinson, A. R., H. G. Arango, A. J. Miller, A. Warn-Varnas, P. -M Poulain and W. G. Leslie (1996). Real-time operational forecasting on shipboard of the Iceland-Faeroe frontal variability. *Bulletin of the American Meteorological Society*, 77(2): 243-259.

Robinson, A. R., D. J. McGillicuddy, J. Calman, H. W. Ducklow, M. J. R. Fasham, F. E. Hoge, W. G. Leslie, J. J. McCarthy, S. Podewski, D. L. Porter, G. Saure and J. A. Yoder (1993). Mesoscale and upper ocean variabilities during the 1989 JGOFS bloom study. *Deep-Sea Research II*, 40: 9-35.

Rossby, C. G. (1940). Planetary flow patterns in the atmosphere. *Quarterly Journal of the Royal Meteorological Society*, 66, Suppl.: 68-97.

Sambrotto, R. N., J. H. Martin, W. W. Broenkow, C. Carlson and S. E. Fitzwater (1993). Nitrate utilization in surface waters of the Iceland basin during spring and summer of 1989. *Deep-Sea Research II*, 40: 441-458.

Sarmiento, J. L. and C. LeQuere (1996). Oceanic carbon dioxide uptake in a model of century-scale global warming. *Science*, 274(5291): 1346-1350.

Sarmiento, J. L., R. D. Slater, M. J. R. Fasham, H. W. Ducklow, J. R. Toggweiler and G. T. Evans (1993). A seasonal three-dimensional ecosystem model of nitrogen cycling in the North Atlantic euphotic zone. *Global Biogeochemical Cycles*, 7(2): 417-450.

Sathyendranath, S., A. D. Gouveia, S. R. Shetye, P. Ravindran and T. Platt (1991). Biological control of surface temperature in the Arabian Sea. *Nature*, 349: 54-56.

Sathyendranath, S., A. Longhurst, C. M. Caverhill and T. Platt (1995). Regionally and seasonally differentiated primary production in the North Atlantic. *Deep-Sea Research*, 42(10): 1773-1802.

Savidge, G., D. R. Turner, P. H. Burkill, A. J. Watson, M. V. Angel, R. D. Pingree, H. Leach and K. J. Richards (1992). The BOFS 1990 Spring Bloom Experiment: Temporal evolution and spatial variability of the hydrographic field. *Progress in Oceanography*, 29: 235-281.

Schmitt, R. W., P. S. Bogden and C. E. Dorman (1989). Evaporation Minus Precipitation and Density Fluxes for the North Atlantic. *Journal of Physical Oceanography*, 19: 1208-1221.

Shaffer, G. (1993). Effects of the marine biota on global carbon cycling. In: *The Global Carbon Cycle*, M. Heimann (ed.), Springer-Verlag, Berlin Heidelberg, pp. 431-456.

Sieracki, M. E., P. G. Verity and D. K. Stoecker (1993). Plankton community response during the 1989 North Atlantic spring bloom. *Deep-Sea Research II*, 40: 213-226.

Smetacek, V. and U. Passow (1990). Spring bloom initiation and Sverdrup's critical depth model. *Limnology and Oceanography*, 35(1): 228-234.

Smith, C. L., K. J. Richards and M. J. R. Fasham (1996). The impact of mesoscale eddies on plankton dynamics in the upper ocean. *Deep-Sea Research I*, 43(11-12): 1807-1832.

Smith, S. D. and F. W. Dobson (1984). The heat budget at Ocean Weather Ship Bravo. *Atmosphere-Oceans*, 22: 1-22.

Smith, S. E. (1936). Environmental control of photosynthesis. *Proceedings of the National Academy of Sciences U.S.A.*, 22: 504-511.

Srokosz, M. A. *et al.* (1997). RRS *Discovery* Cruise 227, 15 Apr-16 May 1997. Plankton patchiness studies by ship and satellite: P^2S^3. Southampton Oceanography Centre Cruise Report, No. 12.

Steele, J. H. and E. W. Henderson (1981). A simple plankton model. *American Naturalist*, 117: 676-691.

Steele, J. H. and E. W. Henderson (1992). The role of predation in plankton models. *Journal of Plankton Research*, 14(1): 157-172.

Stramska, M. and T. D. Dickey (1994). Modeling phytoplankton dynamics in the northeast Atlantic during the initiation of the spring bloom. *Journal of Geophysical Research - Oceans*, 99(C5): 10241-10253.

Stramska, M., T. D. Dickey, A. Plueddemann, R. Weller, C. Langdon and J. Marra (1995). Bio-optical variability associated with phytoplankton dynamics in the North Atlantic Ocean during spring and summer of 1991. *Journal of Geophysical Research - Oceans*, 100(C4): 6621-6632.

Strass, V. (1990). On the calibration of large-scale fluorometric chlorophyll measurements from towed undulating vehicles. *Deep-Sea Research*, 37(3): 525-540.

Strass, V. (1992). Chlorophyll patchiness caused by mesoscale upwelling at fronts. *Deep-Sea Research*, 39: 75-96.

Strass, V. H., H. Leach and J. D. Woods (1992). On the seasonal development of mesoscale variability: the influence of the seasonal pycnocline formation. *Deep-Sea Research*, 39(9), 1627-1639.

Strass, V. and J. D. Woods (1988). Horizontal and seasonal variation of density and chlorophyll profiles between the Azores and Greenland. In: *Towards a theory of biological-physical interactions in the world ocean*, B. J. Rothschild (ed.), Dordrecht, D Reidel, pp. 113-136.

Strass, V. and J. D. Woods (1991). New production in the summer revealed by the meridional slope of the deep chlorophyll maximum. *Deep-Sea Research*, 38: 35-56.

Sugiura, Y. (1965). On the reserved nutrient matters. *Bull. Soc. Franco-japonaise d'Oceanographie*, 2: 7-11.

Sverdrup, H. U. (1953). On conditions for the vernal blooming of phytoplankton. *Journal du Conseil Permanent International pour L'Exploration de la Mer*, 18: 287-295.

Taylor, A. H., R. J. Geider and F. J. H. Gilbert (1997). Seasonal and latitudinal dependencies of phytoplankton carbon-to-chlorophyll *a* ratios: results of a modelling study. *Marine Ecology Progress Series*, 152: 51-66.

Taylor, A. H., D. S. Harbour, R. P. Harris, P. H. Burkill and E. S. Edwards (1993). Seasonal succession in the pelagic ecosystem of the North Atlantic and the utilization of nitrogen. *Journal of Plankton Research.*, 15: 875-891.

Taylor, A. H. and I. Joint (1990). A steady-state analysis of the 'microbial loop' in stratified systems. *Marine Ecology Progress Series*, 59(1/2): 1-17.

Taylor, A. H. and J. A. Stephens (1993). Diurnal variations of convective mixing and the spring bloom of phytoplankton. *Deep-Sea Research II*, 40(1/2): 389-408.

Taylor, A. H., A. J. Watson, M. Ainsworth, J. E. Robertson and D. R. Turner (1991). A modelling investigation of the role of phytoplankton in the balance of carbon at the surface of the North Atlantic. *Global Biogeochemical Cycles*, 5(2): 151-171.

Taylor, A. H., A. J. Watson and J. E. Robertson (1992). The influence of the spring phytoplankton bloom on carbon dioxide and oxygen concentrations in the surface waters of the northeast Atlantic during 1989. *Deep-Sea Research*, 39(2): 137-152.

The DYNAMO Group (1997). Dynamics of North Atlantic Models: Simulation and assimilation with high resolution models. Berichte aus dem Institut für Meereskunde an der Christian-Albrechts-Universität, Kiel, Nr. 294.

Thompson, K. R., R. F. Marsden and D. G. Wright (1983). Estimation of low-frequency wind-stress fluctuations over the open ocean. *Journal of Physical Oceanograhy*, 13(6): 1003-1011.

Tranter, D. J., R. R. Parker and G. R. Cresswell (1980). Are warm-core eddies unproductive? *Nature*, 284: 540-542.

U.S. Joint Global Ocean Flux Study Office (1989). Ocean color, a folio of Coastal Zone Color Scanner imagery. WHOI, Woods Hole, MA, U.S.A.

Walstad, L. and A. Robinson (1993). A coupled surface boundary layer - quasigeostrophic model. *Dynamics of Atmospheres and Oceans*, 18: 151-207.

Wang, D. -P. (1993). Model of frontogenesis: subduction and upwelling. *Journal of Marine Research*, 51: 497-513.

Watson, A. J., C. Robinson, J. E. Robertson, P. J. le B. Williams and M. J. R. Fasham (1991). Spatial variability in the sink for atmospheric carbon dioxide in the North Atlantic. *Nature*, 350: 50-53.

Weeks, A., M. H. Conte, R. P. Harris, A. Bedo, I. Bellan, P. H. Burkill, E. S. Edwards, D. S. Harbour, H. Kennedy, C. Llwellyn, R. F. C. Mantoura, C. E. Morales, A. J. Pomroy and C. M. Turley (1993a). The physical and chemical environment and changes in community structure associated with bloom evolution: the JGOFS North Atlantic Bloom Experiment. *Deep-Sea Research II*, 40: 347-368.

Weeks, A. R., M. J. R. Fasham, J. Aiken, D. S. Harbour, J. F. Read and I. Bellan (1993b). The spatial and temporal development of the spring bloom during the JGOFS North Atlantic Bloom Experiment, 1989. *Journal of the Marine Biological Association of the United Kingdom*, 73: 253-282.

Welschmeyer, N. A., S. Strom, R. Goericke, G. Ditullio, M. Blevin and W. Peterson (1993). Primary production in the subarctic Pacific Ocean: project SUPER. *Progress in Oceanography*, 32, 101-136.

Williams, R. (1988). Spatial heterogeneity and niche differentiation in oceanic zooplankton. In: *Biology of Copepods*, G. A. Boxshall and H. K. Schimke (eds.), *Hydrobiologia*, 167/168, pp. 151-159

Williams, R. and G. A. Robinson (1973). Primary production at Ocean Weather Station India (59°00'N, 19°00'W) in the North Atlantic. *Bulletins of Marine Ecology*, 8: 115-121.

Williams, R. G. and M. J. Follows (1998). The Ekman transfer of nutrients and maintenance of new production over the North Atlantic. *Deep-Sea Research I*, 45(2-3): 461-489.

Williamson (1992). Carbon fluxes in the upper ocean. *Marine Technology Society Journal*, 25(4): 60.

Woodruff, S. D., S. J. Lubker, K. Wolter, S. J. Worley and J.D. Elms (1993). Comprehensive Ocean-Atmosphere Data Set (COADS) release 1a: 1980-92. *Earth System Monitor*, 4(1), 4-8.

Woods, J. and W. Barkmann (1993). The plankton multiplier - positive feedback in the greenhouse. *Journal of Plankton Research*, 15(9): 1053-1074.

Woods, J. D. (1980). Do waves limit turbulent diffusion in the ocean? *Nature*, 288: 219-224.

Woods, J. D. (1985). The physics of thermocline ventilation. In: *Coupled ocean-atmosphere models*, J. C. J. Nihoul (ed.), Elsevier, pp. 543-590

Woods, J. D. (1988). Mesoscale upwelling and primary production. In: *Towards a theory of biological-physical interactions in the world ocean*, B. J. Rothschild (ed.), Dordrecht, D Reidel, pp. 1-30.

Woods, J. D. and W. Barkmann (1986). The response of the upper ocean to solar heating. I: The mixed layer. *Quarterly Journal of the Royal Meteorological Society*, 112: 1-27.

World Meteorological Office (1994). International list of selected, supplementary and auxilliary ships. WMO Report, WMO, Geneva.

Wroblewski, J. (1977). A simulation of the distribution of *Acartia clausii* during Oregon upwelling August 1973. *Journal of Plankton Research*, 2, 43-68.

Wroblewski, J. S. (1989). A model of the spring bloom in the North Atlantic and its impact on ocean optics. *Limnology and Oceanography*, 34(8): 1563-1571.

Wroblewski, J. S., J. L. Sarmiento and G. R. Flierl (1988). An ocean basin scale model of plankton dynamics in the North Atlantic. 1. Solutions for the climatological oceanographic conditions in May. *Global Biogeochemical Cycles*, 2(3): 199-218.

Yentsch, C. S. (1990). Estimates of "new production" in the mid-North Atlantic. *Journal of Plankton Research*, 12(4): 717-734.

Yoder, J. A., C. R. McClain, G. C. Feldman and W. E. Esaias (1993). Annual cycles of phytoplankton chlorophyll concentrations in the global ocean: A satellite view. *Global Biogeochemical Cycles*, 7(1): 181-193.

Zhang, J. W. and A. J. G. Nurser (1995). Numerical modelling of eddy-driven fluid exchange between the oceanic mixed-layer and thermocline. James Rennell Centre for Ocean Circulation Internal Document, No. 18.

SOUTHAMPTON UNIVERSITY LIBRARY

USER'S DECLARATION

AUTHOR: TITLE:

DATE:

I undertake not to reproduce this thesis, or any substantial portion of it, or to quote extensively from it without first obtaining the permission, in writing, of the Librarian of the University of Southampton.

To be signed by each user of this thesis

DATE	SIGNATURE	ADDRESS